Universidade de Aveiro Departamento de Física
2017

Sangeetha Balabhadra

Nanopartículas contendo iões lantanídeos para termometria de luminescência

Ln^{3+}-doped nanoparticles for luminescence thermometry

Universidade de Aveiro Departamento de Física
2017

Sangeetha Balabhadra

Nanopartículas contendo iões lantanídeos para termometria de luminescência

Ln^{3+}-doped nanoparticles for luminescence thermometry

"Measure what is measurable, and make measurable what is not so"

–Galileo Galilei
Administration (1967), 15, 175.

Universidade de Aveiro Departamento de Física

2017

Sangeetha Balabhadra

Nanopartículas contendo iões lantanídeos para termometria de luminescência

Ln^{3+}-doped nanoparticles for luminescence thermometry

Dissertação apresentada à Universidade de Aveiro para cumprimento dos requisitos necessários à obtenção do grau de Doutor em Física, realizada sob a orientação científica do Doutor Luís António Ferreira Martins Dias Carlos, Professor Catedrático do Departamento de Física da Universidade de Aveiro e do Doutor João Carlos Matias Celestino Gomes da Rocha, Professor Catedrático do Departamento de Química da Universidade de Aveiro.

Trabalho desenvolvido no âmbito do projeto EC Marie Curie Initial Training Network LUMINET (316906), Fundação para a Ciência e a Tecnologia, (PTDC/CTM-NAN/4647/2014 e POCI-01-0145-FEDER-016687) e CICECO-Instituto de Materiais de Aveiro POCI-01-0145-FEDER-007679 (FCT UID /CTM /50011/2013).

o júri

presidente

Doutor João Filipe Colardelle da Luz Mano
Professor Catedrático, Universidade de Aveiro

Doutora Jana Berit Nieder
Investigadora, Head of Nanophotonics Department/Group Leader, Laboratório Ibérico Internacional de Nanotecnologia (INL)

Doutor Carlos Miguel Calisto Baleizão
Investigador Principal, Universidade de Lisboa

Doutor Senentxu Lanceros-Méndez
Professor Associado, Universidade do Minho

Doutora Maria Rute de Amorim Sá Ferreira André
Professora Associada com Agregação, Universidade de Aveiro

Orientador

Doutor Luís António Martins Dias Carlos
Professor Catedrático, Universidade de Aveiro

agradecimentos/ acknowledgements

Doing this PhD has been very challenging experience for me and it would not have been possible to do without the great support, motivation and encouragement that I have received from many people over the past years. Foremost, I gratefully acknowledge the funding received towards my PhD from EC Marie-Curie European Network (LUMINET 316906) and CICECO (PTDC/CTM-NAN/4647/2014 and POCI-01-0145-FEDER-016687). I would like to thank to the Department of Physics, Department of Chemistry, CICECO of University of Aveiro and Department of Biotechnology of University of Verona for providing great quality of scientific infrastructure and material conditions to perform my doctoral studies.

I am deeply indebted to my supervisor Prof. Dr. L. D. Carlos for giving me the opportunity to do a PhD in his research group, without his thoughtful guidance, great patience, critical comments and constant feedback this PhD would not have been achievable. I want to express my deep thanks to my esteemed co-supervisor Prof. Dr. J. Rocha and to Prof. Dr. M. Rute for offering valuable advices, for the support during the whole period of the PhD, and especially for the guidance during writing manuscripts. I am profoundly grateful to Prof. Dr. M. Bettinelli for giving me the wonderful opportunity to complete my Secondment under his supervision, it is truly an honor. I am very grateful for his patience, ideas and support.

My deep gratitude to Dr. M. L. Debasu can hardly be expressed in words for his constant assistance in experimental as well as technical works. I extend my thanks for granting to use part of his work. A special note of thanks goes to Dr. C. D. Brites for his willingness to lend a hand throughout PhD. I am very grateful to the present, past and visiting members of group of photonic hybrids and nanomaterials, in specific, Dr. V. Freitas, Dr. S. Correia, Dr. Moliria, Dr. Cintya and MSc. A. Botas. I would like to extend my gratitude to those who gave me access to the equipments and helped me out with the measurements: Dr. R. Soares for powder X-ray diffractometer, M. Ferro and B. Almeida for T/SEM images, Dr. C. Azevedo for UV-VIS and FTIR spectroscopies, Mr. E. Soares and Mrs. L. Carvalho for ICP analysis and Mrs. B. Costa for DLS measurements. I also want to thank, Dr. Z. Lin, Mr. F. Reis, Mr. I. Mateus, and Mr. M. Rocha for their help in many occasions. I am grateful to Prof. Dr. O. L. Malta, Dr. L. A. O. Nunes and Dr. H. Oliveira for their contributions and collaborations to the PhD project. A special note of thanks to Prof. E. Zych (Poland) and Prof. D. Jaque (Spain) for accepting and for evaluating this thesis. I extended my gratitude to the jury of this thesis for their valuable time.

I humbly thank people from group of Luminescent Materials: Dr. F. Piccinelli, E. Viviani, I. Carrasco, P. Cortelletti and G. Lucchini for their support in the laboratory during my Secondment period in University of Verona. I am grateful to all the students and professors in the LUMINET consortium, for the invaluable experience of participating in meetings. The associated discussions and unfolding friendships enriched my scientific and personal life. I owe a big thank to Dr. T. Grzyb for notifying this PhD opportunity. I am all thankful to my friends from Aveiro, Italy, Spain, Poland, Brazil and India for their continuous support and encouragement to strive towards my goal.

My endless gratitude to my family for their love, support and encouragement. Your prayers for me was what sustained me thus far. In the end, I would like to express appreciation for all those people who played an iota role during my PhD life.

palavras-chave

Iões lantanídeos, nanopartículas, fotoluminescência, conversão descendente de energia, conversão ascendente de energia, termometria, relação de intensidade de fluorescência, sensibilidade, janelas biológicas, e termometria primária

resumo

A temperatura é uma variável chave que afeta a maior parte dos sistemas, quer naturais quer construídos pelo Homem. A medida da temperatura é global, uma vez que regula a cinética e a reatividade daqueles sistemas, ao nível atómico e macroscópico. Os sensores convencionais são ineficientes para a medição remota da temperatura à micro e à nanoescala o que, nos últimos anos, tem inspirado o desenvolvimento de nanotermómetros não-invasivos, sem contato, autorreferenciados e exibindo alta sensibilidade térmica. Neste contexto, a utilização de iões lantanídeos trivalentes (Ln^{3+}), devido às suas propriedades fotoluminescentes que dependem fortemente da temperatura, tem sido uma das aproximações mais promissoras. Esta tese discuta as propriedades de nanopartículas dopadas com iões Ln^{3+} emitindo na gama espectral do visível e infravermelho-próximo como sensores de temperatura molecular.

Na primeira parte da tese, estudaram-se nanopartículas de Gd_2O_3 dopadas com Nd^{3+} operando na gama espectral do infravermelho-próximo como nanotermómetros luminescentes baseados num rácio de intensidades. A emissão de nanotubos e nanobastonetes de Gd_2O_3:Nd^{3+} foi medida usando um tubo fotomultiplicador R928 comum na primeira janela biológica (800–920 nm) tendo-se obtido na faixa fisiológica (288–323 K), respetivamente, uma sensibilidade térmica e uma incerteza em temperatura de 1.75±0.04 %·K^{-1} e 0.14±0.05 K. A dependência com a temperatura da emissão de nanoesferas de Gd_2O_3:Nd^{3+} na segunda janela biológica (1250–1550 nm), com excitação a 808 nm na primeira janela biológica, foi, também, estudada mostrando uma sensibilidade térmica máxima de 0.237±0.03 %·K^{-1} a 303 K.

Na segunda parte da tese foram desenvolvidas nanopartículas conversoras ascendentes de energia de Gd_2O_3 e SrF_2 dopadas com Yb^{3+}/Er^{3+} para termometria, tendo como parâmetro termométrico a intensidade integrada das transições $^2H_{11/2}$–$^4I_{15/2}$/$^4S_{3/2}$–$^4I_{15/2}$ do ião Er^{3+}. Desenvolveram-se nanoplataformas combinando nanotermómetros de Gd_2O_3:Yb^{3+}/Er^{3+} com nanopartículas de Ouro (nanoaquecedores) para medir a temperatura induzida pelo plasmão das partículas metálicas. A condição ótima para um aquecimento térmico efetivo foi conseguida ajustando a banda de ressonância de superfície localizada do plasmão (LSPR) na gama fisiológica (302–330 K). Quando comparadas com as nanopartículas de Gd_2O_3:Yb^{3+}/Er^{3+}, as nanopartículas de SrF_2:Yb^{3+}/Er^{3+} apresentam uma eficiência de emissão da conversão ascendente de energia e uma dispersibilidade superiores tendo sido estudada a dependência com a temperatura das suas propriedades de emissão, tanto em forma de suspensão como em pó. Além disso, realizaram-se medições do fluxo espectral e do rendimento quântico absoluto de emissão usando um espectrômetro com uma esfera de integração e um medidor de potência. Foi, também, proposto um método inovador para prever a curva de calibração da intensidade de emissão versus temperatura de qualquer termómetro luminescente baseado em dois níveis eletrónicos termicamente acoplados, utilizando como exemplo nanopartículas de SrF_2:Yb^{3+}/Er^{3+}.

keywords

Lanthanide ions, nanoparticles, photoluminescence, downshifting, upconversion, thermometry, fluorescene intensity ratio, sensitivity, biological windows, primary thermometry

abstract

Temperature is a master variable that affects essentially most of the natural and engineered systems. The measurement of temperature is a virtually ubiquitous requirement as it governs the kinetics and reactivity of these systems from their atomic to macroscopic level. The conventional temperature sensors, proved to be ineffective for remote temperature measurement at the micro and nanoscale. This has been strongly stimulated for the development of non-invasive, non-contact and self-referencing nanothermometers exhibiting high thermal sensitivity. In this context one of the most promising approaches proposes the use of trivalent lanthanide ions (Ln^{3+}) that present photoluminescent properties that are temperature dependent. This thesis reports Ln^{3+}-doped visible emitting upconverting and near-infrared emitting downshifting nanoparticles as molecular temperature sensors.

Primarily, Nd^{3+}-doped near-infrared exciting and near-infrared emitting downshifting Gd_2O_3 nanoparticles as an intensity-based ratiometric nanothermometer were evaluated. The performance of Gd_2O_3:Nd^{3+} nanorods were enquired using a common R928 photomultiplier tube in the first transparent biological window (800–920 nm). The highest thermal sensitivity and temperature uncertainty (1.75±0.04 %·K^{-1} and 0.14±0.05 K, respectively) were reported for Gd_2O_3:Nd^{3+} nanorods in the physiological range (288–323 K). Similarly, the performance of Gd_2O_3:Nd^{3+} nanospheres were briefly investigated for their temperature dependent emission in the second biological window (1250−1550 nm) upon excitation in the first biological window (at 808 nm). The Gd_2O_3:Nd^{3+} nanospheres exhibit a maximum thermal sensitivity of 0.237±0.03 %·K^{-1} at 303 K were obtained.

Secondarily, Yb^{3+}/Er^{3+}-doped near-infrared exciting and visible emitting upconverting Gd_2O_3 and SrF_2 nanoparticles were developed for thermometry based on the thermometric parameter, as the integrated intensity of $^2H_{11/2}\rightarrow{}^4I_{15/2}$/$^4S_{3/2}\rightarrow{}^4I_{15/2}$ Er^{3+} transitions. Gd_2O_3 nanorods as thermometers combined with Au as heater nanoplatforms were constructed, to measure plasmon-induced temperature increase of Au nanorods. The optimal condition for the effective thermal heating was achieved by tuning the localized surface plasmon resonance band in the physiological range (302–330 K). In order to increase upconversion emission efficiency and the dispersibility, further SrF_2 nanoparticles were explored and the thermal sensing properties were exploited both in powder and water suspension forms. Moreover, the measurements of spectral flux and the absolute quantum yield were accomplished followed a method using an integrating sphere-based spectrometer and a power meter. Considered a furtherance step is to demonstrate a straightforward method to predict the temperature calibration curve of any upconverting thermometer based on two thermally-coupled electronic levels independently of the medium, taking SrF_2 nanoparticles as an illustrative example.

కీలక పదాలు

అంతర పరివర్తన మూలకాలు, కాంతి సందీప్తి లక్షణాలు, నానోథెర్మోమీటర్లు, అతినీలలోహిత మరియు పరారుణ ప్రాంతాలు, స్వీయ క్రమాంకనం

సంగ్రహము

ఉష్ణోగ్రత ప్రధానంగా సహజ మరియు ఇంజనీరింగ్ వ్యవస్థలను ప్రభావితం చేసే ముఖ్యమైన ప్రమాణం. ఉష్ణోగ్రత యొక్క కొలత వాస్తవంగా అంతటా సర్వసాధారణంగా ఉంది, ఎందుకంటే ఈ వ్యవస్థల యొక్క గతిశాస్త్రం మరియు క్రియాజనకత వారి అణు నుండి మాక్రోస్కోపిక్ స్థాయిలను ఉష్ణోగ్రతే నియంత్రిస్తుంది. సంప్రదాయ ఉష్ణోగ్రత కొలిచే థెర్మోమీటర్లు, మైక్రో మరియు నానోస్కేల్ వద్ద పరోక్షంగా ఉష్ణోగ్రతని కొలవలేవు. అధిక ఉష్ణ సూక్ష్మగ్రాహ్యత కలిగి, తాకకుండా, ఎందులోకైనా ప్రవేశించగల, మరియు స్వీయ-నిర్దిష్ట నిర్దేశం గల నానోథోరోమీటర్ల అభివృద్ధికి ఇది బలమైన ఉద్దీపన చేసింది. ఈ సందర్భంలో అత్యంత ఉత్తేజకరమైన విధానాల్లో ఒకటి త్రిసంయోగ సామర్థ్యం గల f- బ్లాక్ అంతర పరివర్తన మూలకాలు (Ln^{3+}) ఉపయోగించడం ప్రతిపాదిస్తుంది, ఇవి ఉష్ణోగ్రతపై ఆధారపడిన కాంతి సందీప్తి లక్షణాలను కలిగి ఉంటాయి. ఈ పరిశోధనవ్యాసంలో Ln^{3+} పై ఆధారపడిన అతినీలలోహిత మరియు పరారుణ ప్రాంతాలలో పనిచేసే నానో థెర్మోమేటర్లను తయారుచేయడమైనది.

ప్రాధమికంగా, $Gd_2O_3:Nd^{3+}$ కలిగిన పరారుణ (800-920 తరంగదైర్ఘ్యం) మరియు సమీప పరారుణ (1250-1550 తరంగదైర్ఘ్యం) ప్రాంతాలలో పనిచేసే నానో కణాలను తయారు చేయడమైనది మరియు వాటి యొక్క కాంతి రసాయన లక్షణాలను మరియు వాటి యొక్క పనితీరును పరిశీలించడం జరిగినది. మొదట నానోకాడ్డిలు కాంతి ప్రయాణించే ప్రధమ కణజాల భాగములో అధిక ఉష్ణ సూక్ష్మగ్రాహ్యత ($1.75\pm0.04\ \%\cdot K^{-1}$) కలిగిన భౌతిక శ్రేణి (288-323 K) లో పనిచేసే నానోథెర్మోమీటర్లుగ అభివృద్ధి చేయబడినవి. అదేవిధంగా, నానోగోళాలు కాంతి ప్రయాణించే రెండవ కణజాల భాగములో అధిక ఉష్ణ సూక్ష్మగ్రాహ్యత ($0.24\pm0.03\ \%\cdot K^{-1}$) కలిగిన భౌతిక శ్రేణి (288-323 K) లో పనిచేసే నానోథెర్మోమీటర్లుగ అభివృద్ధి చేయబడినవి.

తర్వాత, $Gd_2O_3:Yb^{3+}/Er^{3+}$ కలిగియున్న బహుళ ప్రయోజక వ్యవస్థలను తయారుచేయడం జరిగినది. ఈ వ్యవస్థలు బహుముఖాలను కలిగి ఉండటం వలన ఇవి కేవలం ఉష్ణోగ్రతను కొలవడమే కాకుండా వేడిని కూడా విడుదల చేస్తాయి. ఇలాంటి వ్యవస్థలను కాన్సర్ వంటి వ్యాధిని లొలగించడానికి ఉపయోగించవచ్చు. అంతేకాకుండా $SrF_2:Yb^{3+}/Er^{3+}$ కలిగిన నానోథెర్మోమీటర్లు కూడా తయారుచేయబడినవి. ఇవి ఎటువంటి క్రమాంకనం అవసరం లేకుండా ఎలాంటి పరిస్థితులలో అయినా పనిచేసే విధముగా ఒక పరిమితిని ప్రతిపాదించడం జరిగినది. ఇంకా ఈ ప్రతిపాదన సరియైనది అని కూడా రుజువు చేయబడినది.

Table of Contents

List of figures

List of tables

List of acronyms

AuNPs	Gold nanoparticles
BW	Biological window
CCD	Charge-coupled device
CW	Continuous wave
DC	Down conversion
DS	Downshifting
FIR	Fluorescence intensity ratio
FTIR	Fourier transform infrared
FWHM	Full width at half maximum
HRTEM	High resolution transmission electron microscopy
ICP-OES	Inductively coupled plasma optical emission spectroscopy
IUPAC	International union of pure and applied chemistry
LSPR	Localized surface plasmon resonance
Ln^{3+}	Trivalent lanthanide ion
LASER	Light amplification by stimulated emission of radiation
MTT	3-(4,5-dimethyl-2-thiazolyl)-2,5-diphenyl tetrazolium bromide
NIR	Near-infrared
NPs	Nanoparticles
NRs	Nanorods
NSs	Nanospheres
PMT	Photomultiplier tube
PTCE	Photothermal conversion efficiency
PXRD	Powder X-ray diffraction
QD	Quantum dots
rpm	Rotations per minute
SEM	Scanning electron microscope
TEM	Transmission electron microscope
UV	Ultraviolet
UV-VIS-NIR	Ultraviolet-visible-near-infrared
UC	Upconversion
UCNPs	Upconverting nanoparticles

List of symbols

A	Absorbance	l	Length
α	Absorption coefficient	a	Lattice parameter
N_a	Number of absorbed photons	$L\ (lm)$	Luminous flux
S_a	Absolute sensitivity	P_D	Laser power density
N_A	Avogadro number	S_m	Maximum sensitivity
k_B	Boltzmann constant	m	Mass
θ	Bragg angle	M	Molar mass
C	Concentration	MW	Molecular weight or molar mass
T_D	Debye temperature	ε	Molar extinction coefficient
g	Degeneracy	η	Photothermal conversion efficiency
D	Diameter	$V(\lambda)$	Photopic luminous function
ΔT	Difference in temperature	B	Pre-exponential constant
ΔE	Energy gap	h	Planck constant
Δq	Error in quantum yield	q	Emission quantum yield
ΔS	Error in spectral power density	Φ	Quantum efficiency
$\Delta\lambda$	Error in wavelength	R_t	Repeatability
δP	Error in laser power	$R(W)$	Radiant flux
$\delta\Delta E$	Error in energy gap	S_r	Relative sensitivity
$\delta\Delta$	Error in thermometric parameter	r	Radius
δP_D	Error in laser power density	K	Scherrer constant
δI	Error in emission intensity	$S(\lambda)$	Spectral power density
r^2	Correlation coefficient	c	Speed of light in vacuum
N_e	Number of emitted photons	SA	Surface area
β	Full width at half maximum	Δ	Thermometric parameter
ν	Frequency	T	Temperature
k	Geometric factor	δT	Temperature uncertainty (calculated)
c_p	Heat capacity	θT	Uncertainty in measured temperature
I	Intensity	μ	Viscosity
τ	Lifetime	V	Volume
P	Laser power	ϕ	Volume fraction

List of publications

Chapters of this thesis were written and formatted based on the following articles published in peer-reviewed journals.

1. **S. Balabhadra**, M. L. Debasu, C. D. S. Brites, L. A. O. Nunes, O. L. Malta, J. Rocha, M. Bettinelli, L. D. Carlos, Boosting the sensitivity of Nd^{3+}-based luminescent nanothermometers, *Nanoscale*, 7 (2015) 17261–17267.
2. M. L. Debasu, C. D. S. Brites, **S. Balabhadra**, H. Oliveira, J. Rocha, L. D. Carlos, Nano platforms for Plasmon-Induced Heating and Thermometry, *ChemNanomat.*, 2 (2016) 520–527.
3. **S. Balabhadra**, M. L. Debasu, C. D. S. Brites, J. Rocha, L. D. Carlos, Implementing luminescence thermometry at 1.3 μm using $(GdNd)_2O_3$ nanoparticles, *J. Lumin*., 180 (2016) 25–30.
4. **S. Balabhadra**, M. L. Debasu, C. D. S. Brites, R. A. S. Ferreira, L. D. Carlos, A cost-effective quantum yield measurement setup for upconverting nanoparticles, *J. Lumin*., 189 (2017) 64–70.
5. **S. Balabhadra**, M. L. Debasu, C. D. S. Brites, R. A. S. Ferreira, L. D. Carlos, Upconverting nanoparticles working as primary thermometers in different media, *J. Phys. Chem. C.* 121 (2017) 13962–13968.

The photoluminescence measurements in article 1 are performed in the collaboration with Dr. L. A. O. Nunes (Universidade de São Paulo, Brazil) and Prof. O. L. Malta (Cidade Universitária, Recife, Brazil). The synthesis, structural and photoluminescence characterization of Gd_2O_3 nanorods-Au nanorods nanoplatforms published in article 2 were performed by Dr. M. L. Debasu, while the biocompatibility and cellular uptake studies were performed by Dr. H. Oliveria (University of Aveiro). The quantum yield measurements of down shifting phosphor standards in Chapter 3 were performed by Dr. C. D. S. Brites. I have learned the synthesis of SrF_2 nanoparticles from the Luminescent materials laboratory (University of Verona, Italy) under the supervision of Prof. M. Bettinelli during the secondment period. The preparation of SrF_2 further adjusted and continued in University of Aveiro resulting the work published in articles 4 and 5.

Motivation and objectives of this thesis

Non-contact, non-invasive, and self-referencing temperature measurements down at the nanoscale emanated from the luminescence of lanthanide ions (Ln^{3+}) have emerged as fascinating field of research over a decade. The Ln^{3+}-based luminescent materials hold unique spectral properties such as narrow bandwidth (<1 nm), sharp emission lines, large Stokes and anti-Stokes emissions and long excited-state lifetimes (10^{-2} to 10^{-6} s)[1, 2]. Moreover, owing to the rich and ladder-like energy level structures, Ln^{3+} provide a great opportunity to tailor novel spectral features ranging from the ultraviolet (UV)-visible (VIS) to the near-infrared (NIR) regions for the development of multifunctional luminescence nanothermometers for the applications in sciences.

At this front, the NIR exciting, NIR emitting sensors are one of the most exploited for luminescence thermometry since they can function within the so called "biological windows" (BWs) of human tissues, where both the tissue absorption and scattering are minimized. Numerous Ln^{3+}-based nanoparticles (NPs) operating in the first (BW-I from 650–950 nm) and second (BW-II from 1000–1400 nm) BWs have been exploited for thermometry[3]. However, these thermometers have shown an inherent limitation of low relative sensitivity (*ca*. 0.1 %·K^{-1})[4, 5]. Hence, there is a great need to boost the thermal sensitivity of the NIR luminescent thermometers functioning with high temperature resolution and penetration depths at the nanoscale. Moreover, in the BW-II the optical scattering is further reduced when compared to the BW-I due to the use of longer wavelengths. This reduction assumed to lead an improvement in the resolution as well as lead longer penetration depths[3]. Yet, to take advantage of the reduced scattering and increase in penetration depth of light at longer wavelengths, an effort is needed for the design of Ln^{3+}-based systems with a suitable host, dopant ion, size and shape of the nanoparticles, and excitation wavelength, that can favor the temperature dependent light emission in BW spectral domain.

NIR exciting, UV-VIS emitting upconverting nanoparticles (UCNPs) has also garnered much attention in the field of thermometry. UCNPs usually consist of an inorganic host doped with Ln^{3+} ions, exhibit several distinctive properties, including no autofluorescence background, low cytotoxicity and high resistance to photobleaching. However, widespread implementation of UCNPs remains limited by the low efficiency of the upconversion (UC) process as well as quantum

yields[6-8]. One approach to enhance UC is to chemical engineer of the material such as tailoring the host to possess low phonon energy, doping ion concentration and nanocrystal morphology. An alternative, parallel strategy involves enhancing the luminescence of phosphors through coupling to plasmonic nanostructures which can greatly facilitate to amplify the efficiency of luminescence.

Apart from the above-mentioned factors, a central bottleneck of luminescent nanothermometry is the lack of luminescent primary thermometers, which are characterized by a well-established equation of state that directly relate a particular measured value to the absolute temperature without the need of calibration. In general, in luminescence thermometry need to perform a usual calibration whenever the temperature sensor operates in different medium to allow the corresponding conversion between relative intensities and temperature, which are called as secondary thermometers[9, 10]. Moreover, recording multiple calibrations in different medium is a time-consuming task and is not always possible (e.g. at the submicrometric scale). Hence, there is a great urge to develop predictable temperature calibration curves for the sensors, to be able to work as intrinsically primary thermometers independent of operating media (solid/suspension), to widen up a possibility to implement their temperature dependent luminescence in various fields from biomedicine, micro-/nano electronics to nanotechnology.

The overall objectives of this PhD thesis were motivated by the aforementioned aspects, to develop Ln^{3+}-based luminescent materials for the applications in the field of nanothermometry. The principal objectives of the work follow synthesis, photoluminescence analysis, thermometry and application of the thermal nanosensors. In brief:

- Design and synthesis of Ln^{3+}-doped luminescent nanoparticles *via* facile wet chemical, precipitation and hydrothermal routes.
- Evaluate the structure and morphology of the synthesized nanoparticles using various characterization techniques.
- Exploit in depth photoluminescence characteristics such as excitation, emission, excited state lifetimes, spectral flux and emission quantum yield of the downshifting and UCNPs.
- A detailed investigation on thermometer performance in the form of thermal sensitivity, uncertainty, repeatability and reproducibility.

- To demonstrate constructed Nd^{3+} based nanosystems for temperature sensing both in NIR transparent window I and II (BW I and II).
- Exemplify the NIR exciting VIS emitting Yb^{3+}/Er^{3+} based upconverting nanothermometers.
- Illustration of state-of-the art applications of UCNPs functioning as primary thermometers, as well as for the treatment of hyperthermia.

Organization of this thesis

The present thesis is organized into three sections as shown in Figure 1. The first section of the thesis (Chapter 1) provides general introduction to thermometry of Ln^{3+}-based luminescent nanomaterials. In brief, chapter 1 deals with the introductory information and the importance of luminescence nanothermometry. The essential principles for sensing temperature with different luminescence properties and the classification and performance of the thermometers were presented. In this chapter, recent examples of luminescent thermometers working at nanometric scale are also reviewed.

The core part of the thesis is covered in the second section (from chapters 2 to 5) and comprises the developed luminescent nanothermometers for applications in temperature sensing ranging from NIR to VIS regions. Chapter 2 and 3 discusses the Nd^{3+} based Gd_2O_3 DS nanorods (NRs) and nanospheres (NSs) for temperature sensing in biological transparent window I and II, respectively. In both chapters, detailed analysis of excitation spectra, emission spectra, emission decay curves, thermal sensitivity and uncertainty were reported. Chapter 4 and 5 devoted to Yb^{3+}/Er^{3+} doped Gd_2O_3 and SrF_2 upconverting NRs and NPs for temperature sensing in VIS region. Chapter 5, also demonstrates the synthesis, photoluminescence, thermometry and cellular uptake studies of the heater-thermometer single nanoplatforms based on Gd_2O_3:Yb^{3+}/Er^{3+} nanoparticles (NRs and NSs) decorated with gold nanoparticles (NRs and NPs). Apart from the general photoluminescence analysis, Chapter 6 also demonstrates SrF_2:Yb^{3+}/Er^{3+} nanoparticles as primary thermometers independent of operating media.

Conclusions and future perspectives based on the findings of this thesis are given in the chapter 6 as third section followed by Appendices and Bibliography.

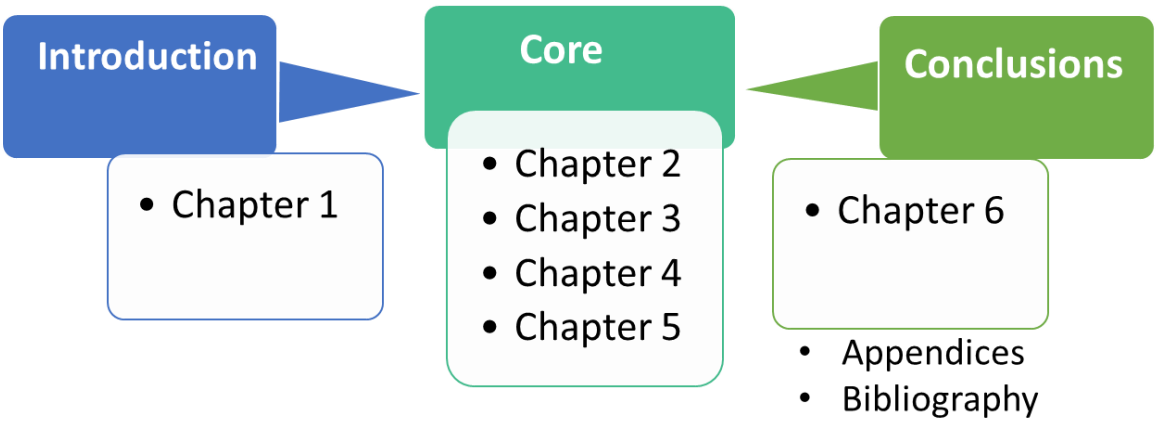

Figure 1. Schematic representation of the structure of this thesis.

Chapter 1

General introduction

Temperature is an objective comparative perception of hot or cold, termed from Latin word '*temperātūra*'[11]. Although this universal definition seems to be plausible, it requires a physical explanation. According to the zeroth law of thermodynamics, if two systems are separately in thermal equilibrium with a third, then they are in thermal equilibrium with each other. We can thus imagine one such system, which we call a thermometer, being brought into thermal contact in turn with other systems to quantitatively measure whether they are in similar or different thermal states. The formal definition of temperature is given as the inverse of the derivative of the body's entropy *S*, with respect to its internal energy *U*, $T^{-1} = \partial S / \partial U$ [12]. Where entropy is a measure of the amount of atomic disorder in a body, temperature describes how strong the intensity of random submicroscopic motions of the body's particle constituents is.

Temperature plays an extremely important role; (i) in the dynamics of various physical phenomena, (ii) determination of physical and chemical properties, (iii) energy conservation and (iv) process and optimization; in virtually all natural and engineered systems. Understanding its central role and the precise and accurate measurement of temperature is vital across a broad spectrum of areas, such as automotive, aerospace and defense, metrology, climate and marine research, chemistry, medicine, biology, military technology, air conditioning, practically in all devices for heating and cooling, in production plants and the storage of food and other goods, are a few to mention represented in Figure 1.1. Presently, the temperature sensors account for *ca*.80% of the sensor market throughout the world. The global market is likely to grow to $6.13 billion by 2020, as recently estimated by Grand View Research consulting firm [13].

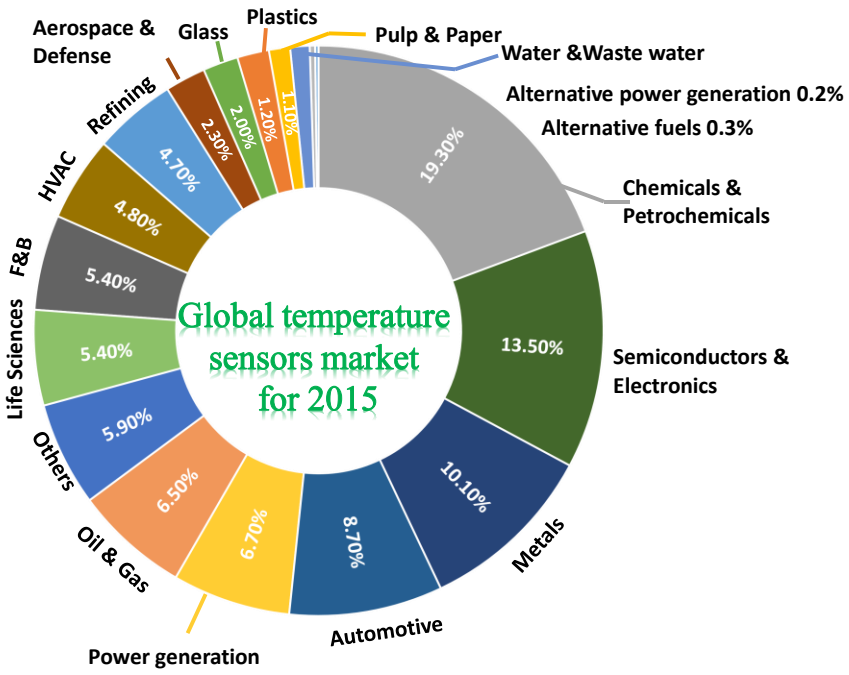

Figure 1.1 Revenue generation for the global temperature sensors market for 2015, source: Grand view research[14].

1.2 Nanothermometry and its current applications

From the very first invention of thermoscope by Galileo, to until now, many new temperature measuring methods and equipments have been developed considering the field of application, measurement accuracy and measurement conditions[15]. However, with the development of the nanotechnology, the temperature of a given system with submicrometric spatial resolution becomes possible to measure. This has led to the development of a new subfield of thermometry named nanothermometry, related to the temperature measurement at the nanoscale level[16, 17]. There are many multidisciplinary research areas where the temperature determination at the nanoscale is of great importance. Few of the most recent cutting-edge examples are highlighted.

Biomedical sciences for research, diagnosis and therapy is solely one of the essential and largely explored area of interest in nanothermometry. In biological cell, the local temperature variation could affect certain cellular functions, such as gene expression, protein stabilization, and enzyme activity. Non-invasive and accurate determination of temperature is, thus, of particular importance for the investigation of the dynamics of cellular heat production and propagation in the different

intracellular compartments[18]. It is also well known, that the pathogenesis of diseases like cancer is characterized by the increment of temperature. Thus, temperature monitoring will provide not only the understanding of cellular activities, but also the possibility of diagnosis of diseases in an early stage of development. Furthermore, heat can be used as a key tool in treatments to increase death rate in cells for instance in hyperthermia[19]. In this context of thermometry in biological sciences, various reports were published, among all, the most promising ones are the works of Wang et al.[20] in which, the authors fabricated single-excitation, dual-emission carbon-dot based fluorescent hybrids functioning as ratiometric nanothermometers. These temperature sensors were also employed to monitor intracellular temperature differences (25–45 °C) in living cells. Laha et al. used cadmium telluride quantum dots as thermal sensors operating with a spatial and thermal resolution of 80 nm and 1 mK respectively, to determine muscle efficiency for early diagnosis and treatment of various metabolic disorders including cancer[21].

Another area that could use the benefits offered by nanothermometry is micro-/nano-fluidics. The principle challenges rely on the increased capability to obtain localized heating, strong thermal gradients and fast temperature cycling with an active control of temperature. Considered as a breakthrough, is the works of Brites et al.[22] in which upconverting $NaYF_4$:Yb^{3+}/Er^{3+} were used to determine the instantaneous Brownian velocity of nanofluids, from the correlation between the heat flux in the nanofluid and the temporal evolution of Er^{3+}emission. An example that exploits the versatility of the nanothermometry can be found in aerospace systems. Aerospace systems are particularly prone to expose for high temperature environment, making it difficult for the materials to sustain at harsh temperatures. To address this challenge, Allison et al.[23], developed paint mixtures combining highly thermal resistive phosphor Y_2O_3 and $Y_3Al_5O_{12}$ and a binder material, that can withstand high temperature environment.

One other notable applications of nanothermometry is in electronics. Rodrigues et al.[24] constructed Si surface functionalized Tb^{3+} and Eu^{3+} complexes, exhibiting reversible bistability that can be used as temperature triggered molecular logical gates. In other example, Antić et al.[25] fabricated a luminescent thin-film to determine the temperature of an alanine dosimeter in a high-energy radiation field. The unprecedented growth of the luminescence materials for diverse applications points out the emergent interest of nanothermometry.

1.3 Classifications of thermometers

In general, thermometers are classified into two groups: primary and secondary thermometers, Figure 1.2. The distinction of these two types of thermometers depends mainly on how the temperature is determined based on the knowledge of thermodynamic laws and quantities and also on the thermometer calibration[26].

1. **Primary thermometry:** If the temperature is measured using a thermometer for which the equation of state can be clearly defined without inserting any unknown quantities is stated as primary thermometry. Which means that the measured values from the state equation are directly related to the absolute temperature without performing any further calibration. Primary thermometers are relatively complex, non-exhaustive and mostly studied for metrology purposes. Furthermore, these are impractical for daily uses due to their size, speed and expenses. So far five thermodynamic measurable quantities are in use to determine temperature in primary thermometry namely[27], (1) Gas thermometry: the pressure of a gas in a constant volume; (2) Acoustic gas thermometry: the speed of sound in a monatomic gas; (3) Dielectric constant gas thermometry: the dielectric constant of a gas; (4) The radiation thermometry: the radiation emitted by a black body; and (5) Noise thermometry: the power spectral density of Johnson-noise in a resistor. Recently, examples of primary luminescent nanothermometers became apparent.
2. **Secondary thermometry:** The knowledge of measurable physical quantity is not sufficient to estimate temperature explicitly from the equation of state in secondary thermometry. Consequently, the thermometers must need to calibrate externally with a well-known thermometer at least at one fixed temperature or at any many temperatures. The secondary thermometry is less complex and highly convenient to operate for several applications. The secondary thermometers are widely used over primary, due to their size, thermal response, resolution and the cost of the thermometer. Few examples to mention are platinum resistance thermometer, thermocouples, capacitance and silicon diode[7]. However, the wide use of secondary thermometers is limited, since it is rather difficult to record multiple calibrations in dissimilar conditions which is a time-consuming task that is not always possible to be implemented, as, for instance, in living cells and operating electronic devices. So far there are no such ideal thermometers with high stability, reproducibility and accuracy working at the nanoscale.

Strictly speaking, by establishing a straight forward equation of state, which means defining all the unknown quantities in the equation of state, intrinsically operating primary thermometers can be reconstructed from the secondary thermometers. So far, the International Temperature Scale of 1990 (ITS-90) based on the thermodynamic data of primary thermometers, is defined from 0.65 K upwards to the highest temperature is used for the secondary thermometer calibrations. However, the newer measurement results lead to the redefinition of the temperature scale which will occur in 2018[10].

Figure 1.2 Types of thermometry: primary and secondary.

1.4 Methods of nanothermometry

Based on the physical contact between the sample under investigation, the temperature determination techniques can be classified into contact, and non-contact method.

1. **Contact/invasive method:** the temperature reading is achieved from the invasive probe material, which is in direct physical contact with the medium. e.g. thermistor or thermocouple based technologies.
2. **Non-contact/non-invasive method:** the invasive probe remotely observes the temperature based on intrinsic temperature dependent properties of the medium such as refractive index, viscosity, absorption or emission of light. e.g. luminescence and infrared thermography.

Although contact thermometers such as thermocouples and thermistors represent the major share of the present market, they require a thermal connection that disturbs the measurements in small systems being, in general, unsuitable for scales below 10 μm[11, 12]. Furthermore, these conventional thermometers require an electrical link in the sensor system that hamper their applications in conditions where electromagnetic noise is strong, and sparks are hazardous [13].

The limitations of contact thermometers at submicron scale have stimulate the development of new non-contact accurate thermometers with micrometric and nanometric spatial resolution. High-resolution non-contact thermometers operating at micro-/nanoscale have been categorized in many ways, as, for instance, depending on whether they make use of electrical or optical signals or are based on near- or far-field applications. However, each method, possesses several advantages as well as drawbacks and exhibit different spatial, temporal, and temperature resolution. Among noninvasive spectroscopic methods for determining temperature, the thermal dependence of phosphor luminescence is one of the most promising accurate techniques (often referred to as thermographic phosphor thermometry). It operates remotely with high-detection relative thermal sensitivity (>1 %·K^{-1}) and spatial resolution (<10 mm) in short acquisition times (<1 ms), in various medium like biological cells, and magnetic field[16, 28, 29].

1.5 Sensing temperature with luminescence

Luminescence is the emission of light from a given substance not resulting from heat. When a luminescent molecule is irradiated with an external excitation source, the molecule absorbs the energy and rise from ground state to the higher energy states, from where it shed the energy in the form of light or heat by returning back to the ground state or intermediate state[2] (scheme shown in Figure 1.3 Jablonski energy level diagram). Thus the emission properties of the emitted photons depend on the properties of the electronic excited states involved in photon emission[30].

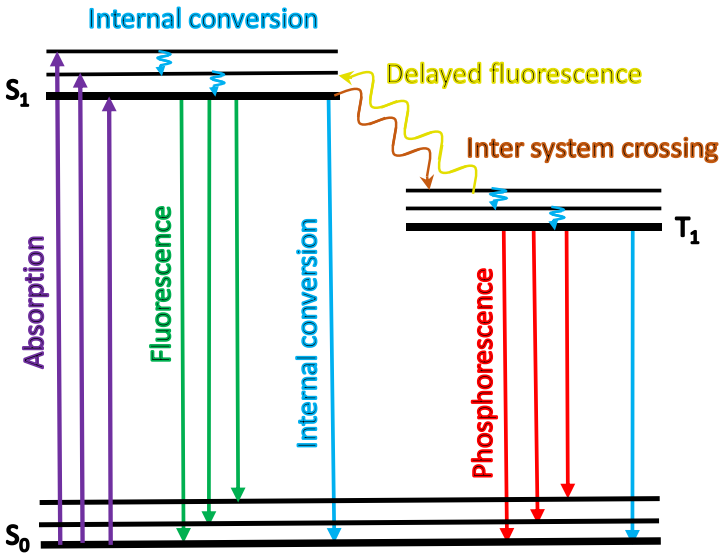

Figure 1.3 Jablonski diagram showing basic photo-physical processes taken from the reference [31]. S_0, S_1 and T_1 represents ground, excited and triplet states, respectively.

Various parameters affect the emission of luminescence materials, one of the prime variable is temperature. When temperature changes, there is an overall change in the number of emitted photons caused by different mechanisms, which in turn drastically affect photoluminescent properties, such as intensity, band-shape, spectral/peak shift, polarization, lifetime and bandwidth, represented in Figure 1.4[28]. Thus, luminescence thermometry operates based on the relationship between temperature and luminescence properties to achieve thermal sensing by temporal or spectral analysis of the emission. Among all, intensity, peak shift and lifetime are the most studied properties for luminescence thermometry.

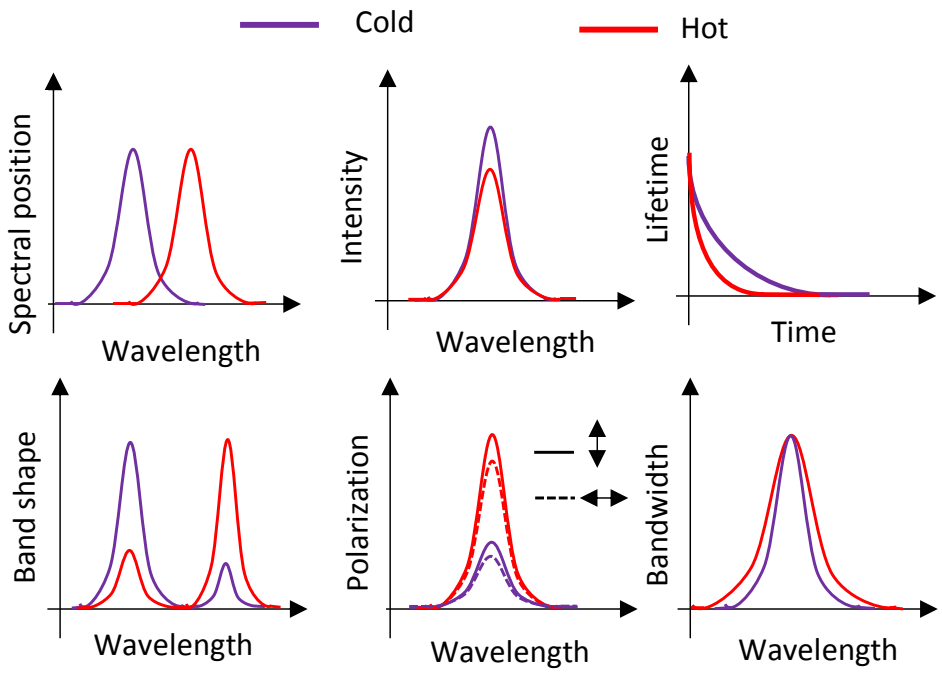

Figure 1.4 Schematic representation of the possible effects caused by an increase in temperature on the luminescence properties.

1.5.1 Intensity measurement

In this case, the knowledge of temperature is achieved from the analysis of thermally dependent luminescence emission intensity. The intensity of luminescence is formulated by Parker's law in 1968.

$$I = I_e \Phi k \varepsilon l C \qquad (1.1)$$

where I is the (measured) luminescence intensity, I_e is the intensity of the excitation, Φ is the quantum efficiency, k is a geometrical factor for the setup used, ε is the molar extinction coefficient, l is the path length, and C is the concentration of the luminescent probe. Ideally, intensity is only affected by variations of quantum efficiency of the luminescent probe with temperature. Unfortunately, it is also affected by the other parameters of Parker's equation, luminescent ion concentration, type of host, and the excitation power (particularly for UC systems) can also account for intensity changes. Such an abundance of mechanisms can influence the thermal dependency of emission intensity.

Apart from system dependent factors, the intensity of the luminescence emission shown to be very sensitive to temperature changes, caused by several mechanisms. (1) Population redistribution due to Boltzmann statistics: The change of temperature would initiate the population redistribution of the various energy states that follow a Boltzmann distribution, (2) Quenching mechanisms: The increasing temperature would activate the processes of cross-relaxation and quenching (lattice defect) such that the emission spectrum becomes more or less intense. (3) Non-radiative process: Electrons relax from excited state to ground state by generating heat instead of light. The electron–phonon interactions may cause non-radiative transition. (4) Appearance of phonon assisted Auger conversion processes.

Intensity-based luminescence nanothermometry has been reported in different systems, including quantum dots (QDs)[32], organic dyes[33], lanthanide ions[34] and polymers[35, 36]. Among all the materials, QDs show a great advantage in intensity-based nanothermometry it is because that mostly they show a linear-dependence of intensity variation with temperature. One of the example to mention is the works of Lee et al.[17, 32] The authors have reported a reversible heterostructure nanothermometer composed of Au NPs as a core covered with poly(ethylene glycol) (PEG) film working as a molecular spring to interconnect to CdTe-QD NPs. The nanothermometer displayed the characteristic exciton luminescence of CdTe QDs at 550 nm and a surface plasmon resonance of the Au nanoparticles at 633 nm. Thus, when the heterostructure was optically excited, plasmon resonance and exciton–plasmon interactions mechanisms takes place. The efficiency of the plasmon-exciton energy transfer strongly depends on the PEG film thickness. When there is a change in the temperature from 293 to 333 K, PEG undergoes a drastic expansion, which leads to a change in the CdTe luminescence intensity. The changes in luminescence intensity further used

to demonstrate (Figure 1.5) the applicability of heterostructure for thermal sensing with sensitivities close to 0.6% K^{-1}.

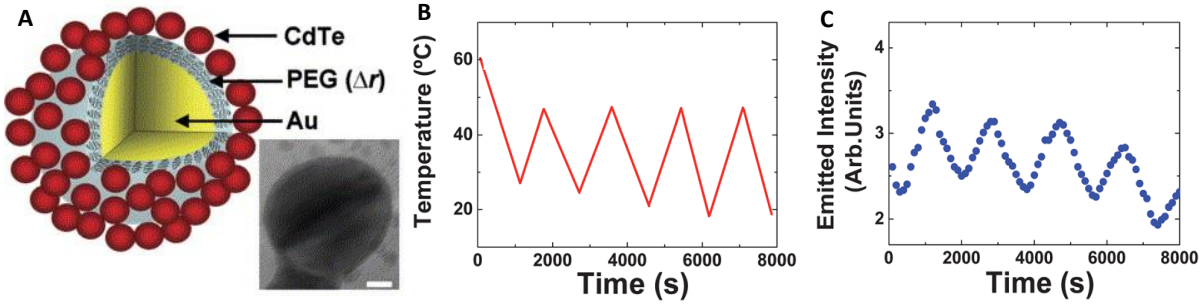

Figure 1.5 (A) Scheme of a hybrid nanothermometer based on two types of light emitting NPs linked by a thermosensitive polymer, PEG, acting as a spring and electron microscope image of the nanothermometer (scale bar is 50 nm). (B) Temperature and experimental emission from the heterostructure as a function of time. Reproduced from reference [17].

Lanthanide ions doped molecular systems are other most widely explored field based on intensity changes. Among all, Eu^{3+} $^5D_0 \rightarrow {}^7F_{0\text{-}4}$ transitions emission intensities exhibit high sensitivity to the temperature changes between 100–500 K. By taking the advantage of Eu^{3+} emission intensity, Suzuki et al. detected real-time intracellular temperature variations as small as 1K in the physiological temperature range[37].

Although the applicability of the luminescence emission intensity for thermometry shows a significant impact, this method owes some limitations. As previously mentioned, a common problem with intensity based techniques is that the observed intensity is also a function of other variables[29]. Even if the experimental conditions such as concentration of luminescent centers, excitation wavelength and power of the excitation source, are kept constant during the measurement process, the absorption and scatter cross-section may vary from the sample to sample reducing the accuracy of temperature sensing[29]. These drawbacks can be eliminated by using the ratio of two emission intensities instead of an individual intensity emission.

1.5.2 Band shape/Intensity ratio

The band shape based nanothermometry exploits the fluorescence intensity ratio (FIR) of two independent transitions of a luminescent system, whose luminescence spectra consist of several emission bands with a relative intensity that is strongly temperature dependent. Since this technique considers two individual transitions, there exist two possibilities to the generation of the

emission bands. In one hand, both emission lines can be generated from a single luminescent center caused, by thermally induced population re-distribution between the different energy levels of the emitting center. In the other hand, the emission bands resulted from two different emitting centers, so that the temperature induced band-shape change arises from the thermally induced changes in the energy transfer rates among these emitting centers or from the different thermal quenching of each center[16, 28]. In both cases, the relative intensity ratio of the luminescence bands utilized for the temperature sensing, which is independent of the concentration of luminescent centers as well as the optoelectronic drifts of excitation source, thus overcoming the main drawbacks of intensity-based measurements of only one transition[38]. Therefore, the band shape luminescence thermometry method grasps much attention to explore its use for thermal sensing using different luminescent molecular probes.

Theory of fluorescence intensity ratio (FIR) method

The FIR (or LIR, luminescence intensity ratio) technique is based on the intensity ratio between two different energy levels that are thermally coupled. This means that both levels are separated by an energy gap (ΔE) small enough to allow the promotion of electrons to the upper level using thermal energy. Since both levels are closely spaced, the non-radiative relaxation from the upper level to the lower one is very likely to be high. Therefore, both levels are linked and share the electronic population in a way that the ratio of intensities between their emissions will be independent of the excitation source and fluctuations in the particle concentration, making it a reliable system to monitor temperature. Thus, this method is often referred as "self-referencing" technique.

Figure 1.6 illustrates a simplified energy level diagram, in which the energy separation between the ground level 0 and the upper levels is much larger than the thermal energy k_BT, where T is the absolute temperature and k_B is the Boltzmann constant. The two closely spaced upper energy levels (1 and 2) with energy separation ΔE can be populated from the ground level 0 by photon excitation. The relative population of such ''thermally coupled'' levels follow a Boltzmann-type population distribution.

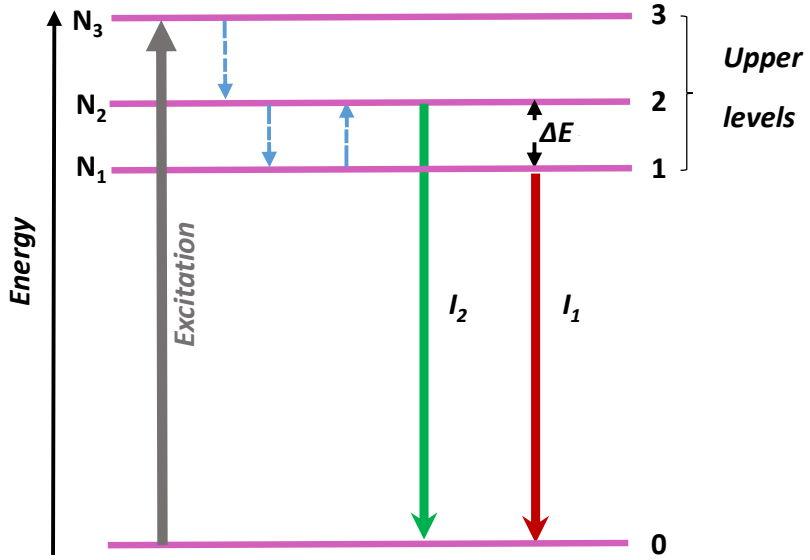

Figure 1.6 Simplified energy level diagram showing the energy levels and transitions of interest in a possible example in which the FIR technique can be used to sense temperature. The dashed lines correspond to non-radiative decay processes, while solid arrows correspond to the fluorescence transitions used to calculate the fluorescence intensity ratio.

Since the emitted intensities are proportional to the population of each energy level, thus the populations of N_1 and N_2 levels are given by[39],

$$N_1 = \exp(-\Delta E_1 / k_B T)$$
$$N_2 = \exp(-\Delta E_2 / k_B T) \qquad (1.2)$$

In which ΔE_1 is the energy gap between levels 1 and 0 and ΔE_2 is the energy gap between levels 2 and 0. The intensities of the luminescence lines I_1 and I_2 corresponds to the de-excitations from levels N_1 and N_2 down to the ground state 0 and are given by[39],

$$I_1 = \varphi_1 N_1$$
$$I_2 = \varphi_2 N_2 \qquad (1.3)$$

where φ_1 and φ_2 are constants. These constants depend on intrinsic properties of the emitting levels (such as degeneracies, branching ratios and luminescence quantum efficiency[39]).

$$\varphi_1 = g_1 A_1 h\nu_1$$
$$\varphi_2 = g_2 A_2 h\nu_2 \qquad (1.4)$$

where $g_{i(i=1,2)}$ is the degeneracy, $A_{i(i=1,2)}$ is the total spontaneous emission rate, $v_{i(i=1,2)}$ is the frequency and h is the Planck constant.

Thus, the ratio between both intensities i.e. FIR (Δ) is given by[40],

$$\Delta = \frac{I_2}{I_1} = \frac{\varphi_2 N_2}{\varphi_1 N_1} = \frac{g_2 A_2 h\nu_2}{g_1 A_1 h\nu_1} \exp\left(-\frac{\Delta E}{k_B T}\right) = B\exp\left(-\frac{\Delta E}{k_B T}\right) \quad (1.5)$$

$B = \frac{g_2 A_2 h\nu_2}{g_1 A_1 h\nu_1}$ and $\Delta E = \Delta E_2 - \Delta E_1$

B is a pre-exponential constant that should be determined. The equation constitutes the so-called fluorescence intensity ratio, FIR, method which enables a self-referenced optical readout of absolute temperature at the nanoscale.

However, it is possible to find some examples in which the temperature dependence of the intensity ratio of two-overlapped transitions was modeled through a slightly different form of equation[22],

$$\Delta = B\exp\left(-\frac{\Delta E}{k_B T}\right) + X \quad (1.6)$$

where X is a constant. The equation proposed above was used for either two Stark components of the same Ho^{3+}[41] level or two distinct transitions of Tm^{3+}[42].

1.5.3 Bandwidth

In general, the broadening of the emission lines of the luminescent ions is caused by two main pathways: one related to the intrinsic vibrations of the lattice, that can be labelled as a type of homogeneous broadening, and one related to the presence of different optical centers and defects, known as inhomogeneous broadening. While the latter normally shows little dependence with temperature, the former can be greatly affected by it, since it is ruled by the characteristics of the lattice phonons. As the temperature of a luminescent material is elevated, there is a variation in bandwidth caused by homogeneous/inhomogeneous broadening of the luminescence spectra, which can be used to achieve a thermal reading in bandwidth luminescence nanothermometry.

However, the magnitude of the temperature-induced luminescence line broadening is small, as a limitation it can be only studied in systems showing inherent narrow emission lines.

Henderson and Imbusch in 1989 showed how the bandwidth of emission/absorption bands W varies with temperature, according to the following expression:

$$W(T) = W_0 \coth(\frac{h\Omega}{2k_B T}) \quad (1.7)$$

where W_0 is the full width at half maximum of the emission band at 0 K, and $h\Omega$ is the energy of the lattice vibration that interacts with the electronic transitions.

There are few reports in which variations in bandwidth line emission is used to get temperature information. For instance, in Y_2O_3:Eu^{3+}[43], the effect is analyzed for the $^5D_0 \rightarrow {}^7F_2$ transition in the range between 10 and 670 K. Below 70 K the bandwidth remains constant within the resolution of the measurements (2 cm^{-1} determined form the experimental conditions), while above this temperature the emission line is broadened following an almost linear-function with a 0.078 $cm^{-1} \cdot K^{-1}$ rate. In a different study, the bandwidth of several emission peaks of Tm^{3+}-doped $NaYbF_4$ microparticles coated with SiO_2 was analyzed[44]. In Figure 1.7, the temperature was elevated from 100 to 700 K, and it was observed that the emissions corresponding to $^3H_4 \rightarrow {}^3H_6$ (798 nm) and $^1D_2 \rightarrow {}^3F_4$ (450 nm) transitions hold a linear-dependence with temperature over the whole range. On the other hand, $^1G_4 \rightarrow {}^3H_6$ (478 nm) and $^3F_2 \rightarrow {}^3H_6$ (697 nm) transitions show more complicated dependencies that are therefore less relevant for thermometry[44].

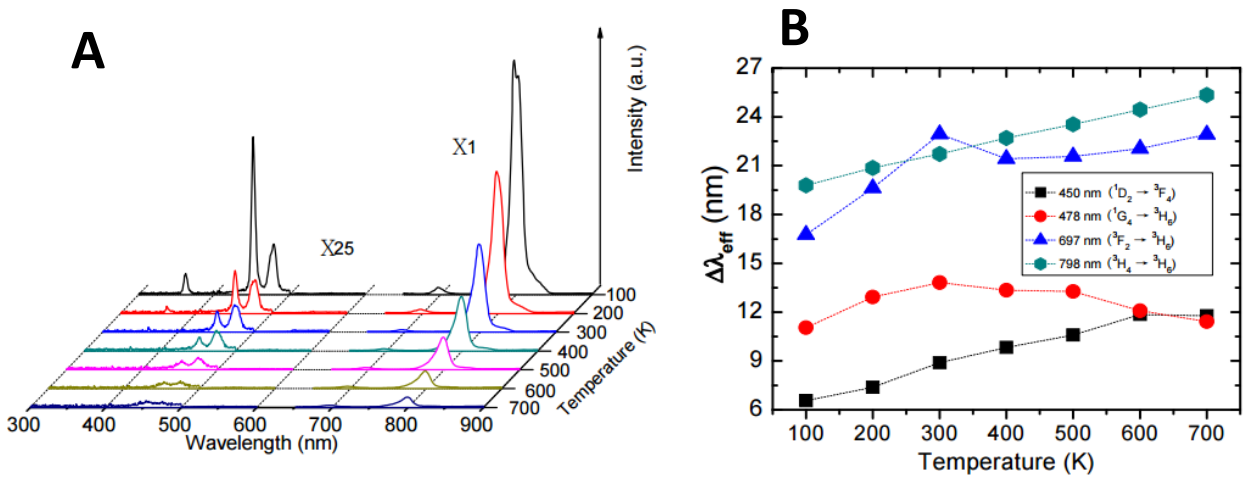

Figure 1.7 (A) Temperature dependent Tm^{3+} fluorescence emissions from the $NaYbF_4:Tm^{3+}/SiO_2$ core-shell micro-particles. (B) Temperature dependent effective bandwidth $\Delta\lambda_{eff}$ fluorescence emissions from the $NaYbF_4:Tm^{3+}/SiO_2$. Reproduced from reference[44].

1.5.4 Polarization and anisotropy

Luminescence anisotropy is the phenomenon where the light emitted by a phosphor has unequal intensities along different axes (horizontal and vertical) of polarization. In brief, when a luminescent molecule is illuminated by a linearly-polarized excitation light, luminescence which is emitted from the molecule is depolarized due to the rotational Brownian motion of the molecule[28]. At an elevated temperature, luminescent molecules alter their Brownian dynamics, as a consequence the emitted radiation shows a variation in its shape and intensity based on its polarization, thus providing an information about temperature from its relation with luminescence anisotropy. The polarization anisotropy factor of the luminescence, r_P, is defined as[28, 45];

$$r_P = \frac{I_{\parallel} - GI_{\perp}}{I_{\parallel} + 2GI_{\perp}} \qquad (1.8)$$

where $I_{//}$ and $I_{\perp}$ are the intensities of the luminescence polarized parallel and perpendicular to the incident polarization. In the equation the grating factor G is an instrumental preference of the emission optics for the horizontal orientation to the vertical orientation. It can be measured by moving the excitation polarizer to the horizontal orientation and comparing the intensities when the emission polarizer is vertically and horizontally polarized respectively.

The theoretical anisotropy in the absence of any motion is called as fundamental anisotropy r_0. When the absorption and emission transition moments are parallel, i.e. when the molecules are excited to the first singlet state, the theoretical value of r_0 is 0.4. However, in the presence of molecular rotation arising from its Brownian dynamics, the r_P is given by Perrin's law[45, 46]:

$$\frac{1}{r_P} = \frac{1}{r_0}(1 + \frac{\tau_F}{\tau_R}) \qquad (1.9)$$

where r_0, τ_f and τ_R are the limiting anisotropy, fluorescence lifetime and rotational correlation time, respectively. This equation means that the molecular rotation induced by its Brownian dynamics during the lifetime of the excited state leads to a fluorescence depolarization, giving a lower value of r_P. In the other hand, the τ_R value can decrease due to a rise in molecular rotation, with an increase in temperature. Based on this relation, the equation is elaborated in terms of temperature by Debye-Stokes-Einstein[28, 45]:

$$\frac{1}{r_P} = \frac{1}{r_0}(1 + \frac{k_B \tau_F}{V_\eta} T) \qquad (1.10)$$

where, $\tau_R = \frac{V_\eta}{k_B T}$, $\eta(T)$ is the dynamic viscosity of the medium, and V is the hydrodynamic molecular volume. Using equation 1.10, from luminescence polarization anisotropy analysis the temperature information can be attained. At this front, Donner et al.[47] reported that the fluorescence polarization anisotropy (FPA) of green fluorescent protein was a measurable temperature-dependent parameter inside living HeLa cells, U-87 MG (human glioblastoma-astrocytoma) and Caenorhabditis elegans cells.

Similarly, Zondervan[46] used Rhodamine 6G in glycerol to study the temperature variations on the fluorescence anisotropy using fluorescence anisotropy correlation spectroscopy between 200 and 350 K. Fluorescence anisotropy images shown in Figure 1.8A. From 0–5 mW, the anisotropy changes from uniform level to high level. At higher power (8.5 mW), a high-anisotropy ring is formed, whereas the anisotropy in the center drops below its initial value. These results are in agreement with the temperature calibration curve shown in Figure 1.8B, in which initially the

anisotropy show an increase with the temperature from 200 to 280 K and then a decrease above 280 K due to rotational diffusion.

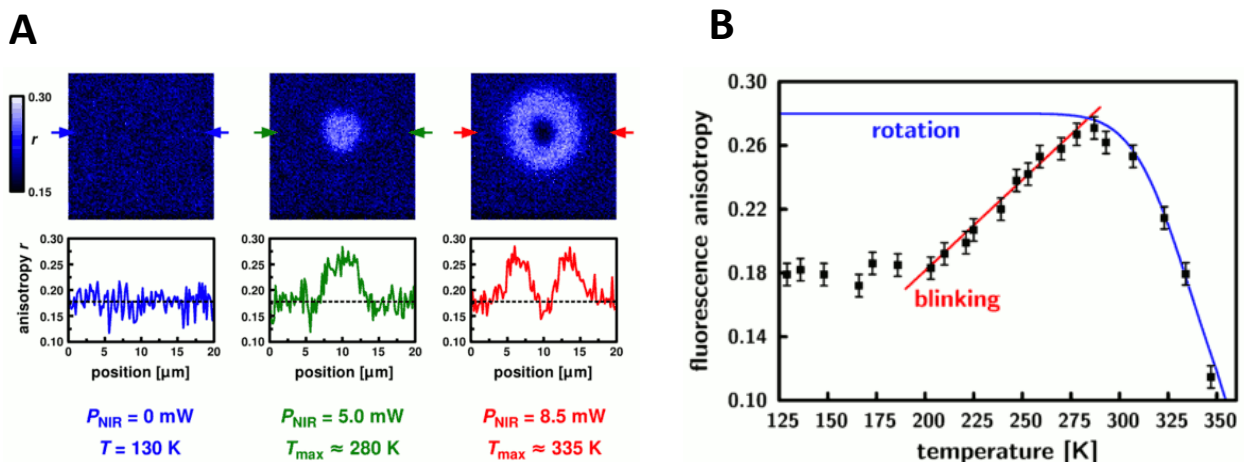

Figure 1.8 (A) Fluorescnce anisotropy images of Rhodamine 6G in glycerol 20×20 mm^2 cross section heating spot at different powers 0 to 5 and 8.5 mW. (B) Variations of the fluorescence anisotropy of R6G in glycerol with temperature. The solid line is the expected dependence of the steady-state anisotropy due to rotational diffusion. The dashed line guides the eye through a variation mainly due to photoblinking. Reproduced from reference[46].

1.5.5 Spectral shift

In some luminescent materials, the luminescence emission lines show a shift (wavelength shift) with increasing the temperature. Such shifts are attributed to interactions between the electronic states and lattice phonons[28]. The magnitude of the shift depends on a large variety of temperature dependent parameters of the emitting material including refractive index and inter-atomic distances. Thus, the thermal reading obtained from the temperature induced spectral shift of luminescence lines. The advantage of this method is that the temperature reading is not affected by luminescence intensity fluctuations caused by variations in the local concentration of emitting centers. However, the temperature induced spectral shift is remarkably less even at higher temperatures for most of the luminescent systems except QDs. Although QDs spectral shifts successfully used for the temperature readouts, the applicability of these materials is limited by its high toxicity and low biocompatibility features.

In general, QD based luminescent systems exhibit a remarkable spectral shift upon the increment of the temperature, occurs as a result of combination of different phenomena. The thermal spectral coefficient of QDs ($d\lambda/dT$, where λ denotes the spectral position of the luminescence line) can be written as[48]:

$$\frac{d\lambda}{dT} = \left(\frac{dE_g^0}{dT}\right) + \left(\frac{dE_{conf}}{dT}\right) + \left(\frac{dJ_{e-ph}}{dT}\right) \qquad (1.11)$$

The three terms in the equation corresponds to the thermally induced variation of the bandgap energy of the QDs, quantum yield of the emitting levels, thermal expansion of the QDs as well as the thermally induced variation of the solvent's refractive index[49]. These profusions of landscape of intrinsic mechanisms as well as the geometrical properties (size) brings complexity to the temperature analysis based on the spectral shift luminescence analysis of QDs. However, much works has been reported at this context[49-51].

Figure 1.9 shows CdTe NPs dispersed in phosphate buffered saline (PBS) QD emission spectral shift is used to estimate the temperature by Maestro et al.[49]. The authors demonstrated that the spectral thermal coefficient ($d\lambda/dT$) grows monotonously from 0.2 to 0.8 nm/°C as the QD size is reduced from 8 nm to1 nm. Subsequently, the QDs were incorporated into HeLa cancer cells and subjected to an external heating process. From the analysis of this spectral red shift and based on the temperature spectral coefficient of CdSe QDs (close to 0.15 nm/°C, Figure 1.9B), the authors were able to determine the cell temperature during the different stages of the heating procedure.

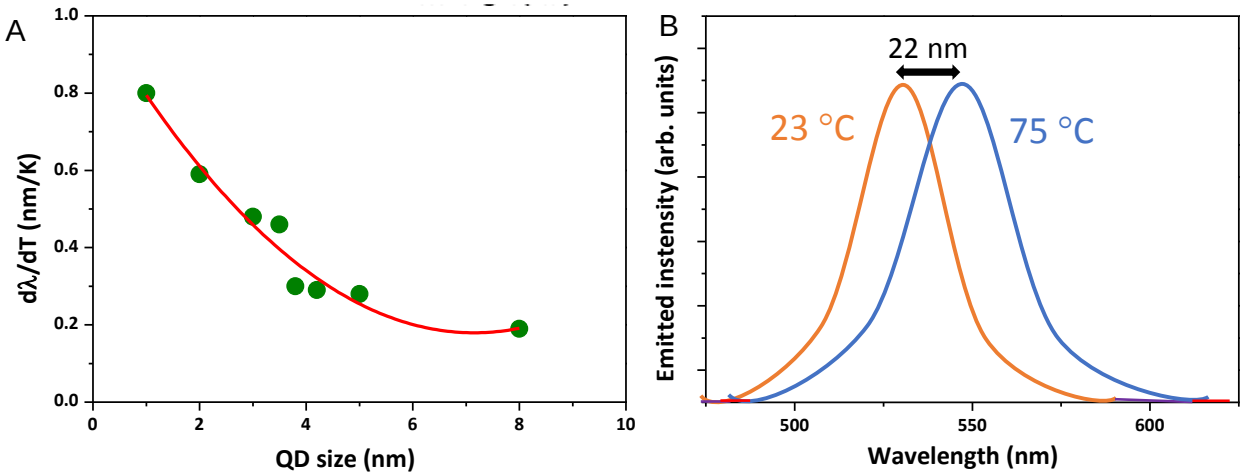

Figure 1.9 (A) Spectral thermal sensitivity of CdTe QDs as a function of the peak emission wavelength and of QD size. Circles are experimental data, solid line is a guide for the eyes. (B) Emission spectra of CdTe QDs emission at 23 °C and at 75 °C. The large thermally induced spectral shift (above 20 nm) is indicated by the arrow. Reproduced from reference[49].

1.5.6 Lifetime

In general, the lifetime is defined as the time in which the initial emission intensity, *I*, drops to a value *I/e*, and normally lies in the range of milliseconds, microseconds up to nanoseconds. The time-dependent luminescence intensity *I*, is related to the lifetime τ via the following equation:

$$I_t = I_0 e^{(-t/\tau)} \qquad (1.12)$$

where I_0 equals the luminescence intensity at time t=0. However, the decay time of the excited energy levels depends on various mechanisms namely, radiative, non-radiative or multiphonon and quenching or energy transfer processes, which in turn related to temperature variations. Thus, the lifetime can be expressed in terms of temperature by the following equation[52, 53]:

$$\tau = \frac{1}{W_r + W_{nr}(T)} \qquad (1.13)$$

where W_r and W_{nr} are the radiative and non-radiative probability, respectively.

Unlike the luminescence intensity methods, the lifetime based technique holds crucial advantage of virtually not being affected by the size, geometry and the concentration of the luminescent probe. Moreover, the value of lifetime shown to be independent on the effects of light scattering, reflection, and intensity fluctuation of excitation source. However, lifetime determination need pulsed excitation source with long illumination and acquisition time which in turn leads to the time consuming, sophisticated measurements limiting the use of this technique. In addition, thermal readout for a large gradient of temperature values at time intervals shorter than or equal to the lifetime of the luminescence are less feasible using lifetime technique.

Some examples for lifetime luminescence thermometry based on dye and polymer systems were briefly investigated in sections 1.7.2 and 1.7.4. Moreover, Savchuk et al.[54] have reported temperature sensing based on the luminescence lifetime $NaY_2F_5O:Yb^{3+}/Er^{3+}$ nanoparticles, Figure 1.10. This work demonstrated the sensitivity of the thermometer as 15×10^{-3} K^{-1} from the analysis of $^4S_{3/2}$ energy level lifetimes values of Er^{3+} emission at 545 nm upon 980 nm excitation. The authors tentatively attributed the more pronounced temperature dependence of the luminescence lifetime in the $NaY_2F_5O:Yb^{3+}/Er^{3+}$ nanoparticles to the fact that non-radiative relaxation and multiphonon phenomena, responsible for the shortening of the luminescence lifetime decays.

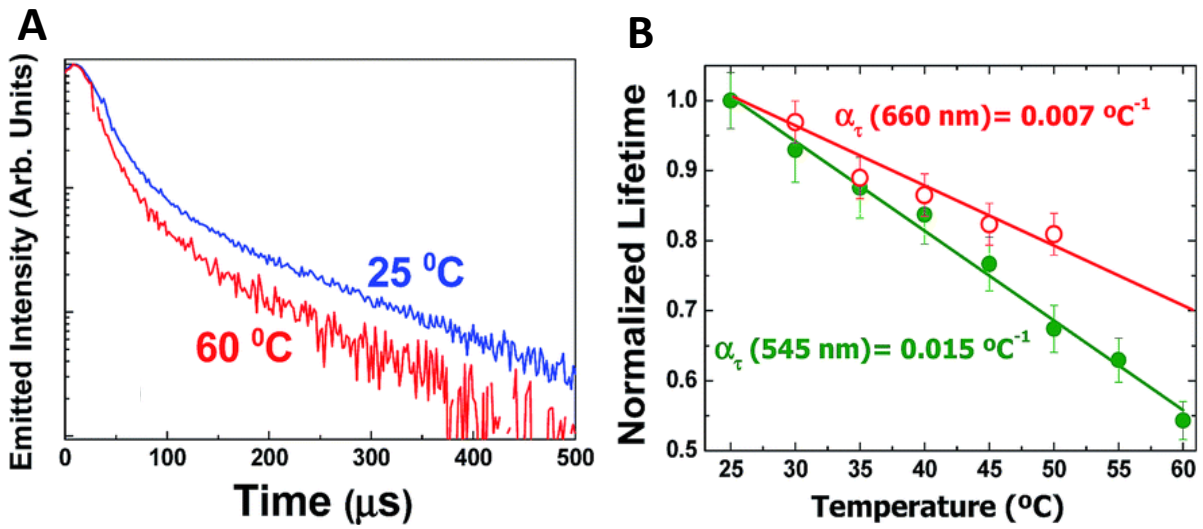

Figure 1.10. (A) Fluorescence decay curves of the 545 nm emission line of $NaY_2F_5O:Yb^{3+}/Er^{3+}$ nanoparticles at 25 and 60°C. (B) Calculated and normalized lifetime values as a function of temperature for green (545 nm) and red (660 nm) emissions. Dots represents for experimental data and solid lines are the best linear-fits. Reproduced from reference[54].

Generally, every molecular thermometer holds unique intrinsic properties, which are based on the kind of luminescent property used to measure the temperature. Thus, it is relatively important to analyse the behavior and the performance of luminescent thermometers. Moreover, it will furthuer allows to compare the ability of various distnictive thermometers.

1.6 Performance of the thermometers

The performance of distinct molecular luminescent nanothermometers can be evaluated based on their characteristics such as:

- thermal sensitivity
- resolution
- temperature uncertainty
- repeatability and reproducibility

A brief discussion on these features is presented in the following section.

1.6.1 Thermal sensitivity

The sensitivity of the thermal sensor exploited as the figure of merit value, especially for the ratiometric thermometers. The appropriate definition for the sensitivity is the rate of change in the Δ (thermometric parameter) in response to the variation of per degree temperature. The absolute sensitivity (S_a) is expressed in the form as[55]:

$$S_a = \frac{\partial \Delta}{\partial T} \quad (1.14)$$

According to this equation, the absolute sensitivity solely depends on the magnitude of the thermally induced spectral variations of the thermometric parameter. However, it is meaningless to quantitatively compare the absolute sensitivity among the different thermometers (optical, electrical, mechanical) that operate by different mechanisms or that are based on different material systems. To compare the performances of the different luminescent thermometers, the relative sensitivity (S_r) is usually utilized and is defined as:

$$S_r = \frac{1}{\Delta}\frac{\partial \Delta}{\partial T} = \frac{\Delta E}{k_B T^2} \quad (1.15)$$

The sensitivity of the thermometers was briefly demonstrated in 1998 by Collins et al.[55]. However, Brites et al.[16] used for the first time, thermometers sensitivity as an indicative figure of merit for the concrete comparison of luminescent thermometers. S_r usually expressed in units of % change per Kelvin of temperature change, (%·K^{-1}), and denoted as S_m at a maximum value of S_r [22]. It is noteworthy to observe that nanoparticles possess different particle sizes and morphologies may account for some minorly noticeable changes regarding the calculated ΔE between the levels, and on the spectroscopic and experimental parameters that define B. However, the geometrical parameters such as size, shape and Ln^{3+} concentration of the nanothermometers does not count for the determination of the thermal sensitivity using Equation 1.15[56].

The error in S_r is given by:

$$\delta S_r = S_r \sqrt{\left(\frac{\delta \Delta E}{\Delta E}\right)^2 + \left(-2\frac{\theta T}{T}\right)^2} \quad (1.16)$$

where θT is the uncertainty in the measured temperature given by the thermocouple manufacturer. Apart from sensitivity, the temperature uncertainty (δT) and repeatability are the additional factors that account for the applicability of the sensor.

1.6.2 Temperature uncertainty

If the relative sensitivity allows comparing the performance of different materials, the temperature uncertainty (or temperature resolution), δT , depends on the smallest temperature resolvable by the material, and on the experimental detection setup. The uncertainty in the temperature can arise from paucity of variables such as experimental detection setup and acquisition conditions, emission intensity or intensity ratio (Δ), and also the size and system dependent fluctuations, thus allowing to access the δT in different ways.

In one hand, the δT values can be derived experimentally from the evolution of temporal fluctuations on the thermometric parameter, Δ. The temperature that corresponds to each Δ is obtained using a calibration curve. The standard deviation of the resulting temperature histogram is the experimental δT of the luminescent thermometer. However, recording a set of temperature readouts as well as a calibration curve is time consuming and might not be always feasible. For instance, to record high-resolution spectra to define Δ, PMT detectors take typically one minute, which makes the evaluation of temporal fluctuations in temperature unpractical. To overcome this limitation, the δT can be defined as the smallest temperature change that can be detected for a given measurement and expressed as[22]:

$$\delta T = \frac{1}{S_r}\frac{\delta\Delta}{\Delta} \qquad (1.17)$$

where $\delta\Delta/\Delta$ is the relative uncertainty in the determination of the thermometric parameter (determined by the acquisition setup), estimated from the errors in Δ resulting from the error propagation in the determination of the integrated areas of I_1 and I_2:

$$\frac{\delta\Delta}{\Delta} = \sqrt{\left(\frac{\delta I_1}{I_1}\right)^2 + \left(\frac{\delta I_2}{I_2}\right)^2} \qquad (1.18)$$

Furthermore, the errors δI_1 and δI_2 in the integrated area of the I_1 and I_2 transitions estimated dividing the readout fluctuations of the baseline (signal-to-noise) by the maximum intensity value (e.g. averaged using 10 emission spectra). This value can be improved by decreasing the signal-to-noise ratio in the acquisition of each emission spectrum, which can be achieved by using larger integration times and/or averaging consecutive measurements of the emission spectrum. Clearly,

there is a compromise between lowering the temperature uncertainty and lowering the acquisition time: the longer the acquisition time the lower the temperature uncertainty.

Moreover the error in δT, $\sigma_{\delta T}$, can be estimated by:[22]

$$\frac{\sigma_{\delta T}}{\delta T} \approx \frac{\delta S_r}{S_r} \qquad (1.19)$$

On the other hand, Alicki et al.[57] demonstrated another strategy to assess the temperature uncertainty based on the size and system-dependent properties using the spin-boson model. For solid-state nanoscale thermometers, the relative fluctuation in temperature is related with the number of atoms in the sample (N_A) and its Debye temperature (T_D):

$$\delta T = \left(\frac{4T}{3\sqrt{3}T_D} e^{3T_D/8T} \right) \frac{1}{\sqrt{N_A}} T \qquad (1.20)$$

For T_D in the range 100 to 2000 K the term in parenthesis changes between 0.9 and 1.3, meaning that the order of magnitude of the temperature uncertainty is essentially determined by[57],

$$\delta T = \frac{1}{\sqrt{N_A}} T \qquad (1.21)$$

In practice, δT is solely controlled by the radius, r, of the thermometer.

1.6.3 Resolution, Reproducibility and repeatability

The spatial(δx) and temporal(δt) resolution of the measurement are defined as the minimum distance or time interval between measurements presenting a temperature difference higher than δT.

While, reproducibility refers to the variation of the same measurement carried out under modified conditions. The modified conditions may be due to the different equipment in use, different measurement methods, measurements being made by different observers, or measurements being made over a period of time in which the measurements could undergo nonnegligible change.

On the other hand, repeatability deals with how consistent a particular sensor is against itself. It can be used to describe the ability of a sensor to provide the same result, under the same

circumstances, over and over again. This is the ability of a sensor to repeat a measurement when put back in the same environment.

The repeatability of the thermometer R_t, in Δ is computed using:

$$R_t = 1 - \frac{\max(\Delta_c - \Delta_i)}{\Delta_c} \quad (1.22)$$

where Δ_c and Δ_i represent, respectively, the thermometric parameter mean value at each laser power density (corresponding to a certain temperature) and the thermometric parameter measured in each cycle.

There are several factors determining the suitability of a thermometer for a given application. Some of them are obviously related to the sensing performance: operating range, sensitivity, uncertainty, time, and spatial resolution of the system. However, others are related to the material itself: physical state, mechanical properties, facility to be implemented, simple and easily processable synthesis method. However, both aspects should be consider equally for diverse types of applications based on luminescent thermometric materials.

1.7 Molecular probes for thermometry

Several luminescent materials were investigated as molecular thermometers depending on the type of application. This section emphasizes some of the widely implemented luminescent probes for molecular nanothermometry.

1.7.1 Quantum dots

Quantum dot (QD) is a semiconductor material with distinctive conductive properties determined by its nanometric size. QDs are one of the most ubiquitous optical sensors due to their excellent photo stability and large luminescence quantum yield. In particular, the high surface-to-volume ratio of the particles results in quantum mechanical properties, such as temperature-dependent photoluminescence, which can be exploited for the purpose of temperature measurement and to use these QDs as highly sensitive luminescent thermal nanosensors[58].

A number of QD luminescence features show strong dependency on the temperature variations[50, 59-61]. Further, QDs were utilized and proved to be good candidates for intracellular, sub-tissue thermal sensing. For the first time, Maestro et al.[62] demonstrated, intracellular thermal sensing

inside HeLa cancer cells under two-photon excitation. The thermal readings were obtained from the peak wavelength determination of the fluorescence generated by CdSe–ZnS QDs shown in Figure 1.11. Moreover, they demonstrated that the two-photon excitation lead to a large spatial resolution (1°C) due to its nonlinear-nature, with a thermal spectral shift of 0.1 nm per 1°C.

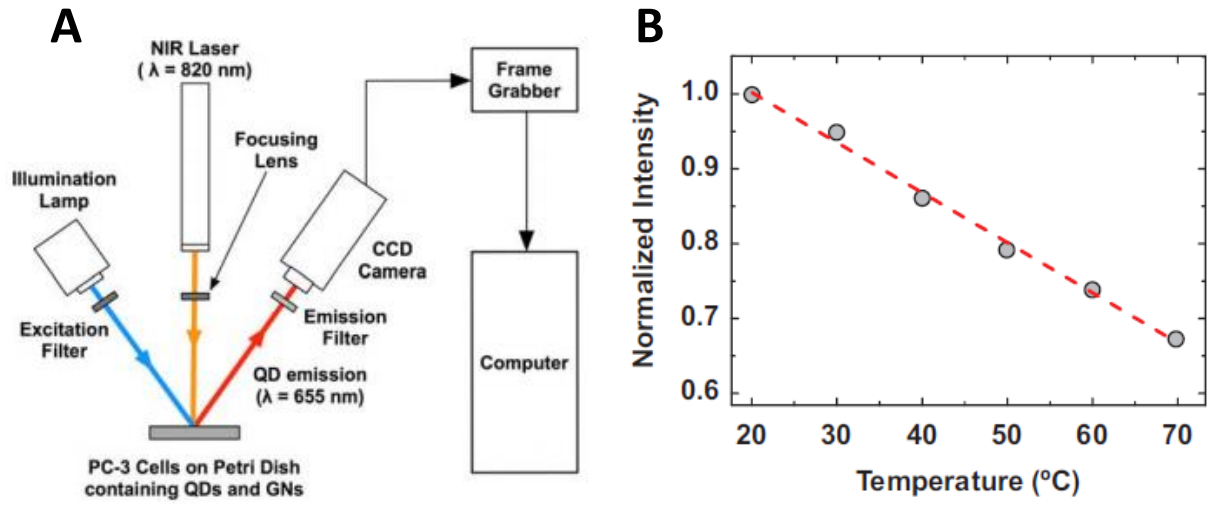

Figure 1.11. (A) Schematic representation of the experimental setup used for QD mediated real-time thermal sensing. (B) Temperature dependence of the CdSe QD fluorescence intensity. Dots are experimental data and the dashed line is the best linear-fit. Reproduced from reference[62].

More advanced studies based on luminescent QDs as high resolution nanothermometers for thermal imaging of microelectronic devices was demonstrated by Li et al.[50]. When the QDs were optically excited, the local change in the microheater temperature was then detected from the presence of red shift in the CdSe QD emission peak (a shift with a rate of 0.1 nm per 1°C). Further, as represented in Figure 1.12, the temperature profiles along the microheater were measured with a scanning microscope at sub-micrometric resolution with temperature uncertainty close to 1°C. A key point highlighted by Li et al. is the fact that the peak emission wavelength varied from dot to dot. This fact constitutes a serious limitation for thermal measurements since different sizes could also lead to different temperature responses. This limitation can be resolved by performing measurements using relatively a large number of QDs or highly efficient QDs.

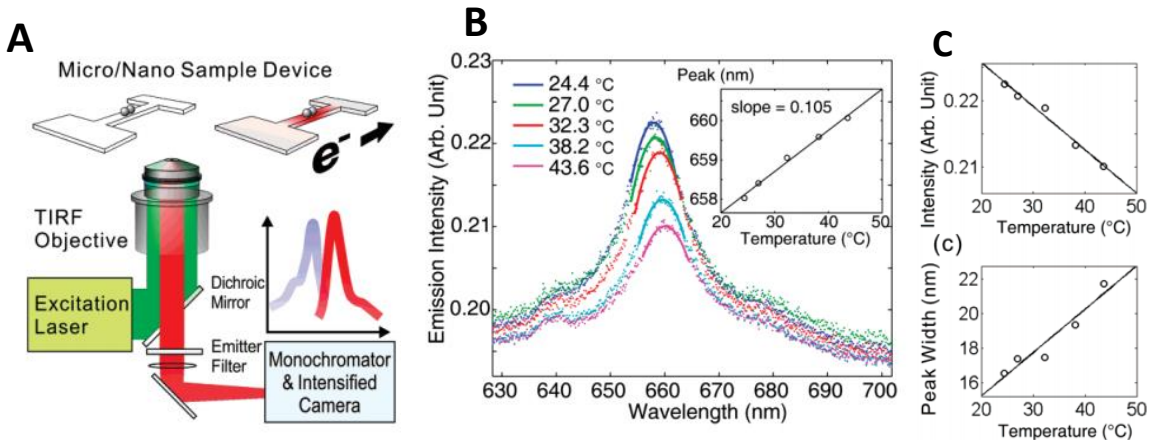

Figure 1.12. (A) Schematic diagram of noncontact temperature characterization using quantum dots through emission spectral shifts. (B) Temperature-dependent spectral shifts of a single QD. Insert: wavelength shift, (C) Average emission intensity, and (D) Spectral width as a function of temperature. Reproduced from reference[50].

These results of QD are accompanied by some concerns, like the probability of biotoxicity and the presence of photobleaching[58, 62]. Moreover, the thermal response of QDs can be dependent on their size distribution that leads to a non-homogeneous luminescence. The poor solubility, the agglutination, and the instability in different environments can also be limitations. These drawbacks can be overcome, by covering the surface of the QDs, and requires much research to achieve reproducible and safe methodologies in several applications.

1.7.2 Polymeric materials

Luminescent polymers are attractive as thermal sensors due to their very good solubility in water, though they show relatively low luminescence efficiencies. Typically, polymers show VIS luminescence when optically excited by UV radiation. The luminescence intensity is dependent on the luminescence properties of the structural units (monomers) of the polymer, which is strongly affected by variety of parameters such as phase transition, micro-environmental polarity, symmetry, and the number of chemical bonds. As a consequence, any change in the structural properties of the luminescent polymer would result a huge variation in the emission intensity[63]. Among all, the phase transition causes a drastic change in the luminescence properties of the polymer, and one of the most studied feature for polymer-based thermal sensing.

Some of the most commonly explored polymer luminescence nanothermometers are based on N-isopropylacrylamide (NIPAM)[35, 64, 65]. The phase-transition temperature of NIPAM, is relatively insensitive to changes in concentration and pH making it quite robust. Moreover, the

extremely low toxicity of NIPAM has made possible to use for biomedical applications. At this regard, Uchiyama et al.[35] showed that the luminescence intensity of the copolymer, poly(DBD-AE-co-DMAPAM-co-NTBAM) is significantly increased with heating from 4 to 40°C, Figure 1.13A. The measured fluorescence quantum yields of the copolymer at 10 and 40 °C were 0.016 and 0.12, respectively. Moreover, the maximum emission wavelength of the copolymer was also shows a significant shift from 550 to 530 nm with temperature (Figure 1.13B inset), the authors further attributed this change to the variation in the micro-environmental polarity. It is noteworthy that this copolymer maintains high solubility even at the higher temperature and thus it can be useful for applications involving the temperature sensing in biomolecules.

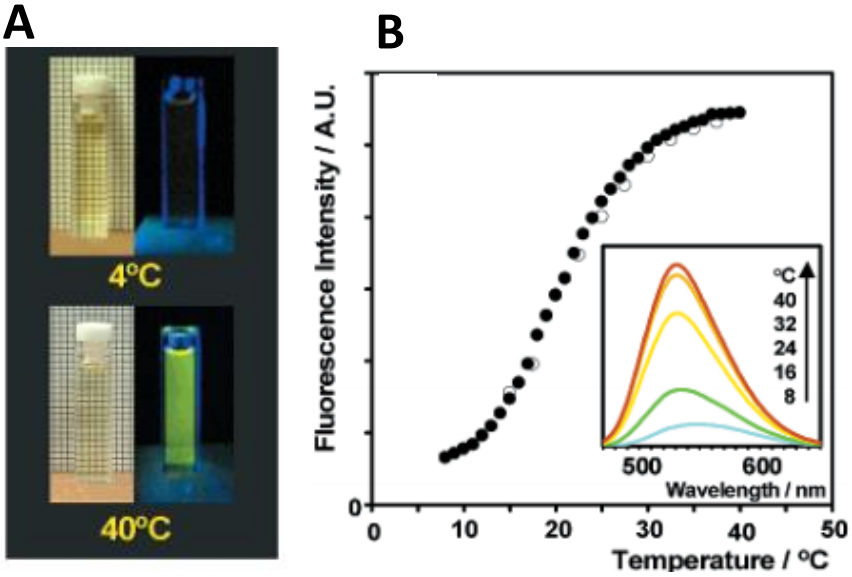

Figure 1.13 (A) Digital photos demonstrating the remarkable temperature increment in the luminescence intensity of an aqueous solution of the N-alkylacrylamide based polymers. (B) Temperature dependence of the luminescence intensity generated from luminescent polymers based on N-alkylacrylamide and fluorophore units. The inset shows the luminescence spectra at different temperatures. Reproduced from reference[35].

Apart from the intensity based technique, NIPAM can also be used to sense temperature based on the variations in luminescence lifetime. Okabe et al.[64] used NNPAM based luminescent polymer with a phase transition at around 35°C. Further, the luminescent polymer was incorporated into COS7 cells and the representative variation of the luminescence lifetime of the polymer obtained in the thermal images with spatial and temperature resolutions as 200 nm and 0.18°C, respectively. Moreover, one can observe in Figure 1.14A and B, the nucleus of the COS7 cells showed higher temperatures than the cytoplasm. In addition, authors also found that majority of cells showed a well-localized temperature singularity (indicated by the arrowheads in Figure 1.14B) that was

tentatively associated with a centrosome-specific thermogenesis. The results demonstrate that polymer-based luminescent thermometers could be used to identify the relationships between the temperature and organelle functions.

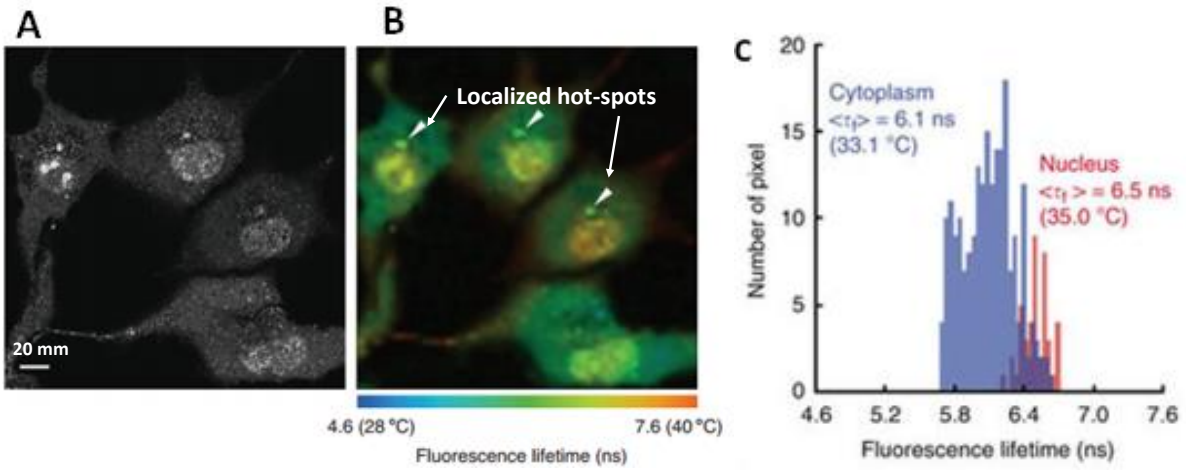

Figure 1.14 (A) Confocal luminescence image of living COS7 cells incubated with a luminescent polymeric thermometer. (B) Thermal image of the cells obtained by lifetime luminescence thermometry technique. (C) Histograms of the fluorescence lifetime and correspondent temperature in the nucleus and in the cytoplasm in a representative cell (the leftmost cell in A) demonstrating a mean temperature gradient of 1.9 K. Reproduced from reference[64].

However, polymer-based thermometers have some drawbacks, such as short operational temperature range limited to the phase transition, hysteresis kind of response, and a possible non-uniformity in the case where the optical response depends on the local chemical environment. Concerning both the hysteresis and limited operation range issues, a significant improvement can be achieved using a smart combination of polymeric thermometers to cover different ranges with higher sensitivity[66]. But still it is expected that the polymer based luminescent nanothermometers should operate also with longer stability and reversibility for continuous sensing applications.

1.7.3 Metal nanoclusters

Metal nanoparticles hold great potential as thermal sensors due to their unique physical and chemical properties. In particular due to their emissions ranging from the VIS to the NIR have been used for thermometry[67]. In addition to that, some other features such as small size, large surface area-to-volume ratio, availability in different sizes and shapes, and stability over high temperatures make them suitable for bio applications[68]. Due to their nano size, their entry is

easily facilitated into various cells posing one of the greatest difficulties in using these nanoparticles. A judicious choice between the size and functionalization method of the luminescent metal NPs is a prerequisite for the use in various biomedical applications apart from thermal sensing.

Most commonly studied metal nanoparticles include gold and silver. However, gold being unique for its optical properties conferred by their localized surface plasmon resonance, and light-to-heat conversion efficiency is used extensively for bio sensing[69]. At this regard, Shang et al.[70] demonstrated the use of gold nanoclusters to measure intracellular temperature based on their luminescence emission intensity, as well as luminescence lifetime showed in Figure 1.15A and B.

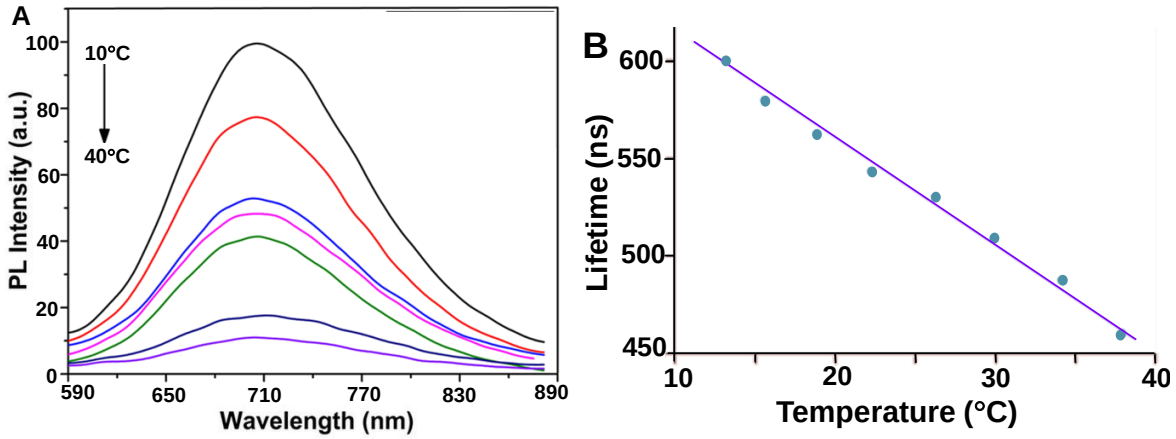

Figure 1.15 Evolution of (A) fluorescence intensity and (B) fluorescence lifetime of Au nanoclusters with temperature incorporated in HeLa cells. Reproduced from reference[70].

For the experiment purpose, Au nanoclusters were introduced into the HeLa cells by simple endocytosis and then temperature was changed through a temperature controlled stage. The thermal resolution that can achieved in this case was estimated from the thermal response of the lifetime value of Au nanoclusters in HeLa cells to be around 0.3–0.5 K in the range of 287–316 K.

However, the temperature induced changes on the luminescence properties arising from Au nanoparticles can be affected by the local environment, including oxygen content, pH, and concentration of material, which might result in accurate temperature measurements. To obviate this problem, AU NPs have been conjugated with various biomolecules and ligands to develop strategies for thermal sensing. At this front, Chen et al.[71] constructed a simple system of Au nanoclusters conjugated with Bovine serum albumin (AuNC@BSA) working as a metal based thermometer at physiological temperatures.

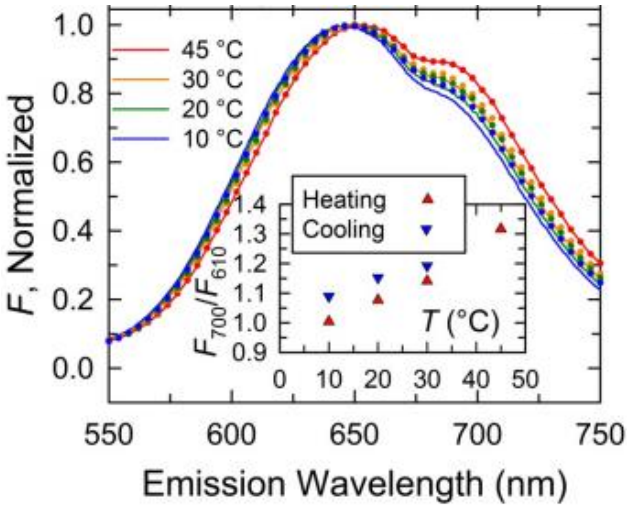

Figure 1.16 Normalized steady-state fluorescence emission spectra of AuNCs@BSA during controlled heating (shown as solid curves) and cooling (symbols) segments of a single thermal cycle upon 400 nm excitation. Reproduced from reference[71].

Employing band shape analysis in the optical properties of AuNCs@BSA, a very good reproducibility was achieved during iterative heating and cooling cycles allows us use AuNCs@BSA as self-referenced nanothermometer, demonstrated in Figure 1.16. Furtherly, by taking the intensity ratio measured at 700 and 610 nm (F_{700}/F_{610}), the temperature can be reliably estimated. However, current results suggest that this approach must need to be improved to optically track temperature using various protein- or ligand-stabilized luminescent metal nanoparticles.

1.7.4 Organic dyes

Organic dyes are known for their strong luminescence when excited with short wavelength radiation. The luminescence properties of organic dyes, depend on many factors, such as the solvent, concentration, pH and temperature. As a general rule, the luminescence intensity generated by organic dyes decreases as the temperature increases. Most commonly used organic dyes for thermometry belongs to Rhodamine (Rh)[72-74], Fluorescein[75] and Pyranine[76]. The solubility, possibility to select organic dyes depending on the required excitation/emission wavelength and easy availability, allows the opportunity to use organic dyes as thermal sensors working in various environments. Mainly, the temperature changes of the organic dyes observed form the variations of typical luminescence parameters like the fluorescence intensity, band-shape and lifetime. However, the sole use of an organic dye for temperature sensing by intensity and band-shape can result in problems due to local fluctuations in both excitation light intensity and

dye concentration. The interference of intensity fluctuations can be solved by two approaches; the introduction of a reference dye, single-probe dual-emission dye or measurement of the luminescence lifetime[77].

According to Sakakibara et al.[74] the introduction of a reference dye could improve the precision of the detection system, because the temperature intensity ratio would not be affected by excitation light fluctuations. For this purpose, authors have been used RhB and the nearly temperature-independent Rhodamine 110 (as a reference dye) to measure the instantaneous 3D temperature distribution. The ratio of fluorescence intensities of these two dyes was calibrated against the temperature and the observed maximum sensitivity is 1.6%·K^{-1}, with an accuracy of 1.3°C in the temperature range of 15 to 40°C. Other approach for measuring 3D temperature distributions using RhB dye is reported by Benninger et al.[78]. The fluorescence lifetime values of RhB were analyzed in temperature range 10–70°C as displayed in Figure 1.17A. And the Figure 1.17B, demonstrates the fluorescence lifetime imaging of RhB in microfluidic channels with a precision of ±1°C fluidic temperature distributions.

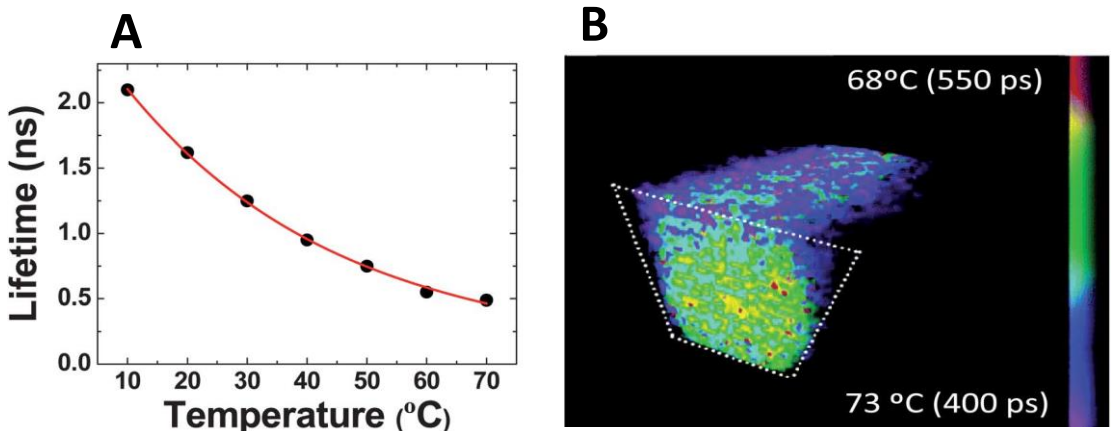

Figure 1.17 (A) Temperature dependence of the Rhodamine B luminescence lifetime. (B) Thermal image obtained for 130×40×100 mm^3 micro-channel device. Reproduced from reference[78].

Although, the use of different approaches like using a reference dye, single-probe dual emission dye or lifetime measurements prove to be effective for temperature measurements. There still exists a limitation i.e. photobleaching of the dye-based thermometers, precluding continuous long-term temperature measurement, to follow temperature changes at different time scales.

1.7.5 Biomolecules

The cell is the smallest structural and functional unit of an organism, which is typically consists of so called organelles such as cytoplasm and a nucleus enclosed in a membrane. In general, nucleus contains the genome and it is the primary site for both DNA and RNA synthesis, and the cytoplasm contains endoplasmic reticulum and mitochondrion which are the sites for protein, lipids and ATP syntheses[79]. Each of the organelle has its own specialized function, supported by numerous chemical reactions (either exothermic or endothermic), thus affecting the overall activity of the cellular temperature when used as a non-luminescent probe. Organelles linked with luminescent probes open the door to track the temperature at intracellular level[80].

Ke et al.[81] reported an L-DNA (the enantiomeric form of natural D-DNA)-based molecular beacon (L-MB) as a fluorescent thermometer represented in Figure 1.18. L-MB is a hairpin-structured dual-labelled oligonucleotide, and the distance between the fluorophore and quencher varies with temperature. L-MB transfected into HeLa cells accumulated in the nucleus and became highly fluorescent at higher temperatures. The utilization of non-natural L-DNA is crucial, as the D-DNA-based molecular beacon (D-MB) did not exhibit any temperature dependent changes, likely due to its rapid digestion by endogenous nucleases.

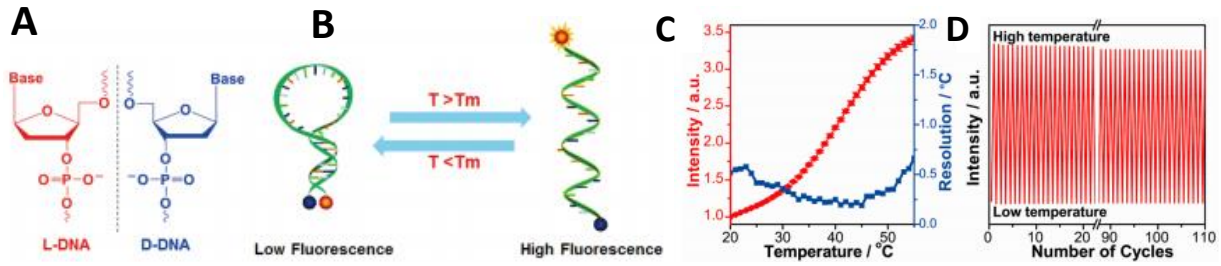

Figure 1.18 (A) Structure of L- and D-DNA. (B) Principle of the L-MB-based intracellular nanothermometer. (C) Temperature-dependent fluorescence intensity and resolution. (D) Reversibility of fluorescence change at different temperatures (20, 50°C) in PBS buffer. Reproduced from reference[81].

The green fluorescent protein (GFP) can act as a T-sensitive intracellular nanoprobe, because its fluorescence polarization anisotropy (FPA) depends on temperature. Donner et al.[47] reported that the fluorescence polarization anisotropy (FPA) of GFP was a measurable temperature-dependent parameter inside living HeLa cells, U-87 MG (human glioblastoma-astrocytoma) cells and Caenorhabditis elegans[82], to monitor the heat generated after photothermal heating using gold nanorods surrounding the cells. The fluorescence polarization anisotropy images in Figure

1.19 B and C demonstrates the temperature dependent behavior of GFP expression in HeLa cells at 296 and 313 K. A spatial resolution of 300 nm and a *T* resolution of about 0.4 K were achieved.

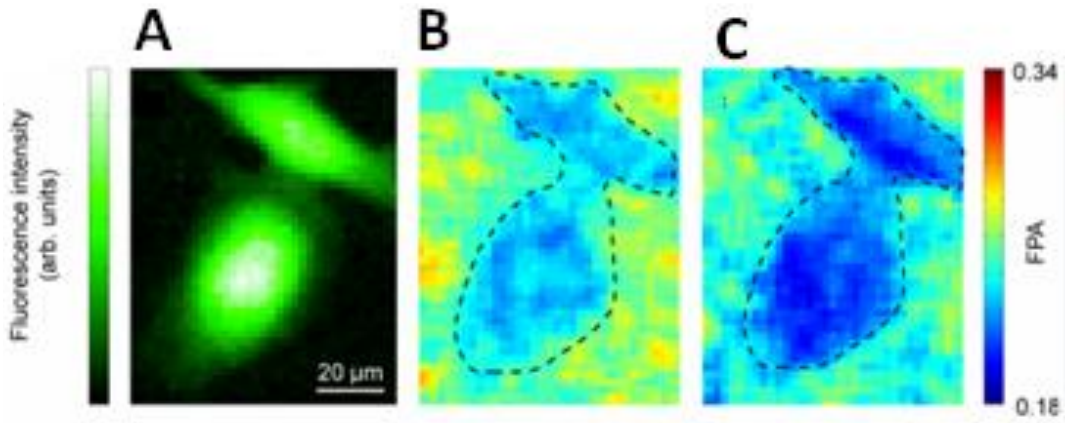

Figure 1.19 (A) Fluorescence image of GFP expressed in HeLa cells. (B and C) FPA images at 296 K and 313 K, respectively.Reproduced from reference[47].

The important point to notice is that the biomolecular thermometry is to sense the temperature variation on the cellular milieu. The responses of cells to temperature changes will likely differ according to the culture and growth conditions of the experiment, which may affect the quantitative measurement of temperature.

1.7.6 Lanthanide ions (Ln^{3+})

Lanthanides are a series of 15 elements from La (57) to Lu (71); when Sc (21) and Y (39) are added to the latter, then the resulting 17 elements should be termed as "rare earths". The electronic configuration of the lanthanides is $[Xe]4f^{\mathbf{0(La)-14(Lu)}}5d^{1}6s^{2}$. The 4f orbitals are well shielded by the 5p and 6s sub-shells resulting unique spectroscopic properties such as very low molar absorption coefficients and characteristic narrow-line emission, and longer lifetimes. Most of the trivalent lanthanide ions are luminescent, either fluorescent or phosphorescent. The emission of the Ln^{3+} ions covers the entire spectrum (0.3–3µm), from UV to VIS, and NIR spectral ranges, as illustrated in the energy level diagram of Ln^{3+} ions in Figure 1.20. Lanthanide ions spectroscopic features results from different mechanisms such as upconversion, down conversion and downshifting as shown in Figure 1.21.

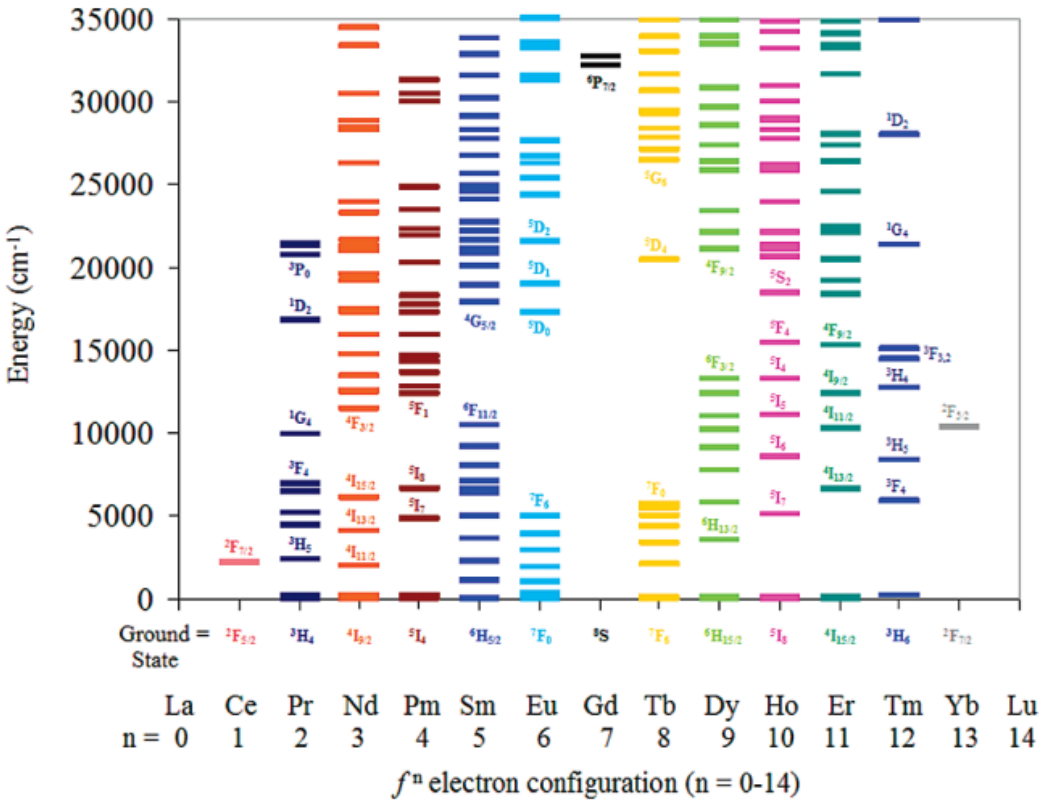

Figure 1.20 Energy level diagram of Ln^{3+} ions in a $LaCl_3$ lattice. Reproduced from reference[83].

Luminescence mechanisms:

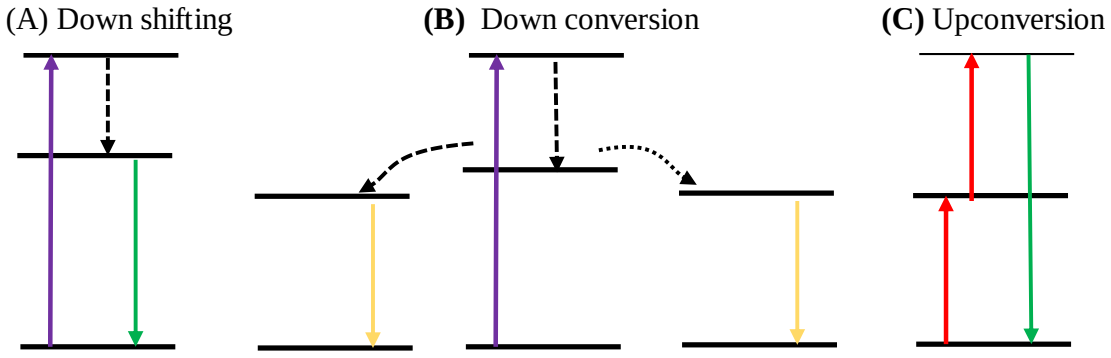

Figure 1.21 Schematic representation of photoluminescence mechanisms: (A) Downshifting, (B) Down conversion and (C) Upconversion. Arrows pointing upward direction reprsents the excitation process, dashed arrows represents the non-radiative process and the arrows pointing the downward direction represents the emission processs.

1.7.6.1 Upconversion

The field of UC investigated initially by Bloembergen[84] in 1959, followed by the ultimate pioneer Auzel[85] in 1966 and Ovsyankin and Feofilov[86] in 1966. UC emission (anti-Stokes

emission) is a phenomenon where the absorption of two (or more) incident low energy photons are converted into a single higher energy photon. It is a process to convert long-wavelength (IR or NIR) excitation into a short-wavelength (UV or IR) emission (Figure 1.23C). Mostly, UC is a two-photon process, although three-photon[87] or multi-photon[88] process can also possible. Being a process, involves at least two-photons, relatively large excitation powers are required. Furthermore, UC luminescence shows a non-linear- dependency on the excitation power density. So, the number of excitation photons required for the UC emission can be estimated by the power law relation [89].

Five distinct probable mechanisms for UC emission were explored (Figure 1.22). The most efficient process is called as energy transfer UC. It involves a sequential ground state absorption from an ion followed by an energy transfer to the neighboring ion. And the second most efficient and simplest mechanism is successive ground state absorption followed by an excited state absorption process in a single ion. And the other higher order and low efficient mechanisms includes co-operative UC, photon avalanche and finally energy migration mediated UC.

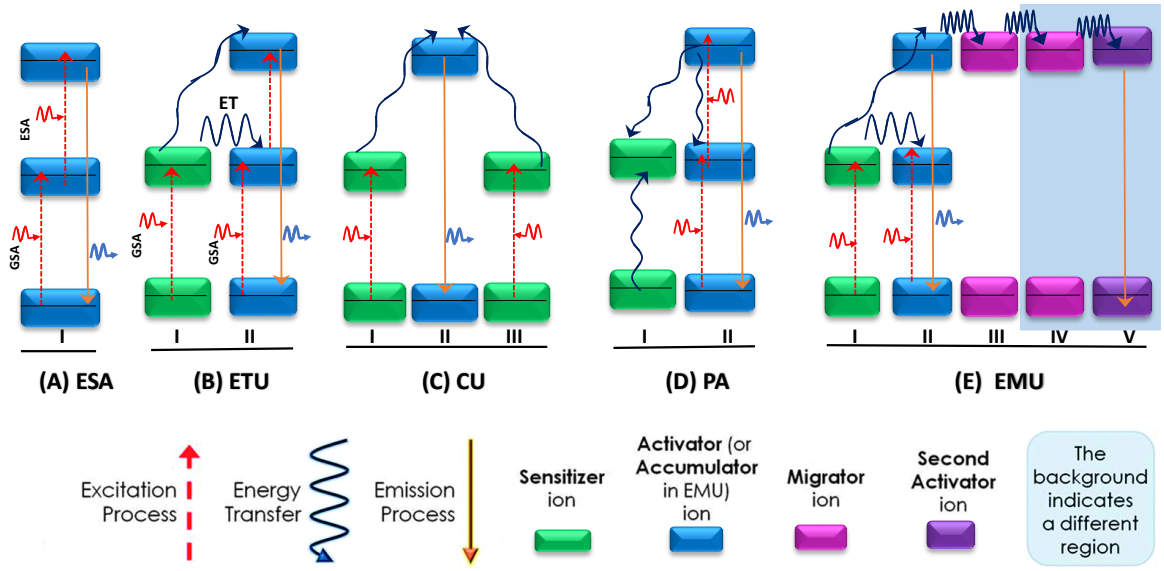

Figure 1.22 Schematic representation of Upconversion mechanisms adapted from ref [90] (A) excited state absorption (ESA), (B) energy transfer upconversion (ETU), (C) co-operative upconversion (CU), (D) photon avalanche (PA) and (E) energy migration mediated upconversion (EMU).

CU emission results when two excited donor ions simultaneously transfer their energies to the excited state of the acceptor ion. PA is the most complex UC mechanism. In the PA process, the metastable state of the acceptor ion, initially populated by a weak, non-resonant GSA, followed

by the resonant ESA. After this, an efficient cross-relaxation takes place between excited state of the acceptor ion to its neighboring ion promoting the acceptor to its excited state, from where it is then able to transfer its energy back to the donor. This results an avalanche effect in the population of the first excited state of the donor resulting an PA UC emission. EMU is the recently proposed UC mechanism, which involves four different type of interacting ions (Ln^{3+}) arranged in a multi-layered structure (core-shell). Initially, the donor (I) absorbs the photon and transfer its energy to the excited state of first acceptor (II). After the successive energy migration from the acceptor (II) to the excited states of the migrators (III, IV) and then through the shell, finally the energy reaches to the final acceptor (V) ion to give the UC emission.

Some essential prerequisites for the UC emission are ladder-like arrangement of energy levels and multiple, long-lived, metastable excited states properties. Owing to these special characteristic properties, d-block transition metals, and f-block lanthanide and actinide ions, are the vastly used elements for the UC [91]. In general, the active ions (emission center) which are responsible for the UC emission are embedded into a crystal lattice of a host material. So the properties of the host matrix, its interactions with the UC active ion, the concentration of UC active ions, the size of the nanoparticles, the laser power density and the excitation source are among the major factors which strongly effects the efficiency of the UC process[92]. At this regard, the low lattice phonon energy host, with high stability and low lattice impurities, co-doped with rare earth metals as an activator or/and a sensitizer are the important parameters for the efficient UC emission.

There are a great number of Ln^{3+}-based UCNPs that were proposed for luminescence nanothermometry. The UC emission can be distinguished as single-center and multi-center, depend on whether the UC luminescence under analysis is generated by a single type of Ln^{3+} or by a combination of different Ln^{3+} ions.

(a) Single-centered upconversion nanothermometry:

Different lanthanide ions were used for single-centered UC nanothermometry. The most common UC systems are based on Yb^{3+} as a sensitizer and Er^{3+}, Ho^{3+} and Tm^{3+} as activators. Yb^{3+} acts as an effective sensitizer owing a large absorption cross-section at 980 nm. Furthermore, the Yb^{3+} excited state energy level matches well with the excited states of the Er^{3+}, Tm^{3+} and Ho^{3+} thus allowing an efficient resonant energy transfer. And as an activator, Er^{3+} is one of the widely used

ion due to its strongly temperature dependent very intense green emission arising from the two transitions $^2H_{11/2} \rightarrow {}^4I_{15/2}$ (520 nm) and $^4S_{3/2} \rightarrow {}^4I_{15/2}$ (540 nm).

Temperature measurements using Er^{3+} ion, thermally coupled electronic levels $^4S_{3/2}$ and $^2H_{11/2}$ emission intensity ratio as thermometric parameter initially documented by Shinn et al., Weber et al. and Berthou et al.[40, 93, 94]. Since then, new aspects have been proposed to use temperature dependent Er^{3+} transitions for thermal sensing [54, 95, 96]. One of the most remarkable works done by Zhu et al.[97] building a core-shell UC nanothermometer $NaLuF_4$:Yb,Er@$NaLuF_4$@Carbon (csUCNP@C), working at sensitivity of 1 %·K^{-1} at 308 K with 0.5 K temperature resolution for applications in Photodynamic thermal therapy. The authors internalized Yb^{3+}, Er^{3+} co-doped UCNP in HeLa cells (*in vitro*, Figure 1.23C), as well as in mouse (*in vivo*). The UCNP ratio between the intensities of the 525 and 545 nm (I_{545}/I_{525}) emission bands of Er^{3+} utilized as an internal reference thermometer (Figure 1.23A and B), to obtain temperature-feedback from real-time monitoring of microscopic temperature in Photodynamic thermal therapy.

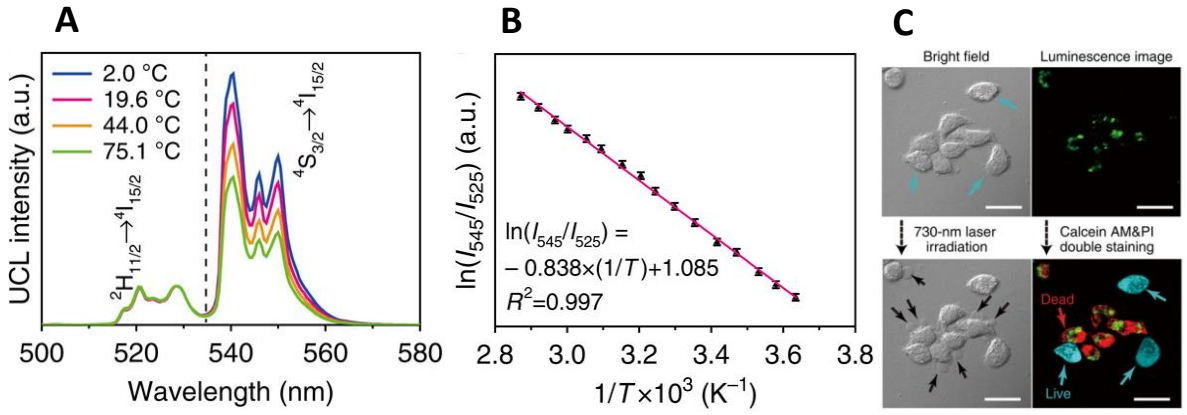

Figure 1.23 (A) UCL emission spectra of Er^{3+}-doping csUCNP@C at different temperatures by external heating. (B) Mono-logarithmic plot of $\ln(I_{525}/I_{545})$ versus 1/T for csUCNP@C. (C) Photothermal therapy of HeLa cells under 730-nm laser irradiation at 0.3 W·cm^{-2} for 5 min. Cells labelled with csUCNP@C showed a strong UCL signal in the cytoplasm (green). Reproduced from reference[97].

Besides Er^{3+}, Tm^{3+} and Ho^{3+} are the other utmost explored activator ions for temperature sensing properties[98-100], owing that the electronic levels are thermally coupled like in Er^{3+} ion and can be used in ratiometric thermometry purposes. At this regard, one of the most interesting work was reported by Lojpur et al.[99] analyzing the temperature dependence intensities of the emissions of Y_2O_3:Yb^{3+}/Ho^{3+} and Y_2O_3:Yb^{3+}/Tm^{3+} ceramic powders. They were able to observe one of the highest relative thermal sensitivity value of 9.7 %·K^{-1} at 85 K for Y_2O_3:Yb^{3+}/Ho^{3+} powders (Figure

1.24A), which is the highest ever found for Ln^{3+}-doped systems by fluorescence intensity ratio method. This sensitivity value was achieved by considering the thermometric parameter as the ratio of the intensities 536 and 772 nm corresponding to the Ho^{3+} ion. Apart from Ho^{3+} ion, the authors were successful to implement Yb^{3+}/Tm^{3+} UC emission for luminescence thermometry. In this case, the ratio of intensities of the emission lines centered at 815 nm and 454 nm were analyzed for thermometry, and the obtained relative sensitivity value is 7.8 %·K^{-1} at 270 K, Figure 1.24B.

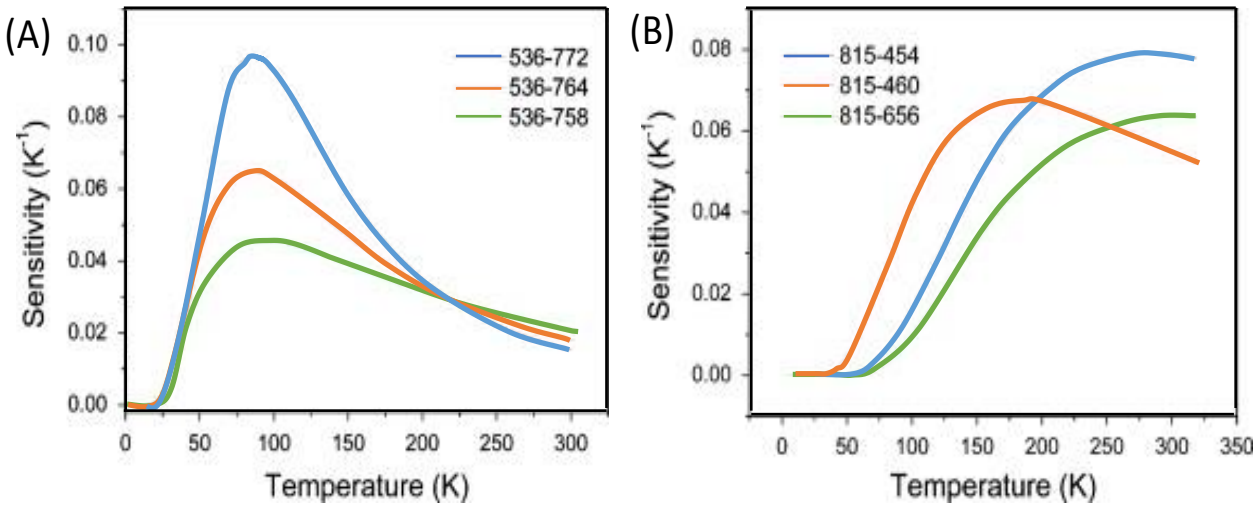

Figure 1.24 The temperature dependence of sensitivity for FIRs in (A)Y_2O_3:Yb^{3+}/Ho^{3+} and (B) Y_2O_3:Yb^{3+}/Tm^{3+}. Reproduced from reference[99].

(b) Multi-centered upconversion nanothermometry:

So far, single-centered UC luminescence for temperature determination based on the analysis of the emission intensity of thermally coupled energy levels proved their potentiality for various applications. However, those systems still suffer from a low thermal sensitivity as well as lower spatial resolution. This is partly due to the fact that the monitored emissions in the above systems come from two adjacent bands of the same ion which exhibit a similar temperature dependence. One of the ways to increase this sensitivity is to work with thermally coupled energy levels located at a larger energy difference. However, this approach also has some drawbacks, since the larger distance between the thermally coupled levels can reduce their thermalization effect with temperature. Moreover, when the energy difference is very large, the electronic population, and hence the fluorescence intensity, of the upper level will decrease, which may introduce problems in detecting the emission arising from it.

Another approach to increase the thermal sensitivity is the use of multi-centered Ln^{3+}-UC for nanothermometry, which is based on the incorporation in a luminescent compound of two different Ln^{3+} ions (both as emitters), whose luminescence intensities follow very different thermal behaviors, in such a way that the luminescence intensity ratio between their emissions would be strongly temperature dependent. At this front, the proposed mechanism is to design core–shell structure, which allows facile incorporation of dopants in order to guide an efficient energy transfer among different ions. It has been shown that such systems are excellent candidates for non-contact temperature measurements with high sensitivities. However, there are only few works on the multi-center UCNPs-based nanothermometry[42, 101-103].

A very recent work to mention, Xu et al.[102] have designed Yb/Ho/Ce:$NaGdF_4$@Yb/Tm:$NaYF_4$ active-core@active-shell for temperature sensors, which exhibit high sensitivity of 2.4 %·K^{-1} over a temperature range from 298 to 393 K. The design of constructed core shell structure and the energy level schemes were represented in Figure 1.25.The thermal sensing operated based on the thermometric parameter as a ratio of two emissions, red luminescence (originated from both Ho^{3+}:$^5F_5 \rightarrow {}^5I_8$ and Tm^{3+}:$^1G_4 \rightarrow {}^3F_4$ transitions) over green luminescence (assigned to Ho^{3+}: $^5S_2$,$^5F_4 \rightarrow {}^5I_8$ transition). The authors have showed increase in thermal sensitivity by applying two strategies:(1) Increase in Ce^{3+} content in the core, the sensitivity increases from 0.7 %·K^{-1} (2.5 mol%) to 2.4 %·K^{-1} (10 mol%), (2) doping the shell with active Tm^{3+} ion increased sensitivity 4.4 %·K^{-1} than in shell without any Tm^{3+} ion (1.4 %·K^{-1}). The joint contribution of Ce^{3+} in the core and Tm^{3+} in the shell in improving temperature sensitivity of the active-core@active-shell sample was attributed to an efficient cross -relaxation process.

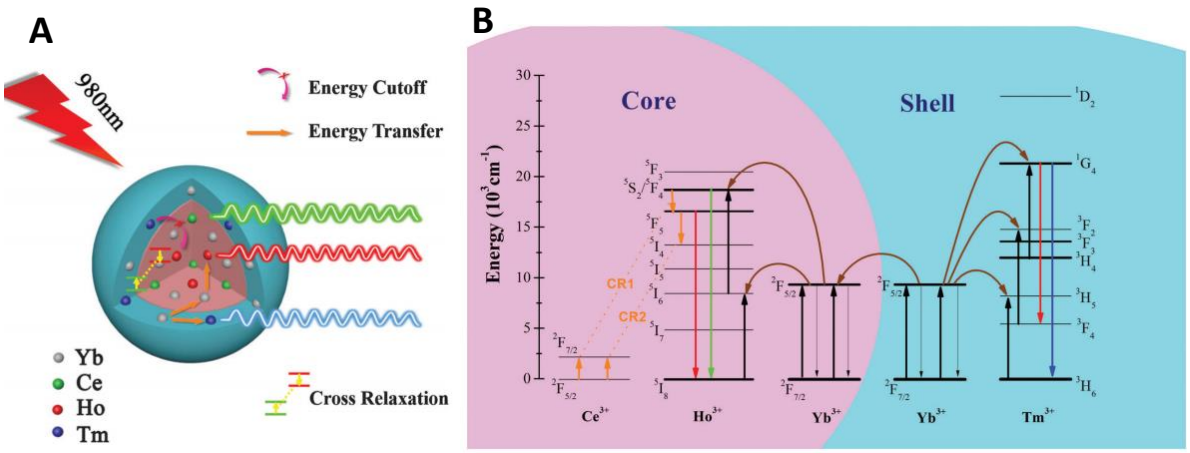

Figure 1.25 (A) Schematic representation of the proposed Yb/Ho/Ce:$NaGdF_4$@Yb/Tm:$NaYF_4$ core@shell nanostructure. (B) Energy level diagrams of Ce^{3+}, Ho^{3+}, Yb^{3+} and Tm^{3+} ions as well as the proposed mechanisms in the Yb/Ho/Ce:$NaGdF_4$@Yb/Tm:$NaYF_4$ core@shell sample. Reproduced from reference[102].

1.7.6.2 Down conversion (DC)

DC or quantum cutting is the opposite of UC, whereby one high-energy photon 'cut' into two low-energy photons. The mechanism involves a simultaneous photon energy transfer from a donor ion excited state to its neighboring activator ions. Then the energy cut into half and absorbed by the two activator ions, resulting two low-photon emission (Figure 1.21B). This DC phenomenon first proposed by Dexter [104] in 1957 and later it was experimentally proved in YF_3:Pr^{3+} simultaneously by Sommerdijk et al. [105] and Piper et al. [106] in 1974. There are not many studies based on lanthanide ion DC emission for thermometry. The limitation of DC process is that the emission light is in the range of wavelengths which can be absorbed by and/or can be damaged surrounding biological tissues.

The DC luminescence also differentiated as single Ln^{3+} ion (Eu^{3+}, $Pr^{3+,}$ Dy^{3+}, Ho^{3+}, Er^{3+} and Tm^{3+}) emission and multi Ln^{3+} ion emission, depending whether the luminescence emission is achieved from a single luminescent center or by a combination of different luminescent centers. Some of the most recent works for single-center DC luminescence for nanothermometry are the works of Liang et al.[107] in which Eu^{3+} doped $LiNbO_3$ non-contact temperature sensor developed with sensitivity of 4 %·K^{-1} at 303 K with 0.3 K temperature resolution. This sensitivity is achieved considering the thermometric parameter as the ratio between $^5D_0 \rightarrow {}^7F_2$ (625 nm) and $^5D_1 \rightarrow {}^7F_1$ (541 nm) transitions of Eu^{3+} ion. Bu et al.[108] reported LaF_3 transparent glass ceramic as an optical sensor working in the temperature range from 298 to 523 K is studied based on the down-

conversion luminescence of Dy^{3+} ion. A minimum relative sensitivity of 1.16×10^{-4} K^{-1} at 294 K was obtained by taking the thermometric parameter as fluorescence intensity ratio of the $^4I_{15/2}$ and $^4F_{9/2}$ thermally coupled levels of Dy^{3+} ion. Further Wang et al.[109] constructed a complex, core-shell system $NaLuF_4$:Gd/Yb/Er@$NaLuF_4$:Yb@$NaLuF_4$:Nd/Yb@ $NaLuF_4$. The multi-centre Ln^{3+} based nanostructures capable of emitting both UC and DC luminescence under 808 nm excitation (Figure 1.26D). The NIR DC emission intensity ratio of Yb^{3+} 980 nm transition ($^2F_{5/2}\rightarrow{}^2F_{7/2}$) and Er^{3+} 1532 nm transition ($^4I_{13/2}\rightarrow{}^4I_{15/2}$) used for thermal sensing applications. Moreover, possessing the extremely strong Yb^{3+} emission centered at 980 nm and high penetration depth of NIR light in tissue, the nanostructures successfully implemented for *in vivo* NIR DC imaging studies shown in Figure1.26A-C.

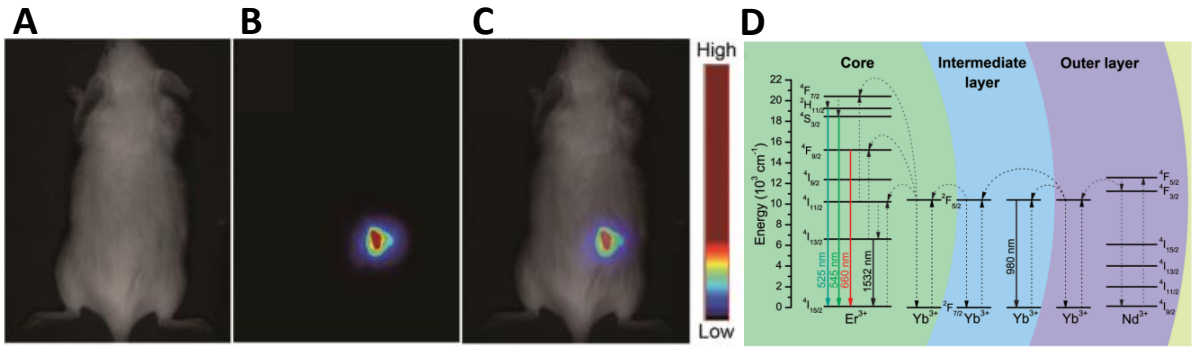

Figure 1.26 *In vivo* NIR DC imaging of a mouse subcutaneously injected with aqueous dispersion of PEG modified $NaLuF_4$:Gd/Yb/Er@$NaLuF_4$:Yb@$NaLuF_4$:Nd/Yb@$NaLuF_4$ core-shell nanostructures. (A) White-light photograph, (B) NIR image under 808 nm laser excitation, and (C) overlapped image. (D) Schematic representation of UC and DC mechanism in core-shell nanostructures. Reproduced from reference [109].

1.7.6.3 Downshifting (DS)

DS is a single photon process, where upon excitation with a high-energy photon, non-radiative relaxation takes place followed by radiative relaxation, thereby resulting in the emission of a lower-energy photon. It is an example for a single photon process, which undergo a Stokes shift (Figure 1.23A). Examples to mention are the works of Ishiwada et al.[110], in which the authors were developed Tb^{3+}/Tm^{3+}:Y_2O_3 particles as visual thermo-sensors, since they can be operated over a wide temperature range, from 323–1123 K. The ratio between the emission intensities of the Tm^{3+} (at 466 nm) and the Tb^{3+} (540 nm) is strongly temperature dependent, under 355 nm (UV) excitation. In the works of Brites et al.[111], demonstrated highly sensitive 4.9 %·K^{-1} thermometer based on the distinct emissions situated at 545 and 612 nm VIS wavelengths

corresponding to Tb^{3+} and Eu^{3+} ions. Moreover, the developed Tb^{3+}/Eu^{3+} based thermometer shows high spatial (1-10 μm) and temporal (100 ms) resolution.

Apart from above mentioned most studied multi-centered Ln^{3+} ion, several other lanthanide pair were developed for DS nanothermometry such as Tb^{3+}/Eu^{3+}[111-114], Tm^{3+}/Tb^{3} Nd^{3+}/Yb^{3+}[115], and Tm^{3+}/Ho^{3+}[103]. However, among all, Nd^{3+} is the one, who receives a lot of hype in recent years for thermal sensing and bioimaging applications, due to its unique features to work in NIR.

Neodymium ion for thermometry:

Nd^{3+} is of particular interest because of its ladder-like intra-4f levels are amenable to NIR excitation (around 800 nm) and emission within the BWs, first (I, 650–950 nm), second (II, 1000–1400 nm) and third (III, 1550-1870), where the transparency of living tissues is high due to low optical absorption [116, 117]. Nd^{3+} possesses five main emission channels $^4F_{5/2}\rightarrow{}^4I_{9/2}$ (800–850 nm), $^4F_{3/2}\rightarrow{}^4I_{9/2}$ (880–1000 nm), $^4F_{3/2}\rightarrow{}^4I_{11/2}$ (1000–1210 nm), $^4F_{3/2}\rightarrow{}^4I_{13/2}$ (1300–1480 nm) and $^4F_{3/2}\rightarrow{}^4I_{15/2}$ (1700–1850 nm), which efficiently matches well with I, II and III BWs. Thus, Nd^{3+} is considered to be a potential candidate for deep-tissue luminescence imaging and thermal sensing applications [29, 118, 119].

Plenty of examples on luminescent thermometry involving Nd^{3+}-doped nanocrystals in I and II are tabulated in Table 1.1. Most of the reports uses the intensity ratio between temperature dependent Nd^{3+} either Stark components or different energy transitions as the ratiometric thermometric parameter. However, the state-of-the art Nd^{3+}-based luminescence thermometers have the inherent limitation of very low relative sensitivity (Table 1.1). Thus, it is necessary to explore the possibilities of new pathways to improve: (i) thermal sensitivity and (ii) penetration depth of Nd^{3+} doped DS nanothermometers, by developing new materials or by combining the Nd^{3+} emission with other Ln^{3+} ions (Table 1.1).

Table 1.1 Excitation wavelength, λ_{exc}, temperature range, ΔT, maximum relative sensitivity, S_m, and temperature for which it occurs, T_m, of Nd^{3+}-based thermometers.

Ref	Host	λexc	Transitions	ΔT (K)	S_m (%·K^{-1})	T_m (K)	Detector	FIR	BW
[4]	YAG	808	$^4F_{3/2}$ (Stark levels)	283–343	0.15	283	Silicon based CCD	938 / 945	I
[120]	$NaYF_4$	830	$^4F_{3/2}$ (Stark levels)	273–423	0.12	273	Raman microscope	863 / 870	I
[5]	LaF_3	808	$^4F_{3/2}$ (Stark levels)	283–333	0.10	283	Silicon based CCD	885 / 863	I
[121]	$NaYF_4$	793 864 574	$^4F_{5/2}$, $^4F_{3/2}$→$^4I_{9/2}$ $^4F_{7/2}$, $^4F_{5/2}$→$^4I_{9/2}$ $^4F_{7/2}$, $^4F_{3/2}$→$^4I_{9/2}$	323–673	0.58 0.55 1.12	500	R928 PMT	770–842 / 842–910 710–770 / 842–910 710–770 / 770–842	I
[122]	$CaWO_4$:Nd,Yb	980	$^4F_{5/2}$, $^4F_{3/2}$ → $^4I_{9/2}$ $^4F_{7/2}$, $^4F_{3/2}$ → $^4I_{9/2}$ $^4F_{7/2}$, $^4F_{5/2}$ → $^4I_{9/2}$	303–873	0.27 0.15 0.30	730 353 668	PMTH-S1-CR131	805 / 872 755 / 872 755 / 805	I
[123]	La_2O_2S	532	$^4F_{5/2,}$ $^4F_{3/2}$→$^4I_{9/2}$	30–600	1.10	358	Acton ID-441-C InGaAs photodiode	818 / 897 891 / 897	I
[124]	$NaGdF_4$-QD-PLGA hybrid	808	Nd^{3+} $^4F_{3/2}$→$^4I_{11/2}$ Yb^{3+} $^2F_{5/2}$→$^2F_{7/2}$	283–328	2.5	303	InGaAs	1060 (Nd^{3+}) / 1220 (Yb^{3+})	II
[125]	LaF_3 Nd@Yb Yb@Nd Nd:Yb	790	Nd^{3+} $^4F_{3/2}$→$^4I_{13/2}$ Yb^{3+} $^2F_{5/2}$→$^2F_{7/2}$	283–323	0.41 0.36 0.1	283	1.7μm InGaAs IDus CCD detector	1300 (Nd^{3+}) / 1000 (Yb^{3+})	II
[115]	$LiLaP_4O_{12}$:Nd, Yb	808	Nd^{3+} $^4F_{3/2}$→$^4I_{9/2}$ Yb^{3+} $^2F_{5/2}$→$^2F_{7/2}$	93–663	0.4	330	R5108 PMT	870 (Nd^{3+}) / 1000 (Yb^{3+})	I
[126]	$NaYF_4$:Yb,Er/$NaYF_4$:Nd, Yb	808	Nd^{3+} $^4F_{3/2}$→$^4I_{11/2}$ Yb^{3+} $^2F_{5/2}$→$^2F_{7/2}$	200–450	0.02 0.02	370 200	OceanOptics HR4000	1060 / 980	II
[127]	YVO_4	808	$^4F_{3/2}$→$^4I_{9/2}$ $^4F_{3/2}$→$^4I_{11/2}$	298–333	0.19 0.15	298	InGaAs	879 / 887 1063 / 1072	I II
[128]	LaF_3, Nd@Yb	808	Nd^{3+} $^4F_{3/2}$→$^4I_{13/2}$ Yb^{3+} $^2F_{5/2}$→$^2F_{7/2}$	283–328	0.74	293	FLIR E40 thermal camera	1350 / 1000	II
[129]	$NaYF_4$, Nd/Yb	980	$^4F_{7/2}$→$^4I_{9/2}$/$^4F_{5/2}$→$^4I_{9/2}$ $^4F_{7/2}$→$^4I_{9/2}$/$^4F_{3/2}$→$^4I_{9/2}$ $^4F_{5/2}$→$^4I_{9/2}$/$^4F_{3/2}$→$^4I_{9/2}$	297–420	1.1 2.3 1.4	297	CR131 PMT	750 / 800 750 / 863 800 / 863	I
[130]	$LiNdP_4O_{12}$	808	$^4F_{3/2}$→$^4I_{9/2}$ (Stark levels)	305–356	0.22	313	R5509-72 PMT	850-900 nm R1/R2 Components	I
[131]	$LiLaP_4O_{12}$:Cr,Nd	665	$Nd^{3+}$$^4F_{3/2}$→$^4I_{11/2}$ + Cr^{3+}	173–473	4.89	473	CCD camera	820–840 (Cr^{3+}) / 1048 $^{3+}$)	I

Apart from above mentioned single doped or multi dopant core-shell nanostructures, Ln^{3+} ions further used in great combination with organic molecules in organic-inorganic hybrids, in metal organic frameworks and also as complex structures in combination with other molecular probes. The organic–inorganic hybrids feature some advantages such as relatively facile synthesis, ability to engineer the emitting centers in the hybrids, enabling the control of non-radiative pathways, improved thermal and mechanical properties arising from the isolated emitting centers, therefore offering their use in thermometry. Much number of examples were reported on organic–inorganic hybrid based thermometers encompassing mixtures of organic dyes with Ln^{3+} β-diketonate complexes, diureasil based frameworks, layered double hydroxides, and metal–organic frameworks[111, 132-134].

Metal–organic frameworks (MOFs) are a class of porous materials consisting of metal ions or clusters coordinated to organic ligands. The choice of metal ions and ligands allows the design and synthesis of materials for targeted functionality[135]. The building blocks of MOFs are the metal centers, ligands, and guest ions or molecules (in porous or layered materials) are all potential sources of light emission, in which Ln^{3+} are so far the most studied emitting centers[135, 136]. Especially, the multiple luminescent centers in MOFs are very useful to develop ratiometric luminescent thermometers. In fact, the thermometric process is based on the energy transfer between ions within the solid framework [137, 138].

Complex systems

Sometimes simple systems may not be enough to possess high thermal sensitivity and high thermal resolution. An approach to improve the sensing properties, is to design more complex systems, formed by the conjugation of different molecular probes discussed before. These multifunctional nanothermometers possess collective luminescence features coming from each individual molecular probe, which can be used to increase thermometric properties for sensing. There are several works reported using the strategy of complex system to thermometry[32, 139-142].

Cerón et al.[124] developed a complex system, combining Nd^{3+}-doped $NaGdF_4$ dielectric NPs and semiconductor PbS/CdS/ZnS QDs in a hybrid nanostructure (HNS) formed by poly(lactic-co-glycolic acid) (PLGA). Figure 1.27 shows the schematic diagram of constructed nanothermometer complex along of its temperature dependent/independent emission spectra. The thermometric

parameter is based on strongly temperature dependent at 1220 nm (arising from QD) and a temperature-independent reference peak at 1060 nm (arising from $NaGdF_4:Nd^{3+}$). The coexistence of these two luminescence bands allows for ratiometric thermal sensing to obtain one of the highest thermal sensitivity 2.5 %·K^{-1} for temperature region 283–323 K. The advantage of this complex system is that the temperature-independent peak behaves as a reference peak for the thermal sensing and intracellular imaging applications.

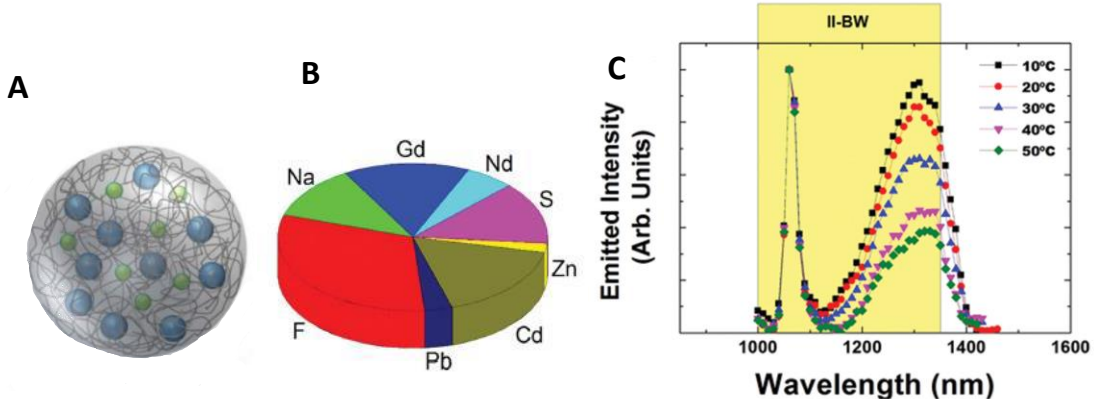

Figure 1.27 (A) Schematic diagram of the PLGA nanostructures encapsulating both $NaGdF_4:Nd^{3+}$ nanoparticles and PbS/CdS/ZnS quantum dots. (B) Compositional analysis of PLGA nanostructure (atomic%). (C) Emission spectra of the hybrid PLGA nanostructures under 808 nm excitation at different temperatures. Reproduced from reference.

1.8 Summary

A brief and detailed study of the luminescent nanothermometry is reviewed. The diversity of luminescent thermometers operating at the sub-micron scale described to clearly point out the emergent interest of nanothermometry in numerous fields, such as biomedicine, optoelectronic, micro- and nanofluidic systems, and in many other conceivable applications. The fundamental principles of luminescence thermometry and thermometer properties were discussed in depth. The aspects discussed in this chapter, are crucial to understand the work performed and presented in coming chapters.

Chapter 2

Boosting the sensitivity of luminescent nanothermometers in the biological window-I

2.1 Introduction

The use of NIR light instead of ultra-violet (UV) and VIS paramount in addressing the thermal sensing of luminescent nanomaterials, because of the operating wavelengths defined as BWs: I (650–950 nm), II (1000–1400 nm) and III (1550-1870). With three distinctive wavelengths, the BW regions provide an increase in optical penetration with an increase in wavelength, thus offering a high-resolution sensing and imaging. At this front, the most commonly explored host matrices are fluoride (phonon energy ~355 cm^{-1}), and oxide (~600 cm^{-1}) due to their high chemical stability and easy fabrication processes. Among them, Rare earth sesquioxides (RE_2O_3) have received much attention in the last decade due to their potential applications in wide range of areas including temperature sensing and bioimaging. For instance, Liu et al.[143] reported, Gd_2O_3:Ln^{3+} (Ln^{3+}=Yb, Er, Tm and Ho) UCNPs for simultaneous magnetic resonance imaging, dual-modal imaging and photodynamic therapy. Debasu et al.[139] evaluated all-in-one optical nanoplatform comprised of Gd_2O_3:Yb^{3+}/Er^{3+} UCNPS as thermometers and gold nanoparticles as heaters. Li et al.[144] demonstrated the feasibility of Sm^{3+} doped Gd_2O_3 downshift nanoparticles incorporated in TiO_2 in dye-sensitized solar cells to improve solar cell efficiency.

In general, sesquioxides exhibit five polymorphisms depending on temperature i.e. cubic C-type, monoclinic B-type and hexagonal A-type (>2000°C) and an additional two types, denoted by H and X (<2000°C). Their crystallographic forms and polymorphism have been briefly reviewed by Adachi and Imanaka [145], Zinkevich [146] and Stanek et al.[147]. Emphasis shall be given to cubic C-type structure as it is more relevant to the work reported in Chapters 2 and 3. The C-type has the bixbyite structure in space group *Ia-3*, having its most common form as Mn_2O_3 [147].

The unit cell contains 32 metal atoms (on the 8b and 24d sites) and 48 oxygen atoms (occupying all 48e sites) [146]. The structure is effectively a fluorite lattice with a quarter of the oxygen sites vacant. Due to this ordered arrangement of the oxygen atoms the structure constitutes two non-equivalent cation sites with C_2 (noncentrosymmetric) and C_{3i} or S_6 (centrosymmetric) local symmetries (as shown in Figure 2.1A along with the polyhedral representation in Figure 2.1B). Therefore, photoluminescence properties of emitting cations residing in the two sites are thus quite different.

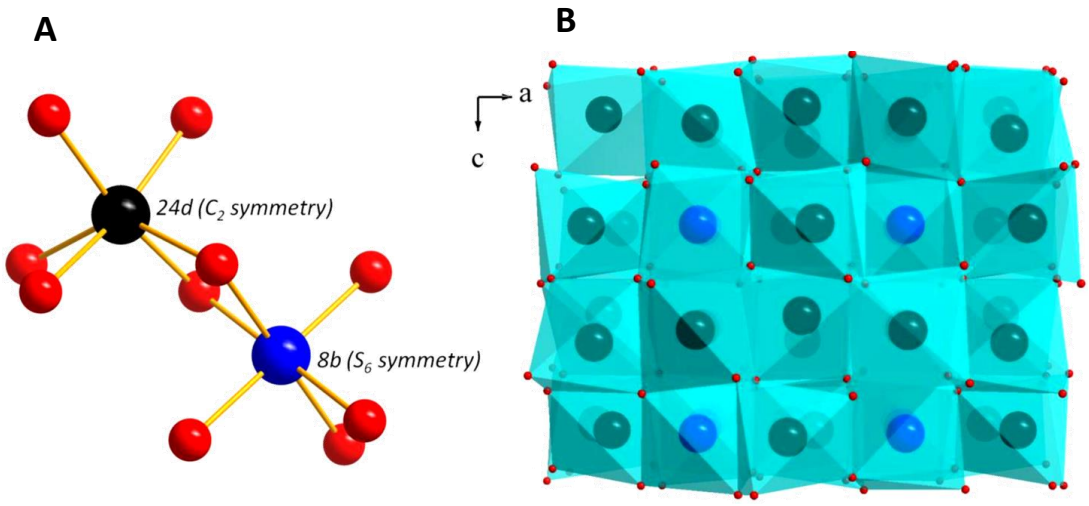

Figure 2.1(A) Cubic C-type structure of Re_2O_3 coordination geometry of the 24d (C_2 symmetry) and 8b (C_{3i} or S_6 symmetry) sites of metal ion (Re^{3+}) and (B) polyhedral representation along [010] direction. Black and blue balls stand for the 24d and 8b sites of Re^{3+} atoms, respectively, and red balls represent O atom. Adopted from reference[148].

In combination with the promising host material, Nd^{3+}(800 to 1850 nm, NIR-I, II, III) ions have been extensively exploited as sensitizer either single doped or co-doped with Yb^{3+}(980 nm, NIR-I) ions [122, 129]. Few research works also investigated Yb^{3+}/Ln^{3+} (Ln^{3+}=Er^{3+},Tm^{3+}) co-doped upconverting materials for thermal sensing in BW's[149, 150]. Out of all, Nd^{3+} serves as an excellent candidate, owing to ladder-like intra-4f energy-level structure facilitates not only the possibility of exciting in NIR but also feasible emission in NIR region. All the Nd^{3+}-based nanothermometers reported so far for the first BW, use a thermometric parameter defined by the intensity ratio between the $^4F_{3/2(1)} \rightarrow {}^4I_{9/2}$ and $^4F_{3/2(2)} \rightarrow {}^4I_{9/2}$ transitions, where $^4F_{3/2(1)}$ and $^4F_{3/2(2)}$ are two Stark components of $^4F_{3/2}$ multiplet. These thermometers have an inherent limitation of very low relative sensitivity (*ca*. 0.1 %·K^{-1}, Chapter 1. Table 1.1) due to the small energy difference between the two Stark components (typically<100 cm^{-1}). The relative sensitivity maybe increased

by more than one order of magnitude, if the thermometric parameter is defined as the intensity ratio between two distinct transitions the $^4F_{5/2}\rightarrow{}^4I_{9/2}$ and $^4F_{3/2}\rightarrow{}^4I_{9/2}$ transitions, in examples like $La_2O_2S:Nd^{3+}$ bulk powder [123], $NaYF_4:Nd^{3+}$ [121], $CaWO_4$: Nd^{3+}/Yb^{3+} [122], and $NaYF_4:Nd^{3+}/Yb^{3+}$ [129].

Despite this, the type of detectors used for measuring the Nd^{3+} emission in the 800–900 nm range essentially determines the choice of defining the thermometric parameter. Figure 2.2 depicts the quantum efficiencies of most commonly used detectors for Nd^{3+} emission in BW region, namely photomultiplier tube (PMT), charge coupled device (CCD) and InGaAs detectors, respectively. However, the use of a silicon-based charge-coupled device (CCD) detector showed a limitation as reported in the works of Wawrzynczyk et al. [120], Rocha et al. [5, 151] and Benayas et al. [4], since, in these works, the experimental apparatus includes filters to avoid the residual laser excitation signal that obscures the $^4F_{5/2}\rightarrow{}^4I_{9/2}$ transition at 830 nm of Nd^{3+} ion.

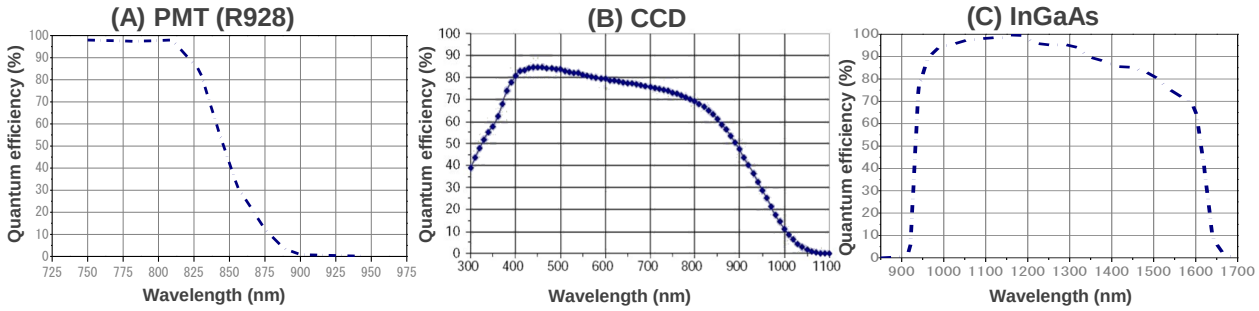

Figure 2.2 Detector quantum effciencies for (A) photomultiplier tube (PMT), (B) charge coupled device (CCD) and (C) InGaAs at room temperature, obtained from Hamamatsu photonics.

This chapter presents one of the pathways to boost the thermal sensitivity of Nd^{3+}-based luminescent nanothermometers in the first BW region, considering the aspects highlighted earlier. For this purpose, Nd^{3+}-doped Gd_2O_3 nanorods were prepared following a simple wet chemical method. Structural and luminescence characterization of the $(Gd_{1-x}Nd_x)_2O_3$ nanorods were studied analysing with powder X-ray diffraction, Transmission electron microscopy and photoluminescence studies in the form of excitation, emission and lifetimes. Furthermore, the temperature dependent luminescence studied, from where the thermal sensing properties of $(Gd_{1-x}Nd_x)_2O_3$ nanorods were obtained. The increase in sensitivity value is achieved using a common R928 photomultiplier tube that allows defining the thermometric parameter as the integrated

intensity ratio between the $^4F_{5/2} \rightarrow {}^4I_{9/2}$ and $^4F_{3/2} \rightarrow {}^4I_{9/2}$ transitions with an energy difference between the barycenters of the two transitions (>1000 cm^{-1}).

2.2 Synthesis and characterization of nanorods

Synthesis of nanorods

A simple wet-chemical route was used to synthesize $(Gd_{0.99}Nd_{0.01})_2O_3$ nanorods (nominal concentration of 1.00 mol% Nd^{3+} relative to Gd^{3+}), following a previously reported procedure [152]. Briefly, aqueous solutions of $Gd(NO_3)_3$ (8.91 mL, 0.4 M), and $Nd(NO_3)_3$ (0.09 mL, 0.1 M) were mixed with distilled water (40 mL) in a 250 mL round-bottom flask. Then, an aqueous NH_3 solution (30 mL, 25 wt%) was added dropwise to the above solution under stirring, at room temperature. The resulting white viscous solution was sonicated for about 10 minutes and then vigorously stirred again for additional 10 minutes. In the next step, the solution was heated up to 343 K and maintained at this temperature for 16 hours under continuous magnetic stirring. After 16 hours, heating and stirring of the reaction were terminated, and the solution was allowed to cool down to room temperature. The white precipitate was collected, centrifuged and washed several times with distilled water and once with ethanol. The resulting precursor was dried at 348 K for 24 hours in air, yielding $(Gd,Nd)(OH)_3$ nanorod powder, which was finely ground in an agate mortar and pestle. Finally, a few milligrams of this fine powder was calcined at 973 K for 3 hours with heating and cooling rates of 2 and 5 $K \cdot min^{-1}$, respectively, affording $(Gd_{0.99}Nd_{0.01})_2O_3$ nanorod powder. The same procedure was followed to obtain $(Gd_{0.975}Nd_{0.025})_2O_3$ and $(Gd_{0.95}Nd_{0.05})_2O_3$ nanorods by changing the relative Gd^{3+} and Nd^{3+} concentrations.

Elemental analysis

Inductively coupled plasma optical emission spectroscopy (ICP-OES-Activa-M, Horiba Jobin Yvon) revealed that the nominal concentrations of 1.00, 2.50 and 5.00 mol% Nd^{3+} relative to Gd^{3+} in the as-synthesised materials were found to be 0.94, 2.43 and 4.91 mol% Nd^{3+}, respectively, in the final $(Gd_{1-x}Nd_x)_2O_3$ nanorods.

Powder X-ray diffraction

The crystal structures of the precursors and as-synthesized nanorods were determined with PXRD. Figure 2.3A, presents the powder X-ray diffraction patterns of the precursors indexed with the

pure hexagonal $Gd(OH)_3$ phase, PDF-01-083-2037 (standard structure data obtained from the International Centre for Diffraction Data (ICDD) database). After calcination at 973 K for 3 hours, the obtained calcined samples powder X-ray diffraction patterns, shown in Figure 2.3B. The samples contain the cubic phase, in agreement with Gd_2O_3 (PDF-04-015-1513) and references [139, 152]. No new reflections or changes in the diffraction peak positions are observed when the amount of Nd^{3+} increases from 1 to 5 mol%, indicating that these ions have been effectively introduced in the Gd_2O_3 host lattice.

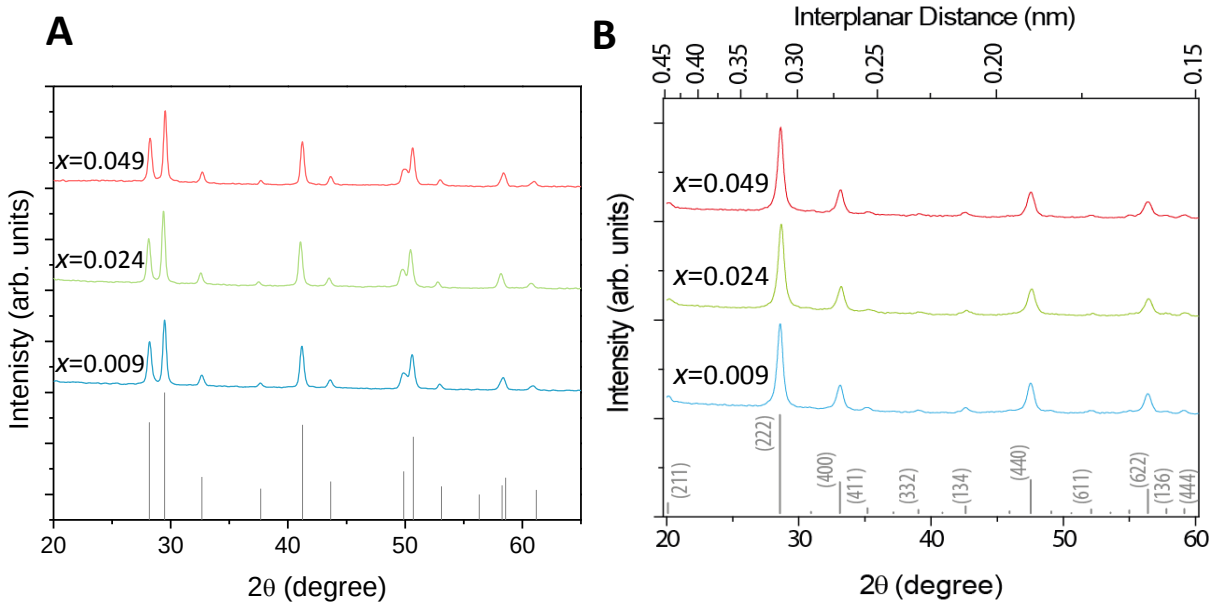

Figure 2.3 Powder X-ray diffraction patterns of (A) precursor hexagonal $(Gd_{1-x}Nd_x)(OH)_3$ nanorods indexed to PDF-01-083-2037 and (B) cubic $(Gd_{1-x}Nd_x)_2O_3$ nanorods indexed to PDF-04-015-1513. Nd^{3+} concentrations x=0.009 (blue), 0.024 (green) and 0.049 (red). The most intense reflections of cubic Gd_2O_3 and the corresponding interplanar distances are also depicted in (B).

Transmission electron microscopy

The representative transmission electron microscopy images show $(Gd_{0.991}Nd_{0.009})_2O_3$ nanorods roughly uniform in diameter and length (Figure 2.4A-C). The measured distances between adjacent planes were determined from these images as 0.314±0.004 nm (222) and 0.275±0.004 nm (400) along with the corresponding orientations of the indexed planes by powder X-ray diffraction (Figure 2.4B, C). The values are in accord with the corresponding interplanar distances listed in the ICDD database, 0.3121160 nm and 0.2703000 nm.

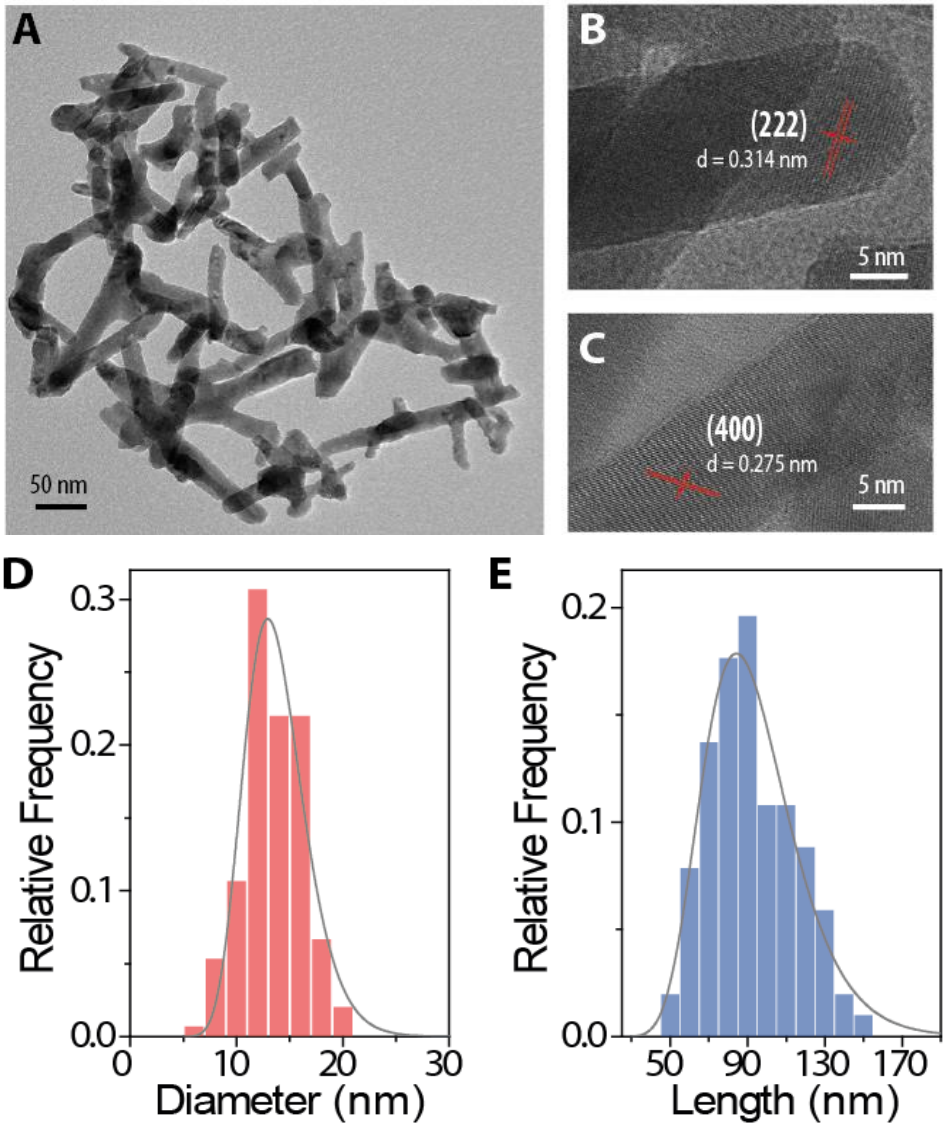

Figure 2.4 (A) Transmission electron microscopy image of $(Gd_{0.991}Nd_{0.009})_2O_3$ nanorods. (B and C) (222) and (400) crystallographic planes and interplanar distances of cubic Gd_2O_3. (D and E) Nanorods diameter and length distribution respectively.

Figure 2.4D and E, represents the diameter and the length distributions of the nanorods measured for over 100 nanorods with sizes between 6 to 20 nm and from 50 to 150 nm range, respectively. The solid lines are the best fit of the experimental data to a log-normal distributions (r^2>0.902) yielding a diameter of 13.5±3.5 nm and a length of 91.0±11.0 nm. Similarly, the size distributions were calculated for $(Gd_{0.976}Nd_{0.024})_2O_3$ and $(Gd_{0.951}Nd_{0.049})_2O_3$ nanorods (Appendix B.1), values of 13.8±3.5 and 14.4±3.5 nm in diameters and 109.0±13.1 nm and 99.2±11.6 nm of lengths.

Results and discussion

2.3 Excitation and emission spectra

Figure 2.5A presents the room temperature excitation spectra of the nanorods in the range 300–850 nm, recorded by monitoring the $^4F_{3/2} \rightarrow {}^4I_{11/2}$ transition at 1075 nm, exhibit several sharp peaks ascribed to the Nd^{3+} intra-4f transitions [153, 154]. The spectra were normalized to the corresponding Nd^{3+} concentrations. The energy of the excitation peaks is independent of the Nd^{3+} concentration. All the transitions starting from the ground state $^4I_{9/2}$ to the excited states of Nd^{3+} ion. The excitation intensity is stronger for the $^4I_{9/2} \rightarrow {}^4G_{5/2}+{}^4G_{7/2}$ (580 nm) transition. The room temperature emission spectra of the nanorods recorded in the range 800–1500 nm with InGaAs detector, by exciting at 580 nm shown in Figure 2.5B. Regardless of the Nd^{3+} concentration, the emission spectra display three main intra-4f transition regions, assigned to the $^4F_{3/2} \rightarrow {}^4I_{9/2}$ (880–1000 nm), $^4F_{3/2} \rightarrow {}^4I_{11/2}$ (1000–1210 nm), and $^4F_{3/2} \rightarrow {}^4I_{13/2}$ (1300–1480 nm) transitions [155]. The energy of the transitions is independent of the Nd^{3+} molar concentration.

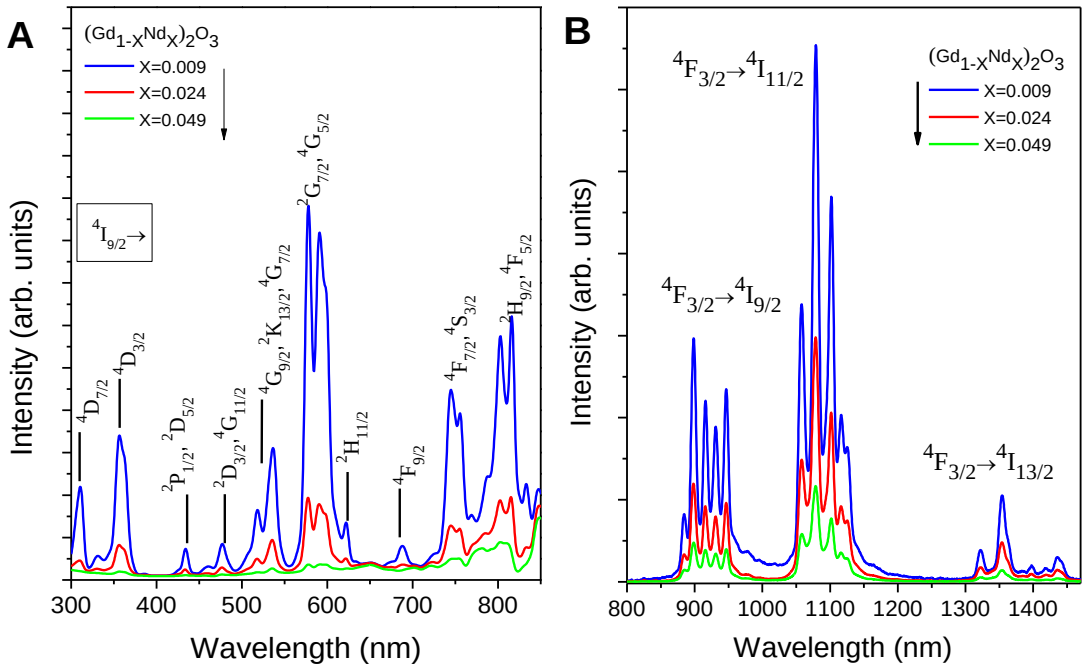

Figure 2.5 Room temperature (A) excitation spectra monitoring the $^4F_{3/2} \rightarrow {}^4I_{11/2}$ transition at 1075 nm, and (B) emission spectra exciting the $^4I_{9/2} \rightarrow {}^4G_{5/2}+{}^4G_{7/2}$ transition at 580 nm, of $(Gd_{1-x}Nd_x)_2O_3$, x=0.009 (blue), 0.024 (red) and 0.049 (green) nanorods measured in solid form. The spectra were normalized to the corresponding Nd^{3+} concentration of the samples.

Moreover, owing to the hygroscopic nature, Gd_2O_3 is sensitive to the moisture. Thus, the emission spectra were measured for the investigation of water uptake (hygroscopicity). $(Gd_{0.991}Nd_{0.009})_2O_3$

nanorods emission spectra obtained during one week in laboratory atmosphere shown in Figure 2.6A, displays no significant differences, proving that the nanorods are quite insensitive to moisture. As previously stated, the emission spectra recorded with InGaAs detector in Figure 2.6B. However, due to the detection limit of the detector in the 720−850 nm region (Figure 2.2C), the $^4F_{5/2} \rightarrow {}^4I_{9/2}$ transition (800−850 nm) could not be discerned. In contrast, this transition is clearly seen in the spectrum recorded using the R928 detector. Figure 2.6B displays the emission spectrum of $(Gd_{0.991}Nd_{0.009})_2O_3$ in the 725−975 nm range measured with a R928 photomultiplier and an InGaAs-based detector at 580 nm excitation. Moreover, as the three more energetic Stark components of the $^4F_{3/2} \rightarrow {}^4I_{9/2}$ transition are observed in the spectrum measured using the R928 detector (Figure 2.6B). This detector may be used to measure the Nd^{3+} emission in the 800−920 nm range and further to study thermometry of the nanorods in the BW-I.

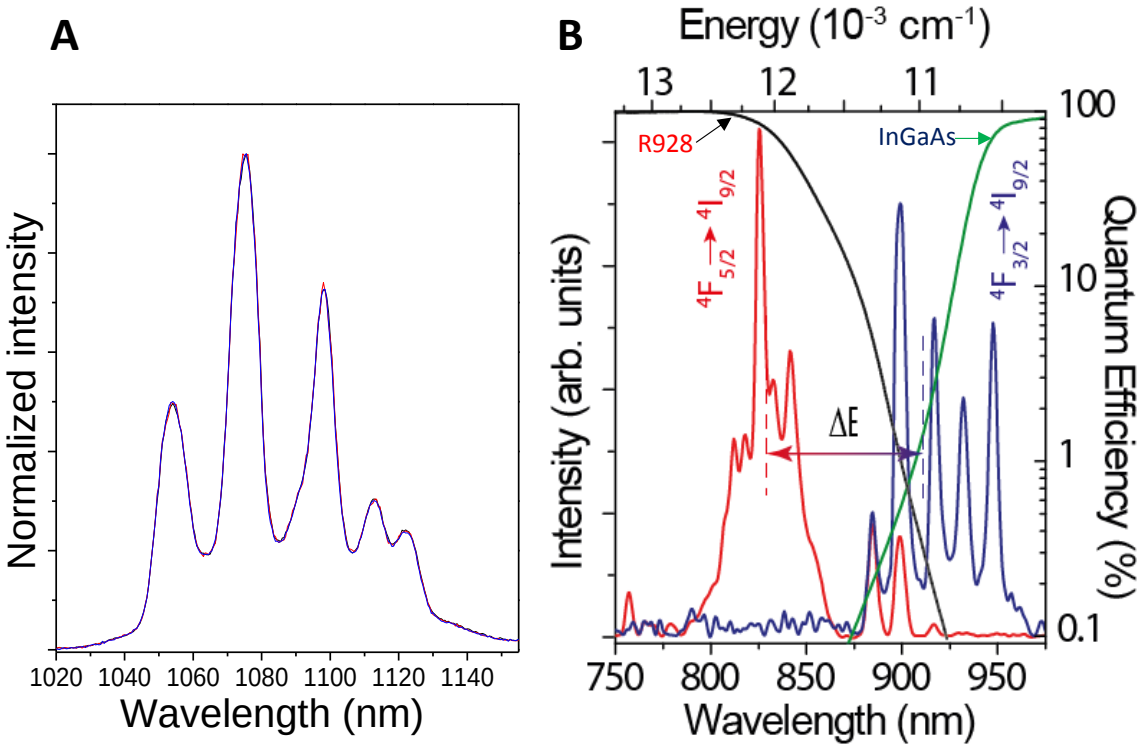

Figure 2.6 Emission spectra of $(Gd_{0.991}Nd_{0.009})_2O_3$ powder nanorods (A) recorded at room temperature. After synthesis, the sample was kept 1 day (black line), 5 days (red line) and 7 days (blue line) in laboratory atmosphere and (B) recorded in the 750−980 nm range measured with the R928 (red) and InGaAs (blue) detectors. Black and green lines depict, respectively, the photosensitivity of the R928 photomultiplier and InGaAs-based detector. The excitation wavelength is 580 nm.

2.4 Decay times

Emission decay times

Figure 2.7A shows the semi-logarithmic plot of the experimental decays of the $^4F_{3/2}$ level for the

$(Gd_{1-x}Nd_x)_2O_3$ nanorods (x=0.009, 0.024 and 0.049) obtained at 300 K. As can be seen, the decay curves deviate from a single exponential at short times and the $^4F_{3/2}$ lifetime shortens with increasing Nd^{3+} concentration, $(0.134\pm0.005)\times10^{-3}$ s, for x=0.009, $(0.060\pm0.002)\times10^{-3}$ s, for x=0.024, and $(0.020\pm0.001)\times10^{-3}$ s, for x=0.049. The $^4F_{3/2}$ average lifetime values calculated using the initial delay $t_0=0.05\times10^{-3}$ s in Equation A.[156, 157]. As stated before, cubic Gd_2O_3 contains two crystallographically non-equivalent Nd^{3+} sites with C_2 (non-centrosymmetric) and C_{3i} or S_6 (centrosymmetric) local symmetries in a 3:1 occupation ratio [152]. However, as the $^4F_{3/2}\rightarrow{}^4I_{11/2}$ transition is forbidden in C_{3i} or S_6 local symmetry, the deviation from a single-exponential character of the $^4F_{3/2}$ decays, and the reduction of the corresponding lifetime values as concentration increases can be due to Nd^{3+}-to-Nd^{3+} energy transfer that is dominated by cross-relaxation processes, such as $(^4F_{3/2}, {}^4I_{9/2})\rightarrow(^4I_{15/2}, {}^4I_{15/2})$ [157-160]. Multiphonon relaxation is expected to be small because of the energy gap between the $^4F_{3/2}$ and $^4I_{15/2}$ levels and the values of the phonon energy involved. Thus, in order to minimize energy losses, the low Nd^{3+} concentration $(Gd_{0.991}Nd_{0.009})_2O_3$ sample is used in all subsequent measurements. Furthermore, the longer lifetime of Nd^{3+} in this sample is preferable for applications in bioimaging due to the potential screening of tissue autofluorescence under VIS light excitation, e.g. 580 nm.

Temperature dependent emission decay times

The dependence of the $^4F_{3/2}$ lifetime with temperature for $(Gd_{0.991}Nd_{0.009})_2O_3$ nanorods between 133 and 323 K displayed in Figure 2.7B. As can be seen, the decay curves deviate from a single exponential and the $^4F_{3/2}$ lifetime does not show a significant change with the temperature, $(0.143\pm0.005)\times10^{-3}$ s, for 323 K, $(0.141\pm0.005)\times10^{-3}$ s, for 273 K, $(0.140\pm0.005)\times10^{-3}$ s, for 223 K, and $(0.133\pm0.005)\times10^{-3}$ s, for 133 K (the minimal change lies within the error of experimental conditions). Hence $^4F_{3/2}$ emission decay curves clearly show that the temperature dependence of the $^4F_{3/2}$ lifetime is irrelevant for temperatures near 300 K evidencing that these nanorods cannot be used as luminescent temperature sensors based on the emission lifetime near room temperature.

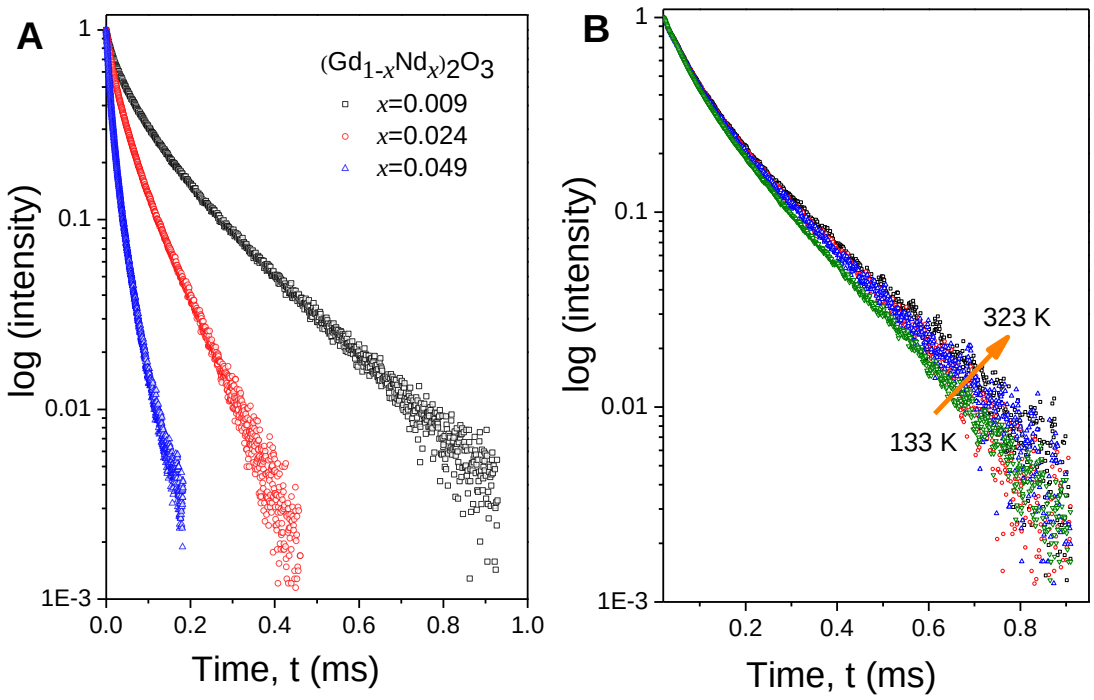

Figure 2.7 Semi-logarithmic plot of the $^4F_{3/2}$ emission decay curves: (A) Measured for $(Gd_{1-x}Nd_x)_2O_3$ nanorods (x=0.009, 0.024 and 0.049, black, red and blue symbols, respectively) at 300 K. (B) Measured for $(Gd_{0.991}Nd_{0.009})_2O_3$ nanorods at 133 K, 223 K, 273 K and 323 K, green, blue, red and black symbols, respectively. The decay curves were obtained exciting at 808 nm and monitoring the $^4F_{3/2}\rightarrow{}^4I_{11/2}$ transition.

2.5 Thermometry

Temperature dependent emission spectra

In order to study thermal sensing properties of the $(Gd_{0.991}Nd_{0.009})_2O_3$ nanorods, the temperature dependent emission spectra of $(Gd_{0.991}Nd_{0.009})_2O_3$ measured with the R928 detector in the 288–323 K (physiological range) at 580 nm excitation. Figure 2.8A, shows that increasing the temperature results in a significant variation in the ratio of intensities of the $^4F_{5/2}\rightarrow{}^4I_{9/2}$ and $^4F_{3/2}\rightarrow{}^4I_{9/2}$ transitions: while I_2 is nearly constant, I_1 increases approximately 60% (Figure 2.8B). This allows defining the thermometric parameter $\Delta=I_1/I_2$, where I_1 and I_2 are the integrated intensities of the $^4F_{5/2}\rightarrow{}^4I_{9/2}$ and $^4F_{3/2}\rightarrow{}^4I_{9/2}$ transitions, respectively. Moreover, these two transitions are particularly good for thermal sensing because their intensity ratio shows a significant temperature dependence owing to a remarkable experimental energy gap between two transitions.

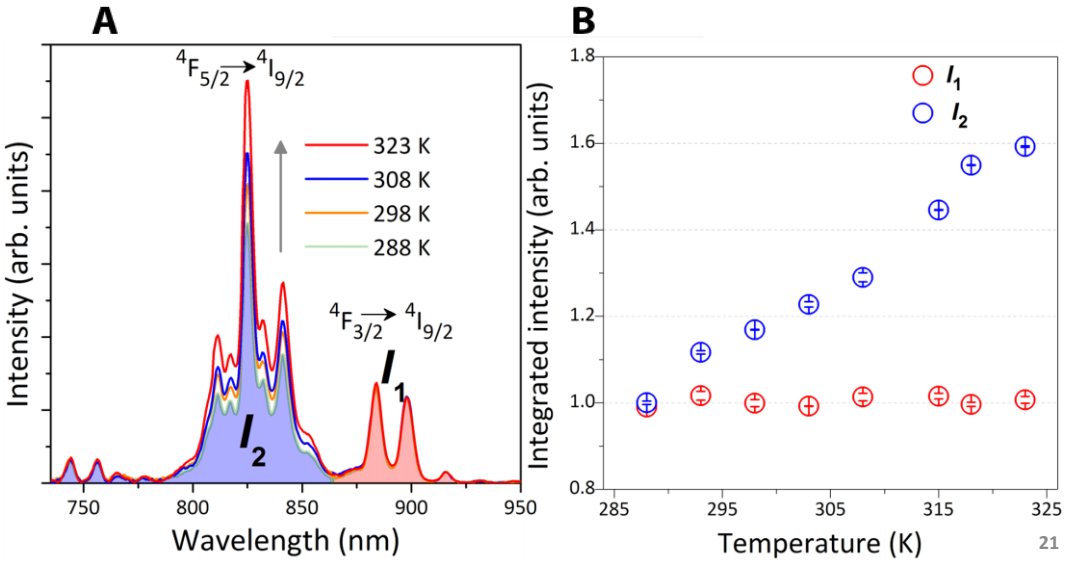

Figure 2.8 (A) Emission spectra of $(Gd_{0.991}Nd_{0.009})_2O_3$ powder nanorods in the 288−323 K range under 580 nm excitation. (B) Normalized integrated intensity of $^4F_{5/2} \rightarrow {}^4I_{9/2}$ (I_1, blue) and of $^4F_{3/2} \rightarrow {}^4I_{9/2}$ (I_2, red) computed using the782−865 nm and the 865−925 nm wavelength range, respectively.

The emission intensity ratio Δ was converted to temperature using the calibration curve represented in Figure 2.9. The experimental thermometric parameter Δ, was then fitted to a straight line to obtain a local calibration curve between 288–323 K range. The errors in thermometric parameter Δ, were calculated from the error in the determination of the integrated areas of each transition.

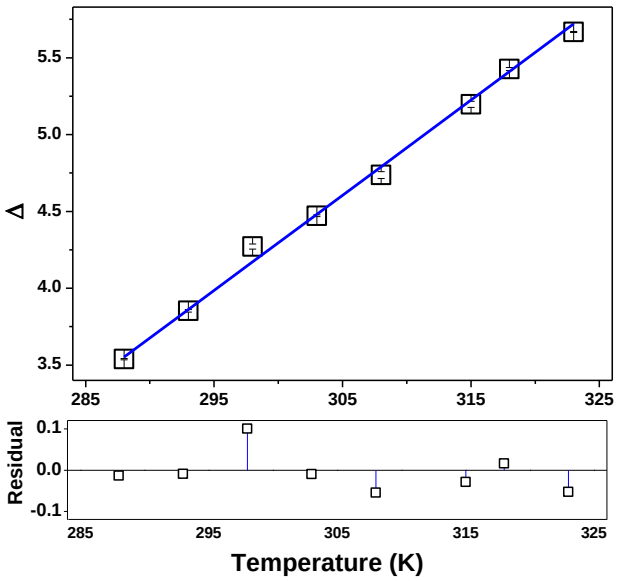

Figure 2.9 Calibration curve in the 288−323 K range. The open points correspond to the experimental thermometric parameter Δ and the error bars result from the error in the determination of the integrated areas of each transition. The solid line is the best fit of the experimental data to a straight line (r^2>0.996). The fit residuals are presented in the bottom of the plot.

Determination of barycenter

For the better understanding of the thermal properties of the nanorods it is pivotal to determine the energy gap between the two thermally coupled levels. Since the barycenter of the Nd^{3+},$^4F_{5/2}$, $^4F_{3/2} \rightarrow ^4I_{9/2}$ transitions were determined using the emission spectra measured with both R928- and InGaAs-based detectors, respectively. In order to minimize the experimental difficulties in assigning precisely the Stark-Stark transitions rather than using the most conventional method of determining the barycenters *J-J'* transitions, the barycenter was determined in another way in terms of fitting the envelope of the $^4F_{3/2} \rightarrow ^4I_{9/2}$ and $^4F_{5/2} \rightarrow ^4I_{9/2}$ transitions. Since it is not a very standard and common way of determining barycenter, a brief explanation is given for the better understanding of the process.

The experimental energy gap between the barycenter energy of the $^4F_{5/2}$ and $^4F_{3/2}$ levels was determined, deconvoluting the emission transitions to a set of Lorentzian peaks (using the minimum number of peaks, 8 and 5 respectively, in
Figure 2.10A and B) with the peak analyzer routine of the OriginLab© software. The barycenter's of the $^4F_{5/2}$ and $^4F_{3/2}$ levels are calculated by a weighted arithmetic mean using the fitted area (A_i) and peak energy (position of the centre of gravity(C_i), of the fitting enveople) of each Lorentzian function. Thus, the energy gap is the difference between the barycenter's $\Delta E = E_2 - E_1$, calculated by

$$E_{j=1,2} = \frac{\sum_{i=1}^{n} A_i C_i}{\sum_{i=1}^{n} A_i} \qquad (2.1)$$

and the corresponding error, $\delta\Delta E = \delta E_1 + \delta E_2$, is the error in the difference given by

$$\delta E_{j=1,2} = \frac{1}{\sum A_i} \sqrt{(A_i \delta C_i)^2 + (C_i \delta A_i)^2 + (E_j \sum A_i \delta A_i)^2} \qquad (2.2)$$

The minimum error in ΔE should be the difference between the barycenter energy of the $^4F_{5/2}$ and $^4F_{3/2}$ levels obtained as $\Delta E = 1092 \pm 10$ cm^{-1} (

Figure 2.10C), which is much larger than that between two $^4F_{3/2}$ Stark sublevels (<100 cm^{-1}). A good agreement was obtained with the value computed by Carnall et al. for $LaF_3:Nd^{3+}$ (1039 cm^{-1})[161].

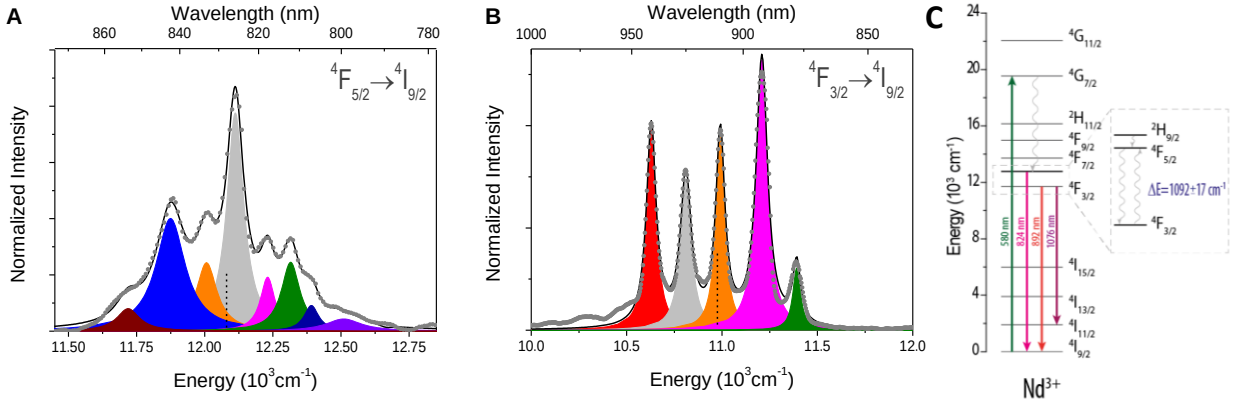

Figure 2.10 (A and B) Experimental emission spectra (points) of powder nanorods in the spectral region corresponding to the $^4F_{5/2}$, $^4F_{3/2} \rightarrow {}^4I_{9/2}$ transitions. The experimental curves were fitted to a set of 8 and 5 Lorentzian peaks, respectively, (r^2>0.991), resulting in the components (shadowed areas) and to the envelope (solid line). The interrupted vertical line marks the position of the centre of gravity of the envelope and was taken as the barycenter of the transition. (C) Partial energy-level diagram of Nd^{3+} ions highlighting the absorption at 580 nm and the emissions at 824, 892 and 1076 nm. The expansion depicts the thermally coupled $^4F_{3/2}$ and $^4F_{5/2}$ levels [162].

2.6 Relative thermal sensitivity and temperature uncertainty

Figure 2.11. depicts the temperature dependence of the relative sensitivity of $(Gd_{0.991}Nd_{0.009})_2O_3$ nanorods (detailed explanation of S_r is presented in Chapter 1.6). The maximum relative sensitivity value of 1.75±0.04 %·K^{-1} (accessed using Equation 1.15) attained at 288 K is the highest reported (by one order of magnitude) for the physiological range for luminescent Nd^{3+}-based thermometers (Table 1.1). As the emission spectra of $(Gd_{0.991}Nd_{0.009})_2O_3$ measured with the R928 photomultiplier (Figure 2.8A) were not corrected for the detector response, thus the calculated sensitivity values are somehow convoluted by that response. However, this correction is a multiplicative factor affecting essentially I_2 and, thus, we should not anticipate significant changes on the S_r values. Furthermore, the total integration of the $^4F_{3/2} \rightarrow {}^4I_{9/2}$ transition (I_2) cannot be acquired completely, which in turn limits the possibility of correlating the measured thermal sensitivity with the Boltzmann statistics for temperature-induced population distribution.

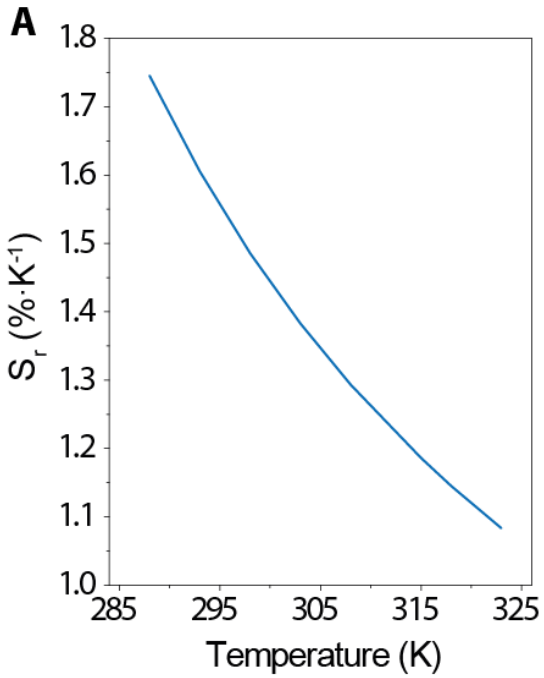

Figure 2.11 Relative sensitivity of the $(Gd_{0.991}Nd_{0.009})_2O_3$ thermometer decreasing from 1.75±0.04 to 1.08±0.03 %·K^{-1} in the 288−323 K.

Moreover, the reported maximum S_r value is one of the highest value reported so far for nanothermometers operating in the first transparent NIR window at temperatures in the physiological range [124]. For instance, the value presented here is comparable with the maximum S_r value of CaF_2:Tm^{3+},Yb^{3+} nanoparticles, around 2 %·K^{-1} at 299 K [100]. One should emphasize, however, that the thermal sensitivity comparison presented for nanothermometers in Figure 1.29 [124] is mix relative with absolute thermal sensitivity values (for instance the value reported for Y_2O_3:Tm^{3+},Yb^{3+} nanoparticles [99] is the absolute sensitivity S_a). Compared to the absolute sensitivity, $S_a=\partial\Delta/\partial T$, S_r presents the critical advantage for being independent of the nature of the thermometer (*i.e.* mechanical, electrical, luminescent) allowing the direct and quantitative comparison between thermometers, a powerful tool for all applications were different techniques must be pondered.

Estimation of Temperature uncertainty

If the relative sensitivity allows comparing the performance of different materials, the temperature uncertainty, δT, depends on the actual temperature resolvable by the material, and on the experimental detection setup.

Figure 2.12 shows the temperature dependence of the temperature uncertainty of the $(Gd_{0.991}Nd_{0.009})_2O_3$ nanorods. The minimum temperature uncertainty is δT=0.14±0.05 K, estimated from the value of $\delta\Delta/\Delta$=0.24% (Equation 1.17 and 1.18). This value can be improved by decreasing the signal-to-noise ratio in the acquisition of each emission spectrum, which can be achieved by using larger integration times and/or averaging consecutive measurements of the emission spectrum. However, there is a compromise between lowering the temperature uncertainty and lowering the acquisition time: the longer the acquisition time the lower the temperature uncertainty. The minimum achievable temperature uncertainty is defined by the uncertainty of the experimental setup, in the order of $\delta\Delta/\Delta$~0.05% for the case of a laboratory-grade fluorimeter.

Temperature uncertainty and thermometer size

The temperature uncertainty can also be assessed based on the size and system-dependent properties using the spin-boson model, Equation 1.20[163]. The number of atoms in the sample (N_A) were obtained from the volume of the nanorods and the density of Gd_2O_3 at 298 K, 7.41×10^3 $kg\cdot m^{-3}$. The volume of the nanorods was calculated using the diameter (13.5±3.5 nm) and length (91.0±11.0 nm) values shown in Figure 2.4B and C. The maximum (δT_{max}) and minimum (δT_{min}) temperature uncertainty values were determined by considering the error in length (10%) and radius (20%) of the nanorods. These values further compared with the value (δT) obtained with the nanorods mean radius and length. The error in the temperature uncertainty corresponds to the maximum deviation, (δT_{max}–δT or δT–δT_{min}).

Figure 2.12 shows the temperature dependence of the temperature uncertainty calculated with Equation 1.20 using N_A=(1.5±0.5)×10^5 and T_D=362 K [164]. In this case, the number of atoms in a single nanorod is sufficient to assure, in the due time, equilibrium for any state function to be measured. Even though the estimation of the temperature uncertainty of a single nanorod is about 5 times larger than the experimental value (Equation 1.17), the latter interrogates not a single nanoparticle but an ensemble of nanorods in thermal contact. In fact, considering 20–30 nanorods in contact as shown in Figure 2.4A, the agreement between theoretical (0.14–0.18 K) and experimental (0.16 K) uncertainties are very good. Thus, the theoretical temperature uncertainty should be the upper limit of the experimental temperature error. TEM images were captured for around 5-10 distinct spots in the carbon film which show similar aggregation sizes of the rods

which confirms the discrepancies between experiment and theory examine the around 100 or above number of nanoparticles.

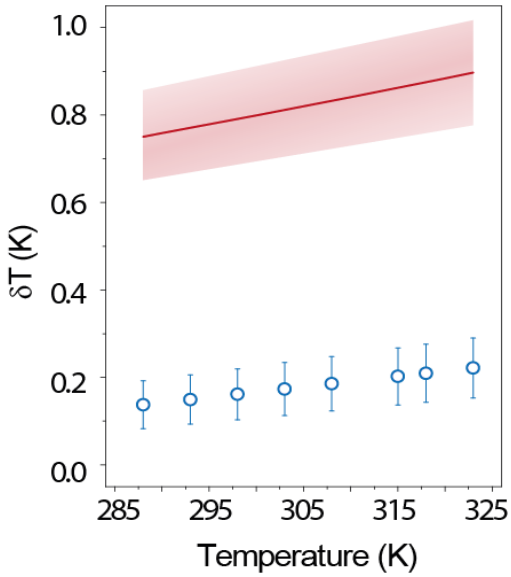

Figure 2.12 Temperature uncertainty computed using Equation 1.17 (open points) and Equation 1.20 (solid line). The error bars result from error propagation in the determination of the temperature uncertainty by Equation 1.17 and the shadowed area marks the error in the temperature uncertainty using Equation 1.20.

2.7 Summary

Cubic phase $(Gd_{1-x}Nd_x)_2O_3$ (x=0.009, 0.024 and 0.049) nanorods have been successfully synthesized by a simple wet-chemistry route. The samples were characterized by powder XRD, ICP-OES, TEM and photoluminescence spectroscopy in the form of excitation, emission and decay curves. The emission decay curves of $(Gd_{0.991}Nd_{0.009})_2O_3$ shown to be irresponsive to the temperature variations. Furthermore, the performance of $(Gd_{0.991}Nd_{0.009})_2O_3$ as an intensity-based ratiometric nanothermometer was evaluated in the 288–323 K range. These nanorods exhibit the highest thermal sensitivity and temperature uncertainty reported so far (1.75±0.04 %·K^{-1} and 0.14±0.05 K, respectively, at 288 K) for a nanothermometer operating in the first NIR window. The sensitivity value is one order of magnitude higher than those reported for other Nd^{3+}-based nanothermometers. Moreover, this high sensitivity was achieved using a common R928 photomultiplier tube to measure the Nd^{3+} emission in the 800−920 nm range, which allowed defining the thermometric parameter as the integrated intensity ratio of the $^4F_{5/2}\rightarrow{}^4I_{9/2}$ and $^4F_{3/2}\rightarrow{}^4I_{9/2}$ electronic transitions, rather than the two Stark components of the $^4F_{3/2}$ multiplet. The increase by one order of magnitude in the relative sensitivity of nanothermometers operating in

the first biological window permits to overcome the main drawback of previous Nd^{3+}-based nanothermometers, therefore widening the scope for using Nd^{3+} ions in deep-tissue imaging and thermal sensing.

Chapter 3

Implementing luminescence nanothermometry in biological window-II

3.1 Introduction

NIR light (700–2500 nm) can penetrate biological tissues (e.g. skin and blood) more efficiently than VIS light because of the low scattering and absorption of light at longer wavelengths. The absorption spectrum of human skin in Figure 3.1 explicitly demonstrates that the NIR light compared to VIS light results an increase in transparency of biological tissue for thermal sensing and bioimaging applications. Hereof, the implementation and the applicability of NIR light arising from the Ln^{3+}-doped NIR emitting nanoparticles for thermal sensing in the first BW have been briefly discussed in the Chapter 2.

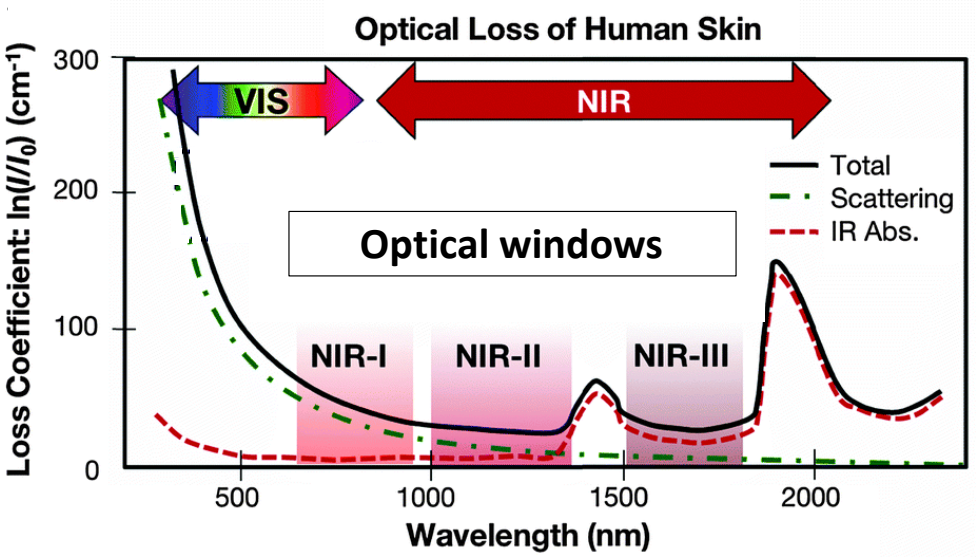

Figure 3.1 Absorption spectrum of human skin showing the first (NIR-I), second (NIR-II) and third (NIR-III) BWs. Adopted from reference [3].

Although the thermal sensing seems to be promising using Nd^{3+}-doped nanoparticles, the application of these materials limited by substantial background noise caused by the tissue autofluorescence in optical window I [117]. Moving from BW first to second, there is a reduction

in the optical scattering due to the higher wavelengths used. As a consequence, nanoparticles for thermal sensing applications in the second BW show an improvement in the resolution as well as longer penetration depths [165, 166]. At this front, numerous Ln^{3+} ions have been exploited, mainly Nd^{3+}(800 to 1850 nm), Yb^{3+}(980 nm), Ho^{3+}(1200 nm), Tm^{3+}(1475 nm), Er^{3+}(1550 nm), and Pr^{3+}(1000 to 1600 nm). Among all, owing to its much probable, intense luminescence emission transitions ($^4F_{3/2}\rightarrow{}^4I_{11/2}$, and $^4I_{13/2}$ in BW-II), Nd^{3+}-doped DS materials widens up their potential for thermal sensing in the BW as well.

So far, the thermal sensing operated in the second BW was predominantly from the analysis of temperature dependent/independent Nd^{3+} emission, when excited with NIR light. For instance, Cerón et al. [124] reported composites comprising $NaGdF_4$:Nd^{3+} nanoparticles and PbS/CdS/ZnS quantum dots in a poly(lactic-co-glycolic acid) organic–inorganic hybrid nanostructure operating in the second BW between 283 and 328 K, where the Nd^{3+} emission at 1060 nm is temperature independent. Similarly, Marciniak et al. combined the Nd^{3+} emission at 1060 nm ($^4F_{3/2}\rightarrow{}^4I_{11/2}$) and Yb^{3+} emission at 980 nm ($^2F_{5/2}\rightarrow{}^2F_{7/2}$) in $NaYF_4$ core/shell to achieve wide range temperature responsive thermometer (150–450 K) [126]. Only in the particular example of, Ximendes et al. [125] showed that Nd^{3+}/Yb^{3+} co-doped LaF_3 core/shell nanostructures are operative in the second BW region using the emissions arising from the Nd^{3+} 1300 nm ($^4F_{3/2}\rightarrow{}^4I_{13/2}$) and Yb^{3+} 1000 nm ($^2F_{5/2}\rightarrow{}^2F_{7/2}$) transitions. It can be noticed that the thermal sensing based solely on the Nd^{3+} emission transitions is certainly not much discussed.

As previously stated, temperature sensing based on the Nd^{3+} luminescence has relied on either two Stark components of the $^4F_{3/2}$ multiplet or on two distinct thermally coupled Nd^{3+} levels. As there are no thermally coupled Nd^{3+} levels in the second BW region, the thermal sensing can be achieved following two strategies; (1) using Stark-components of the $^4F_{3/2}$ multiplet, or (2) using two distinct levels arising from two different Ln^{3+} ions (as discussed for Nd^{3+}/Yb^{3+} pair). Up to this point, the second mentioned approach is the only pathway implemented to achieve thermal sensing in the second BW region. At this regard, a major contribution is required to exploit solely the thermal sensing nature of Nd^{3+} emission at higher wavelengths (≈1300 nm) based on the Stark-components of the $^4F_{3/2}$ multiplet upon variations in the temperature.

The present chapter focuses on the development of DS thermometer consisting of Gd_2O_3:Nd^{3+} nanospheres, with an operative emission in the second BW under excitation at 808 nm. The relative

sensitivity of this nanothermometer is investigated using the thermometric parameter as the $^4F_{3/2}(1)\rightarrow{}^4I_{13/2}$ and $^4F_{3/2}(2)\rightarrow{}^4I_{13/2}$ intensity ratio, in which $^4F_{3/2}(1)$ and $^4F_{3/2}(2)$ are two Stark components of the $^4F_{3/2}$ multiplet. A simplest spectral deconvolution technique has been employed for the systematic investigation of Nd^{3+} Stark components. Furthermore, the Nd^{3+} ion concentration dependent excited states decay times were also examined. Thus, the Gd_2O_3:Nd^{3+} nanospheres open other possibility to compare the photoluminescence and thermometry properties with Gd_2O_3:Nd^{3+} nanorods (Chapter 2).

3.2 Synthesis and characterization of nanospheres

Synthesis of nanospheres

A simple precipitation method [167] was used to prepare Gd_2O_3:Nd^{3+} nanospheres with no template. In a typical procedure, $Gd(NO_3)_3$ (8.91 mL, 0.4 M), $Nd(NO_3)_3$ (0.09 mL, 0.1 M) and urea (6.00 g) were mixed with distilled water (200 mL) in 500 mL round-bottom flask. The mixed solution was stirred at 348 K in an oil bath for 4 hours. The obtained precursor was washed with distilled water, dried in air at 353 K for 24 hours, and denoted as $(GdNd)(OH)CO_3$. Subsequently, the precursor was calcined at 1073 K for 3 hours with heating and cooling rates of 2 and 5 $K\cdot min^{-1}$, respectively, resulting in spherical $(Gd_{0.99}Nd_{0.01})_2O_3$ nanoparticles. The same procedure was used to obtain $(Gd_{0.975}Nd_{0.025})_2O_3$ and $(Gd_{0.95}Nd_{0.05})_2O_3$ nanospheres by changing the relative Gd^{3+} and Nd^{3+} concentrations.

Elemental analysis

Inductively coupled plasma optical emission spectroscopy (ICP-OES-Activa-M, Horiba Jobin Yvon) revealed that the nominal concentrations of 1.00, 2.50 and 5.00 mol% Nd^{3+} relative to Gd^{3+} in the starting materials were found to be 2.00, 2.80 and 6.40 mol% Nd^{3+}, respectively, in the final $(Gd_{1-x}Nd_x)_2O_3$ nanospheres.

Powder X-ray diffraction

The crystal structures and the phase purity of the nanospheres were identified with PXRD. As presented in Figure 3.2A. are the diffraction patterns of the $(Gd_{1-x}Nd_x)(OH)CO_3$ (PDF-04-014-4504) precursor phase formed after the first step of the synthesis at 1073 K for 3 hours. After the calcination of the precursors, $(Gd_{1-x},Nd_x)_2O_3$ (x=0.020, 0.028 and 0.064) nanospheres were

obtained. Figure 3.2B shows the diffraction patterns of the calcined samples correspond to the pure cubic phase of Gd_2O_3, PDF-04-015-1513 [139, 152, 168]. No new reflections or changes in the peak positions are observed when the amount of Nd^{3+} increases from 1 up to 5 mol%, indicating that these ions have been effectively introduced in the Gd_2O_3 host lattice.

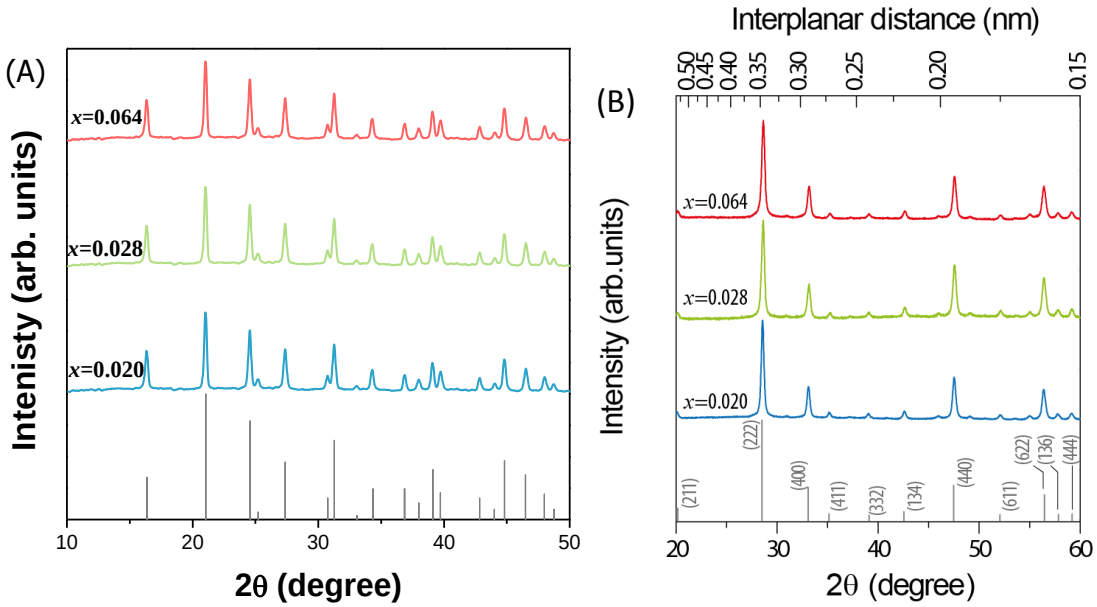

Figure 3.2 Powder X-ray diffraction patterns of (A) $(Gd_{1-x}Nd_x)(OH)CO_3$ and (B) $(Gd_{1-x}Nd_x)_2O_3$ nanospheres, where x=0.020, 0.028 and 0.064. The reflections of $(Gd_{1-x}Nd_x)(OH)CO_3$ and cubic Gd_2O_3 are also depicted (ICDD Card No 04-014-4504 and 04-015-1513, respectively).

Transmission Electron microscopy (TEM)

The representative transmission electron microscopy images are given in Figure 3.3A show that the nanospheres are well-dispersed and are relatively uniform in size. The high resolution TEM image in Figure 3.3B depicts obvious distances between adjacent (222) planes, which were determined to be 0.332 nm, is in accord with the interplanar distances listed in the ICDD database, 0.312 nm. Figure 3.3C represents the particle size distribution measured for over 100 nanospheres with sizes between 85 to 125 nm. The calculated average diameter value for the $(Gd_{1-x},Nd_x)_2O_3$ nanospheres are 108±21 nm (x=0.020), 101±19 nm (x=0.028), and 111±20 nm (x=0.064).

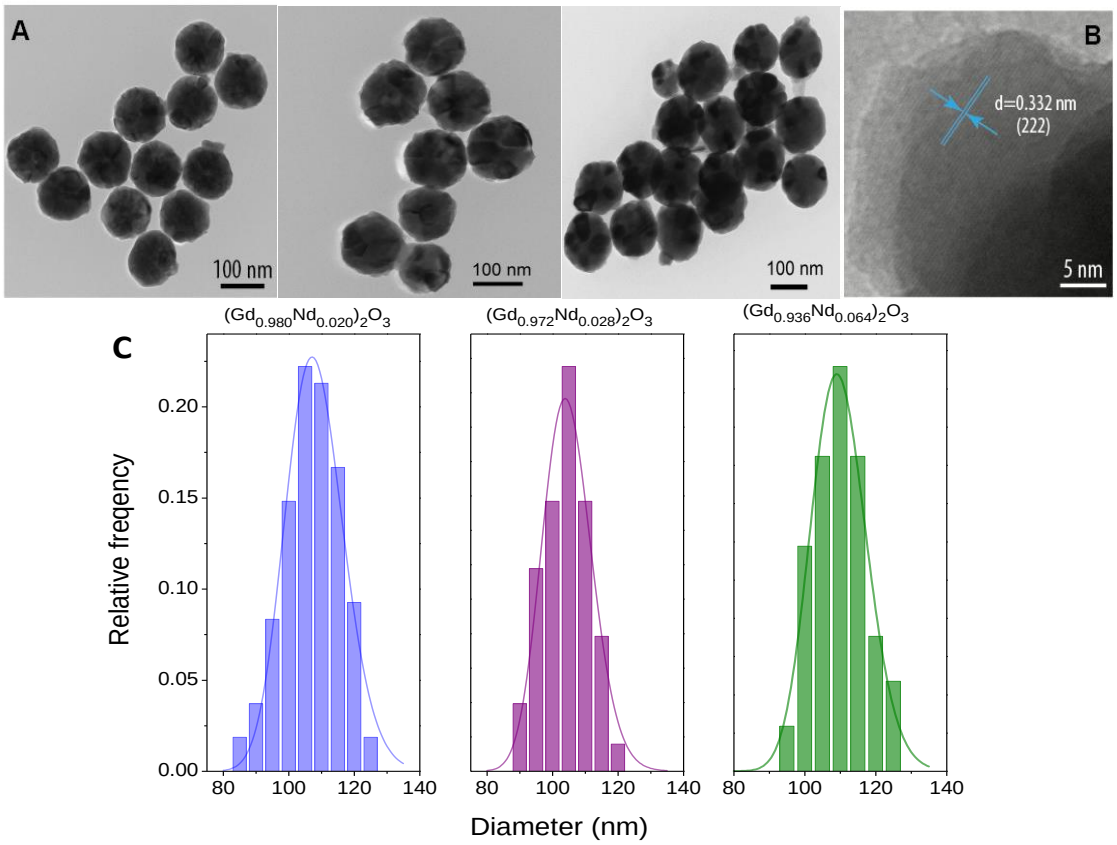

Figure 3.3 (A) TEM images of $(Gd_{1-x}Nd_x)_2O_3$ nanospheres, x=0.020, 0.028 and 0.064. (B) (222) crystallographic planes and interplanar distances of cubic $(Gd_{0.980}Nd_{0.020})_2O_3$. (C) Size distribution computed from TEM images (over 100 spheres were measured). The solid line is the best fit of the experimental data to a log-normal distribution (r^2>0.975).

Results and discussion

3.3 Excitation, emission spectra and decay times

Excitation and emission spectra

Figure 3.4A presents the room temperature excitation spectra of the nanospheres in the range 300–850 nm, recorded by monitoring the $^4F_{3/2} \rightarrow {}^4I_{11/2}$ transition at 1075 nm, exhibit several sharp peaks ascribed to the Nd^{3+} intra-4f transitions [153, 154]. The energy of the excitation peaks is independent of the Nd^{3+} concentration, while their relative intensity grows with increasing Nd^{3+} content. All the transitions starting from the ground state $^4I_{9/2}$ to the excited states of Nd^{3+} ion. The excitation intensities are stronger for the $^4I_{9/2} \rightarrow {}^4G_{5/2}+{}^4G_{7/2}$ (580 nm) and $^4I_{9/2} \rightarrow {}^2H_{9/2}+{}^4F_{5/2}$ (808 nm) transitions. The room temperature emission spectra of the nanospheres in the range 800–1500 nm, recorded by exciting at 580 nm shown in Figure 3.4B. Regardless of the Nd^{3+} concentration, the

emission spectra display three main intra-4f transition regions, assigned to the $^4F_{3/2} \rightarrow {}^4I_{9/2}$ (880–1000 nm), $^4F_{3/2} \rightarrow {}^4I_{11/2}$ (1000–1210 nm), and $^4F_{3/2} \rightarrow {}^4I_{13/2}$ (1300–1480 nm) transitions [155].

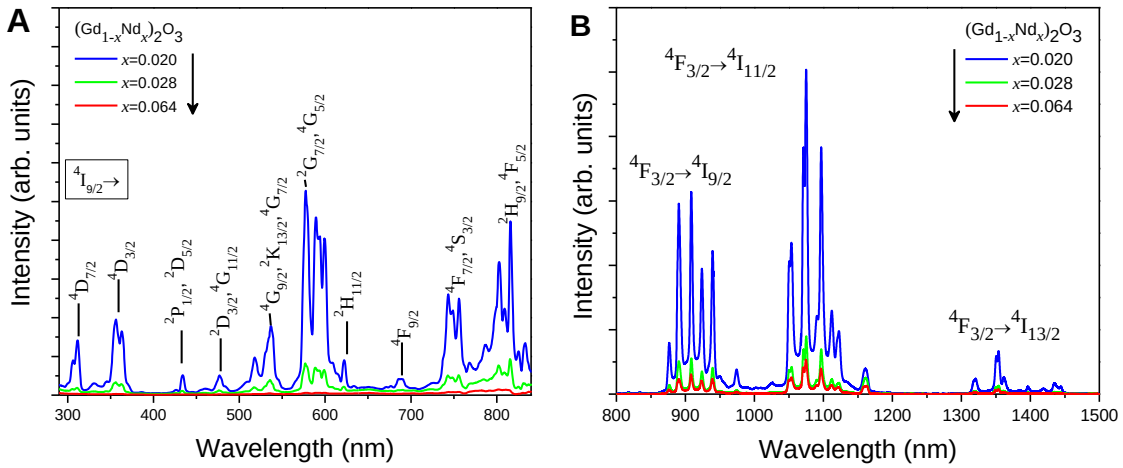

Figure 3.4 Room-temperature (A) excitation spectra monitoring the $^4F_{3/2} \rightarrow {}^4I_{11/2}$ transition at 1075 nm, and (B) emission spectra exciting the $^4I_{9/2} \rightarrow {}^4G_{5/2}+{}^4G_{7/2}$ transition at 580 nm, of $(Gd_{1-x}Nd_x)_2O_3$, x=0.020 (blue), 0.028 (green) and 0.064 (red) nanospheres in solid form. The spectra were normalized to the corresponding Nd^{3+} concentration of the samples.

Decay times

In order to have an insight of Nd^{3+} concentration on the energy transfer among Nd^{3+} ions and on the $^4F_{3/2}$ lifetime, the emission decay curves were measured. In fact, the room temperature decay curves recorded, by monitoring the most predominant emission intensity transition, $^4F_{3/2} \rightarrow {}^4I_{11/2}$ at 1075 nm upon excitation at 580 nm. The emission $^4F_{3/2}$ decay curves (Figure 3.5) for different concentration of Nd^{3+} materials, deviate from a single exponential behavior, being well described by a bi-exponential function in good agreement with the presence of two emission components. Furthermore, the lifetime shortens with increasing Nd^{3+} concentration.

The average lifetimes, were calculated using $t_0=0.05\times10^{-3}$ s in Equation A. resulted as $(0.299\pm0.007)\times10^{-3}$ s for x=0.020, $(0.155\pm0.005)\times10^{-3}$ s for x=0.028, and $(0.118\pm0.036)\times10^{-3}$ s for x=0.064, are in accordance with reported values [169]. As previously stated (Chapter 2.4) the deviation of the $^4F_{3/2}$ decays from a single-exponential, and the reduction of the corresponding lifetimes as the concentration increases, may be due to Nd^{3+}-to-Nd^{3+} energy transfer that is dominated by cross-relaxation processes, such as $(^4F_{3/2}, {}^4I_{9/2}) \rightarrow ({}^4I_{15/2}, {}^4I_{15/2})$ [158, 159, 170, 171].

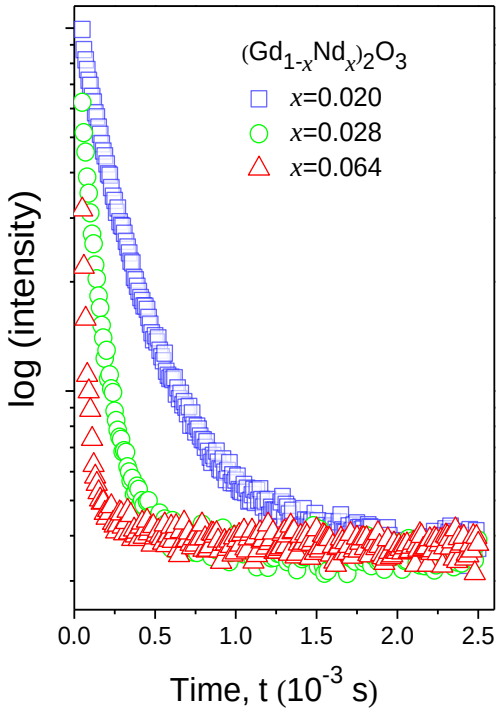

Figure 3.5 Semi-logarithmic plot of the $^4F_{3/2}$ emission decay curves of $(Gd_{1-x}Nd_x)_2O_3$ nanospheres (x=0.020, 0.028 and 0.064, squares, circles and triangles, respectively) measured at 298 K, exciting at 580 nm, and monitoring the $^4F_{3/2} \rightarrow {}^4I_{11/2}$ transition (1075 nm).

The calculated $^4F_{3/2}$ lifetime values for both Gd_2O_3:Nd^{3+} nanospheres and nanorods are listed in Table 3.1. Much longer $^4F_{3/2}$ lifetimes were determined for Gd_2O_3:Nd^{3+} nanospheres, compared to the lifetimes of nanorods [168]. Such a significant difference in the lifetimes of nanorods and nanospheres is ascribed to the differences in the surface area-to-volume ratios of these nanocrystals, which exhibit distinct geometry and sizes. The surface area (SA) and volume (V) for nanospheres and nanorods calculated using the radius (r) and length (l) of the NPs:

For nanospheres: $SA = 4\prod r^2$ and $V = \frac{4}{3}\prod r^3$

For nanorods: $SA = 2\prod r(r+l)$ and $V = \prod r^2((l-2)\frac{r}{3})$

where, 13.5±3.5 nm, and 91.0±11.0 nm are the diameter and lengths of the nanorods from Figure 2.4, Chapter 2 [168] and 108±21 nm is the diameter of the nanospheres, calculated from their respective TEM images (Figure 3.3). And the surface area-to-volume ratios were determined as 3.35×10^8 and 5.56×10^7, for nanorods and nanospheres, respectively. The values indicate that for a given Nd^{3+} concentration, fewer Nd^{3+} ions reside on the nanosphere's surface than on the surface

of the nanorods. Thus, surface-related quenching of Nd^{3+} emission and non-radiative channels are strongly reduced in the nanospheres resulting in longer Nd^{3+} lifetimes, even at the highest Nd^{3+} concentration. The increased surface quenching effect can be due to defect sites and/or moisture related–OH [159] in turn, leads to shorter Nd^{3+} lifetime values [170, 172, 173].

Table 3.1 Calculated decay times and surface area-volume ratio for nanospheres and nanorods with different Nd^{3+} ion concentration.

Morphology of nanoparticles	Sample	Decay time (10^{-3} s)	Surface area-to-volume ratio
Nanospheres	$(Gd_{0.980}Nd_{0.020})_2O_3$	0.299±0.007	5.56×10^7
	$(Gd_{0.972}Nd_{0.028})_2O_3$	0.155±0.005	
	$(Gd_{0.936}Nd_{0.064})_2O_3$	0.118±0.036	
Nanorods	$(Gd_{0.991}Nd_{0.009})_2O_3$	0.134±0.005	3.35×10^8
	$(Gd_{0.976}Nd_{0.024})_2O_3$	0.060±0.002	
	$(Gd_{0.951}Nd_{0.049})_2O_3$	0.020±0.001	

3.4 Thermometry and relative thermal sensitivity

Temperature dependent emission spectra

The thermal sensing ability was assessed for a selected sample of $(Gd_{0.972}Nd_{0.028})_2O_3$ nanospheres, using the Nd^{3+} emission from 1250−1550 nm as shown in Figure 3.6A within the second BW, while also exciting at 808 nm, within the first BW. Xe-lamp with power density of 2.5 $W\cdot cm^{-2}$ was used as excitation source rather than laser diode (power density of 20 $W\cdot cm^{-2}$) excitation to avoid laser-heating effects. With an increase in the sample temperature from 303−393 K, results in a significant variation in the intensities of the Stark components of the $^4F_{3/2}\rightarrow{}^4I_{13/2}$ transition.

In order to analyse the variation in the emission intensities upon temperature and to determine the thermometric parameter, requires the systematic assignment of the Stark components arising from the $^4F_{3/2}$ multiplet. The Nd^{3+} ion $^4F_{3/2}$ and $^4I_{13/2}$ levels split by the crystal field into 2 (J=3/2) and 14 (J=13/2) components (Kramer's doublets, J+1/2 [174]). Labelling of each component is performed considering the energy level scheme of the Nd^{3+} ion [161] and that the higher energy

line involves the highest $^4F_{3/2}$ Stark component (R_2) to the $^4I_{13/2}$ ground state (X_1). Figure 3.6B shows the simplified energy level scheme of $(Gd_{0.972}Nd_{0.028})_2O_3$ nanospheres.

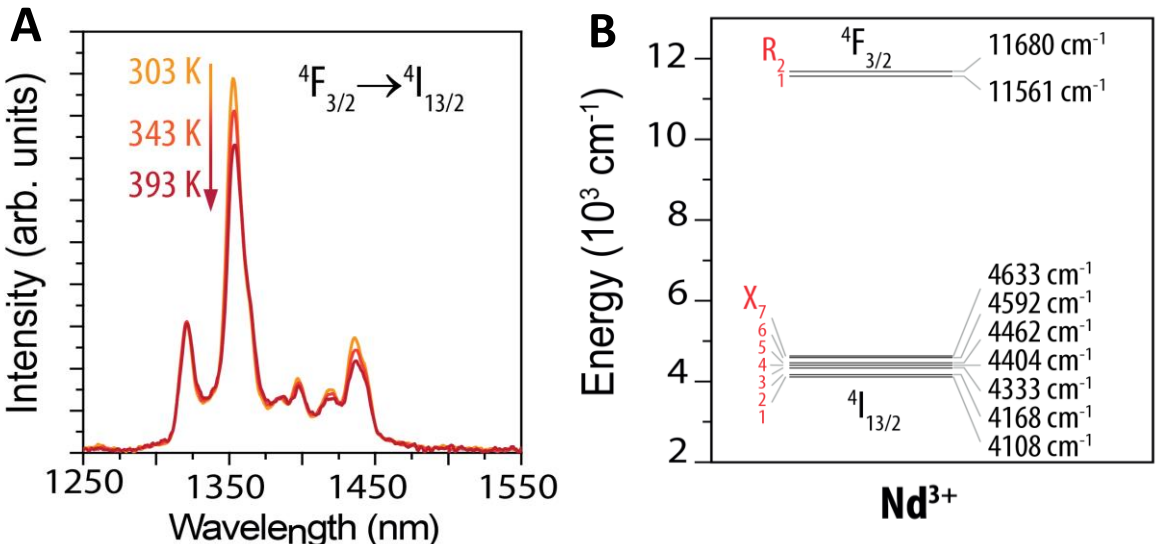

Figure 3.6 (A) Part of emission spectra of $(Gd_{0.972}Nd_{0.028})_2O_3$ powder nanospheres recorded in the 303−393 K range under 808 nm excitation. (B) Simplified energy level diagram of Nd^{3+} ion $^4F_{3/2} \rightarrow {}^4I_{13/2}$ transition.

Resolving of each component can be performed applying deconvolution technique. The fundamental principle of this technique is to determine individual components (14 components) in the form of Gaussians, from $^4F_{3/2} \rightarrow {}^4I_{13/2}$ transition through a least square fit, as shown in Figure 3.7A. Thus, the deconvoluted emission spectra allows to define, the thermometric parameter Δ as the ratio between the integrated intensity of all the seven transitions originated from R_2 (I_2) and all the seven transitions from R_1 (I_1), presented in Figure 3.7B:

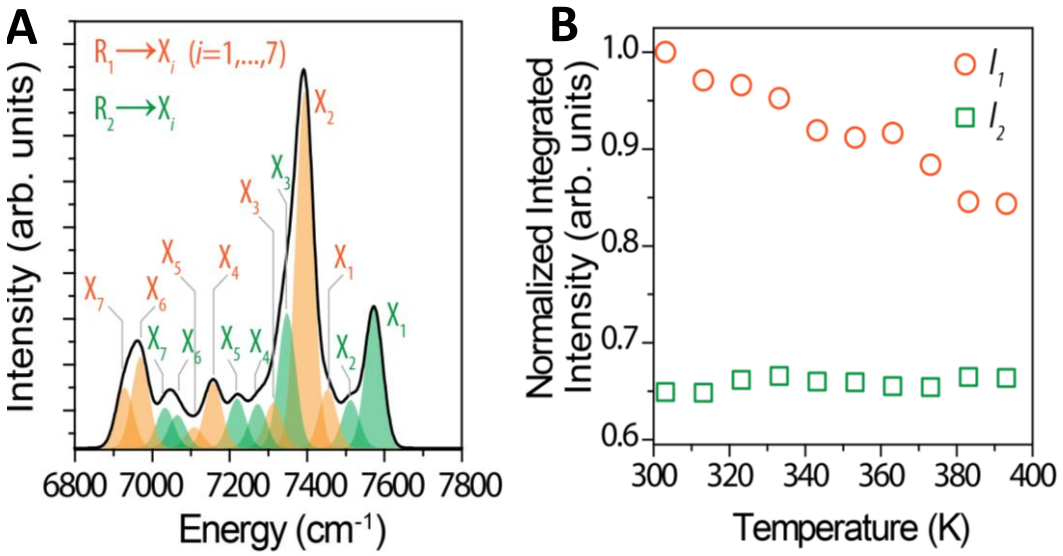

Figure 3.7 (A) Deconvoluted emission spectrum of powder nanopsheres obtained at 323 K. (B) Normalized integrated intensity of I_1 (red, squares) and I_2 (blue, circles).

Figure 3.8A represents the mono-logarithmic plot of Δ as a function of the inverse absolute temperature for $(Gd_{0.972}Nd_{0.028})_2O_3$ nanospheres. Similar behavior was recorded after the deconvolution process for $(Gd_{0.976}Nd_{0.024})_2O_3$ nanorods as shown in Figure 3.8B. The values $\ln(B)=-0.28\pm0.04$, -0.19 ± 0.03 and $\Delta E=150.43\pm20$ cm^{-1}, 76.90 ± 18 cm^{-1} are readily determined from the fitting curve of $\ln(\Delta)$ *vs*. $1/T$ in Figure 3.8 for nanospheres and nanorods, being the ΔE value in accord with the reported value (119 ± 17 cm^{-1}) (Figure 3.6B).

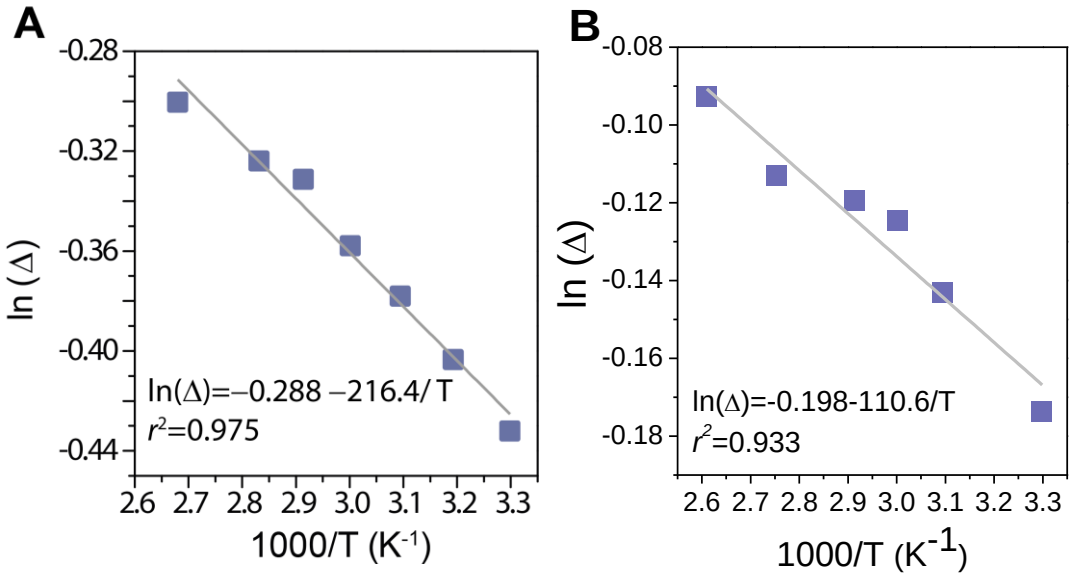

Figure 3.8 Mono-logarithmic plot of Δ as a function of the inverse absolute temperature for: (A) $(Gd_{0.972}Nd_{0.028})_2O_3$ nanospheres and (B) $(Gd_{0.976}Nd_{0.024})_2O_3$ nanorods. The solid lines are the best fit to the experimental data using Equation 1.5.

Thermal sensitivity

Figure 3.9A represents the sensitivity curve as a function of the temperature for $(Gd_{0.972}Nd_{0.028})_2O_3$ nanospheres (calculated from Equation 1.15). Since the other two samples have the same ΔE (Figure 3.4B) their thermal sensitivity values are the same (Equation 1.15). The maximum relative sensitivity is 0.23±0.03 $\%\cdot K^{-1}$ at 303 K. A similar value was reported using the intensity ratio between two transitions involving the two $^4F_{3/2}$ Stark components in the 935−950 nm spectral region (0.15 $\%\cdot K^{-1}$ at 283 K [4]). For $(Gd_{0.976}Nd_{0.024})_2O_3$ nanorods, the thermal sensitivity is lower (0.12±0.02 $\%\cdot K^{-1}$) due to changes in ΔE, 150.43±20 cm^{-1} and 76.90±18 cm^{-1} for nanospheres and nanorods, respectively.

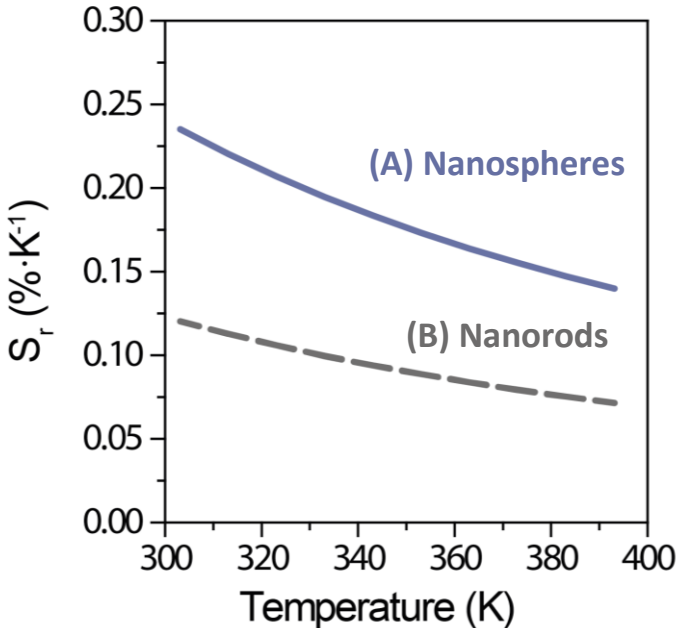

Figure 3.9 Relative temperature sensitivity of (A) $(Gd_{0.972}Nd_{0.028})_2O_3$ nanospheres and (B) $(Gd_{0.976}Nd_{0.024})_2O_3$ nanorods as a function of temperature (303−393 K).

3.5 Summary

Cubic phase $(Gd_{1-x}Nd_x)_2O_3$ (x=0.020, 0.028 and 0.064) nanospheres have been successfully synthesized by a simple precipitation method. The samples were characterized by powder XRD, ICP-OES, TEM and photoluminescence spectroscopy in the form of excitation spectra, emission spectra and decay times. The morphology effect on emission decay curves of Gd_2O_3:Nd^{3+} nanospheres and nanorods was investigated in brief. The performance of $(Gd_{0.972}Nd_{0.028})_2O_3$ as a

ratiometric nanothermometer was evaluated in the 303–393 K range. The nanothermometers operate upon excitation within the first (at 808 nm) and emission in the second (1250–1550 nm) BW s. From the deconvoluted spectra, the thermometric parameter was defined by the ratio between the integrated intensity of all the transitions originated from the $^4F_{3/2}$ highest-energy Stark component and all the transitions from the $^4F_{3/2}$ lowest-energy, and maximum thermal sensitivity of 0.23±0.03 %·K^{-1} at 303 K was obtained. The nanothermometers widens the scope for using Nd^{3+} for thermal sensing in the second BW.

Chapter 4

$Gd_2O_3:Yb^{3+}/Er^{3+}$ nanoplatforms for plasmon-induced heating and thermometry

4.1 Introduction

The study presented in this chapter was broached by the work of all-in-one nanoplatform consisting of $Gd_2O_3:Yb^{3+}/Er^{3+}$ nanorod thermometers decorated with Au nanoparticle heaters observed by the former PhD student[1]. However, the reported nanoplatforms possess some limitations such as the thermometric probe was over-sized relatively to the heater and the laser excitation was off-resonance with the LSPR band. The principle objective of this chapter is to improve the local temperature measurement of laser-excited gold nanostructures, by controlling the heater-thermometer distance and particle dispersion by tuning the size and shape of the heaters as well as thermometers.

Plasmonic nanostructures concentrate light and heat within a small volume at the nanoscale offering potential applications in photothermal therapy [175, 176], thermal sensors [177], and microfluidic devices [178]. The light-matter interaction in these nanostructures relies on the collective oscillation of the free electrons confined within a given dimension, constituting the localized surface plasmon resonance (LSPR) [69]. In such nanosystems, focused light irradiation results in high-temperature local heating [179]. So far, Ln^{3+}-doped luminescent nanothermometers were explored to assess the local temperature change caused by minute heating objects, such as magnetic [180, 181] and plasmonic [5, 139, 182, 183] nanoparticles or by phonon-induced heating [151, 184].

[1] M.L. Debasu, D. Ananias, I. Pastoriza-Santos, L.M. Liz-Marzan, J. Rocha, L.D. Carlos, All-in-one optical heater-thermometer nanoplatform operative from 300 to 2000 k based on Er^{3+} emission and blackbody radiation, *Adv. Mater.*, 25 (2013) 4868-4874.

Laser-excited plasmonic nanoheating possess some advantages over other methods, i.e. it has a high penetration depth, and its more efficient heat conversion (limitation of phonon-induced heating) and relatively low metal dosages (limitation of magnetic-induced heating) [185, 186].

Among of the few recent studies, only three reports (including the work of all-in-one thermometer-heater nanoplatform) make use of the ratiometric thermometers to sense the plasmon-induced temperature increase upon NIR laser excitation [139, 183, 187-189]. For instance, in the case of nanoplatform combining a plasmonic gold nanorod within a porous thermometric $NaYF_4$:Yb/Er nanoshell [187], the heater and the thermometer were separated by 94–113 nm, limiting the local temperature sensing capability. Another nanosystem consisting of Au nanorods and SiO_2-coated $NaGdF_4$:Yb/Er nanoparticles [183] suffers from a large dispersion of heater-thermometer sizes and distances. The major challenges in these nanoplatforms are controlling the heater-thermometer distance and size dispersion, and increasing the plasmonic efficiency in order to heat at the desired laser excitation wavelength.

Two different nanoplatforms comprised of luminescent thermometers ($Gd_2O_3:Yb^{3+}/Er^{3+}$) and heaters (Au) were designed by tuning the size, morphology (NRs/NSs/NPs) and the distances. The LSPR band is shifted from ~550 nm (Au NPs) to close to resonance with the 980 nm laser by using Au NRs in order to have a single excitation source for heating and for measuring the temperature [139]. The structural, morphological and photoluminescence properties of fabricated NSs–AuNPs platforms were compared with the NRs–AuNRs platforms, which were prepared and studied by Dr. Mengistie L. Debasu. Furthermore, the heating and thermal sensing properties were carried out solely for NRs–AuNRs platforms, since later nanoplatforms show low emission intensity and heating efficiency in comparison with former nanoplatforms. For the application of these nanosystems in biology, the *in vitro* cytotoxicity and cellular uptake of the NRs-AuNRs platform was assessed and demonstrated in MG-63 cells by Dr. Helena Oliveira.

4.2 Synthesis and characterization

Synthesis of $Gd_2O_3:Yb^{3+}/Er^{3+}$ nanorods and nanospheres

$(Gd_{0.95}Yb_{0.03}Er_{0.02})_2O_3$ nanorods and nanospheres were synthesized as explained in Chapter 2.2 and Chapter 3.2 by taking stoichiometric amounts of Gd, Yb and Er nitrates.

Synthesis of Gd_2O_3:Yb^{3+}/Er^{3+} NSs-AuNPs-*C* nanoplatforms

A similar procedure developed in ref [139] was followed to decorate Gd_2O_3:Yb^{3+}/Er^{3+} nanospheres with AuNPs. Gd_2O_3:Yb^{3+}/Er^{3+} nanosphere powder (25 mg) was dispersed in distilled water (40 mL) under sonication for 15 minutes. An aqueous solution of $HAuCl_4 \cdot 3H_2O$ (0.250 mL, 0.01 M) was then added to the dispersion and the solution was stirred for 2 hours. Freshly prepared aqueous $NaBH_4$ solution (0.16 mL, 0.1 M) was instantly added to this solution under strong magnetic stirring. The stirring was continued for 20 minutes and a light-pink precipitate was formed. The precipitate was washed several times with water and centrifugation (6000 rpm, 40 minutes) and finally dried in air at 348 K, affording NSs-AuNPs-*C*, where *C*=5 is the nominal Au amount (expressed in μmoles of Au), per 25 mg of powdered oxide nanospheres. The zeta potential of the bare and AuNPs decorated nanospheres dispersions were 12.3±1.2 and 62.7±3.5 mV (Figure 4.1B and E).

Synthesis of Gd_2O_3:Yb^{3+}/Er^{3+} NRs-AuNRs-*C* nanoplatforms

The attachment of Au nanorods to Gd_2O_3:Yb^{3+}/Er^{3+} nanorods was accomplished as follows. Because both the CTAB-stabilized Au nanorods and the Gd_2O_3:Yb^{3+}/Er^{3+} nanorods exhibit positive surface charges in distilled water (46.4±2.3 and 24.8±0.6 mV, respectively, Figure 4.1C and D), the former was first modified with a negative polyelectrolyte polymer, which also avoids the toxicity of CTAB. Briefly, as-received CTAB stabilized aqueous dispersion of Au nanorods (1.32 mL, 35 $\mu g \cdot mL^{-1}$) was added dropwise under sonication and shacking to an aqueous solution of NaCl (4 mL, 0.5 M) containing the negative polyelectrolyte (1 $mg \cdot mL^{-1}$), poly(sodium 4-styrenesulfonate)-PSS, M_w=70,000 $g \cdot mol^{-1}$, in a 15 mL centrifugation tube. This solution was left undisturbed for 2 hours for adsorption of PSS on the CTAB capped Au nanorods. Excess PSS was removed by centrifugation (6000 rpm, 30 minutes) and the precipitated pellet was redispersed in water (4 mL); the zeta potential of the dispersion was –48.2±2.0 mV (Figure 4.1A). This dispersion was added dropwise under sonication and shaking to an aqueous dispersion of positively charged Gd_2O_3:Yb^{3+}/Er^{3+} nanorods (5 mg, 5 mL) in a 15 mL centrifugation tube. The final precipitate was washed several times with water and dried at 348 K in air, and is labeled NRs-AuNRs-*C*, where *C*=1.17 is the nominal Au amount (expressed in μmoles of Au), per a 25 mg of powdered oxide nanorods. A similar synthesis procedure was employed for preparing samples with different *C*

values (0.91 and 3.55) by adjusting the volume of the aqueous solution containing CTAB stabilized Au nanorods.

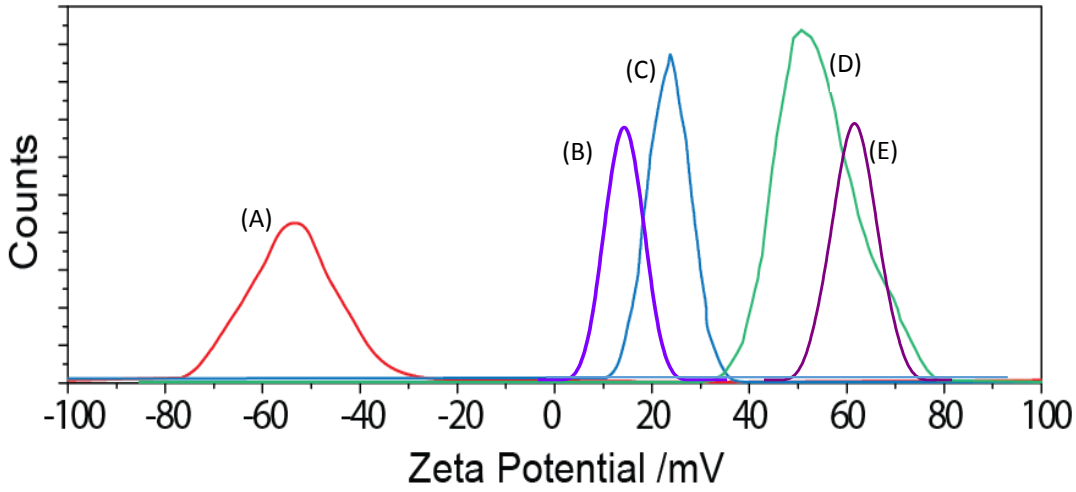

Figure 4.1 Zeta potential distributions of (A) PSS-CTAB capped AuNRs, (B) AuNPs coated nanospheres, (C) CTAB capped AuNRs with longitudinal LSPR peak at 850 nm, (D) bare NRs, and (E) bare NSs, suspended in distilled water measured for a single measurement in each case.

UV-VIS-NIR absorption spectroscopy

Figure 4.2 represents the UV-VIS-NIR absorption spectra for aqueous suspensions of as-prepared samples exhibiting the localized surface plasmon resonance (LSPR) bands ascribed to AuNPs or NRs, respectively. The VIS absorption spectra of NSs-AuNPs-5 nanoplatforms in Figure 4.2A displays LSPR band maximum at 550 nm, in comparison with bare nanospheres. Whereas, Figure 4.2B shows the VIS-NIR absorption spectra of Au nanorods and NRs-AuNRs-1.17 nanoplatforms, both exhibiting LSPR bands with maximum at 850 nm and 1020 nm, respectively. The shift in LSPR band is tuned from ~550 nm (AuNPs) to close to resonance with the 980 nm laser by using Au nanorods of appropriate aspect ratio.

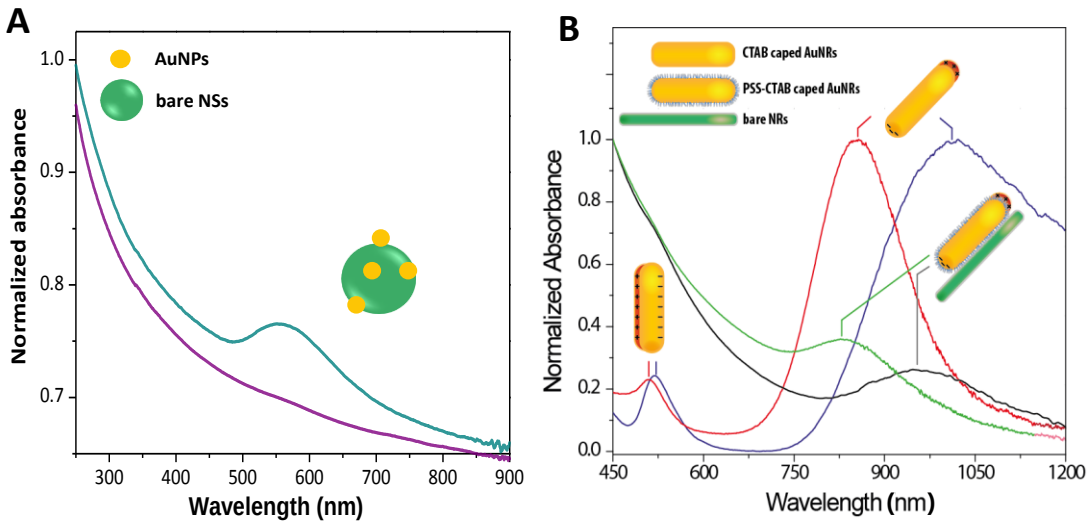

Figure 4.2 (A) Visible absorption spectra of bare nanospheres (purple) and NSs-AuNPs-5 (blue). (B) Visible-infrared absorption spectra of Au nanorods with 850 nm (red line) and 980 nm (blue) longitudinal LSPR bands, NRs-AuNRs-850nm-1.17 (green) and NRs-AuNRs-980nm-1.17 (black).

Transmission electron microscopy

Transmission electron microscopy images in Figure 4.3 witnesses the fine tuning of Gd_2O_3:Yb^{3+}/Er^{3+} thermometer and Au heater nanoparticles. In one hand, Figure 4.3A and B represents the Au NP decorated Gd_2O_3:Yb^{3+}/Er^{3+} NSs and NRs. The number of AuNPs decoration may be easily tuned by changing the Au precursor concentration. Few AuNPs were found away from the surface of the NRs and NSs. On the other hand, the NRs-AuNRs-850nm-3.55 nanoplatforms in Figure 4.3C, show that Au nanorods and Gd_2O_3:Yb^{3+}/Er^{3+} nanorods stick together along their longest dimensions. Further, Figure 4.3D suggest that these two types of nanorods are covalently bonded *via* the PSS polyelectrolyte. By adjusting the C values, it is possible to achieve a single Gd_2O_3:Yb^{3+}/Er^{3+} nanorod linked to one Au nanorod only. A few isolated lanthanide oxide nanorods were present due to the low C values used. The HRTEM image in Figure 4.3E depicts the interplanar spacing of adjacent Au and Gd_2O_3 planes.

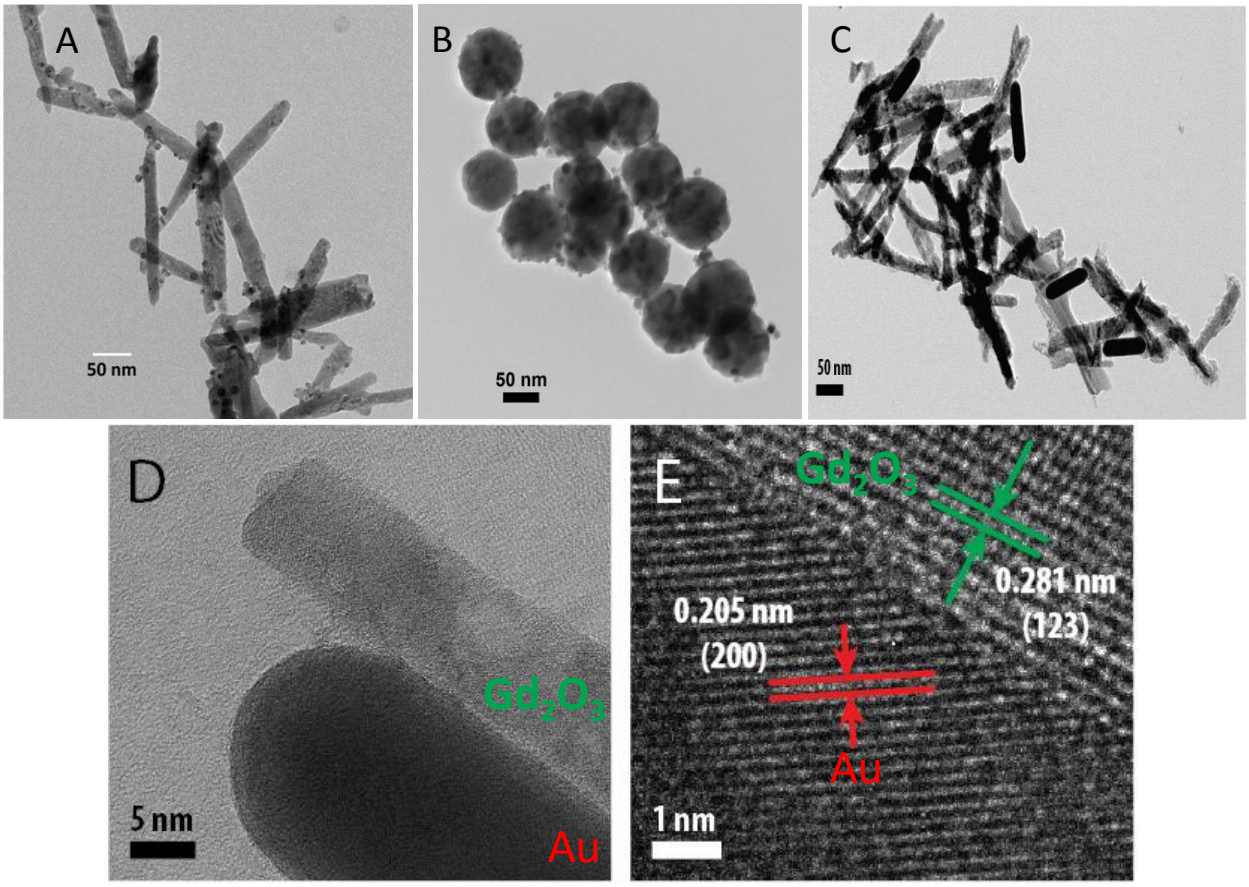

Figure 4.3 Representative transmission electron micrographs of (A) NRs-AuNPs-1.5 (taken from reference[139]), (B) NSs-AuNPs-5, (C) NRs-AuNRs-850nm-3.55. (D) the interface of Au (dark gray) and lanthanide oxide (light gray) nanorods and (E) the crystallographic planes and interplanar spacing between adjacent planes of cubic Au (red) and cubic Gd_2O_3 (green).

Results and discussion

4.3 Upconversion emission spectra

The Er^{3+} UC emission spectra in Figure 4.4 exhibits the $^2H_{11/2} \rightarrow {}^4I_{15/2}$ (510–542 nm) and $^4S_{3/2} \rightarrow {}^4I_{15/2}$ (542–570 nm) transitions of bare Gd_2O_3:Yb^{3+}/Er^{3+} bare NRs and NSs, NSs-AuNPs-5, NRs-AuNRs-850nm-0.91 and NRs-AuNRs-980nm-0.91, excited with a 980 nm laser with a power density of 102 $W \cdot cm^{-2}$. For comparison, the emission spectrum of NRs-AuNPs-1.25,[139] is also shown. The population of the two closely-spaced $^2H_{11/2}$ and $^4S_{3/2}$ energy levels varies with temperature according to the Boltzmann's distribution. The heating effect of the Au nanoparticles and nanorods is evident from the relative emission intensity of the $^2H_{11/2} \rightarrow {}^4I_{15/2}$ transition of NRs-AuNRs-850nm-0.91 and NRs-AuNRs-980nm-0.91, which is higher than that of the other

nanosystems (Figure 4.4). The high rise in the heating effect of NRs-AuNRs-*C* is attributed to the strong Au nanorods absorption at 980 nm (Figure 4.2).

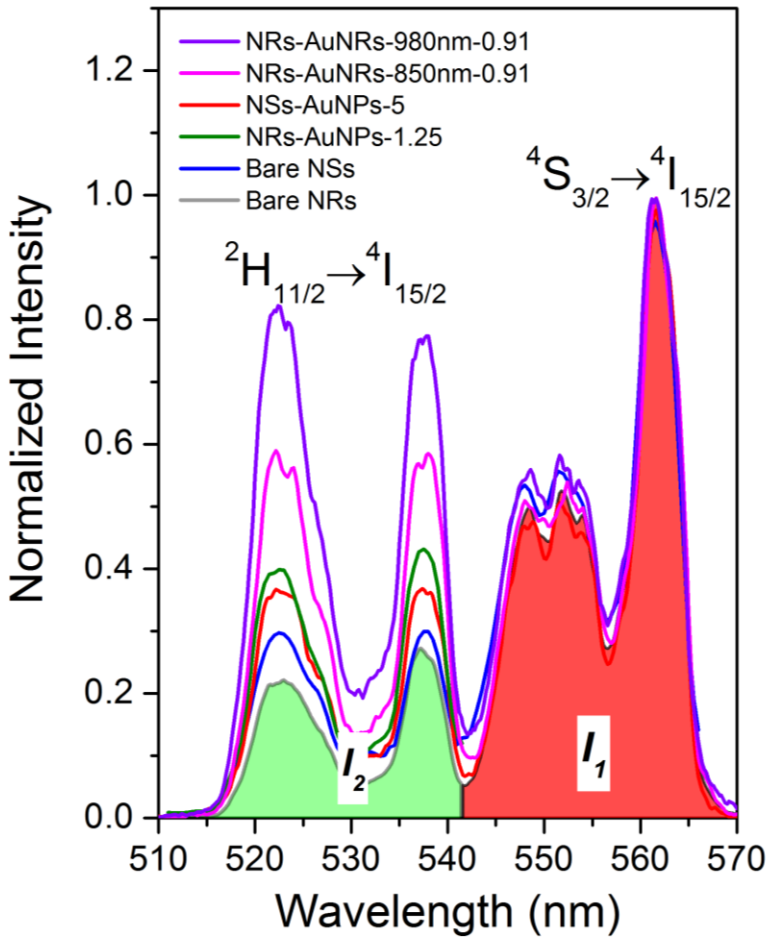

Figure 4.4 Normalized Er^{3+} UC emission spectra of powder nanoparticles under 980 nm excitation at 102 $W \cdot cm^{-2}$ laser power density. The shaded regions represent the integrated areas of the $^2H_{11/2} \rightarrow {}^4I_{15/2}$ and $^4S_{3/2} \rightarrow {}^4I_{15/2}$ transitions.

4.4 Thermometry

From the emission spectra, the thermometric parameter Δ, can be defined as the integrated intensity ratio of $^2H_{11/2} \rightarrow {}^4I_{15/2}$ (I_1, 510–542 nm) and $^4S_{3/2} \rightarrow {}^4I_{15/2}$ (I_2, 542–570 nm) transitions. The Δ value, in Figure 4.5 increases with increasing laser power density, which is ascribed to the increase of the local temperature. In addition, at a given laser power density and Au content, Δ is higher for Au nanorods with a longitudinal LSPR peak closer to 980 nm than that for Au nanoparticles, showing that the in-resonance excitation results in the highest plasmon-induced local heating. This is in accord with previous theoretical and experimental reports showing that the off-resonance plasmon excitation of gold nanoparticles may result inefficient heat generation. However, the most efficient

plasmon-induced local heating is achieved by in-resonance light irradiation at the LSPR bands [200-202].

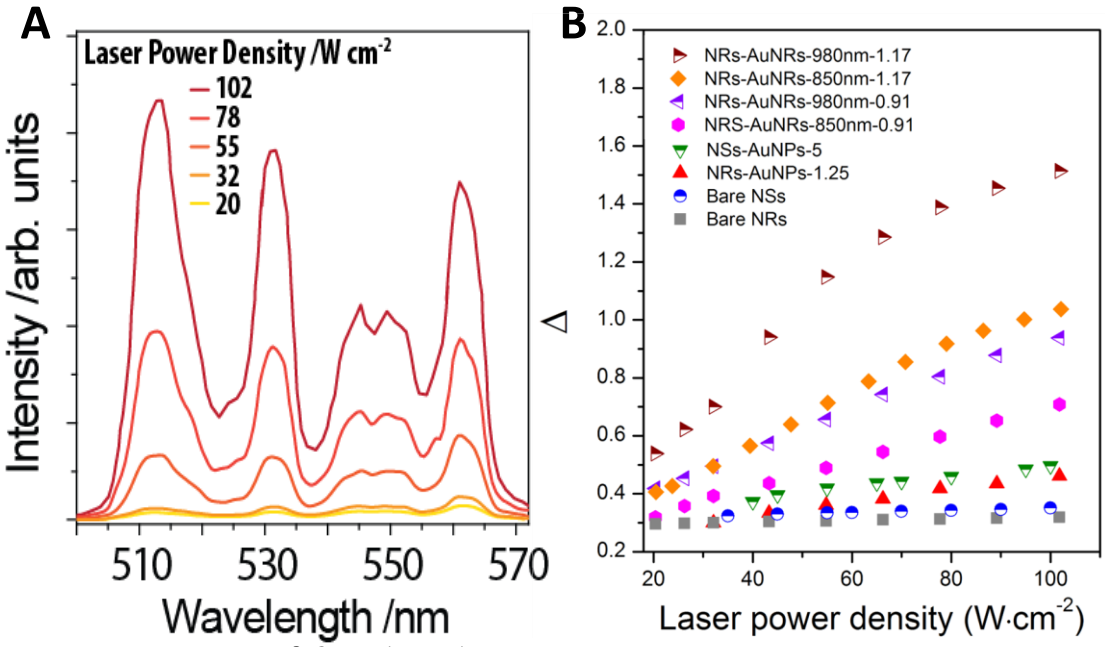

Figure 4.5 Evolution of (A) Er^{3+} $^2H_{11/2}$,$^4S_{3/2}$→$^4I_{15/2}$ UC emission spectra for NRs-AuNRs-980nm-1.17 excited at different laser power density of the 980 nm laser diode and (B) the thermometric parameter Δ of bare Gd_2O_3:Yb^{3+}/Er^{3+} and heater-thermometer nanoplatforms with the laser power density.

The absolute temperature can be computed by

$$T = \frac{\Delta E}{k_B} \frac{1}{\ln\left(\frac{B}{\Delta}\right)} \qquad (4.1)$$

Apart from the thermometric parameter values, to evaluate the absolute temperatures of the nanothermometers from above equation one must determine the pre-exponential constant *B* and energy gap Δ*E*.

Determination of parameter *B* and Δ*E*

The emission spectral curves in the spectral region corresponding to the $^2H_{11/2}$→$^4I_{15/2}$, and $^4S_{3/2}$→$^4I_{15/2}$ transitions were fitted to three and four Gaussian functions, respectively. This is the minimum number of Gaussian peaks required to get a good envelop, as displayed in the Figure 4.6. Brief explanation of the procedure is given in Chapter 2.5. The obtained energy separation for bare

nanorods is ΔE=762.9±10 cm^{-1} is in accord with our previous report [139], the ΔE is the same for the bare nanospheres (Figure 4.4).

The Equation 4.1 can be expressed in terms of B as,

$$\ln(B) = \ln(\Delta_0) + \frac{\Delta E}{k_B T} \qquad (4.2)$$

where, Δ_0 is the value of Δ at no-laser excitation. In Figure 4.6 by extrapolating the linear-curve to the limit of no laser excitation power the value of Δ_0 at 300 K is determined from the fitting curve intercept as 0.289 for bare NRs and 0.303 for bare NSs [121, 137]. Plugging the values Δ_0=0.289 (NRs) and 0.303 (NSs), ΔE=762.2 cm^{-1} at T=300 K and using k_B=0.6950 $cm^{-1}\cdot K^{-1}$ into Equation 4.2 gives the pre-exponential constant ln(B)=2.41 (NRs) and 2.46 (NSs) (B=11.2±0.8 for NRs and 11.7±0.9), which is in agreement with previously reported range (1.5≤ln(B)≤2.5) for this constant [139, 190].

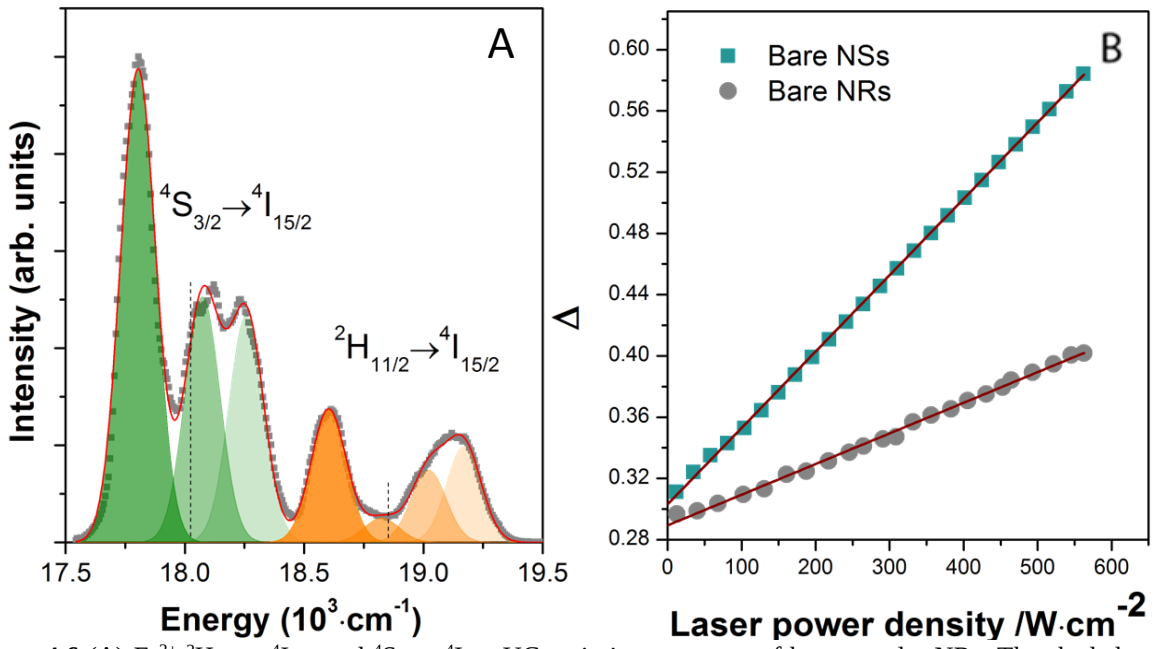

Figure 4.6 (A) Er^{3+} $^2H_{11/2}\rightarrow{}^4I_{15/2}$ and $^4S_{3/2}\rightarrow{}^4I_{15/2}$ UC emission spectrum of bare powder NRs. The shaded regions represent the $^2H_{11/2}\rightarrow{}^4I_{15/2}$ (orange) and $^4S_{3/2}\rightarrow{}^4I_{15/2}$ (green) transitions. (B) A calibration plot of Δ *vs.* laser power density for bare NRs. The solid line is the best fit to the experimental points, r^2>0.997.

At this point, using Equation 4.1, T is readily determined, and the obtained result is displayed in Figure 4.7. By varying the laser power and the Au coverage on NRs or NSs, it is possible to sense different range of temperatures (*ca.* 302–548 K). Particularly, for AuNRs-850nm-0.91 and AuNRs-980nm-1.17 in the physiological range using low laser power densities between 8.3 and

24.8 W·cm^{-2} are measured (inset in Figure 4.7). Moreover, for a given LSPR band, heating depends on the Au concentration. For example, at 102 W·cm^{-2} and C=1.17, the local temperature is 308, 352, 356, 461 and 548 K for, respectively, Gd_2O_3:Yb^{3+}/Er^{3+} nanorods, NSs-AuNPs-2.5, NRs-AuNPs-1.25, NRs-AuNRs-850nm-1.17 and NRs-AuNRs-980nm-1.17 (Figure 4.7). Hence, Au nanorods with 850 and 980 nm LSPR bands produce, respectively, a 49.7 and 77.9% local temperature increase over the 308 K measured for bare Gd_2O_3:Yb^{3+}/Er^{3+} nanorods (102 W·cm^{-2}). When compared with NRs-AuNPs-1.25 and NSs-AuNPs-2.5 [139] Au nanorods present a stronger heating effect due to the presence of longitudinal LSPR bands (Figure 4.7), in accord with previous work [183, 191]. In particular, $NaGdF_4$:Er^{3+}/Yb^{3+} UCNPs mixed with Au nanorods reveal a 150 K increase in temperature when irradiated with a laser power density of 20 W·cm^{-2} (corresponding to an increase of 7.5 KW^{-1}·cm^2) [183]. This value is similar to that of NRs-AuNRs-980nm-*C* (5.4 KW^{-1}·cm^2).

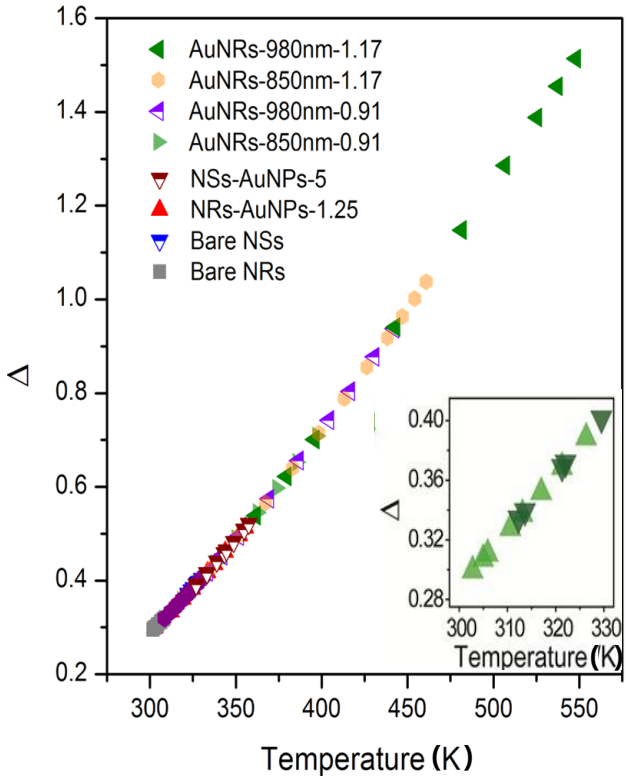

Figure 4.7 Evolution of the thermometric parameter Δ of bare Gd_2O_3:Yb^{3+}/Er^{3+} nanoparticles and heater-thermometer nanoplatforms with the temperature, estimated using Equation 4.2. The inset shows a magnification of the Δ temperature dependence of AuNRs-850nm-0.91 and AuNRs-980nm-1.17 in the physiological range using low laser power densities between 8.3 and 24.8 W·cm^{-2}.

These results show that the plasmon-induced local temperature rise at a given laser power density and Au concentration may be fine-tuned by adjusting the LSPR band with respect to the excitation laser. Accordingly, the highest temperature increment was observed for NRs-AuNRs-980nm-*C* platforms (Figure 4.7).

However, these nanoplatforms have several limitations due to the resonance of the LSPR band with the excitation wavelength: (i) there is competition between LSPR and Yb^{3+} absorption, reducing the Yb^{3+}-to-Er^{3+} energy transfer efficiency and quenching Er^{3+} emission; and (ii) the Er^{3+} emission may also be quenched by Er^{3+}-to-Au energy transfer[183, 192, 193]. Therefore, the optimal condition for Er^{3+} $^2H_{11/2}\rightarrow{}^4I_{15/2}$ and $^4S_{3/2}\rightarrow{}^4I_{15/2}$ UC emission lines at the lowest possible laser power density (*ca*. 8.3–24.8 $W\cdot cm^{-2}$), causing thermal heating in the physiological temperature range, was achieved using Au nanorods with a 850 nm longitudinal LSPR band (inset in Figure 4.7). Such power density is within the range of values reported for *in vitro* studies [3, 186, 194, 195].

4.5 Relative thermal sensitivity, temperature uncertainty and Δ parameter cycling

Relative thermal sensitivity

The computed (Equation 1.15) relative thermal sensitivity curve is plotted as a function of temperature in Figure 4.8A. The maximum temperature sensitivity for NRs-AuNRs-850nm-1.17 is 1.01 $\%\cdot K^{-1}$ at 330 K (Figure 4.8A) with an uncertainty of 0.28 K.

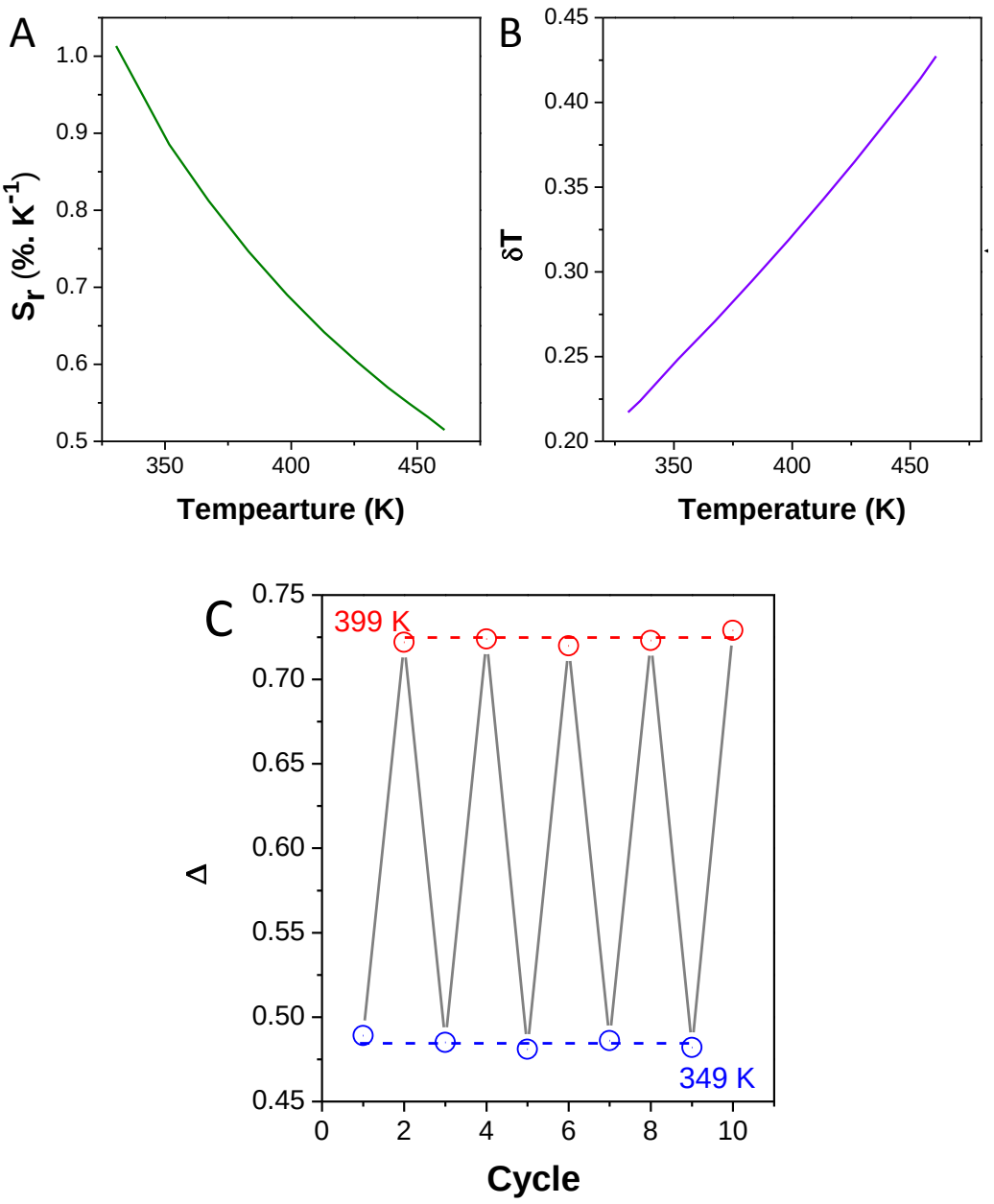

Figure 4.8 (A) Relative sensitivity, (B) temperature uncertainty and (C) Δ cycling for NRs-AuNRs-850 nm-1.17. Open circles in (C) represent the mean value and the error bars the uncertainty in Δ (standard deviation). The lines are guides to the eye.

Apart from sensitivity, it is of interest to assess the uncertainty, stability, and repeatability of the nanothermometers. Figure 4.8 B shows the temperature dependence of the temperature uncertainty of the NRs-AuNRs-850 nm-1.17. The minimum temperature uncertainty is δT=0.21±0.05 K, estimated from the value of $\delta\Delta/\Delta$=0.22% (Equation 1.17 and 1.18). The repeatability of the NRs-AuNRs-850nm-1.17 was accessed upon 980 nm laser excitation with power densities of 32 and

102 W·cm^{-2}, corresponding to average temperature values of 349 and 399 K, respectively, Δ remains unchanged (>99% accuracy) in ten consecutive cycles (Figure 4.8C).

4.6 Cell viability and cellular uptake studies

Cell viability

The *in vitro* biocompatibility of the nanoplatforms was assessed and the UCNPs were imaged in cells using hyperspectral imaging. Figure 4.9 shows the cell viability of bone cell line MG-63 treated with bare Gd_2O_3:Yb^{3+}/Er^{3+} nanorods and NRs-AuNRs-850 nm–1.17. The relatively low toxicity (cell viability >80% up to a platform concentration of 250 mg·mL^{-1}) indicates that the CTAB layer (potentially toxic [49]) on the surface of Au nanorods is inaccessible due to PSS coating.

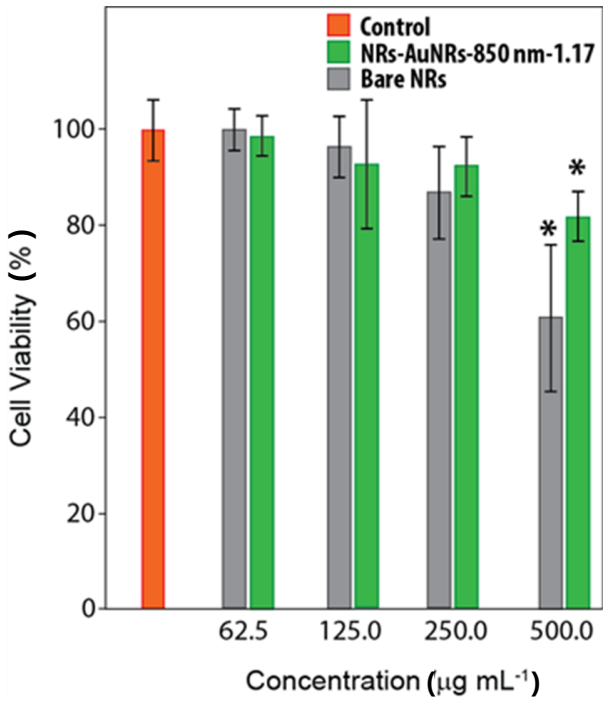

Figure 4.9 Viability of MG-63 cells after incubation for 24 hours with bare Gd_2O_3:Yb^{3+}/Er^{3+} nanorods and NRs AuNRs-850 nm-1.17. Each data point is represented as mean value ± standard deviation from three independent assays. The asterisk indicates statistical significant difference between control and NR-exposed cells ($p<0.05$).

Cellular uptake studies

The MG-63 cells were treated with NRs-AuNRs-850nm-1.17 at the lowest concentration (62.5 μg ·mL^{-1}). In Figure 4.10, nanoplatform-treated cells clearly exhibit typical fibroblast morphology

with size *ca.* 2 µm (Figure 4.10C), which is too big for cellular uptake through endocytosis [196] and, thus the nanoparticle clusters are located outside the cells.

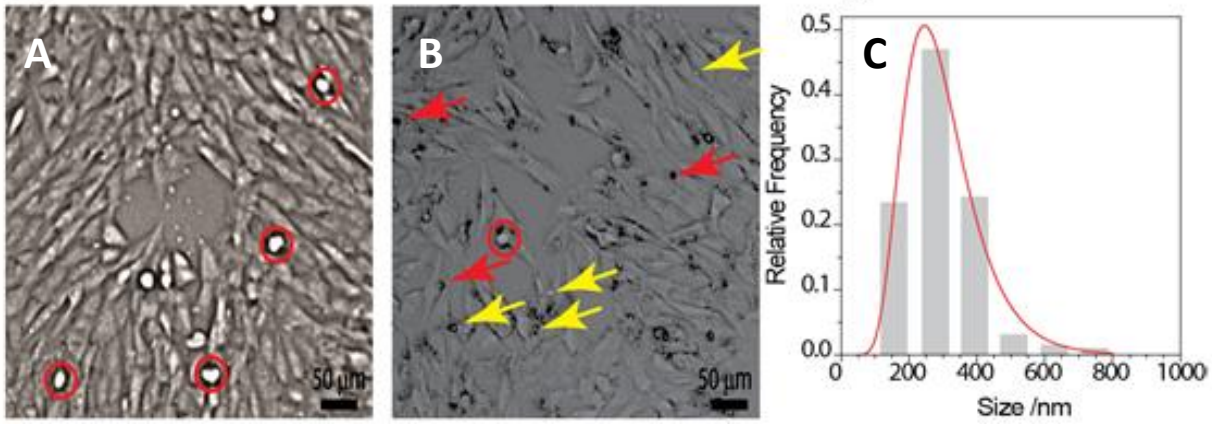

Figure 4.10 Bright-field optical images in the transmission mode recorded using 10x objective of (A) control MG-63 cells and (B) MG-63 cells treated with NRs-AuNRs-850 nm-1.17 (62.5 mg·mL^{-1}). The red circles denote cells undergoing division, and the red and yellow arrows in (B) depict black and white points, respectively, not visible in the images of control cells (A), ascribed to nanoplatform clusters. (C) Histogram of cluster size for mapped contours; the sizes were calculated using QImaging® software; the solid line is the best fit to the data using a log-normal distribution resulting in an average size (± half-width-at-half-maximum) of 281±102 nm (r^2>0.981).

An effective *in vitro* and *in vivo* use of these nanoplatforms, that is, the measurement of local temperature in cells under hyperspectral imaging conditions, will require: (i) increasing the Er^{3+} UC emission efficiency, using 980 nm low power density within the limits set for human skin (0.726 W·cm^{-2}), and (ii) improving the dispersibility of the nanoplatforms in a physiological medium. On the other hand, due to the overlap of the maximum absorption of water molecules and Yb^{3+} excitation at 980 nm, the tissue penetration depth is reduced with the associate increase in the local temperature of the biological medium [197]. To overcome this limitation, similar Nd^{3+}-based nanoplatforms excited at approximately 800 nm should be developed.

4.7 Summary

A new heater–thermometer nanoplatform were developed for plasmon-induced optical heating andtemperature sensing consisting of Au nanoparticles (NRs and NPs) linked to Gd_2O_3:Yb^{3+}/Er^{3+} nanoparticles (NRs and NSs). Upon 980 nm infrared laser excitation (up to 102 W·cm^{-2}) the plasmon-induced heating of the Au nanoparticles was assessed by monitoring the relative intensity of the Er^{3+} UC $^2H_{11/2}\rightarrow{}^4I_{15/2}$ and $^4S_{3/2}\rightarrow{}^4I_{15/2}$ green emission lines, and temperatures in the range 302–548 K were determined from Boltzmann's distribution. The optimal condition for reaching

temperatures in the physiological range (302–330 K), using the lowest possible laser power density (8.3–24.8 $W \cdot cm^{-2}$), was achieved by tuning the LSPR band to 850 nm. The nanoplatforms are very stable upon continuous laser irradiation for power densities up to 102 $W \cdot cm^{-2}$, with corresponding temperatures up to 400 K, and repeatability >99 %. For NRs-AuNRs-850 nm–1.17, a maximum thermal sensitivity of 1.01 $\% \cdot K^{-1}$ at 330 K with an uncertainty of 0.28 K was determined. *In vitro* studies showed the low cytotoxicity of the nanoplatforms to MG-63 cells (for NRs-AuNRs-850 nm–1.17, viability>80% after 24 hours incubation and at a platform concentration up to 250 $mg \cdot mL^{-1}$). Hyperspectral imaging mapped the nanoplatforms within cells, based on a reference spectral library generated from a white-light scattering spectral profile, opening a new avenue to monitor the cellular uptake of Ln^{3+}-bearing nanoplatforms.

Chapter 5

$SrF_2:Yb^{3+}/Er^{3+}$ nanoparticles working as a primary thermometer in different medium

5.1 Introduction

Despite significant progress achieved in nanothermometry by the implication of heater-nanothermometer platforms (Chapter 4) it demands additional requirements, such as enhanced emission efficiency within the limits set for human skin (0.726 $W \cdot cm^{-2}$), as well as improving the dispersibility and thermal sensing properties of the nanoparticles in a physiological medium. This motivated for the work of present chapter, to demonstrate the possibility of purposeful design of water dispersible, low phonon host (fluoride), smaller size (<50 nm) upconverting nanothermometers that can operate in different media, without need of an external calibration. Ln^{3+}-doped SrF_2 micro and nanostructures have attracted extensive attention in the last decade due to their technological importance in photovoltaics ($Ln^{3+}=Pr^{3+}$,Yb^{3+})[198], as scintillators ($Ln^{3+}=Ce^{3+}$)[199], upconverting UV emitters ($Ln^{3+}=Yb^{3+}/Tm^{3+}$)[56], in *in vivo* bio imaging ($Ln^{3+}=Nd^{3+}$),[200] and for tissue visualization and single-particle spectroscopy ($Ln^{3+}=Yb^{3+}/Er^{3+}$ [201-203] and $Ln^{3+}=Yb^{3+}/Tm^{3+}$[204]).The main reasons for this interest are i) the well-controlled size and morphology of SrF_2 micro/nano structures; ii) the wide bandgap (10 eV), iii) the low phonon energy (~350 cm^{-1}), and the clustering of the Ln^{3+} ions, favouring an enhancement in the UC process when the divalent Sr^{2+} ions are substituted [198].

The Ln^{3+}-based luminescent thermometers belongs to the class of secondary thermometers, in which the calibration procedure requires an independent measurement of the temperature to allow the corresponding conversion between the thermometric parameter (usually an intensity ratio) and temperature. A new calibration procedure is, then, necessary whenever the thermometer operates in a different medium, as other variables, such as the ionic strength, pH, pressure, or atmosphere composition may impact the thermometric parameter value.

However, recording multiple calibrations in dissimilar conditions is a time-consuming task that is not always possible to be implemented, as, for instance, in living cells and operating electronic devices. Typically, a unique calibration relation is assumed to be valid, independently of the medium, which is a bottleneck in the operating procedure of the secondary luminescent thermometers developed up to now. Although several examples of gas, acoustic, noise and radiation primary thermometers have been reported in the literature,[9] examples of primary luminescent thermometers are, up to now, very scarce. So far, only three cases can be found in the literature: i) CdSe(ZnS)[205] QDs, ii) Si nanoparticles functionalized with 1-dodecene[206], in both cases the thermometric parameter (the emission peak position) is described by the Varshni's law, and iii) Y_2O_3:Eu^{3+} micro- and nanoparticles,[207] in which the thermometric parameter is defined as the ratio between the emission intensities of the $^5D_0 \rightarrow {}^7F_4$ transition when the $^5D_0$ emitting level is excited through the $^7F_2$ and $^7F_0$ levels (physiological temperatures) or through the $^7F_1$ and $^7F_0$ levels (for temperatures down to 180 K).

This chapter demonstrates a straightforward method to predict the temperature calibration curve of any upconverting thermometer based on two thermally-coupled electronic levels independently of the medium, indicating that these systems are intrinsically primary thermometers by taking SrF_2:Yb^{3+}/Er^{3+} UCNPs in powder and in water suspensions as an illustrative example.

5.2 Synthesis and characterization of nanoparticles

Synthesis of SrF_2:Yb^{3+}/Er^{3+} nanoparticles

The sodium citrate capped SrF_2 NPs prepared by the hydrothermal method developed by Pedroni et al. [204]. In a typical synthesis, 3.5×10^{-3} mol of $SrCl_2\cdot6H_2O$ was dissolved in 7 mL of deionized water. To this solution, 20 mL of 1 M solution of sodium citrate dihydrate and 2.5 mL of 3.5 M aqueous NH_4F was added dropwise under vigorous stirring. The resultant clear solution was transferred into a 100 ml Teflon autoclave and treated at 463 K for 6 hours. The nanoparticles were obtained after washing with deionized water and acetone for 10 minutes at 6000 rpm and the sample denoted as SrF_2-1. Similarly, Yb^{3+}/Er^{3+} co-doped SrF_2 nanoparticles (Sr^{2+}:Yb^{3+}:Er^{3+}=0.78:0.20:0.02 nominal molar ratios) were prepared following the same procedure by taking stoichiometric quantities of $SrCl_2\cdot6H_2O$, $YbCl_3\cdot6H_2O$ and $ErCl_3\cdot6H_2O$ (total cations amount of 3.5×10^{-3} mol). The SrF_2-2, SrF_2-3, and SrF_2-4 nanoparticles were prepared after

treating the autoclaves at 463 K for 6 hours, 24 hours and 48 hours to obtain different sizes of nanoparticles. The optimal molar concentrations of Yb^{3+}/Er^{3+}:0.20/0.02 was used, in order to avoid any concentration quenching or non-radiative relaxation processes[208, 209].

Elemental analysis

Inductively coupled plasma optical emission spectroscopy (ICP-OES-Activa-M, Horiba Jobin Yvon) revealed that the nominal concentrations of 20.00, 2.00 mol% Yb^{3+} and Er^{3+} relative to Sr^{2+} in the in the final SrF_2:Yb^{3+}/Er^{3+} materials were found to be 18.32, 1.98 (SrF_2-2) and 19.04, 2.04 (SrF_2-3) and 20.87, 2.10 (SrF_2-4) mol% Yb^{3+} and Er^{3+}, respectively (Table 5.1).

Powder X-ray diffraction

The crystal structures and the phase purity of the calcined nanospheres were identified with PXRD. Figure 5.1 shows the powder X-ray diffraction patterns of the undoped and Yb^{3+}/Er^{3+} doped SrF_2 nanoparticles, as well as the standard data. The samples show the presence of a pure phase, in agreement with cubic SrF_2 (space group $Fm\bar{3}m$) standard structure data listed in the International Centre for Diffraction Data (ICDD) database (00-06-0262) and references [210-212]. No new reflections or changes in the diffraction peak positions are observed, indicating that Yb^{3+} and Er^{3+} ions have been effectively introduced in the SrF_2 host lattice. All the peaks of samples have a slight shift to higher 2θ angle in comparison to pure SrF_2 (Figure 5.1). It can be justified by the fact that the eight-coordinate Yb^{3+} and Er^{3+} ions have a smaller radius than Sr^{2+} ion (0.0985 nm for Yb^{3+}, 0.1004 nm for Er^{3+}, and 0.1260 nm for Sr^{2+}) [213], as the reason the Yb^{3+}/Er^{3+} doped SrF_2 shows a slight decrease in the cubic lattice parameter in comparison to the pure SrF_2 sample [210-212]. To affirm this, the crystal cell parameters of SrF_2, and SrF_2:Yb^{3+}/Er^{3+} calculated by their XRD data from Rietveld refinement. The refinement was carried out by fitting to specimen displacement, isotropic temperature factor, and peak shape parameters. The Goodness of fit (χ^2), values are reported in Table 5.1. the values agree with literature data [214-216]. While, the lattice parameter, a=5.803 Å for the pure SrF_2 sample is well matched to the standard data 5.800 Å, there is a reduction in the lattice parameter for Yb^{3+}/Er^{3+} doped SrF_2 nanoparticles. The calculated lattice parameter values are 5.727 Å (SrF_2-2), 5.727 Å (SrF_2-3) and 5.729 Å (SrF_2-4), respectively. The slight decrease in the lattice parameter can be the result of increase in size of NPs [217, 218]. The

XRD peaks, show (Figure 5.1) the obvious broadening of diffraction peaks with the decrease in size, as reported in literature [219].

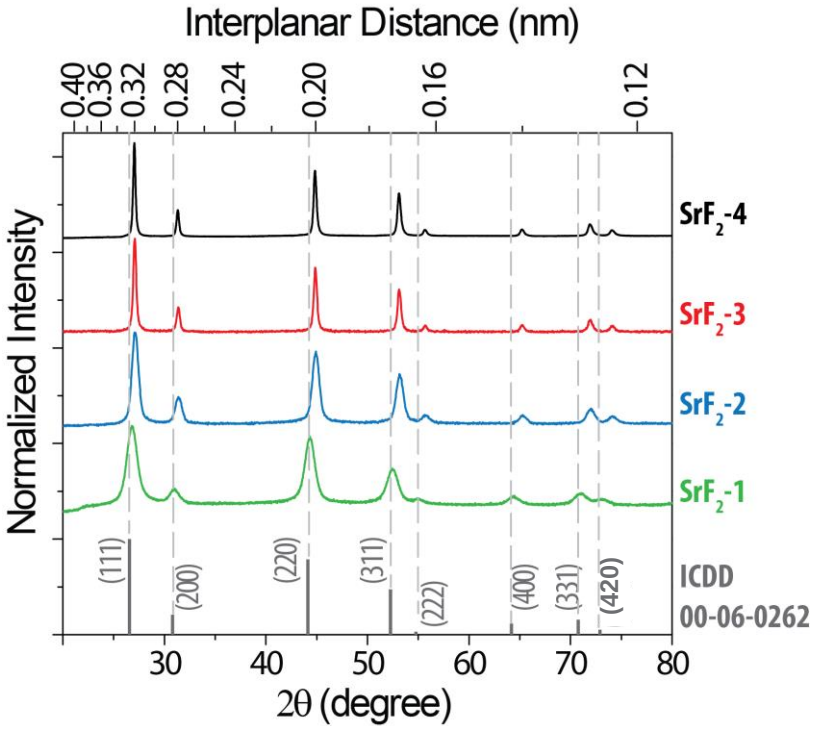

Figure 5.1 Powder X-ray diffraction patterns of pure SrF_2 and Yb^{3+}/Er^{3+} doped SrF_2 nanoparticles. The reflections of cubic SrF_2 are also depicted (ICDD Card No 00-06-0262) along with their corresponding interplanar distances.

In addition, the average crystallite size for pure and doped SrF_2 is calculated using the Scherrer's equation (Equation A.1). The FWHM was calculated for the diffraction peak at 2θ value of 44.7° assigned to the (220) plane of samples SrF_2-2, SrF_2-3 and SrF_2-4 in Figure 5.2a-c. The points are the experimental data and the solid lines represents the fit of a Gaussian peak to the experimental data (r^2>0.992). The resulting fitting parameters were used in Scherrer's equation. The calculated average crystallite sizes 7±2 nm, 10.5±0.4 nm, 22±2 nm and 25±2 nm for SrF_2-1, SrF_2-2, SrF_2-3 and SrF_2-4, respectively.

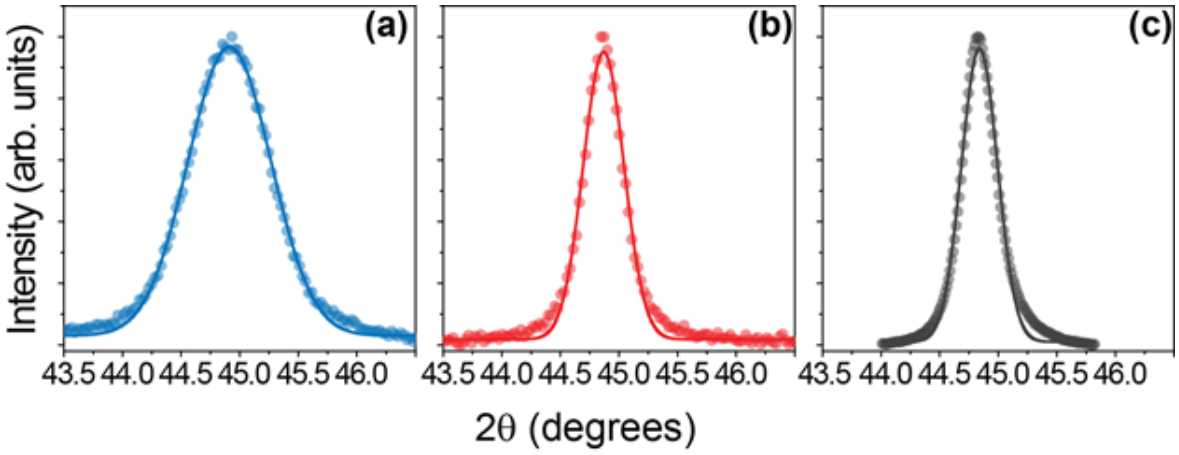

Figure 5.2 Magnification of the diffraction peak assigned to the (220) plane of samples (a) SrF_2-2, (b) SrF_2-3 and (c) SrF_2-4. The points are the experimental data and the solid lines represents the fit of a Gaussian peak to the experimental data (r^2>0.992). The resulting fitting parameters were used in Scherrer's equation.

Transmission electron microscopy

Representative transmission electron microscopy images, shown in Figure 5.3a-c, for SrF_2:Yb^{3+}/Er^{3+} nanoparticles reveal a high degree of crystallinity, in agreement with the powder XRD patterns. The nanoparticles are spherical and increasing the reaction time, an increase in the particle's average size and in its clustering, is observable. The nanoparticles are virtually spherical and some of the lattice planes are clearly visible in the HRTEM images. As shown in Figure 5.3d-f, the size distribution histograms of the nanoparticles range, respectively, from 5 to 70 nm, with average values of 10±2 nm, 27±8 nm and 41±10 nm, for SrF_2-2, SrF_2-3, and SrF_2-4, respectively. The measured distances between adjacent planes were determined from these images as 0.332±0.002 nm (111) and 0.288±0.005 nm (200) along with the corresponding orientations of the indexed planes by powder X-ray diffraction (Figure 5.3g and h). The values are in accord with the corresponding interplanar distances listed in the ICDD database, 0.335 nm and 0.290 nm. The difference in the average sizes from XRD for SrF_2-4 may observed due to the uncertainty in the determination of XRD data acquisition. The monocrystalline structure of the NPs was observed by the electron diffraction pattern in Figure 5.3i. The NPs electron diffraction measured in different areas of the NPs shows high monocrystalline structure of the NPs.

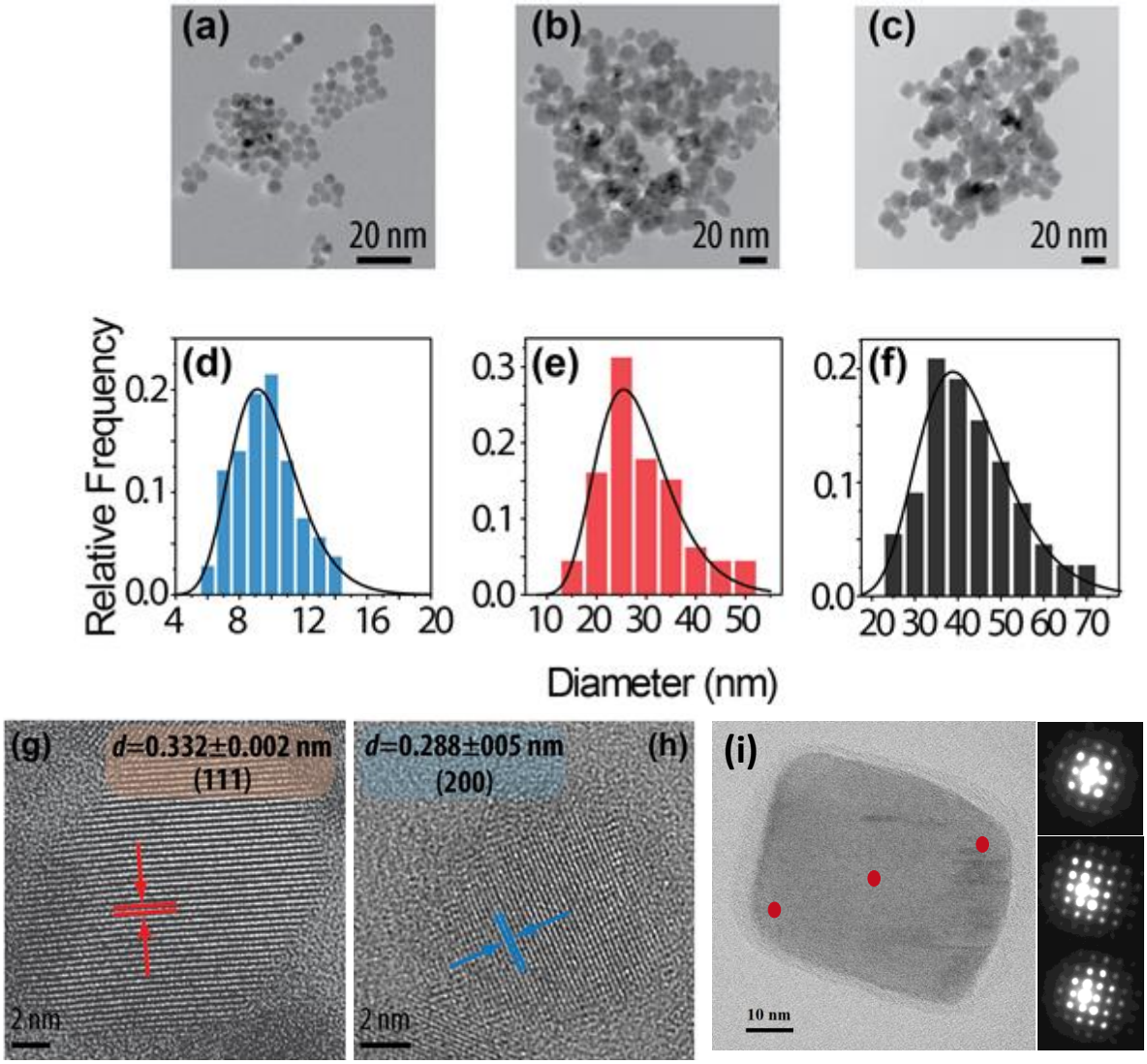

Figure 5.3 HRTEM images of SrF_2:Yb/Er nanoparticles and their size distribution histograms (over 100 nanoparticles measured): (a,d) SrF_2-2, (b,e) SrF_2-3, and (c,f) SrF_2-4. The solid lines are the best fit of the experimental data to log-normal distributions (r^2>0.922). HRTEM images of SrF_2-2 nanoparticles showing the (g) (111) and (h) (200) crystallographic planes and the corresponding interplanar distances. (i) Electron diffraction pattern of SrF_2-4 obtained from three different spots highlighted in red.

Table 5.1 Results of ICP analysis, average crystal sizes (from PXRD and microscopy) and the calculated lattice parameter values for the SrF_2 nanoparticles. The nominal concentration was 20.00, 2.00 mol% Yb^{3+} and Er^{3+}.

Sample	Size of the nanoparticles (TEM) nm	Sr^{2+} Concentration (mol%)	Yb^{3+} Concentration (mol%)	Er^{3+} Concentration (mol%)	Size of the nanoparticles (PXRD) nm	Lattice parameter *a* (Å)	χ^2
SrF_2-1	Undoped	100.00	00.00	00.00	7±2	5.803	2.3
SrF_2-2	10±2	79.70	18.32	1.98	10.5±0.4	5.727	2.3
SrF_2-3	27±8	78.92	19.04	2.04	22±2	5.727	2.5
SrF_2-4	41±10	77.03	20.87	2.10	25±2	5.729	2.5

Results and discussion

5.3 Upconversion emission spectra

Luminescence spectra of SrF_2:Yb^{3+}/Er^{3+} phosphors under the excitation of a 980 nm laser with the power density 1.3±0.1 W·cm^{-2} in the 500–700 nm range, are shown in Figure 5.4a. The Er^{3+} UC emission spectra exhibit three emission bands in green (520 and 540 nm) and red regions (650 nm), for all the samples. Figure 5.4b depicts a partial energy-level diagram of Yb^{3+} and Er^{3+} ions showing the UC mechanism responsible for the $^2H_{11/2} \rightarrow {}^4I_{15/2}$ (520 nm), $^4S_{3/2} \rightarrow {}^4I_{15/2}$ (540 nm) and $^4F_{9/2} \rightarrow {}^4I_{15/2}$ (650 nm) transitions, respectively.

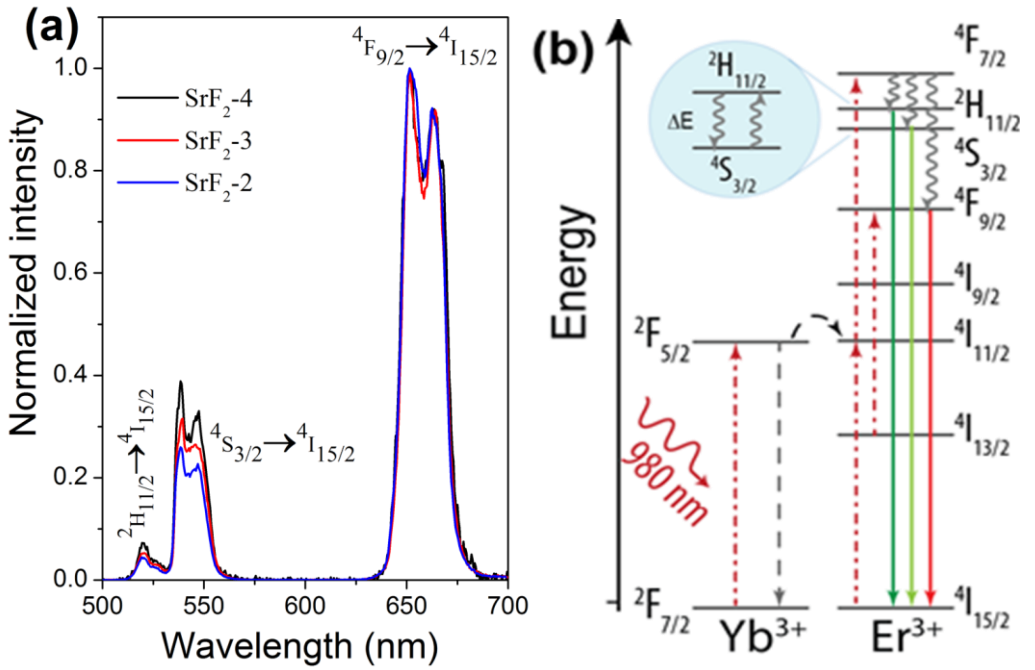

Figure 5.4 (a) Room-temperature emission spectra of SrF_2:Yb^{3+}/Er^{3+} powder nanoparticles. The emission spectra were normalized to the 650 nm transition. (b) Partial-energy level diagram of Yb^{3+}/Er^{3+} ions, highlighting the absorption at 980 nm and the emissions at 520 nm, 540 nm and 650 nm.

Upconversion emission as a function of the pump power

Photon UC is a non-linear process which is highly dependent on the excitation power density [8, 89, 220-222]. In the low excitation power density regime, the two-photon absorption process dominates the emission; a slope equals to 2 characterizes the two-photon UC process in a log-log plot. As the excitation power density increases, however, the competition between the UC process and the linear decays in the individual excitation steps starts to play an important role [89, 222, 223]. In fact, when the excitation intensity is high enough to induce such saturation of the intermediate energy state involved in the UC process the multiphoton UC luminescence dependence on the laser power density presents a slope near 1 (in a log-log plot) [89, 224]. Therefore, it is relevant the study of the emission intensity as a function of the excitation power.

The UC emission mechanism for the $^2H_{11/2}$,$^4S_{3/2}$→$^4I_{15/2}$ (green region) and $^4F_{9/2}$→$^4I_{15/2}$ (red region) Er^{3+} transitions can be deduced from a power law relation,

$$I \propto P_D^n \qquad (5.1)$$

where I is the integrated emission intensity, P_D is the laser power density and n is the number of photons involved in the emission [89, 225]. For low laser excitation power densities (P_D<$10^{2.4}$

W·cm^{-2}) the slope of the dependency of the UC intensity on the excitation power is 2.04±0.02 (SrF_2-2), 1.68±0.05 (SrF_2-3) and 1.89±0.07 (SrF_2-4) in Figure 5.5. When the excitation laser power density is high enough the saturation of the upconverting process occurs and the multiphoton upconverting luminescence will appear in the log-log plot with a slope near to the unit [89]. Therefore, a two-photon absorption process is responsible for both green and red emission bands of Er^{3+} $^2H_{11/2}\rightarrow{}^4I_{15/2}$, $^4S_{3/2}\rightarrow{}^4I_{15/2}$ and $^4F_{9/2}\rightarrow{}^4I_{15/2}$ upon excitation with a 980 nm diode laser, which is in accordance with the reported data [139, 226].

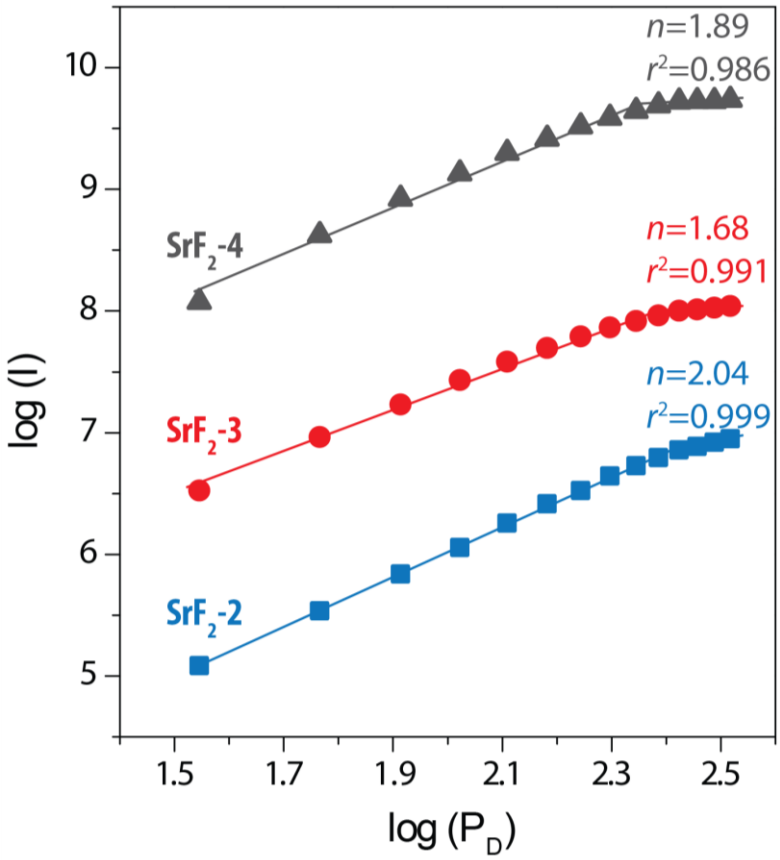

Figure 5.5 Double-log plot of the two emission bands of Er^{3+} *vs.* pump power for SrF_2-2, SrF_2-3 and SrF_2-4 NPs, respectively. The solid lines are the best fit to the experimental points.

5.4 Upconversion emission quantum yield

The UC emission quantum yield (*q*), was calculated from the measured spectral radiant flux using integrated sphere. Figure 5.6 shows the UC spectral radiant flux *(S(λ))*, of the SrF_2:Yb^{3+}/Er^{3+}nanoparticles under 160±16 W·cm^{-2} excitation. The spectral radiant flux increases with the particle size. The corresponding radiant flux (or radiant power, *R*(W)) values can be

computed integrating $S(\lambda)$ from Equation A.12, and the maximum radiant flux values measured are 1.8×10^{-6} W, 7.8×10^{-6} W and 13.0×10^{-6} W, for SrF_2-2, SrF_2-3 and SrF_2-4, respectively. Subsequently, the luminous flux L(lm) values are deduced from Equation A.13 are 0.57×10^{-3}, 1.3×10^{-3} and 1.3×10^{-3} lm (Table 5.2).

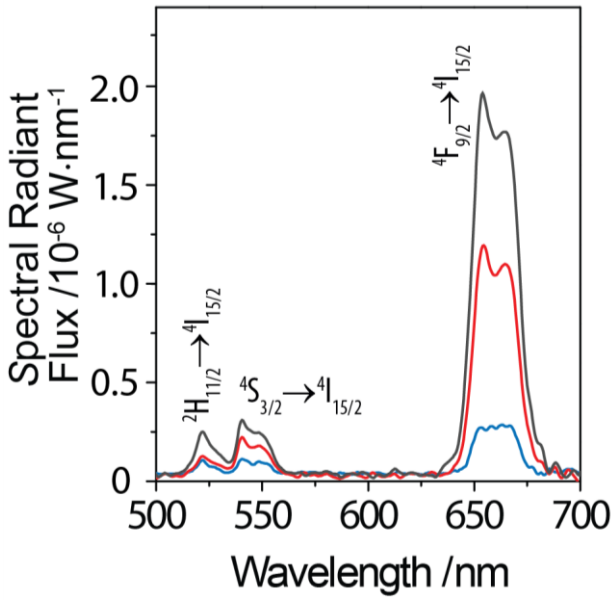

Figure 5.6 Upconversion emission spectral radiant flux of (a) SrF_2-2, (b) SrF_2-3 and (c) SrF_2-4 powder NPs, respectively, under 980 nm excitation with 160±16 W·cm^{-2} laser power density.

Figure 5.7A show the laser power density dependence of the spectral radiant flux of SrF_2-4 powder nanoparticles. The integrating sphere setup (Appendix A.4.3) allows to measure this curve straightforwardly since the excitation power can be tuned in the laser source and then the $S(\lambda)$ curve recorded. Similar behaviour was observed for the same nanoparticles in water suspension. The corresponding numbers of emitted photons were calculated from the radiant flux using Equations A.8 and absorbed photons were measured with a power meter using Equations A.9 are represented in Figure 5.7B.

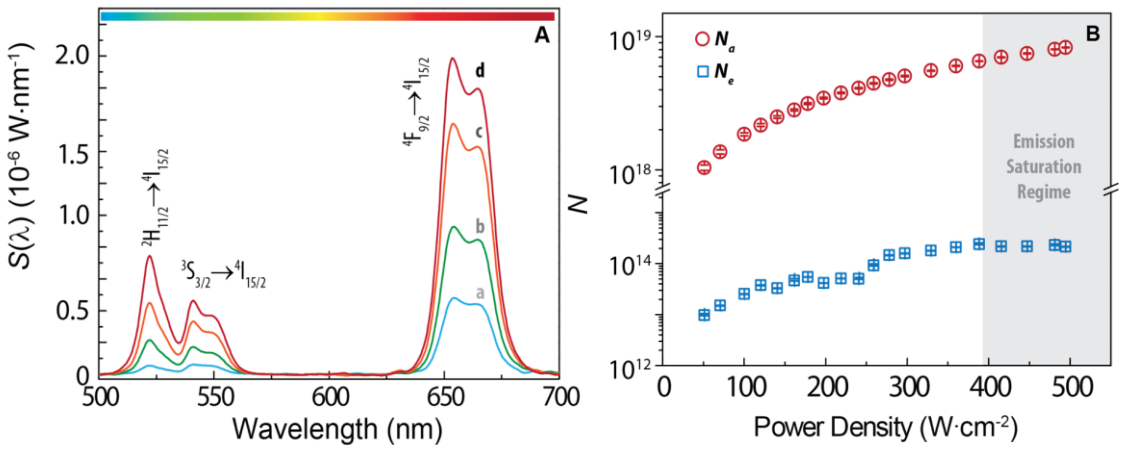

Figure 5.7 (A) Emission spectral radiant flux $S(\lambda)$ (980 nm) of powder SrF_2-4 nanoparticles measured for distinct laser power densities (a) 218, (b) 258, (c) 297 and (d) 494 W·cm^{-2} and (B) Number of emitted (N_e) and absorbed (N_a) photons.

From the number of absorbed and emitted photons (Figure 5.7b) the q values are deduced (Equation A.10) and reported in Table 5.2. Owing to its nonlinear nature, the q are strongly dependent on the excitation laser power density corresponding the maximum value to the beginning of the saturation regime of the power dependence [220, 227-229]. This is exactly observed (Figure 5.8a) for SrF_2-2, SrF_2-3 NPs in powder and SrF_2-4 NPs in powder and in suspension, with the maximum q (at the onset of the saturation regime) of 0.00036±0.00002% (at 162±16 W·cm^{-2}), 0.0019±0.0001% (at 250±28 W·cm^{-2}), 0.0057±0.0006% and 0.0028±0.0003% (at 388±42 W·cm^{-2}), respectively.

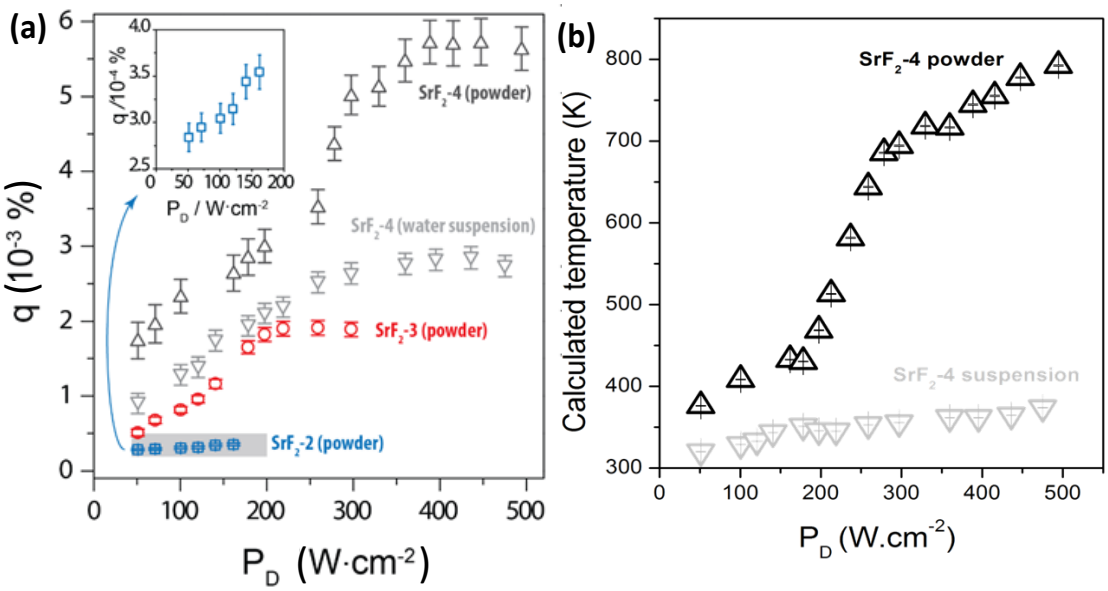

Figure 5.8 Dependence of the laser power density (a) with the emission quantum yield of SrF_2 NPs. For a better visualization, the inset shows a magnification of the SrF_2-2 values and (b) with the temperature calculated form the Equation 5.3, using Δ=0.6252, ΔE=747±10 cm^{-1}, Δ_0=0.120±0.001, and T_0=299.4±0.1 K (refer to section 5.6 for the calculations).

The uncharacteristic dependence of the q for SrF_2-4 in powder, with the laser power density for values >220 $W \cdot cm^{-2}$ can be explained by the thermal decomposition of the sodium citrate shell of the nanoparticles. Sodium citrate starts to partially decompose at temperatures above 573 K (Figure D.1B) [230], that is nearly the temperature calculated for 220 $W \cdot cm^{-2}$, Figure 5.8b. For the same laser power density, the calculated temperature in the water suspension is much lower (326 K, Figure 5.8b), due to a partial absorption of the excitation radiation by the water and to a more efficient dissipation processes. For SrF_2-2 only the onset of the saturation regime can be discerned (inset of the Figure) as the local temperature increase is so high for P_D>160 $W \cdot cm^{-2}$ than incandescence starts to be observed. A point should be noted that the increase of the laser power density induces a local increase of the sample temperature, which, especially for powers, can be very high reaching the temperature threshold of incandescence [139, 231, 232]. Then, the dependence of the emission intensity (or the emission quantum yield) on the excitation power density is intrinsically coupled to a change of the local temperature. This point has been completely ignored in the literature up to now.

Table 5.2 Radiant flux (R), luminous flux (L) values at the fixed laser power density of 197±20 $W \cdot cm^{-2}$ and the calculated quantum yield (q) values for SrF_2 nanoparticles.

Sample	Radiant flux R (10^{-6}·W)	Luminous flux L (10^{-3}·lm)	P_D ($W \cdot cm^{-2}$)	q (%)
SrF_2-2	1.8	0.57	162±16	0.00036±0.00002
SrF_2-3	7.8	1.3	250±28	0.0019±0.0001
SrF_2-4	13.0	1.3	388±42	0.0057±0.0006[a] 0.0028±0.0003[b]

[a] Powders and [b] Phosphors suspended in water.

The q values calculated (using Equation A.10) for SrF_2:Yb^{3+}/Er^{3+} cannot be directly comparable with the research works present in the literature [201, 233], because the authors calculate the quantum efficiency of analogous SrF_2:Yb^{3+}/Er^{3+} UCNPs using a distinctive definition in which the ratio between the emitted and absorbed power does not dependent on the energy of the photons. Care must to be taken when distinct emission quantum yield values are compared, as some of the values reported in the literature are not recorded at the beginning of the saturation regime, being, then, lower than the maximum value that can be recorded. Moreover, the threshold of the saturation

regime differs from system to system as it depends on a series of factors, such as the size of the particles, the doping ion (both donors and acceptors) concentration, the surface to volume ratio and the distance between ions in the crystal structures of the phosphors [223].

The lower values found for the water suspension, compared with those found for the powders, can be explained because the method assumes that all the incident photons N_a are absorbed by the sample, which is reasonable for the powder but not for the suspension due to the water absorption at 980 nm (α=0.4311 cm^{-1} [234]). Moreover, the interaction between the Yb^{3+}/Er^{3+} ions and the solvent could increase non-radiative deactivations, decreasing the number of emitted photons N_e and the emission quantum yield. Therefore, the q values of the nanoparticles suspended in water are underestimated. This limitation can be overcome by coupling the power meter to a port of the integrating sphere as in the case described in ref. [235].

Although not often discussed in the literature, when exciting at 980 nm besides UC Er^{3+} DS emission may also occur. In this case, the emission q of the upconversion process differs from the overall emission q. To evaluate this aspect, Figure 5.9 compares the UC and DS emission spectra of SrF_2:Yb^{3+}/Er^{3+} nanoparticles acquired using two distinct detectors: R928 and H9170 Hamamatsu (notice that the spectral mismatch between the two detectors was not corrected). The experimental conditions were kept constant in the two spectra, namely an integration time of 0.2 s, slits width of 1 mm and the 980 nm CW laser (Thorlabs LDM21 mount, LDC220 laser diode controller) excitation source operating at a laser power density of 390±30 $W \cdot cm^{-2}$. The detection of NIR Er^{3+} emission (at ~1500 nm) indicates that the emission quantum yield of the UC process here reported are the inferior limit of the overall emission q. Moreover, the use of two distinct photomultipliers disables any quantitative estimative of the DS emission for the overall q.

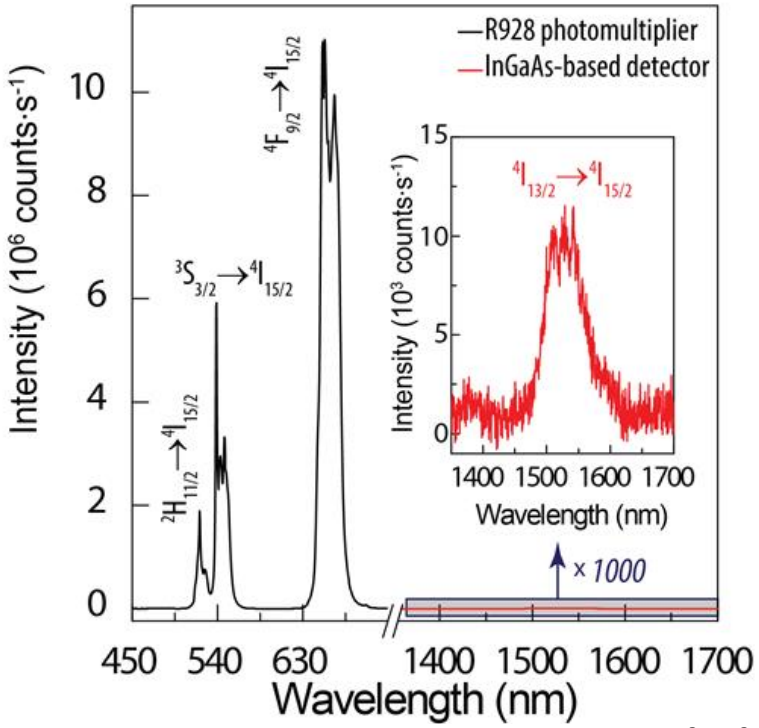

Figure 5.9 Upconverting (black) and downshifting (red) emission spectra of SrF_2:Yb^{3+}/Er^{3+} powder under 980 nm excitation, measured with two distinct detectors (R928 and H9170 Hamamatsu, respectively).

5.5 Photothermal conversion efficiency

The photothermal conversion (or transduction) efficiency (PTCE) of SrF_2-2 and SrF_2-4 UCNPs were briefly investigated. NIR absorbing nanomaterials with the ability to convert NIR light energy to thermal energy are indispensable in photothermal therapy[236] and solar energy technologies[237]. PTCE was evaluated by measuring the absorbance (Appendix D.3) and time dependent temperature changes under 980 nm laser irradiation (1.6 $W \cdot cm^{-2}$). The time dependent temperature changes were obtained for solutions in the presence and in the absence of UCNPs placed in quartz cuvette (1.5 mL, 7.6 $mg \cdot mL^{-1}$ of SrF_2-2 and 1.5 mL, 17.8 $mg \cdot mL^{-1}$ of SrF_2-4).

Due to the balance between light-induced heating and thermal dissipation by the environment, the temperature triggered by the laser power gradually reaches equilibrium with an increase of illumination time followed by a continuous cooling process. The results are summarized in Figure 5.10, from which it can be concluded that after 5 minutes of laser irradiation, the difference in temperatures for aqueous suspensions containing NPs was 8.4 °C and 7.5 °C for SrF_2-2 and SrF_2-4, respectively. However, aqueous suspension without any NPs shows a temperature difference lower than in the presence of NPs as of 5.9 °C. Further, the time constant τ, for heat transfer from

the suspensions is determined to be 286±17 for distilled water, 192±7 s for SrF_2-2 and 229±33 for SrF_2-4 NPs from the slope of the exponential decay curve of time data (from the cooling period, after 780 s) versus the temperature show in Figure 5.10 (Table 5.3).

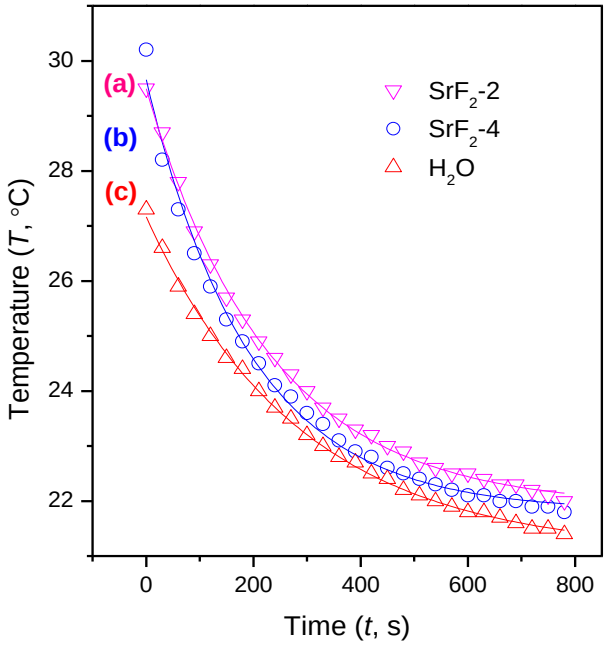

Figure 5.10 Time dependent temperature variation curves obtained from the cooling period for aqueous dispersions containing, (a) SrF_2-2 (b) SrF_2-4 and (c) distilled water.

Table 5.3 Temperature difference ΔT_{max} *(℃)* and concective decay time τ, acquired from the time vs. Temperature cuve in Figure 5.10.

	ΔT_{max} *(℃)*	τ
H_2O	5.9	286±17
SrF_2-2	8.4	192±7
SrF_2-4	7.5	229±33

Thus, according to Equation A.10 and A.11, substituting $c_{p,H2O}$=4180 $J{\cdot}K^{-1}{\cdot}kg^{-1}$ and $c_{p,SrF2}$=543 $J{\cdot}K^{-1}{\cdot}kg^{-1}$ the photothermal conversion efficiency at 980 nm absorbance (Figure D.3) can be calculated as 26% and 19% for SrF_2-2 and SrF_2-4, respectively. Since, η can be understood as the absorption/extinction ratio and is often used to describe the efficiency of the nanoparticles to convert light into heat; in this sense, these results indicate that the 26% and 19% of the light extinction by these SrF_2 NPs is transformed into heat, demonstrating that these NPs can be potentially applied as excellent photothermal agents for Photodynamic thermal therapy and for solar energy technology applications. The difference in η between the SrF_2-2 and SrF_2-4 may be

due to size and/or the concentration[238]. Up to now, the PTCE at 980 nm is hardly reported for UCNPs, in fact for any nanoparticles. However, the obtained PTCE values of SrF_2 NPs at 980 nm (26%) can only be compared with η=25.7% (calculated using time constant method) for the Cu_9S_5 NPs at the same laser incident power (0.5 W)[235, 239]. Furthermore, the photothermal conversion efficiency of SrF_2 UCNPs (at 980 nm, P_D=1.6 W·cm^{-2}) is similar to the upconverting hybrid systems such as $NaYF_4$:Yb,Er@$NaYF_4$:Yb@PDA-ICG with η=16% (at 808 nm, P_D=0.6 W·cm^{-2})[240], $NaYF_4$:Yb,Er@SiO_2/Dye with η=14% (at 750 nm, P_D=2.5 W·cm^{-2})[241] and $NaLuF_4$:Yb,Er@$NaLuF_4$@Carbon with η=38% (at 730 nm, P_D=1.0 W·cm^{-2})[97].

5.6 Thermometry

Relative thermal sensitivity, temperature uncertainty and repeatability

Figure 5.11a-c shows the temperature dependence of the emission spectra of SrF_2:Yb^{3+}/Er^{3+} powder nanoparticles in the range 298–383 K. The temperature values were measured using a thermocouple (I620-20147, VWR) positioned in contact with the powder sample holder. A time interval of 10 minutes is taken between the consecutive measurements to ensure that the nanoparticles reaches the equilibrium temperature. Increasing the temperature results in a significant variation in the emission intensities of the Er^{3+} thermally coupled levels of the $^2H_{11/2}\rightarrow{}^4I_{15/2}$ (I_1, 510–533 nm) and $^4S_{3/2}\rightarrow{}^4I_{15/2}$ (I_2, 533–570 nm) transitions. In Figure 5.11d-f while the intensity of the I_1 transition decreases approximately 50% that of I_2 is nearly constant, allowing to extract the thermometric parameter Δ as the ratio between the integrated intensities of I_2/I_1. The figures of merit usually used to compare the performance of the thermometers, independent of their nature, are the thermal sensitivity S_r, the temperature uncertainty δT, and the repeatability [16, 22].

To compute the relative thermal sensitivity of the SrF_2:Yb^{3+}/Er^{3+} nanoparticles by Equation 1.15. the energy gap ΔE is the energy difference between the barycenters of the Er^{3+} two transitions, should be determined for a thermometer.

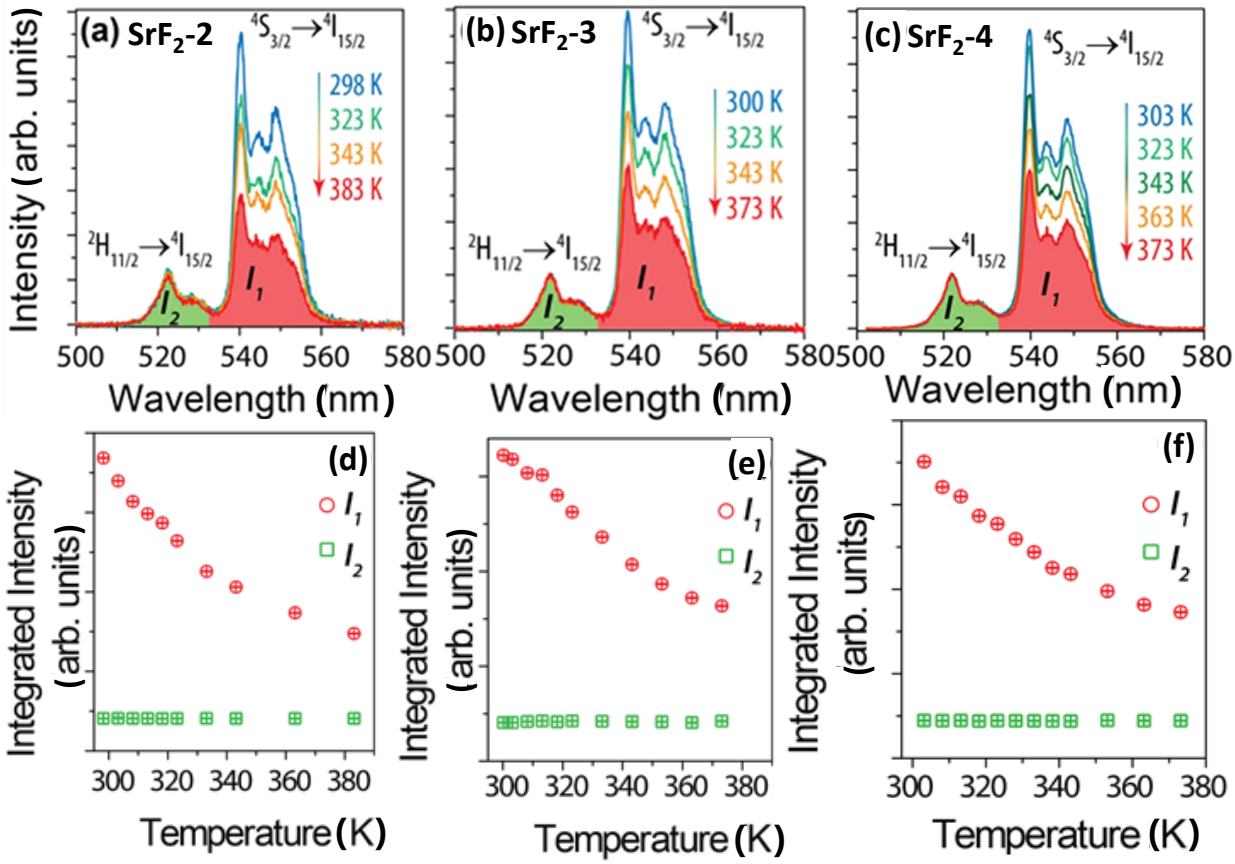

Figure 5.11 Upconversion emission spectra of (a) SrF_2-2, (b) SrF_2-3 and (c) SrF_2-4 powder NPs. The corresponding integrated emission intensities of the spectral regions are depicted in (d), (e) and (f).

Determination of barycenter

Figure 5.12a-c shows the 300 K emission spectra of SrF_2-2, SrF_2-3, and SrF_2-4 measured exciting with 980 nm diode laser at power density of 42±5 $W{\cdot}cm^{-2}$. The emission spectral curves in the spectral region corresponding to the $^2H_{11/2}\rightarrow{}^4I_{15/2}$, and $^4S_{3/2}\rightarrow{}^4I_{15/2}$ transitions for all the particles were fitted to two and five Gaussian functions, respectively. This is the minimum number of Gaussian peaks required to get a good fit, as indicated by the residues displayed in the Figure.

Although the UC at 12 K spectrum permits to discern the $^4I_{15/2}$ and $^4S_{3/2}$ Stark components with high resolution (Figure 5.12d for the SrF_2-2 illustrative example), the very low intensity of the $^2H_{11/2}\rightarrow{}^4I_{15/2}$ transition does not allow the precise identification of the $^2H_{11/2}$ Stark components preventing, then, the accurate determination of ΔE using the definition of barycenter. However, we should notice that the barycenter of the $^4S_{3/2}\rightarrow{}^4I_{15/2}$ transition measured at 12 K coincides with the value measured at 300 K, validating, therefore, the calculus of the energy gap ΔE performed at 300 K. Although the energy gap ΔE does not depend on the temperature, we should note that a

laser power density value of 42±5 W·cm^{-2} induces a local temperature increment in the nanoparticles. As mentioned above, the effective temperature is calculated through Equation 5.3. Brief explanation of the procedure is given in Chapter 2.5. The calculated energy gap values (Table 5.5) are in good agreement with the value computed by Carnall et al. for LaF_3:Er^{3+} (764 cm^{-1}) [161]. There are no differences in the ΔE values if Lorentzian or Voight-type functions were used in the fittings.

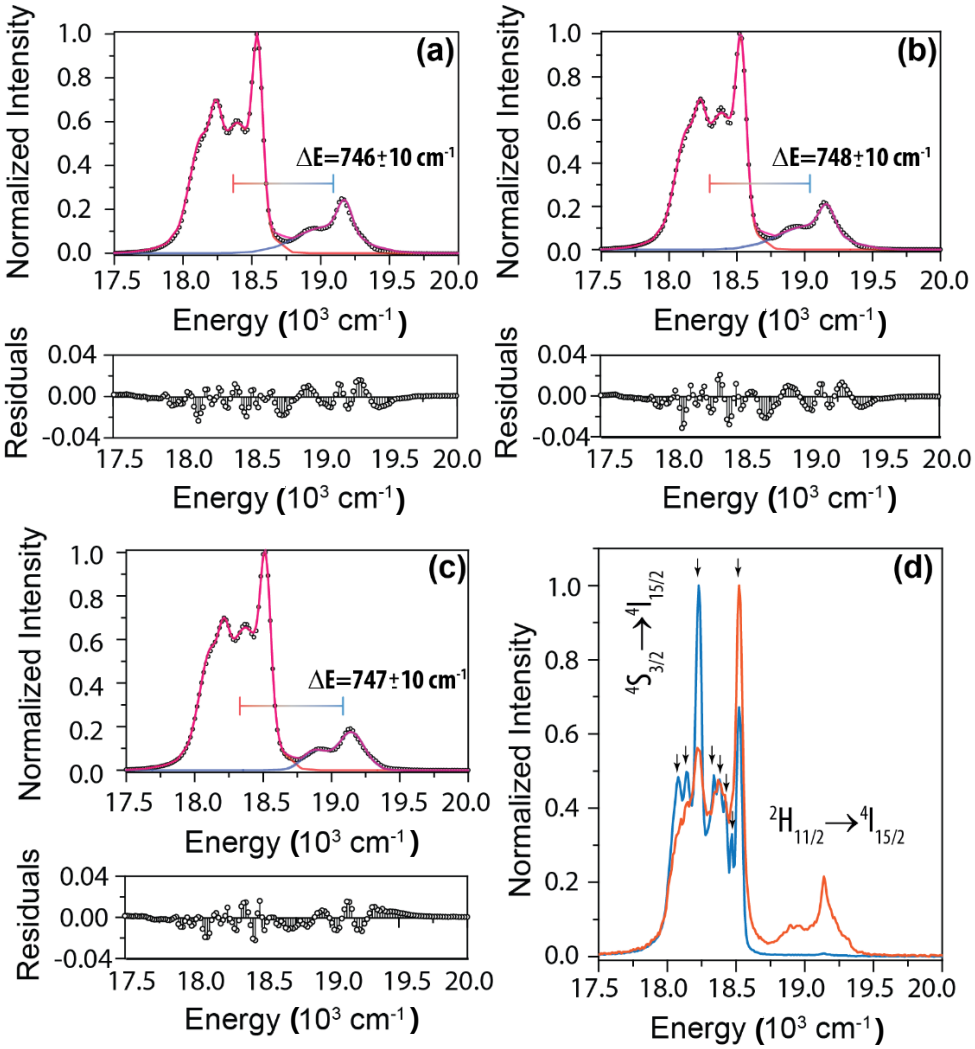

Figure 5.12 Emission spectra (points) in the spectral region corresponding to the $^2H_{11/2}\rightarrow{}^4I_{15/2}$, and $^4S_{3/2}\rightarrow{}^4I_{15/2}$ transitions for (a) SrF_2-2, (b) SrF_2-3 and (c) SrF_2-4. The corresponding residues are also displayed. The red and blue lines represent the fit envelope of the $^4S_{3/2}\rightarrow{}^4I_{15/2}$ and $^2H_{11/2}\rightarrow{}^4I_{15/2}$ transitions (r^2>0.9998), respectively, whereas the magenta line assigns the envelope of the sum of the two transitions. (d) Comparison of the emission spectra of SrF_2-2 at 12 K (blue line) and 300 K (red line), recorded with a laser power density of 0.81±0.08 W·cm^{-2}. The eight Stark components expected for the $^4I_{15/2}$ level in an Er^{3+} low symmetry local site are assigned in the $^4S_{3/2}\rightarrow{}^4I_{15/2}$ transition.

Now, the relative thermal sensitivities of the thermometer can be inferred using the calculated ΔE values in Equation 1.15 as shown in Figure 5.13a, maximum S_r values 1.207±0.016 %·K^{-1} (298.2 K), 1.195±0.016 %·K^{-1} (300.2 K), 1.169±0.016 %·K^{-1} (303.2 K) and 1.193±0.016 %·K^{-1} (300.2 K) for SrF_2-2 powder, SrF_2-3 powder, SrF_2-4 powder and SrF_2-4 water suspension, respectively. The similarity between these values is expected as the ΔE values are similar for all the nanothermometers within the corresponding uncertainties. Moreover, for SrF_2:Yb^{3+}/Er^{3+} nanoparticles, and in the 298–383K range, T_m values correspond to the first measured temperature. Therefore, the small differences in S_m are due to distinct experimental starting temperatures. The S_m values are almost 4 times higher than the value reported for bulk SrF_2:Yb^{3+}/Er^{3+} (0.31 %·K^{-1} at 305 K)[242]. The reason is because the ΔE value reported for bulk (675 cm^{-1}) is smaller than the values estimated here for the nanoparticles. However, the value reported for bulk, obtained from a fit using Equation 1.15, is in disagreement with the reported emission spectra (Figure 6 of reference [242]), characterized by a larger ΔE value similar to present work and to what was computed by Carnall et al. for LaF_3:Er^{3+} (764 cm^{-1}).

Furthermore, the temperature uncertainty of the nanothermometers δT evaluated from Equation 1.17, substituting the resulting signal-to-noise value is $\delta\Delta/\Delta$=0.32%. The value of $\delta\Delta/\Delta$ estimated from the Equation 1.18 dividing the readout fluctuations of the baseline by the maximum intensity value (averaged using 10 emission spectra) for I_1 and I_2 transitions. The calculated temperature uncertainties represented in Figure 5.13b is 0.265–0.438 K (298–383 K), for SrF_2-2, 0.268–0.414 K (300–373 K), for SrF_2-3, 0.274–0.415 K (303–373 K) for SrF_2-4 powders and 0.268–0.401 K (300–365 K) for SrF_2-4 water suspension. Furthermore, plugging the values of S_m and the corresponding errors in Equation 1.19 one can easily access the error in temperature uncertainty, $\sigma_{\delta T}$. All the SrF_2:Yb^{3+}/Er^{3+} nanothermometers exhibit $\sigma_{\delta T}$ values between 0.004-0.006 K. Temperature uncertainty δT, appear to be dependent on the experimental detection setup used to acquire the emission spectra (then converted into thermometric parameter), decreasing with the improvement of the signal-to-noise ratio of the spectrum (by increasing the integration time or the number of scans, for instance). In this case, the reported δT values can be further improved by decreasing $\delta I_i/I_i$ (Equation 1.18) that is far from the detection limit, which is determined by the detector used, typically 0.03% for a photomultiplier tube as that used in this work [243].

Additionally, the repeatability of the samples in Δ is computed using the thermometric parameter mean value at each laser power density (corresponding to a certain temperature) and the thermometric parameter measured in each cycle. Figure 5.13c shows the repeatability of the nanothermometers was measured in ten consecutive temperature cycles of laser irradiation between 0.81±0.08 and 36±4 W·cm^{-2}, corresponding to average temperature values (derived from Equation 1.22) of 310 and 393 K (SrF_2-2), 303 and 337 K (SrF_2-3) and 300 and 316 K (SrF_2-4) respectively. The computed repeatability in Δ is >99%, indicating a highly reversibility without significant changes induced by the exposure to high laser power densities.

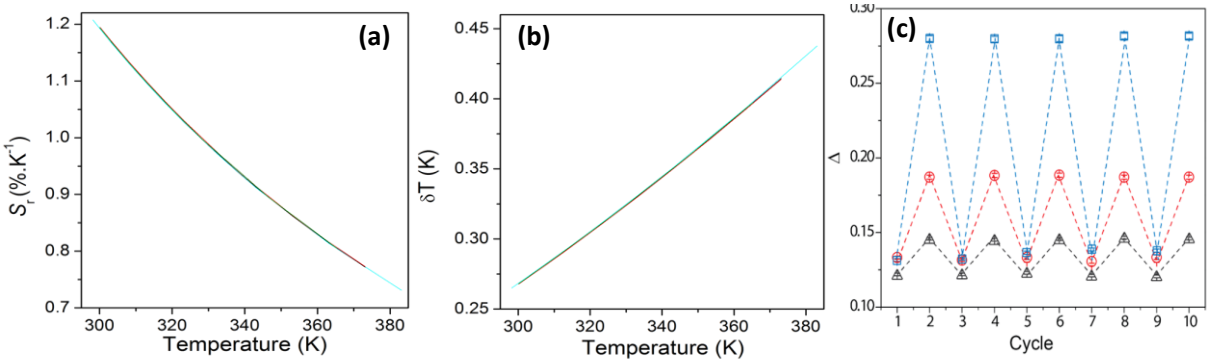

Figure 5.13 (a) Relative temperature sensitivity and (b) temperature uncertainty and (c) cycling of thermometric parameter for SrF_2-2 (blue), SrF_2-3 (red), SrF_2-4 (black, powder) and SrF_2-4 (green, suspension) in the 298–383K range. The maximum error in S_r is 0.02 %·K^{-1}. For cycling two distinct laser power densities 0.81±0.08 W·cm^{-2} and 36±4 W·cm^{-2} were used. The error bars represent $\delta\Delta$, calculated as described in the section 1.6.2.

Table 5.4 Maximum relative thermal sensitivity (S_m), with the respective errors δS_m, and corresponding temperature (T_m) for SrF_2-2, SrF_2-3, and SrF_2-4.

Sample	S_m (%·K^{-1})	T_m (K)
SrF_2-2	1.207±0.016	298.2
SrF_2-3	1.195±0.016	300.2
SrF_2-4	1.193±0.016	300.2

5.7 Primary thermometry

To demonstrate a straightforward method to predict the temperature calibration curve of any upconverting thermometer based on two thermally-coupled electronic levels independently of the medium, the SrF_2 nanoparticles were used as an illustrative example. Primarily a temperature calibration curve was calculated for powder SrF_2-2, SrF_2-3 and SrF_2-4 nanoparticles. Then the

SrF_2-4 water suspension used to prove the concept of an Yb^{3+}/Er^{3+}-based primary thermometry. The relative Er^{3+} UC emission intensity at a given laser power density was much stronger for SrF_2-4 than for SrF_2-2 and SrF_2-3 nanoparticles, both in powder and water suspension. For instance, in powders, the spectral radiant power is 7.2 and 1.6 times higher, respectively. Thus, the SrF_2-4 water suspension was used to predict the temperature calibration curve in two different mediums (air and water).

Generally in upconverting thermometers based on two thermally-coupled electronic levels Δ increases linearly with the laser excitation power, as demonstrated in Figure 5.14 [139]. In the limit of zero pump power the temperature, T_0, corresponds to no laser-induced heating and the thermometric parameter Δ_0 is:

$$\Delta_0 = \frac{I_2}{I_1} = B\exp\left(\frac{-\Delta E}{k_B T_0}\right) \qquad (5.2)$$

The value of Δ at no-laser excitation (Δ_0) is determined from the intercept (graph inset in Figure 5.14) resulting in the values listed in the Table 5.5.

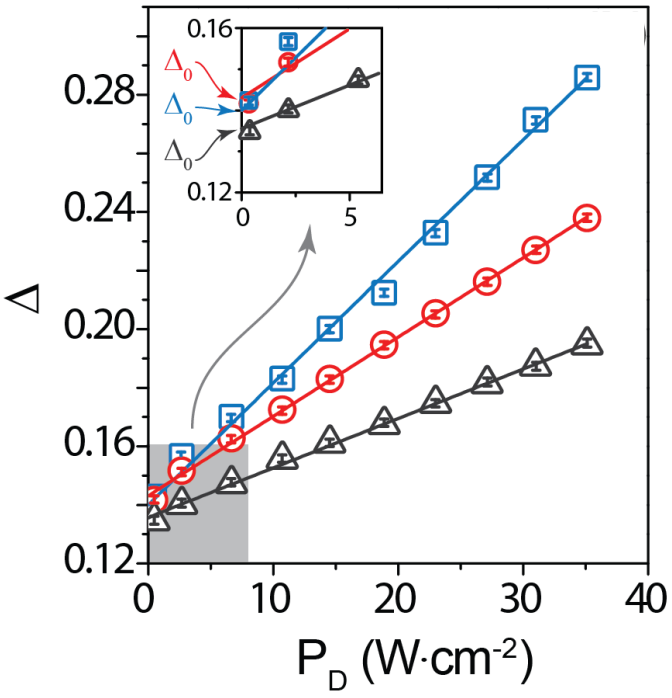

Figure 5.14 Evolution of the thermometric parameter with the laser power density for SrF_2-2 (blue), SrF_2-3 (red) and SrF_2-4 (black). The solid lines are the best fit to experimental points using straight lines, r^2 >0.997.

Table 5.5 Calculated ΔE, Δ_0 and respective errors for SrF_2:Yb^{3+}/Er^{3+} nanoparticles. The corresponding measured T_0 temperatures are also indicated.

Sample	Δ_0	T_0 (K)	ΔE (cm^{-1})
SrF_2-2	0.119±0.001	299.1±0.1	746±10
SrF_2-3	0.127±0.001	300.4±0.1	748±10
SrF_2-4	0.120±0.001	299.4±0.1	747±10

Although the Judd-Ofelt theory can be used to calculate the constant *B*,[40, 227, 244] here this is unnecessary as the absolute temperature is directly determined by the Δ/Δ_0 ratio (calculated through the ratio between Equation 1.5 and 5.2) allows to establish an Equation of state as:

$$\frac{1}{T} = \frac{1}{T_0} - \frac{k_B}{\Delta E} \ln\left(\frac{\Delta}{\Delta_0}\right) \qquad (5.3)$$

The error ΔT in the calculated temperature, is given by:

$$\Delta T = T^2 \sqrt{\left(\frac{\delta T_0}{T_0}\right)^2 + \left(\frac{\delta \Delta E}{k_B} \ln\left(\frac{\Delta}{\Delta_0}\right)\right)^2 + \left(\frac{\Delta E}{k_B}\right)^2 \left[\left(\frac{\delta \Delta_0}{\Delta_0}\right)^2 + \left(\frac{\delta \Delta}{\Delta}\right)^2\right]} \qquad (5.4)$$

Replacing ΔE, T_0, Δ_0 (Table 5.5) values and plugging the experimental Δ values (Figure 5.11d and e), the temperatures can be easily calculated for SrF_2-2 and SrF_2-3 powder nanoparticles, Figure 5.15a and b. In the Figure 5.15a and b, the experimental temperature is reading from a thermocouple positioned in contact with the powder sample holder. The temperatures calculated form the Equation of state are in excellent agreement with the measured values as shown Figure 5.15c and d, validating, therefore, the method proposed here to calculate the absolute temperature. The small deviations of the measured temperatures relatively to the calculated ones for SrF_2-2 (Figure 5.15a and c) can be due to the local increment of the particle's temperature induced by the laser excitation (1.5±0.1 $W \cdot cm^{-2}$).

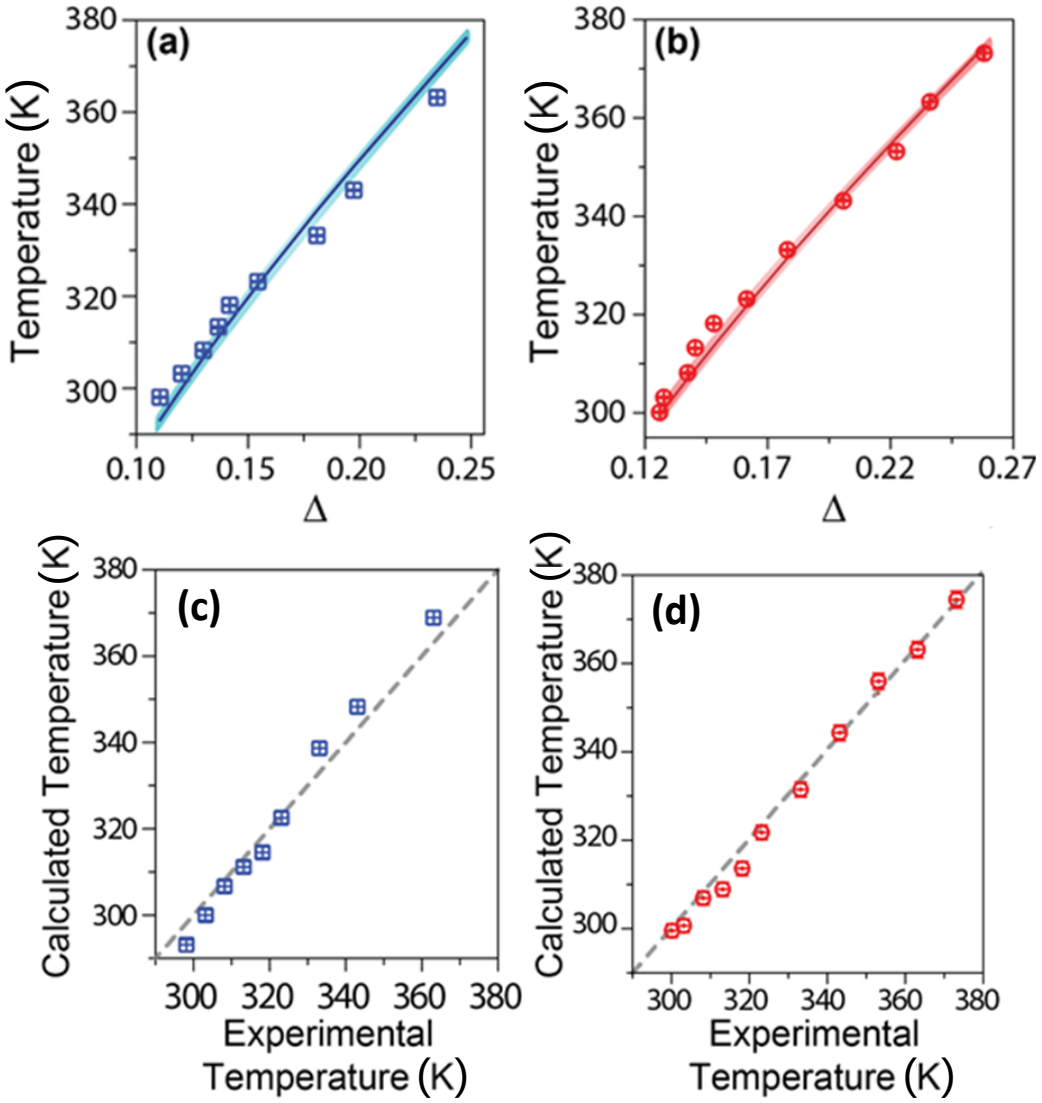

Figure 5.15 Temperature dependence of the experimental Δ values for (a) SrF_2-2 and (b) SrF_2-3 NPs in powders. The solid line is the theoretical predication of temperature using Equation 5.3. The horizontal error bars represent the uncertainty in Δ, whereas the vertical error bars represent the uncertainty of the temperature considering the thermocouple accuracy (0.1 K) and the shadowed area marks the error in the determination of temperature (Equation 5.4). Calculated temperature (Equation 5.3, *y*), *versus* temperature reading using a thermocouple (experimental temperature, *x*) for SrF_2-2 (c) and SrF_2-3 (d). The dashed lines are guides for the eyes corresponding to *y*=*x*. The horizontal error bars represent the thermocouple accuracy and the vertical ones the error in the calculated temperature (Equation 5.4).

Figure 5.16 represents data obtained for two different experiments measured for two distinct samples (1) calculated temperatures obtained from emission spectra recorded at P_D=1.5±0.2 W·cm^{-2} with 1.0 mm slits, 0.2 ms integration time, and 5 consecutive averaged scans (blue squares in Figure 5.16b), (2) temperatures calculated from emission spectra recorded at P_D=1.2±0.1 W·cm^{-2}, with 1.0 mm slits, 0.1 ms integration time, and 1 single scan (red circles in Figure 5.16b).

Lowering the power density to 1.2±0.1 W·cm^{-2} the shifts diminish, as depicted in Figure 5.16. Furthermore, the method is reproducible as Figure 5.16 show for the illustrative case of SrF_2-2.

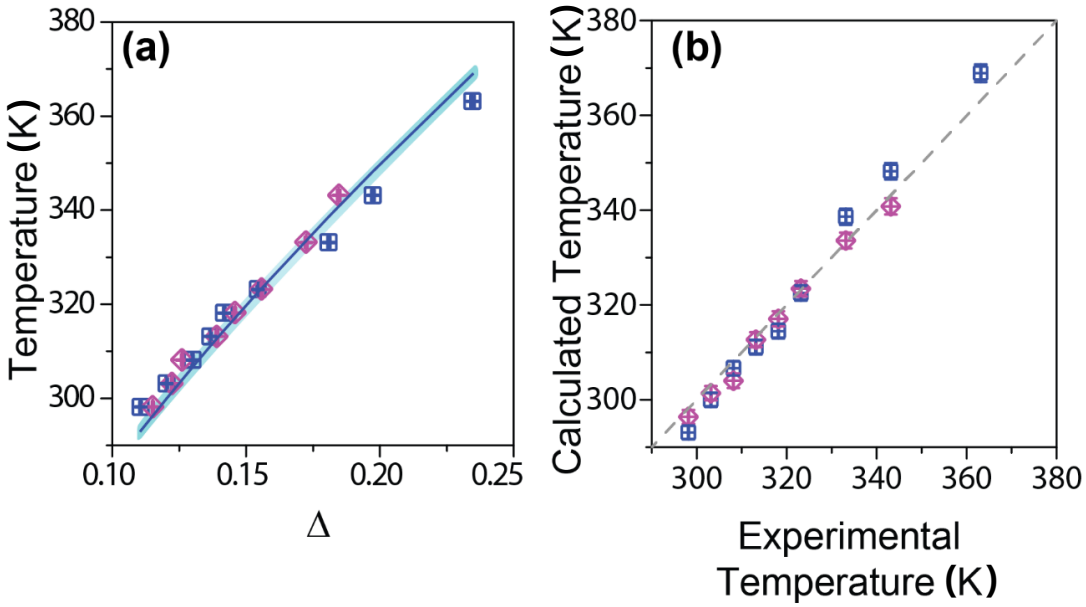

Figure 5.16 (a) Reproducibility of the thermometric parameter for SrF_2-2 under distinct experimental conditions (corresponding to distinct spectral resolutions). (b) Calculated temperature (Equation 5.3, *y*), *versus* temperature reading using a thermocouple (experimental temperature, *x*). The dashed line is a guide for the eyes corresponding to *y*=*x*. The horizontal error bars represent the thermocouple accuracy and the vertical ones the error in the calculated temperature (Equation 5.4).

Figure 5.17a represents the emission spectra of SrF_2-4 were recorded in a 0.59% aqueous suspension at a fixed laser power density (5.0±0.5 W·cm^{-2}) in the 300–365 K range. For this volume fraction and at this laser power density there is no noticeable laser induced local heating, in agreement with previous reports in pure water (local temperature increment around 1 degree[22]). Calculated temperatures obtained by substituting in Equation 5.3, T_0=299.9±0.1 K, ΔE, Δ_0 (Table 5.5) and the experimental Δ values (Figure 5.15c and f), are in excellent agreement with the measured values (using the thermocouple immersed in the suspension). Moreover, the calculated temperatures are independently of the nanoparticles medium (air or water), demonstrating that a new calibration procedure is unnecessary and no other variables apart temperature, such as the ionic strength, pH, pressure, Ln^{3+} local surroundings, or atmosphere composition, impact the thermometric parameter value. Therefore, the SrF_2:Yb^{3+}/Er^{3+} nanoparticles are, indeed, primary thermometers based on the Boltzmann distribution between the $^2H_{11/2}$ and $^4S_{3/2}$ thermally-coupled electronic Er^{3+} electronic levels.

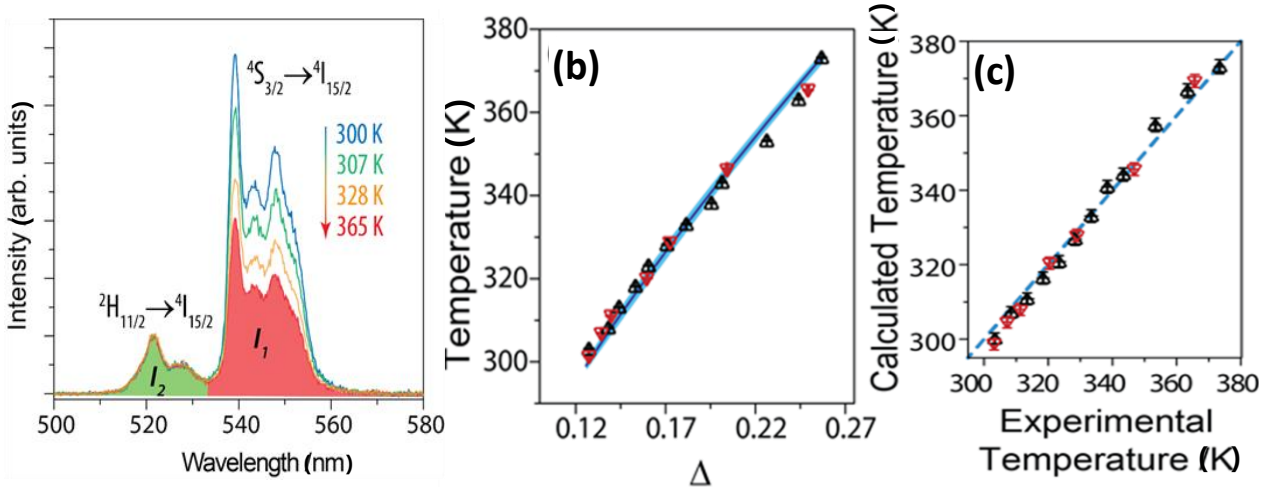

Figure 5.17 (a) Upconversion emission spectra of SrF_2-4 in water suspension. (b) Temperature dependence of the experimental Δ values. The solid line is the theoretical predication of temperature using Equation 5.3, marking the shadowed area the error in the determination of temperature. The horizontal error bars represent the uncertainty in Δ. (d) Calculated temperature (Equation 5.3, *y*) *versus* temperature reading using a thermocouple (experimental temperature, *x*). The dashed line is a guide for the eyes corresponding to *y*=*x*. The vertical error bars are the error in the calculated temperature (Equation 5.4). The vertical error bars in (b) and horizontal error bars in (c) represent the uncertainty of the temperature considering the thermocouple accuracy (0.1 K). In (b) and (c) up triangles for powder and down triangles for water suspension of SrF_2-4, respectively.

5.8 Summary

Cubic phase SrF_2:Yb^{3+}/Er^{3+} UCNPS have been successfully synthesized by a simple hydrothermal route at mild temperature and ambient pressure. The samples were characterized by ICP-OES, DLS, powder XRD, TEM and photoluminescence spectroscopy. The performance of SrF_2:Yb^{3+}/Er^{3+} nanoparticles as intensity-based ratiometric nanothermometers was evaluated yielding to a maximum relative thermal sensitivity up to 1.169±0.016 %·K^{-1} (at *ca.* 303 K) in two distinct mediums (powder and water suspension) at a fixed minimum laser power density (1.5±0.2 and 5.0±0.5 W·cm^{-2}, respectively). The repeatability and the minimum temperature uncertainty of the nanothermometers were determined to be >99% and 0.265 K, respectively.

Furthermore, the SrF_2:Yb^{3+}/Er^{3+} nanoparticles were used here as an illustrative example of a primary Yb^{3+}/Er^{3+} co-doped luminescent nanothermometers. Despite the numerous works on Yb^{3+}/Er^{3+} co-doped luminescent nanothermometers reported in the past decade (the most reported systems in Ln^{3+}-luminescent thermometry), this is the first time that the temperature calibration curve of such thermometers is predicted independently of the medium. The example of the primary thermometers demonstrated here would open the door to the general implementation of luminescent thermometry overcoming one of its main limitations: the requirement of a new calibration procedure whenever the thermometer operates in a different medium

than that in which it was calibrated (or, when not possible, the *ad hoc* assumption that a single calibration is valid independently of the medium).

Chapter 6

Conclusions and prospectives

Luminescence thermometers have experienced a continuous and unprecedented growth over the past decade. In particularly, Ln^{3+} based nanoparticles were emerged as reliable fluorescent nanothermometers based on their temperature-dependent luminescence features in the VIS and NIR regions. However, these thermometers suffer for their low sensitivities for sensing and imaging at the nanoscale. In this context, Nd^{3+}-doped downshifting and Yb^{3+}/Er^{3+} co-doped upconverting oxide and fluoride nanoparticles were synthesized and their photoluminescence properties and increase in thermal sensitivity for applications in temperature sensing was demonstrated.

- In chapter 2, the performance of $(Gd_{0.991}Nd_{0.009})_2O_3$ as an intensity-based ratiometric nanothermometer was evaluated in the 288–323 K range. These nanorods exhibit the highest thermal sensitivity and temperature uncertainty observed so far (1.75±0.04 $\%\cdot K^{-1}$ and 0.14±0.05 K, respectively, at 288 K) for a nanothermometer operating in the first transparent BW. Moreover, this high sensitivity was achieved using a common R928 photomultiplier tube to measure the Nd^{3+} emission in the 800−920 nm range, which allowed defining the thermometer parameter as the integrated intensity ratio of the $^4F_{5/2}\rightarrow{}^4I_{9/2}$ and $^4F_{3/2}\rightarrow{}^4I_{9/2}$ electronic transitions, rather than the two Stark components of the $^4F_{3/2}$ multiplet. The increase by one order of magnitude in the relative sensitivity of nanothermometers operating in the first biological transparent window widens the scope for using Nd^{3+} ions in deep-tissue imaging and thermal sensing.

- Likewise, in chapter 3, the performance of $(Gd_{0.972}Nd_{0.028})_2O_3$ as a ratiometric nanothermometer was evaluated in the 303–393 K range. The nanothermometers operate upon excitation within the first (at 808 nm) and emission in the second (1250–1550 nm) BW.

From the deconvoluted spectra, the thermometric parameter was defined by the ratio between the integrated intensity of all the transitions originated from the $^4F_{3/2}$ highest-energy Stark component and all the transitions from the $^4F_{3/2}$ lowest-energy, and maximum thermal sensitivity of 0.23±0.03%·K^{-1} at 303 K was obtained. The nanothermometers widens the scope for using Nd^{3+} for thermal sensing in the second BW. Furthermore, the effect of morphology (nanorods and nanospheres) on thermal sensitivity was also demonstrated in terms of their changes in the energy gap.

- In chapter 4, a new heater–thermometer nanoplatform were developed for plasmon-induced optical heating and temperature sensing, consisting of Au nanoparticles (NRs and NPs) linked to Gd_2O_3:Yb^{3+}/Er^{3+} nanoparticles (NRs and NSs). Upon 980 nm infrared laser excitation (up to 102 W·cm^{-2}) the plasmon-induced heating of the Au nanorods was assessed by monitoring the relative intensity of the Er^{3+} UC $^2H_{11/2}\rightarrow{}^4I_{15/2}$ and $^4S_{3/2}\rightarrow{}^4I_{15/2}$ green emission lines, and temperatures in the range 302–548K were determined from Boltzmann distribution. The optimal condition for reaching temperatures in the physiological range (302–330 K), using the lowest possible laser power density (8.3–24.8 W·cm^{-2}), was achieved by tuning the LSPR band to 850 nm. For NRs-AuNRs-850 nm–1.17, a maximum thermal sensitivity of 1.01 %·K^{-1} at 330 K with an uncertainty of 0.28 K was determined. Furthermore, the performed *in vitro* cytotoxicity (MG-63 with NRs-AuNRs-850 nm–1.17, viability>80% after 24 hours incubation and at a platform concentration up to 250 mg·mL^{-1}) and cellular uptake studies opens a new avenue for biological applications based on Ln^{3+}-bearing nanoplatforms.

- In chapter 5, Yb^{3+}/Er^{3+} UC in SrF_2 host based nanoparticles were successfully demonstrated as luminescent primary thermometers. The performance of SrF_2:Yb^{3+}/Er^{3+} nanoparticles as intensity-based ratiometric thermometer was evaluated by defining the thermometric parameter Δ as the integrated intensity ratio of the $^2H_{11/2}\rightarrow{}^4I_{15/2}$ and $^4S_{3/2}\rightarrow{}^4I_{15/2}$ Er^{3+} transitions. Moreover, a maximum relative thermal sensitivity up to 1.169±0.016 %·K^{-1} (at *ca.* 300 K) in two distinct mediums (powder and water suspension) at a fixed minimum laser power density (1.5±0.2 and 5.0±0.5 W·cm^{-2}, respectively) was recorded. Furthermore, SrF_2:Yb^{3+}/Er^{3+}nanoparticles demonstrated as fully functioning primary thermometers, operating independent of the medium.

This thesis directs towards several pathways to implement in the future in luminescence nanothermometry. That include the development of luminescent molecular thermometers, operating in VIS and in NIR regions, with high thermal sensitivity in the physiological temperature range adapted to specific applications.

- One open route is to implement small, water dispersed, bright emitting $SrF_2:Yb^{3+}/Er^{3+}$ UCNPs for biological and therapeutic applications. On this sense, primarily the *in vivo* viability tests of the nanoparticles, their applicability and processability were explored.

Few steps were moved at this front, the initial outcomes of the $SrF_2:Yb^{3+}/Er^{3+}$ *in vivo* viability tests were shown in Figure 6.1. The viability studies were performed by incubating the Macrophages cell line treated with varying concentration of SrF_2-2 NPs suspension in the growth media for time periods of 24 and 48 hours.

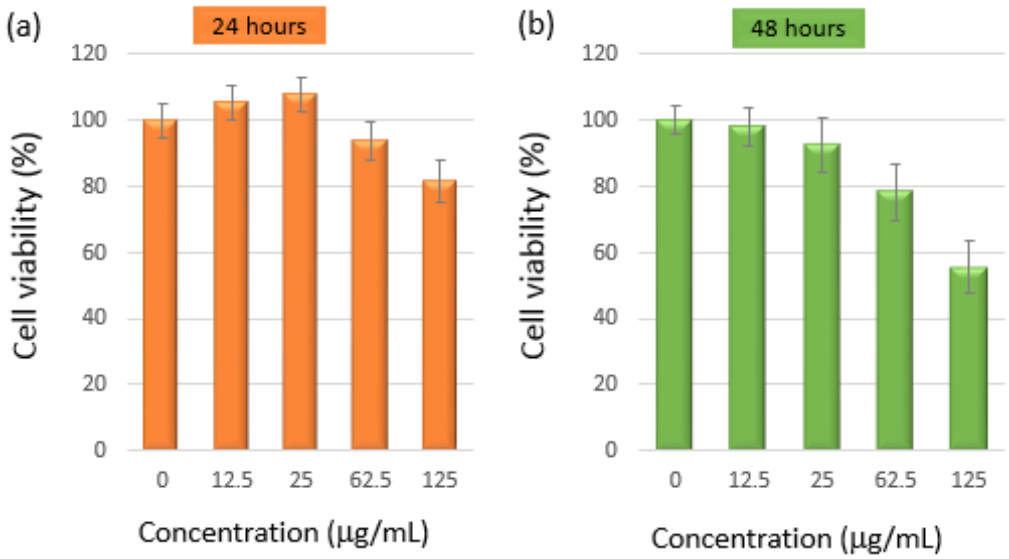

Figure 6.1 Viability of Macrophage cells after incubation with SrF_2-2 NPs (a) for 24 hours and (b) for 48 hours. Each data point is represented as mean value ±standard deviation from three independent assays.

The viability of exposed cells was significantly reduced with the nanoparticle concentration from 12.5 $\mu g \cdot mL^{-1}$ to 125 $\mu g \cdot mL^{-1}$. Moreover, increasing the time periods from 24 hours (Figure 6.1a) to 48 hours (Figure 6.1b), the viability further decreased for a given concentration. Majority of the cells appeared to have continued normal growth, which represents the relatively low toxic (Figure 6.1a, cell viability >80% up to a concentration of 125 $\mu g \cdot mL^{-1}$) behaviour of SrF_2 nanoparticles on this cell line.

- Next in order, is the investigation of the nanoparticles safe entry into cells (cellular uptake) to achieve prognostic and therapeutic efficacy, which will be followed by their bio-distribution studies in different organs. Using hyperspectral imaging, nanoparticles can be further analysed and characterized to determine properties such as the spatial location, agglomeration status, wavelength differentiation, and partial size of the NPs.

Up till now, the SrF_2-2 NPs size distribution and their corresponding Yb^{3+}/Er^{3+} UC emission were evaluated using the hyperspectral imaging. SrF_2-2 NPs (50 and 100 $\mu g \cdot mL^{-1}$) were injected in the DMEM (Dulbecco's modified eagle's medium, 1 mL) culture medium. The distribution of nanoparticles was observed by hyperspectral imaging under white-light and under 980 nm irradiation and the corresponding images are presented in Figure 6.2. Decreasing the NPs concentration from 100 $\mu g \cdot mL^{-1}$ to 50 $\mu g \cdot mL^{-1}$ lowers the average size of the nanoparticle agglomeration from 5 μm (Figure 6.2B) to 1 μm (Figure 6.2C).

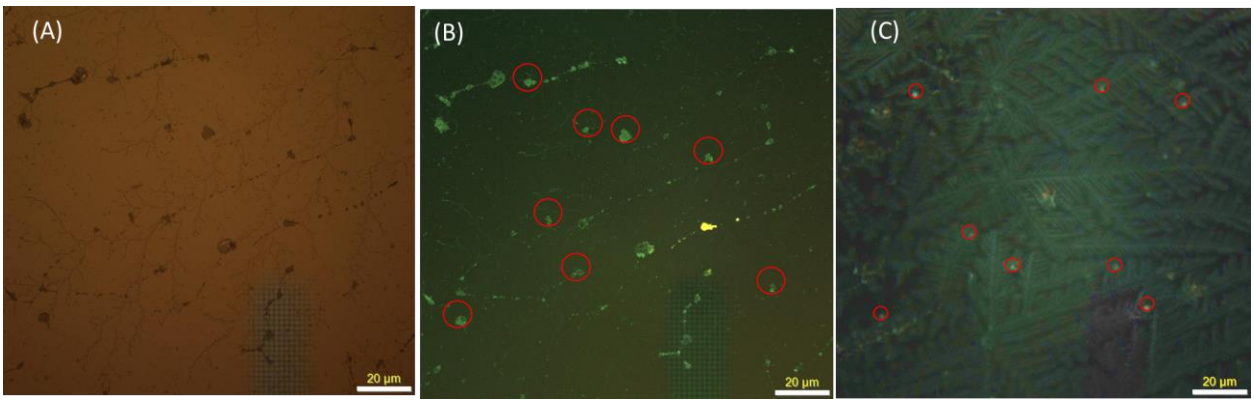

Figure 6.2 Images of SrF_2-2 upconverting nanoparticles under (A) white-light and (B and C) 980 nm excitation at 241 $W \cdot cm^{-2}$. The calculated average agglomerate size is around 5 and 1 μm estimated from the red circles in B and C, respectively.

Figure 6.3 shows the Er^{3+} UC emission spectra of the SrF_2:Yb^{3+}/Er^{3+} NPs incorporated in the culture medium and it was recorded at 980 nm excitation with laser power density of 241 $W \cdot cm^{-2}$ by hyperspectral imaging. From the emission spectra, the integrated intensity ratio of $^2H_{11/2} \rightarrow {}^4I_{15/2}$ (I_1) and $^4S_{3/2} \rightarrow {}^4I_{15/2}$ (I_2) transitions, Δ, was calculated as 0.172. Benefiting from the work reported in Chapter-5, using the equation of state the temperature can be estimated for the NPs suspended in DMEM culture medium. Substituting ΔE, T_0, Δ_0 (Table 5.5) values and inserting the

experimental Δ value (0.172, Figure 6.3), in Equation 5.3, the temperature can be easily calculated for SrF_2-2 nanoparticles as T=332.2 K, which is in excellent agreement with the experimental one, as well as the calculated temperature for powder and suspension (Figure 5.15 and 5.16). Furtherance step is to implement the experiment in the Macrophage cells and to evaluate the particle and temperature distribution.

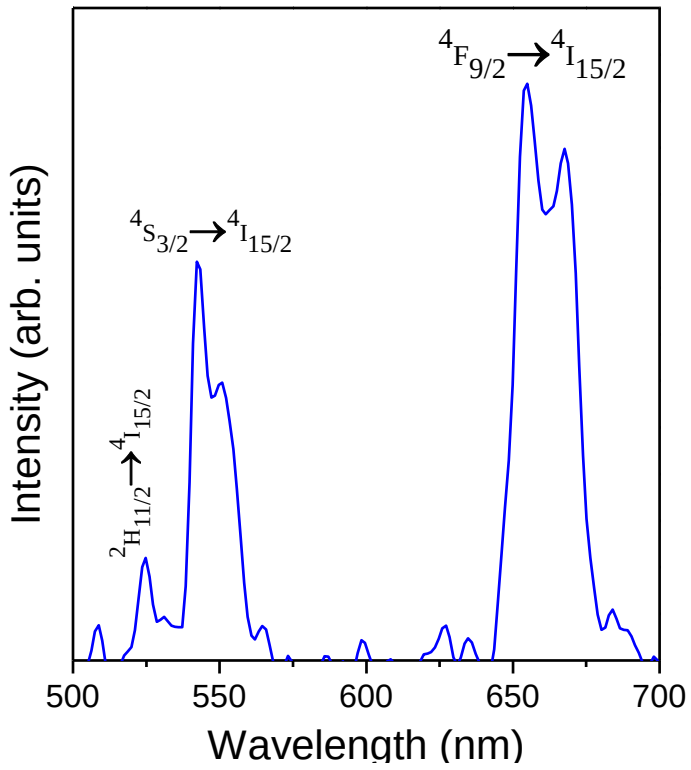

Figure 6.3 Er^{3+} upconversion emission spectra of SrF_2-2 powder nanoparticles under 980 nm excitation at 241 W·cm^{-2}. The spectrum is an average of the emission spectrum collected from red circles in Figure 6.2B.

- Another work is intended to construct and synthesize luminescent nanothermometers that can emit and be excited in BW regions I, II and III avoiding the heating effect caused by the laser excitation, such as 980 and 808 nm lasers. Various Ln^{3+} (Ln^{3+}=Nd^{3+}, Pr^{3+}, Ho^{3+}, Tm^{3+}, Er^{3+}) doped hosts will be evaluated for the purpose. In brief structural, morphological and Ln^{3+} photoluminescence characterization of the synthesized nanoparticles will follow using XRD, TEM and luminescence spectroscopy, respectively. Furthermore, the thermal sensing properties will be investigated, and the potential application of constructed materials will be demonstrated.

Some of the constructed nanoplatforms along of this way are single Pr^{3+}-doped $LuPO_4$ nanoparticles (Figure 6.4A) and doubly-doped Gd_2O_3:Nd^{3+}/Ho^{3+} nanospheres (Figure 6.4B) for luminescent thermometry. Besides having temperature dependent emission channels located in BW, certainly, Nd^{3+}, Pr^{3+} and Ho^{3+} ions also exhibits excitation channels in the BW regions, mainly at far infrared region (900−1500 nm) that can be effectively used to minimize the heating effect.

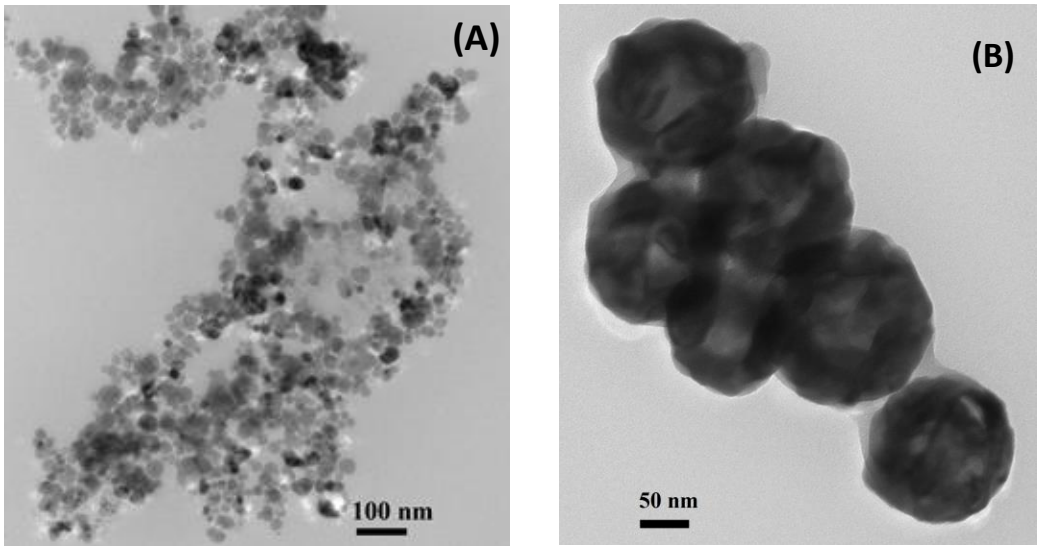

Figure 6.4 TEM images of (A) $LuPO_4$:Pr^{3+} nanoparticles and (B) Gd_2O_3:Nd^{3+}/Ho^{3+} hollow spheres.

Figure 6.5 represents the temperature-dependent emission spectra recorded for $LuPO_4$:Pr^{3+} NPs in VIS and NIR regions. The excitation used is Xe lamp at 900 nm. The emission spectra show several intense transitions corresponding to the Pr^{3+} ion. As the temperature is raised from 298 K to 353 K, the overall intensity of the fluorescence decreases but the rate of decrease is different for different peaks. The difference in the intensity ratio of thermally coupled levels further is used to sense the temperature.

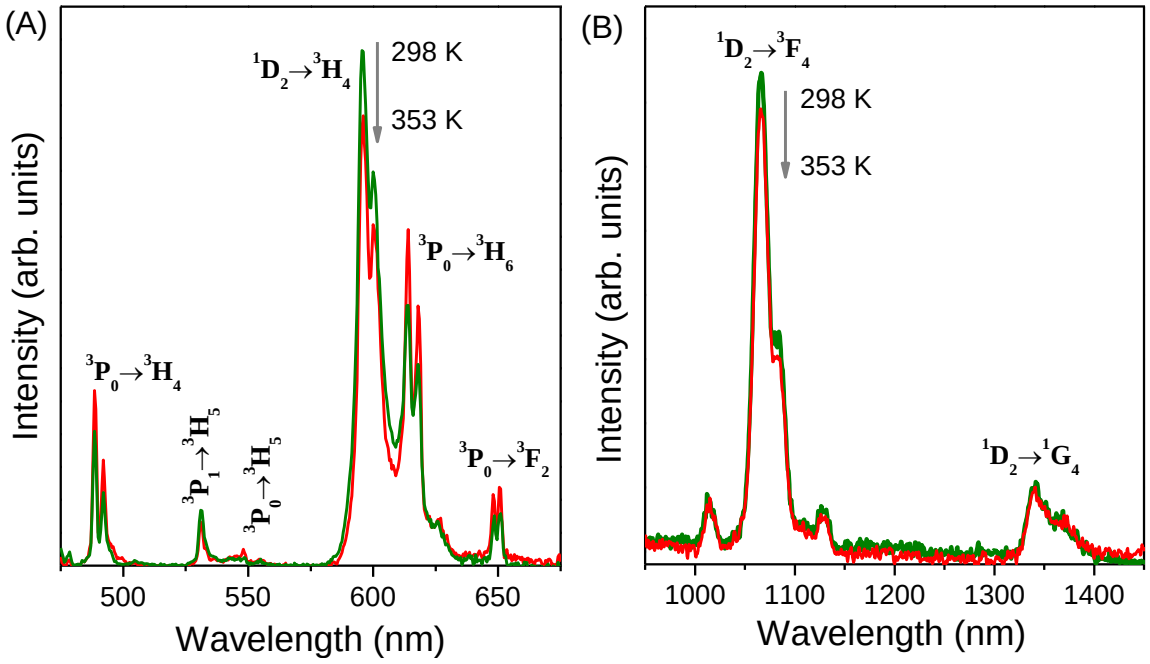

Figure 6.5 Temperature dependent emission spectra of Pr^{3+} doped $LuPO_4$ powder nanoparticles under 900 nm lamp excitation.

Appendix A

In this annex, the experimental techniques used in this thesis work are described in detail.

A.1 ICP-OES elemental analysis

Inductively coupled plasma optical emission spectrometry (ICP-OES-Activa-M, Horiba Jobin Yvon) was handled to determine the relative content of the lanthanide metal ions in the synthesized nanomaterials. Samples in powder form (around 5 mg) was well dissolved in ultra-pure HNO_3 (0.5 mL, 65 wt% PA-ISO) to prepare 10 mL of aqueous solution containing the Ln^{3+}. An aliquot of the solution was transferred into a high-frequency plasma in the form of an aerosol. Therein, the constituents are atomized and partially ionized at temperatures above 6000 K. As a result of the total destruction of the sample and conversion into atoms or ions, there is no influence of the original binding form of the element on the measurement. The atoms and ions excited by the plasma return to lower energy states and release the energy difference in the form of electromagnetic radiation. The emitted radiation consists of lines characteristic of particular element. A calibration with standard solutions is required for the quantitative determination, which is based on a linear- correlation of the signal intensities and the concentration of the element.

A.2 Powder X-ray diffraction

The powder X-ray diffraction patterns of the powder samples were collected on a PANalytical Empyrean X-ray diffractometer (Figure A1) operating at 45 kV and 40 mA, with CuKα1 radiation at 1.5406 Å, in the 2θ range 20^o–80^o with a 0.02^o step size and 40 seconds acquisition time per step in the reflection scanning mode. The obtained data were treated taking in to account of the instrumental broadening factor measured with a LaB_6 (NIST 660a) standard. The reference data were taken from the International Centre for Diffraction Data (ICDD) database. The structural features like lattice parameters have been investigated using Rietveld refinement with High Score Plus software.

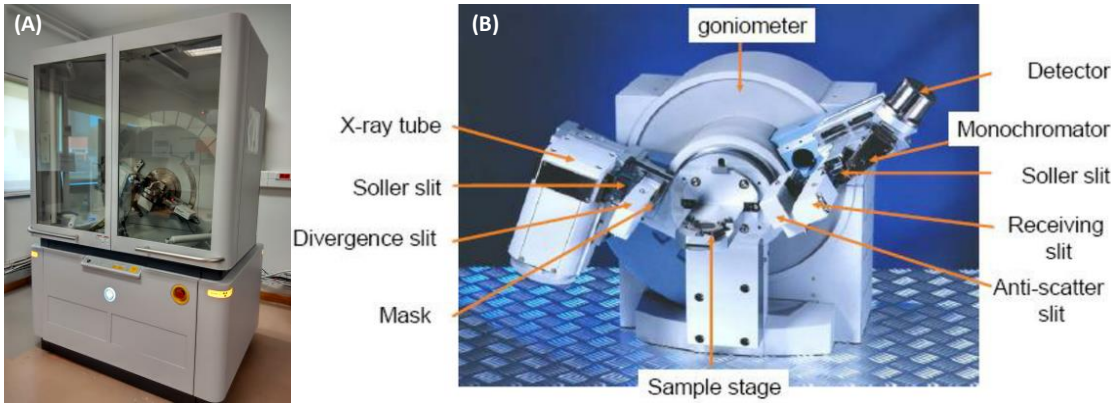

Figure A. 1 (A) PANalytical Empyrean X-ray diffractometer in University of Aveiro, used in this thesis work. (B) X-ray diffractometer compartment setup, taken from PANalytical.

In 1918, P. Scherrer showed that when a parallel monochromatic radiation falls into crystals, the diffracted beam is broadened when the particle size is small. Then the Scherrer given an expression that relates the average sizes of sub-micrometer particles, or crystallites, in a solid to the broadening of a peak in a diffraction pattern [245].

$$D = \frac{K\lambda}{\beta \cos\theta} \qquad (A.1)$$

where D is the average diameter of the nanocrystal, K is the Scherrer's constant (for spherical crystal K=0.94), λ is the wavelength of X-rays (1.5406 Å), β is the full width at half maximum of the diffraction peak (in radian) at the Bragg angle θ. The uncertainty in the crystal size is mostly dominated by the uncertainty in the parameter β than those of the instrumental factors θ and λ.

A.3 Electron microscopy

The morphology of the samples was analysed on a Jeol JEM-2200FS transmission electron microscope (TEM), Hitachi H9000 transmission electron microscope (TEM), both operated at 200 kV and on a Hitachi SU-70 scanning electron microscopy (SEM) operated at 300 kV. Figure A2 shows the electron microscopy equipments established in University of Aveiro. Powder form and as-synthesized nanoparticles were well dispersed in distilled water under sonication. A drop of the sample was then dispersed on the carbon film or holey carbon film on 300 square mesh copper grids. Then the grids were dried in air. The sizes are calculated from TEM/SEM images, respectively, using ImageJ software analysis (www.imagej.nih.gov/ij/). The microcopy images

were captured for around 5-10 distinct spots in the carbon film in order to acquire around 100 or above number of nanoparticles. Nearly sizes of 100 nanoparticles were computed to determine the average sizes of nanoparticles. Further, the interplanar distances were determined form the high resolution TEM (HRTEM) images using Gatan digital micrograph software.

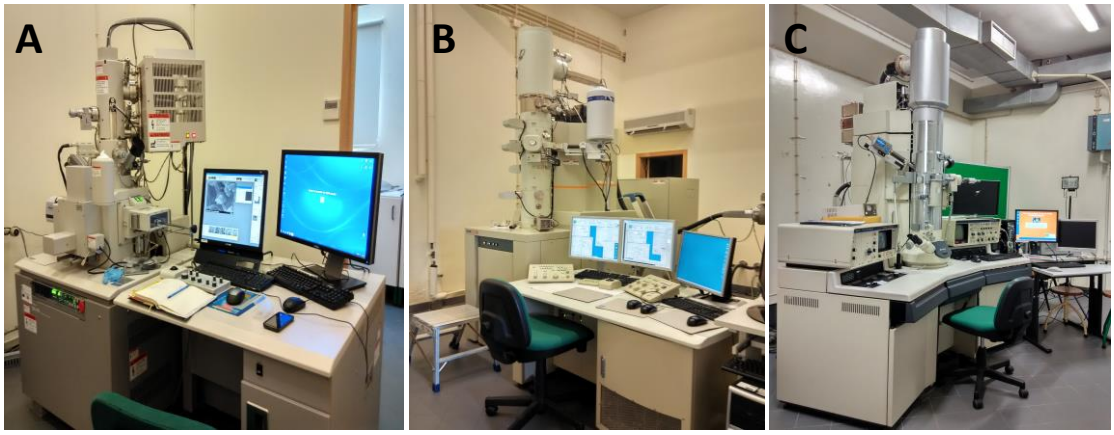

Figure A. 2 (A) Hitachi SU-70 SEM (B) Jeol JEM-2200FS TEM and (C) Hitachi H9000 TEM, respectively installed in University of Aveiro, were used for the electronic micrographs acquisition.

A.4 Photoluminescence

Luminescence measurements can be broadly classified into two types of measurements: steady-state and time-resolved.

A.4.1 Steady-state photoluminescence

Steady-state fluorescence is the simplest and the most common type of fluorescence spectroscopy. Measurements are performed with continuous illumination and detection. It constitutes of emission and excitation processes, which are the basic spectroscopic analysis of a material. An emission spectrum is acquired by exciting the sample with an absorbed wavelength, usually the maximum intensity absorption (or excitation) peak, and the emission monochromator scans the luminescence within a wavelength interval. An excitation spectrum is measured by setting the emission monochromator fixed at a given emission wavelength (for instance the one corresponding to the maximum of the emission spectrum). The excitation monochromator is then scanned at a given wavelength interval and the luminescence intensity corresponding to the monitored emission wavelength is measured.

The measurement of the excitation and the emission spectra requires a monochromator to select a narrow wavelength interval of an excitation source and another monochromator to select a narrow wavelength interval of the emitted spectra. Typically, both requirements are fulfilled by an experimental layout including mirrors and diffraction gratings, using, for example, a Czerny–Turner configuration (Figure A3). The fluorescence emission is collected at 90 or at a lower angle (known as right-angle and front-face configurations, respectively) from the excitation, to prevent the interference of the excitation light with the detection of the fluorescence emission.

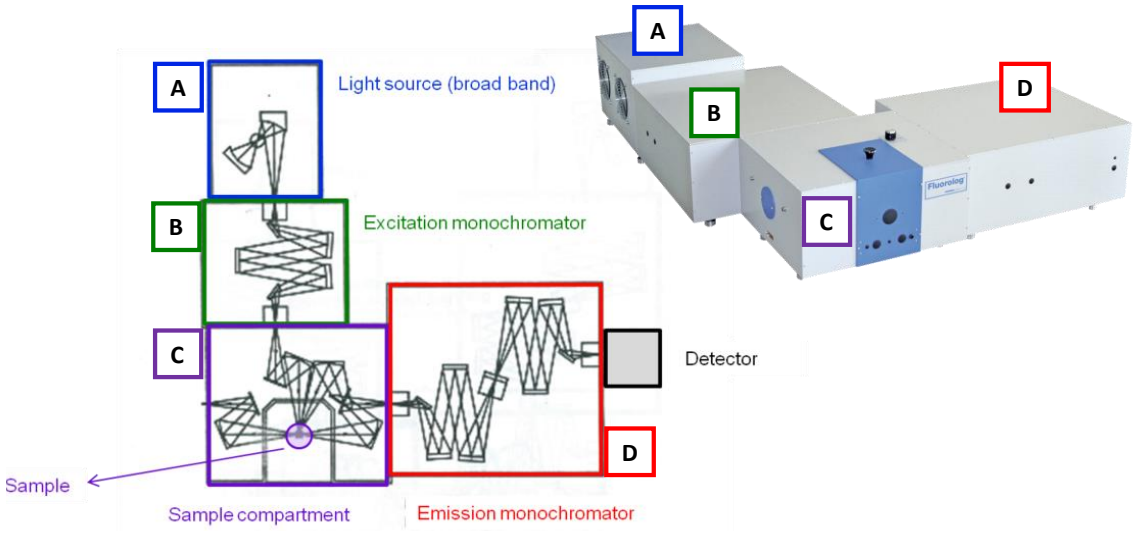

Figure A. 3 Internal components of Fluorolog-3, Horiba. The black letters are the source compartment (A) lamp, (B) a single-grating excitation monochromator, (C) sample chamber with a helium cryostat and (D) a double-grating emission monochromator and the detector (taken from Horiba Scientific).

A.4.2 Time-resolved photoluminescence

Time resolved fluorescence spectroscopy is used to investigate dynamical processes and to characterize the interaction of the fluorescent probe molecule with its chemical environment. The main difference between steady-state and time-resolved measurements is the excitation mode of the light source. In the former, a continuous excitation source is required while in the later a pulsed excitation coupled with time sensitive detecting system is employed. The basic experimental output of time resolved spectroscopy is a decay curve, that corresponds to the temporal evolution of the intensity at the selected wavelength as represented in Figure A4. The measurement provides some of the important temporal parameters include the excitation pulse, decay time and measurement time.

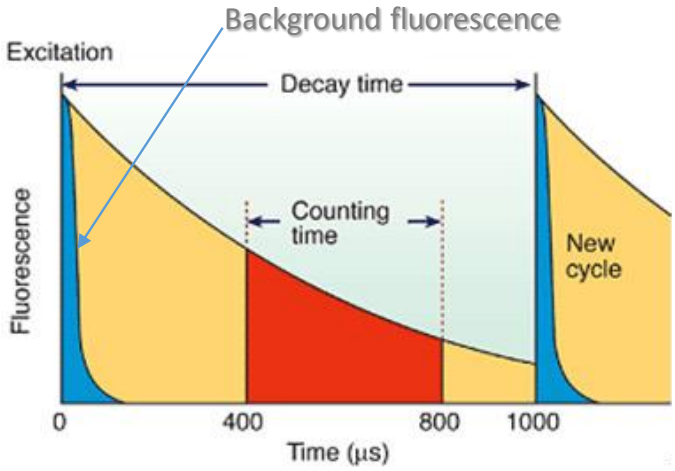

Figure A. 4 Principle of time-resolved spectroscopy with delay time of 400 µs, counting time of 400 µs, and cycle time of 1000 µs [246].

The luminescence decay time (or lifetime) defined as the average time, the emitting system spends in the excited state prior to return to the ground state after an infinitely short pulse of exciting light [45]. Then the decay process of the luminescence intensity *I(t)* after the termination of excitation at *t=0* is generally represented by an exponential function of the elapsed time after the excitation:

$$I_{(t)} = I_0 \exp\left(-\frac{t-t_0}{\tau}\right) \qquad (A.2)$$

where, I_0 is the intensity at time zero (upon excitation) and τ is the decay time. This is defined as the time for the intensity to drop by 1/e. The above equation is valid for an emitting system with single-exponential decay.

In the case of multi-exponentials, the decay curve was fitted with a sum of exponential decay functions:

$$I_{(t)} = \sum_i I_{0i} \exp\left(-\frac{t-t_0}{\tau_i}\right) \qquad (A.3)$$

If the decay curve is non-exponential, then the average decay time $<\tau>$, was calculated to allow for comparison of different samples[247]

$$\langle \tau \rangle = \frac{\int_{t_0}^{t_1} I(t)tdt}{\int_{t_0}^{t_1} I(t)dt} \qquad (A.4)$$

Experimental set up in University of Aveiro

Photoluminescence spectra were recorded with a Fluorolog-3, Horiba Scientific installed in the PHANTOM group, Department of Physics, University of Aveiro. Briefly, the spectrofluorometer is a Fluorolog®-3 Model FL3-2T with a double excitation monochromator and a single emission monochromator (Triax 320) fitted with gratings used in UV-VIS and NIR regions. The spectra were acquired using a modular double grating excitation spectrofluorometer with a TRIAX 320 single-emission monochromator (Model FL3-2T) coupled to a H9170–R928 Hamamatsu photomultiplier, using a front face acquisition mode. The excitation source was a 450 W Xe arc lamp. The emission spectra were corrected for the detection and optical spectral response of the spectrofluorometer and the excitation spectra were corrected for the spectral distribution of the lamp intensity using a photodiode reference detector. The emission decay time measurements were carried out with a pulsed Xe-Hg lamp excitation, in front face acquisition mode.

The thermal heating was carried out using a Kapton thermofoil heater (Minco) mounted on a Cu holder (2.5 cm×2.5 cm) and coupled to a temperature controller (IES-RD31). Powder samples were placed on a smaller Cu plate (1.0 cm×0.5 cm) attached to the holder by a thermal conductive paste (WLP 500, Fischer Elektronik). The temperature was measured with a Barnant thermocouple 100 (model 600-2820) with a temperature accuracy of 0.1 K, according to the manufacturer. Water suspensions (1 mL) were placed in a quartz cuvette (CV10Q1400, Thorlabs) in which the temperature was measured by a thermocouple (I620-20147, VWR) with an accuracy of 0.1 K, according to the manufacturer.

Apart from the above mentioned photoluminescent setup in Department of Physics, University of Aveiro, two other equipment's (Luminescent Materials Laboratory, Department of Biotechnology,

University of Verona, and Instituto de Física de São Carlos, Universidade de São Paulo) were also used to study the photoluminescence properties of the samples studied in this thesis.

Experimental set up in University of São Paulo

Photoluminescence spectra were obtained using a dye laser (Coherent-599/Rhodamine 6G) pumped with a Inova 400 Coherent Ar ion laser. The emission was dispersed by a single Monospec 27 Spex monochromator coupled to a R928 (Hamamatsu) photomultiplier. The temperature was varied from 288 to 328 K using a N_2 cryostat equipped with a 320 Auto tuning temperature controller (LakeShore). Luminescence decay curves were measured by exciting the samples at 808 nm with an optical parametric oscillator (OPO, Surelite/Continumm SLII-10) pumped by the third harmonic (355 nm) of a Nd-YAG laser (Surelite II/Continumm, 10 Hz, 5 ns) using the Monospec 27 Spex monochromator and the InGaAs detector. A digital oscilloscope (TekTronix/TDS380) was used to register the decay curves.

Experimental set up in University of Verona

A modular double grating excitation spectrofluorometer with a TRIAX 320 emission monochromator (Nanolog, Horiba Scientific) coupled to a Symphony II detector with an InGaAs array was also used to record room temperature emission spectra between 800 and 1200 nm. The excitation source was a Xe lamp. The emission spectra were corrected for detection and optical spectral response of the spectrofluorometer.

In all the cases, the samples can be in powder or suspension forms. Powder samples usually placed on a solid sample holder and the suspensions (1 mL) were filled in quartz cuvettes and mounted on suspension holder.

Laser excitation source and determination of laser power density

A 980 nm continuous wave (CW) laser (Thorlabs LDM21 mount, LDC220 laser diode controller and TED200 temperature controller) was used as the excitation source. The air propagating laser beam was focused on the sample using a C230TM-B aspheric lens (Thorlabs). A customized optical fiber (SarSpec, 0.6 mm core diameter with an adaptable-length ferrule) guides a CW

infrared laser diode (CNI, MDL-H-980 laser controlled by a PSU-H–LED power source, emission wavelength of 980 nm). Acting on the laser driving current allows controlling the excitation power up to a maximum of 5.0 W.

Laser powers (*P*, W) were measured with a thermal power sensor (ThorLabs, thermopile-S310C) coupled to an optical power and energy meter (Thorlabs, PM100D). The power measurements present a 5% relative error, according to the manufacturer. The Laser power densities (P_D) determined by, $P_D = \frac{P}{D}$. To determine P_D, on the samples the illumination area produced by each laser source was computed. For the CNI laser (fiber guided) the fiber numerical aperture and the geometric parameters were used resulting in a diameter of illumination of D=660±30 μm. For the Thorlabs laser (air propagating) the dimensions of the emission head and the lenses focal distance are used to compute a diameter of illumination of D=450±20 μm. For comparison, pellet samples with power values of P=0.285 W (fiber guided laser) and of P=0.735 (air propagating laser) were illuminated. The resulting marks on the surface of the samples were inspected by microscope observation, resulting in average diameters of 655 and 406 μm, for the fiber guided and air propagating laser, respectively. The experimentally determined values are in good agreement with the calculated diameters, thus validating the approximations made. The error in the laser power density is given by:

$$\delta P_D = P_D \sqrt{\left(\frac{\delta P}{P}\right)^2 + \left(-2\frac{\delta D}{D}\right)^2} \qquad (A.5)$$

with $\delta P/P$=5%. For the experimental conditions used, the corresponding $\delta P_D / P_D$ is found to be 10%, for both laser fiber guided and air propagating lasers.

A.4.3 Upconversion emission quantum yields

Upconversion emission quantum yield is an important figure of merit for luminescent materials. It is directly related to the intensity of the emission as the quantum yield (*q*) defined by the ratio of the number of photons emitted (N_e) divided by the number of photons absorbed (N_a), according to [248]:

$$q = \frac{N_e}{N_a} \qquad (A.6)$$

q requires the independent quantification of N_e and N_a.

The most common method of q determination is to compare the luminescence spectra of the studied sample and a standard with normalized absorption. However, this method suffers from several drawbacks such as the need for an appropriate standard absorbing and emitting in the same wavelength region as the sample under study. Moreover, the sample needs to be isotropic, rendering weakly absorbing (dilute) solutions proper candidates for this method. In case of nanocrystalline powder characterized by a high refractive index, the angular distribution of the emission, reflectivity and absorbance is not uniform. Thus, a different technique has to be applied [248, 249]. A suitable technique involves the use of an integrating sphere. The latter consist of a hollow sphere, whose interior is coated with a diffusely reflective material, such as barium sulfate or sintered polytetrafluoroethylene. In an ideal integrating sphere, an incoming light beam is redistributed isotropically resulting in a uniform illumination of the interior of the sphere. Hence, the outcoming light is proportional to the incoming light irrespective of the angle of observation. Thus, a q determination requires a comparison of the intensities of an incoming light beam, the intensity of the outgoing light beam and the intensity of the emission of the luminescent material under study.

An integrating sphere coupled to a CCD enables the quantification of the spectral power density S(units of power per wavelength) in the VIS spectral range:

$$S(\lambda) = \frac{dP}{d\lambda} = \frac{d}{d\lambda}\left(\frac{dN}{dt}\frac{hc}{\lambda}\right) = \frac{hc}{\lambda}\frac{d}{d\lambda}\left(\frac{dN}{dt}\right) \qquad (A.7)$$

where c denotes the speed of light in vacuum, dN/dt is the photon flux per unit of time and λ is the photon wavelength. The power P is given by the product of the number of photons by its energy. Thus, from the experimental measurement of $S(\lambda)$, the number of photons N (N_e or N_a) is determined by:

$$\frac{dN}{dt} = \frac{1}{hc}\int_{\lambda_1}^{\lambda_2}[S(\lambda)\lambda]d\lambda \qquad (A.8)$$

where the integral limits correspond to the emission ($N=N_e$) or absorption ($N=N_a$) spectral ranges. Experimentally, N_a is the difference between the number of photons not absorbed by the reference and by the sample [220, 250].

When the excitation wavelength lays outside the CCD responsivity limits (370-808 nm) and additional detection system is required to quantify N_a (this is the case presented in the thesis for $SrF_2:Yb^{3+}/Er^{3+}$ UCNPS). In this particular case, N_a will be quantified by:

$$\frac{dN_a}{dt} = \frac{P\lambda}{hc} \qquad (A.9)$$

where P is measured using a power meter. The ability of a power meter device to accurately quantify N_a in the NIR (808 nm and 980 nm) was also recently demonstrated [235]. Combining Equations. 2.4, 2.6 and 2.7, the quantum yield values can be quantified by:

$$q = \frac{\int_{\lambda_1}^{\lambda_2}[S(\lambda)\lambda]d\lambda}{P\lambda} \qquad (A.10)$$

The corresponding error (Δq) is given by:

$$\begin{aligned}(\Delta q)^2 &= \left(\frac{\partial q}{\partial P}\Delta P\right)^2 + \left(\frac{\partial q}{\partial \lambda}\Delta\lambda\right)^2 + \left(\frac{\partial q}{\partial S}\Delta S\right)^2 \\ &= \frac{1}{(P\lambda)^2}\left(-\int S(\lambda)\lambda\, d\lambda\ \frac{\Delta P}{P}\right)^2 + \left(\left(S(\lambda)\lambda^2 - \int S(\lambda)\lambda\, d\lambda\right)\frac{\Delta\lambda}{\lambda}\right)^2 + \left(\int(\lambda\, d\lambda)\,\Delta S\right)^2\end{aligned} \qquad (A.11)$$

in which $\Delta S/S$ (0.10, according to the manufacturer), $\Delta\lambda$ (emission spectra resolution, 0.1 nm), and $\Delta P/P$ (0.05), respectively.

The absolute emission quantum yield values were measured at room temperature using an integrating sphere (ISP 150L-131, Instrument Systems). Figure A5 represents the integrating sphere experimental setup. The integrating sphere ($BaSO_4$ coating) has internal diameter of 150 mm and was coupled to an array spectrometer (MAS-40, Instrument Systems). The excitation

source consists of a CW NIR laser diode (PSU-H-LED, CNI Lasers) emitting at 980 nm coupled to customized optical fiber (SarSpec, 600×10^{-6} m core diameter with an adaptable-length ferrule) that guides the NIR radiation to the suspensions filling the quartz tube that was placed at the integrating sphere port entrance. Before the measurements, the setup's self-absorption correction was implemented using the ISP 150L-131 reference lamp. P_{abs} was directly measured with a power meter (FieldMaxII-TOP, Coherent) in the excitation wavelength, λ_{abs}. The integrating sphere detector quantifies S_{em} in the 370 to 808 nm wavelength range.

The emission spectral radiant flux, or spectral radiant power, ($S(\lambda)$, $W\cdot nm^{-1}$) of powders and suspensions were measured using an integrating sphere, as shown in Figure A6. All the spectra were acquired with a resolution of 0.1 nm, 200 ms integration time and 5 averaged spectra scans. The integrating sphere ($BaSO_4$ coating) has an internal diameter of 150 mm and was coupled to an array spectrometer (MAS-40, Instrument Systems). The measurements have an accuracy within 5%, according to the manufacturer.

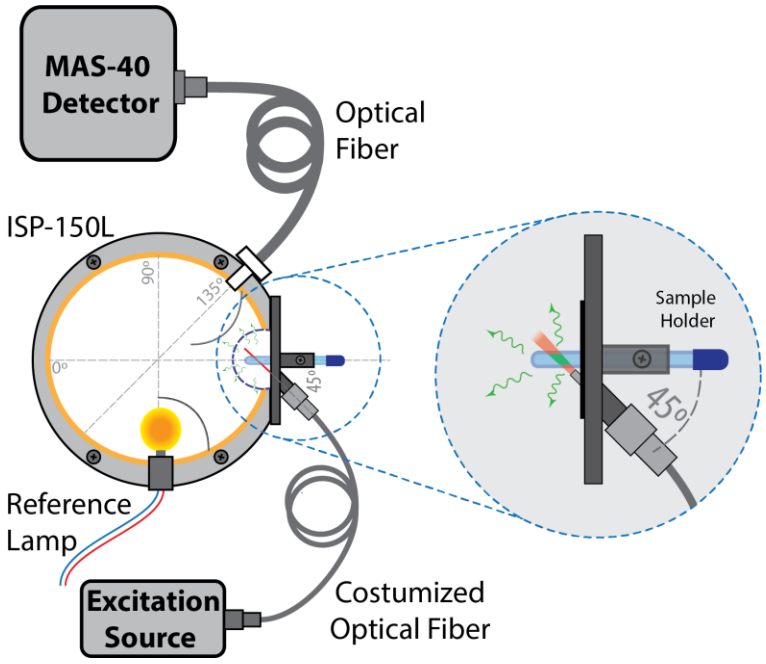

Figure A. 5 Scheme of the experimental setup used to measure the emission quantum yields. The sample holder is illuminated using a customized optical fiber that guides the excitation radiation. The emission is collected by the ISP-150L integrating sphere and then guided through an optical fiber to the CCD of the MAS-40 detector, that quantifies $S(\lambda)$.

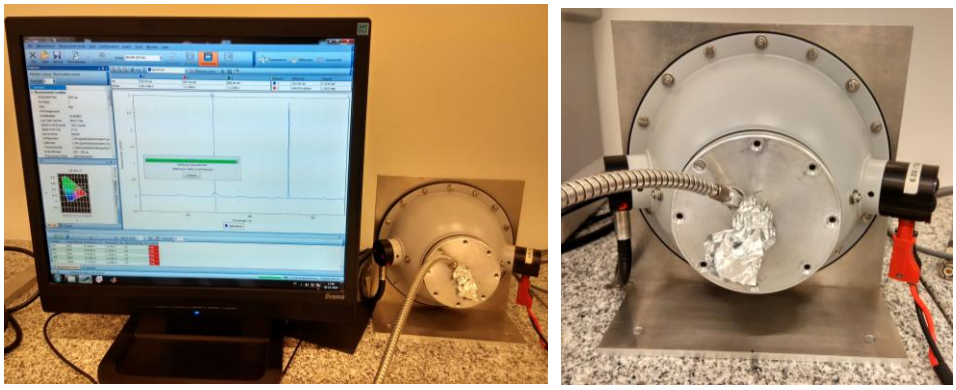

Figure A. 6 Quantum yield experimental setup established in PHANTOM group, Depatment of Physics, Aveiro.

Radiant flux and Luminous flux

Apart from quantum yields, the data obtained from the integrated sphere can be used to determine the radiant flux and luminous flux of the luminescent materials. The spectral radiant flux (or spectral radiant power) $S(\lambda)$, defined as the radiant flux R (W) per unit of wavelength (nm), was measured with an integrated sphere. The corresponding radiant flux values can be computed integrating $S(\lambda)$, according to:

$$R = \int_{\lambda_{min}}^{\lambda_{max}} S(\lambda)\, d\lambda \qquad (A.12)$$

The luminous flux L (lm) is calculated from the spectral radiant power and the tabulated relative photopic luminous function $V(\lambda)$,[251] at the maximum luminescence efficacy value (683 lm·W^{-1}):[252]

$$L \equiv 683 \cdot \int_{\lambda_{min}}^{\lambda_{max}} S(\lambda) V(\lambda)\, d\lambda \qquad (A.13)$$

A.5 UV-VIS-NIR Absorption spectroscopy

Absorption of UV-VIS or NIR light in atoms, molecules or compounds means the absorption of energy by excitation of electronic transitions. The measurement involves a comparison of the initial intensity of a beam of light and the intensity of the same beam after passing the sample, given by Lambert-Beer law:

$$A = \log_{10}\left(\frac{I_0}{I}\right) = \varepsilon l c \qquad (A.14)$$

where $I_0(\lambda)$ is the initial beam intensity and $I(\lambda)$ is the intensity of the output beam after passing the sample.

Absorption measurements in the UV, VIS and NIR regions for aqueous suspensions of powder samples were recorded at room temperature using a Lambda 950 UV-VIS-NIR spectrophotometer (PerkinElmer) with a 150 mm diameter Spectralon integrating sphere and a Jasco V-560 UV-VIS spectrophotometer. Quartz cells (10 mm optical path length) were used.

A.6 Fourier transform infrared spectroscopy

The absorption of infrared (IR) radiation by molecules leads to an excitation of vibrational (and rotational) modes. According to, the group frequency concept, functional groups can be considered as individual oscillators negligibly influenced by their surroundings. Thus, tables of specific frequencies can be used to characterize substances. In attenuated total reflection mode, a beam of infrared light passing a crystal in total reflection spreads partially in the adjacent medium similar to a tunneling process. This evanescent wave can be absorbed by the sample and an absorption spectrum can be detected.

The Fourier transform infrared (FTIR) spectra were acquired in conjunction with attenuated total reflection mode at room temperature using a BRUKER spectrometer. The spectra were collected over the 4,000–350 cm^{-1} range by averaging 256 scans at a spectral resolution of 4 cm^{-1}. FTIR spectra were obtained on a MATTSON 7000 FTIR spectrometer fitted with the Spectra-Tech diffuse reflectance (DRIFT) accessory. The compound was finely ground (about 2 mg) and placed on the diamond stage.

A.7 Zeta potential

The surface charges of the samples were measured using a Malvern Zetasizer Nano ZS instrument operating with a laser 50mW at 532nm. The zeta potential data were measured for sample suspensions with conductivities comprised in the range 0.02−0.08 mS/cm. The sample suspension was prepared by dissolving around 1 mg of sample in 1 mL of water. The sample was sonicated before the measurement to promote the complete dispersion on the solvent. The suspension was transferred to a capillary cuvette (DTS1070) that is placed inside the Zeta-Sizer. The equipment stabilized the temperature for one minute and begins the measuring of the zeta potential. The

reported value corresponds to three consecutive agreeing measurements, to ensure that the reported values characterize the samples in an accurate way.

In principle, the particle motion due to the applied electric field is measured by light scattering. The particles are illuminated with laser light and therefore the particles scatter light. The frequency of the scattered light is a function of particle velocity due to the Doppler shift. The measured magnitude of the frequency shift is then used to determine the particle velocity. From the known applied electric field and measured particle velocity, the particle mobility is readily determined. Zeta potential is then calculated from mobility by using Smoluchowski model and some other parameters such as liquid dielectric constant, refractive index, and viscosity of the solvent.

A.8 Hyperspectral imaging

Optical images were collected on an Olympus microscope (BX51, Japan) equipped with a hyperspectral imaging system (CytoViva Inc., Auburn, AL). The system integrates an optical imaging CCD camera (QImaging® Retiga 4000R), a VIS-NIR hyperspectral camera (Cytoviva®), a motorized stage, a halogen light source (Fiber-lite®, DC-950) and an optical fiber guided continuous wave 980 nm laser excitation source (CrystaLaser®, MDL-H-980, PSU-H-LED power control). The light scattered from the sample in the 400 to 1000 nm spectral region was captured by the hyperspectral camera at each line, for each pixel in the sample, combining motion of the microscope stage. A spectral classification algorithm (Spectral Angle Mapper, SAM) was employed to create a reference spectral library from bright-field hyperspectral data collected on powder samples upon 980 nm laser and white-light illuminations of the same spot. All the hyperspectral data were acquired and analyzed using ENVI 4.8 software.

A.9 Photothermal conversion efficiency

Photothermal conversion efficiency is produced by the photoexcitation of material, resulting in the production of thermal energy (heat). Determining efficiency of transducing resonant light to heat by suspended NPs is of a great interset for applications in photothermal therapy[236] and solar energy technologies[237]. PTCE usually estimated from the absorbance and the time dependent temperature measurements of the nanoparticle suspension.

The conversion efficiency, η, determined by:

$$\eta = \frac{Q_{ext} - Q_{ext,0}}{Q_{abs}} \quad (A.15)$$

where Q_{ext} denotes the external heating, computed using the convective heat dissipated to the surrounding media by convection:

$$Q_{ext} = hA(T_{\max} - T_{amb}) \quad (A.16)$$

where T_{max} is the maximum temperature reached by the sample and T_{amb} is the ambient temperature of the surroundings. hA is the inverse of the thermal resistance, given by $hA = \frac{\sum_i m_i c_{p,i}}{\tau}$, where m_i, and $c_{p,i}$ are the mass and the thermal capacity of the constituents of the suspension. τ is the characteristic convective decay time, deduced from $T = \exp(-t/\tau)$.

On the other hand, the absorbed power is quantified using the incident laser power (P) and the absorbance, A_λ, of the suspension in the presence of the suspension (assumed as constant, in the presence and in the absence of the nanoparticles in the suspension).

$$Q_{abs} = P(1-10^{-A_\lambda}) \quad (A.17)$$

Combining the previous relations results:

$$\eta = \frac{\sum_i m_i c_{p,i}(\Delta T/\tau) - m_w c_{p,w}(\Delta T_0/\tau_0)}{P(1-10^{-A_\lambda})} = \frac{(m_w c_{p,w} + m_{NP} c_{p,NP})(\Delta T/\tau) - m_w c_{p,w}(\Delta T_0/\tau_0)}{P(1-10^{-A_\lambda})} \quad (A.18)$$

where,

$$m_w = \left[V_{solution} - \frac{m_{NP}}{\rho_{NP}}\right]\rho_w \quad (A.19)$$

The external heating due to the presence of the nanoparticles corresponds to the difference between the values measured in the presence and in the absence of the nanoparticles in suspension denoted by the *0* subscript.

The experiment conditions to measure UV-VIS-NIR absorbance of the nanoparticles is detailed in Appendix A.5. The convective decay time τ is calculated from the time *vs*. temperature plot

obtained for solutions in the presence and in the absence of UCNPs placed in quartz cuvette. Aqueous solutions were irradiated with a CW 980 nm laser (solid state 3W Crystalaser) at 1.6 $W \cdot cm^{-2}$ for 5 minutes. Then the laser irradiation was turned off and the apparent temperature changes of the solutions in the cooling process were recorded for 780 s by a thermocouple thermometer immersed in the suspensions.

Appendix B

B.1Transmission electron microscopy

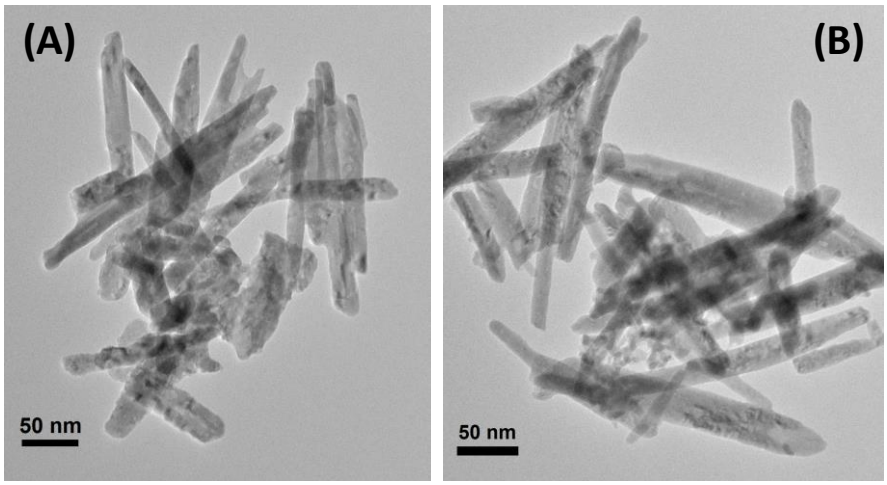

Figure B. 1 Transmission electron microscopy image of (A) $(Gd_{0.976}Nd_{0.024})_2O_3$ and (B) $(Gd_{0.951}Nd_{0.049})_2O_3$ nanorods.

Appendix C

C.1 Cell culture

Human osteoblast-like cell line MG-63, kindly provided by University of Porto, was cultured *in vitro* in minimal essential medium with α modification (MEM-α). Both culture media were supplemented with 10% (v/v) FBS, 100 Units mL^{-1} penicillin/100 $\mu g \cdot mL^{-1}$ streptomycin and 2.5 $\mu g \cdot mL^{-1}$ fungizone (all medium components from Life Technologies, Carlsbad, CA, USA) and cells were grown in at 310 K, 5% CO_2, in a humidified atmosphere. Cell confluence and morphology were daily observed under an inverted phase contrast microscope Nikon Eclipse TS100 (Japan). Cells were sub-cultured when confluence reached 80% using 0.25% trypsin/1 mM EDTA (Life Technologies, Carlsbad, CA, USA). For nanorod exposure, cells were left 24 hours for adhesion and then medium was replaced with fresh medium containing bare Gd_2O_3:Yb^{3+}/Er^{3+}

nanorods and NRs-AuNRs-850nm-1.17 in a concentration range from 0-500 μg·mL^{-1} and incubated for 24 hours.

C.2 Cell viability

Cell viability was determined by the colorimetric 3-(4,5-dimethyl-2-thiazolyl)-2,5-diphenyl tetrazolium bromide (MTT) assay, which measures the formation of purple formazan in viable cells (Twentyman and Luscombe, 1987). Briefly, cells were seeded in 96-well plates and after cell adhesion they were exposed to nanorods, as described above. At the end of each exposure time, 50 μL of MTT (Sigma-Aldrich, St. Louis, MO) solution (1 mg·mL^{-1} in PBS pH 7.2) were added and cells were incubated for 4 hours at 310 K, 5% CO_2, in darkness. Medium was then removed and 150 μL of dimethyl sulfoxide (DMSO) were added to each well for crystal solubilization. The optical density of reduced MTT was measured at 570 nm using a microplate reader Synergy™ HT Multi-Mode (BioTeK®, Winooski, VT, USA).

Appendix D

D.1 Fourier transform infrared spectroscopy and thermogravimetry

Figure D.1A shows the representative FTIR spectra measured for pure sodium citrate dihydrate and sodium citrate capped SrF_2:Yb^{3+}/Er^{3+} NPs. The observed main vibrational features are in accordance with the references [204, 211, 212]. From a comparison of the FTIR spectra, it is evident that the sodium citrate capped SrF_2 spectra is similar to that of pure sodium citrate dihydrate, which confirms the presence of citrate groups on the surface of the NPs. The broadband at 3000−3750 cm^{-1} is usually originated from stretching vibrations of the (–OH) groups and the sharp peaks in the region of 1700−1350 cm^{-1} come from antisymmetric and symmetric (COO^-) stretching vibrations corresponding to the sodium citrate, respectively. From the TGA profile of pure sodium citrate in Figure D.1B, there are three stages of weight loss [230]. The weight loss with about 12 wt% in the first stage around 443 K is attributed to the loss of the crystal water. The second stage, which starts at around 573 K, corresponds to the partially degradation of the sodium citrate. The last stage is from 673−773 K, owing to the decomposition of the residues. The sodium citrate capped SrF_2:Yb^{3+}/Er^{3+} nanoparticles shows, Figure D.1B an earlier initial and the faster weight loss, as compared to the pure sodium citrate.

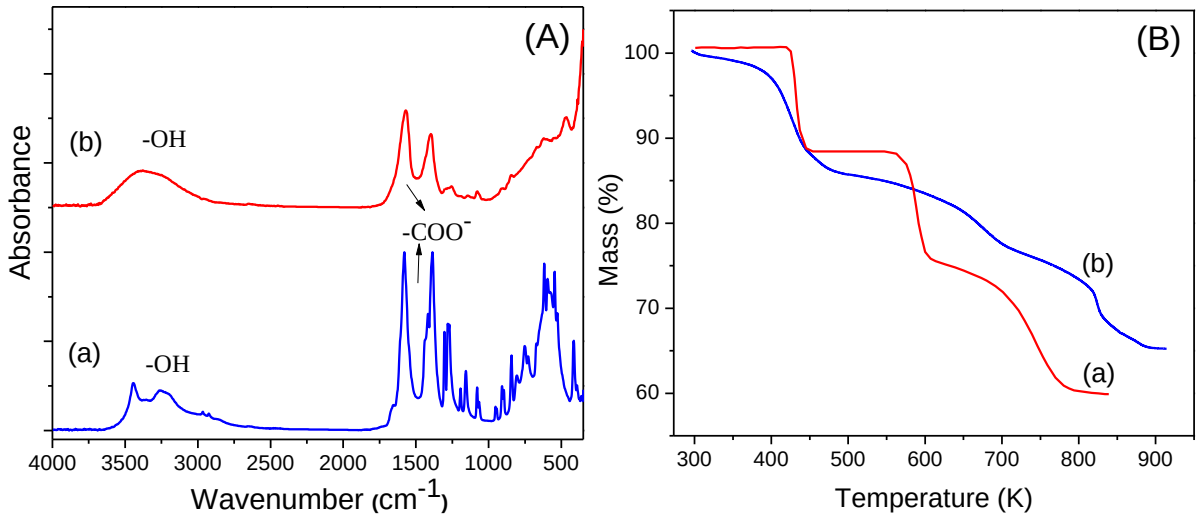

Figure D. 1 (A) FTIR absorption spectra and (B) Thermogravimetric analyses of (a) pure sodium citrate dihydrate and (b) sodium citrate capped SrF_2-2.

D.2 Dynamic light scattering

The surface zeta potential and hydrodynamic size distribution of SrF_2:Yb^{3+}/Er^{3+} nanoparticles for different sizes have been carried out by DLS measurements for water dispersions and are shown in Figure D.2. Water suspensions were prepared by dissolving 2.5 mg of nanoparticles in 1 mL of distilled water (volume fraction is 0.59%). The recorded zeta potentials in Figure D.2 A, for sodium citrate capped SrF_2-2, SrF_2-3 and SrF_2-4 nanoparticles exhibits around −16.9±7.8, −10.5±5.2 and −6.4±3.4 mV respectively, clearly indicating the negative charge present on the surface of the NPs as reported [204]. From the zeta potential analysis, it is also cleared that the nanosuspensions are very well stabilized. The results for the hydrodynamic sizes in Figure D.2B B are in with in the error with the TEM results. The average hydrodynamic sizes are 16±4 nm, 36±7 nm and 57±12 nm, for SrF_2-2, SrF_2-3, and SrF_2-4, respectively.

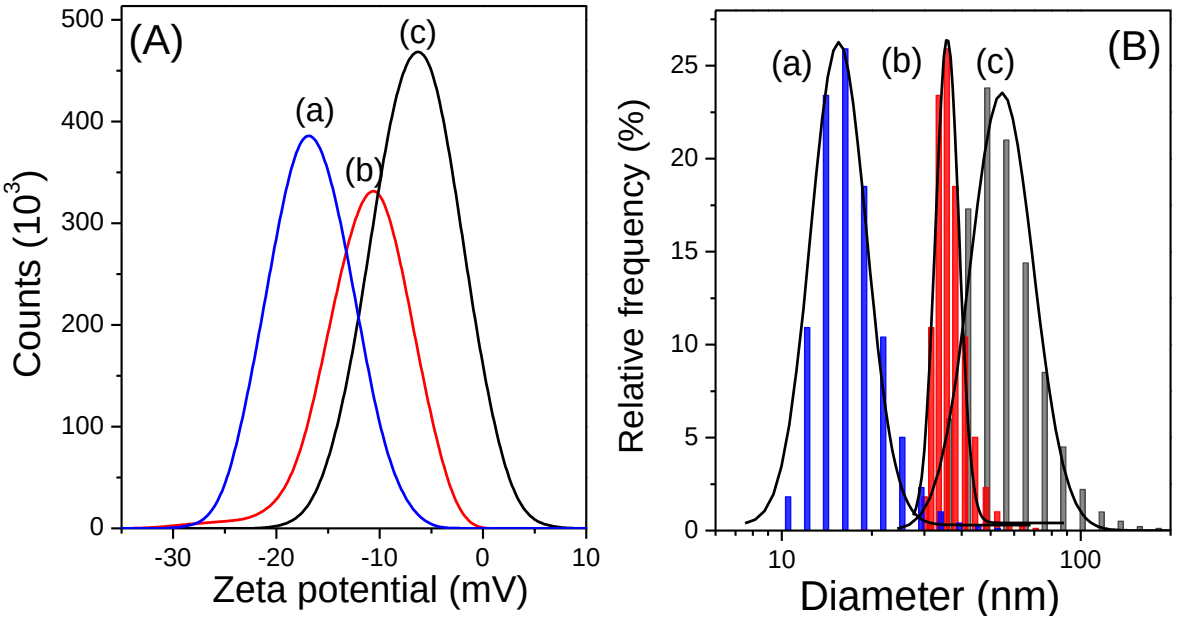

Figure D. 2 (A) Zeta potential and (B) hydrodynamic sizes of water dispersed sodium citrate capped (a) SrF_2-2, (b) SrF_2-3 and (c) SrF_2-4 nanoparticles, respectively. The solid lines in (B) are the best fit to experimental data using a log-normal distribution r^2>0.977.

D.3 UV-VIS-NIR absorption spectroscopy

Figure D.3 represents the Yb^{3+}/Er^{3+} doped SrF_2 absorbance spectrum measured in NIR region for samples in aqueous suspensions (7.6 $g{\cdot}L^{-1}$ of SrF_2-2 and 17.8 $g{\cdot}L^{-1}$ of SrF_2-4). The strongest absorbance band centred at 975 nm is the result of $^4F_{5/2}$ (Yb^{3+}) and $^4I_{11/2}$ (Er^{3+}) transitions[253].

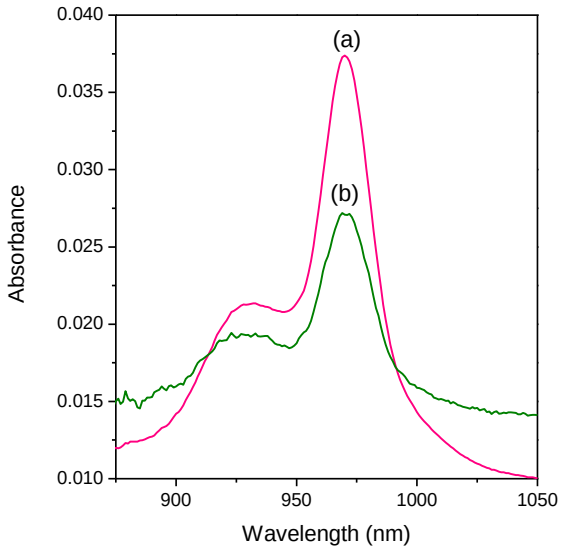

Figure D.3 Absorption spectra of (a) SrF_2-2 and (b) SrF_2-4 nanoparticles in NIR region.

Bibliography

[1] J.C.G. Bunzli, On the design of highly luminescent lanthanide complexes, *Coordination Chemistry Reviews*, 293 (2015) 19-47.
[2] S.V. Eliseeva, J.-C.G. Bünzli, Lanthanide luminescence for functional materials and bio-sciences, *Chem. Soc. Rev.*, 39 (2010) 189-227.
[3] E. Hemmer, N. Venkatachalam, H. Hyodo, A. Hattori, Y. Ebina, H. Kishimoto, K. Soga, Upconverting and NIR emitting rare earth based nanostructures for NIR-bioimaging, *Nanoscale*, 5 (2013) 11339-11361.
[4] A. Benayas, B. del Rosal, A. Perez-Delgado, K. Santacruz-Gomez, D. Jaque, G.A. Hirata, F. Vetrone, Nd:YAG Near-Infrared Luminescent Nanothermometers, *Adv. Opt. Mater.*, 3 (2015) 687-694.
[5] U. Rocha, C. Jacinto da Silva, W. Ferreira Silva, I. Guedes, A. Benayas, L. Martínez Maestro, M. Acosta Elias, E. Bovero, F.C.J.M. van Veggel, J.A. García Solé, D. Jaque, Subtissue Thermal Sensing Based on Neodymium-Doped LaF_3 Nanoparticles, *ACS Nano*, 7 (2013) 1188-1199.
[6] F. Wang, D. Banerjee, Y. Liu, X. Chen, X. Liu, Upconversion nanoparticles in biological labeling, imaging, and therapy, *Analyst*, 135 (2010) 1839-1854.
[7] M. Bettinelli, L.D. Carlos, X. Liu, Lanthanide-doped upconversion nanoparticles, *Phys. Today*, 68 (2015) 38-44.
[8] G.Y. Chen, H.L. Qju, P.N. Prasad, X.Y. Chen, Upconversion Nanoparticles: Design, Nanochemistry, and Applications in Theranostics, *Chem. Rev.*, 114 (2014) 5161-5214.
[9] T.J. Quinn, Academic Press INC., San Diego, CA, 1990.
[10] B. Fellmuth, J. Fischer, G. Machin, S. Picard, P.P.M. Steur, O. Tamura, D.R. White, H. Yoon, The kelvin redefinition and its mise en pratique, *Philosophical Transactions of the Royal Society a-Mathematical Physical and Engineering Sciences*, 374 (2016).
[11] R.P. Benedict, Fundamentals of Temperature, Pressure and Flow Measurements, John Wiley and Sons, New York, 1977.
[12] F. Reif, McGraw-Hill, Fundamentals of statistical and thermal physics, New York, 1965.
[13] Global Temperature Sensors Market By Application, in, Grand View Research, Inc., 2015, pp. 60.
[14] D.R. Thusu, Temperature Sensor Technology Transition and End-user Growth Trends, in, *Sensors online*, 2011.
[15] T. Sridhar, Developments in Thermometry from 1984 to 2011: A Review, *Recent Patents on Mechanical Engineering*, 5 (2012) 4-44.
[16] C.D.S. Brites, P.P. Lima, N.J.O. Silva, A. Millán, V.S. Amaral, F. Palacio, L.D. Carlos, Thermometry at the nanoscale, *Nanoscale*, 4 (2012) 4799-4829.
[17] J. Lee, N.A. Kotov, Thermometer design at the nanoscale, *Nano Today*, 2 (2007) 48-51.
[18] S.U. N. Inada, Methods and benefits of imaging the temperature distribution inside living cells, *Imaging Med.* , 5 (2013) 303–305.
[19] B. Hildebrandt, P. Wust, O. Ahlers, A. Dieing, G. Sreenivasa, T. Kerner, R. Felix, H. Riess, The cellular and molecular basis of hyperthermia, *Crit. Rev. Oncol. Hematol.* , 43 (2002) 33-56.
[20] C.X. Wang, H.H. Lin, Z.Z. Xu, Y.J. Huang, M.G. Humphrey, C. Zhang, Tunable Carbon-Dot-Based Dual-Emission Fluorescent Nanohybrids for Ratiometric Optical Thermometry in Living Cells, *ACS Appl. Mater. Interfaces*, 8 (2016) 6621-6628.
[21] S.S. Laha, A.R. Naik, E.R. Kuhn, M. Alvarez, A. Sujkowski, R.J. Wessells, B.P. Jena, Nanothermometry Measure of Muscle Efficiency, *Nano Lett.*, 17 (2017) 1262-1268.
[22] C.D.S. Brites, A. Millán, L.D. Carlos, in: J.-C. Bünzli, K. Pecharsky Vitalij (Eds.) *Handbook on the Physics and Chemistry of Rare Earths*, Elsevier, 2016, pp. 339-427.
[23] S. Allison, A. Hollerman, M. Cates, T. Bencic, J. Eldridge, C. Mercer, in: *39th AIAA/ASME/SAE/ASEE Joint Propulsion Conference and Exhibit*, American Institute of Aeronautics and Astronautics, 2003.

[24] M. Rodrigues, R. Piñol, G. Antorrena, C.D.S. Brites, N.J.O. Silva, J.L. Murillo, R. Cases, I. Díez, F. Palacio, N. Torras, J.A. Plaza, L. Perez-García, L.D. Carlos, A. Millan, Implementing thermometry on silicon surfaces functionalized by lanthanide-doped self-assembled polymer monolayers, *Adv. Funct. Mater.*, 26 (2016) 200-209.
[25] Ž. Antić, M.D. Dramićanin, K. Prashanthi, D. Jovanović, S. Kuzman, T. Thundat, Pulsed Laser Deposited Dysprosium‐Doped Gadolinium–Vanadate Thin Films for Noncontact, Self–Referencing Luminescence Thermometry, *Adv. Mater.*, 28 (2016) 7745-7752.
[26] T.J. Quinn, Elsevier Science, 2013.
[27] J. Fischer, S. Gerasimov, K.D. Hill, G. Machin, M.R. Moldover, L. Pitre, P. Steur, M. Stock, O. Tamura, H. Ugur, D.R. White, I. Yang, J. Zhang, Preparative Steps Towards the New Definition of the Kelvin in Terms of the Boltzmann Constant, *Int. J. Thermophys.*, 28 (2007) 1753-1765.
[28] D. Jaque, F. Vetrone, Luminescence nanothermometry, *Nanoscale*, 4 (2012) 4301-4326.
[29] X.D. Wang, O.S. Wolfbeis, R.J. Meier, Luminescent probes and sensors for temperature, *Chem. Soc. Rev.*, 42 (2013) 7834-7869.
[30] B. Henderson, G.F. Imbusch, Oxford University Press, New York, 2006
[31] J. Heine, K. Muller-Buschbaum, Engineering metal-based luminescence in coordination polymers and metal-organic frameworks, *Chem. Soc. Rev.*, 42 (2013) 9232-9242.
[32] J. Lee, A.O. Govorov, N.A. Kotov, Nanoparticle assemblies with molecular springs: a nanoscale thermometer, *Angewandte Chemie*, 44 (2005) 7439-7442.
[33] P. Löw, B. Kim, N. Takama, C. Bergaud, High-Spatial-Resolution Surface-Temperature Mapping Using Fluorescent Thermometry, *Small*, 4 (2008) 908-914.
[34] S. Allison, G. Gillies, A. Rondinone, M. Cates, Nanoscale thermometry via the fluorescence of YAG: Ce phosphor particles- Measurements from 7 to 77 C, *Nanotechnology*, 14 (2003) 859-863.
[35] S. Uchiyama, N. Kawai, A.P. de Silva, K. Iwai, Fluorescent polymeric and logic gate with temperature and pH as inputs, *J. Am. Chem. Soc.*, 126 (2004) 3032-3033.
[36] S. Uchiyama, Y. Matsumura, A.P. de Silva, K. Iwai, Fluorescent molecular thermometers based on polymers showing temperature-induced phase transitions and labeled with polarity-responsive benzofurazans, *Anal. Chem.*, 75 (2003) 5926-5935.
[37] M. Suzuki, V. Tseeb, K. Oyama, S. Ishiwata, Microscopic detection of thermogenesis in a single HeLa cell, *Biophys. J.*, 92 (2007) L46-L48.
[38] Y.J. Cui, F.L. Zhu, B.L. Chen, G.D. Qian, Metal-organic frameworks for luminescence thermometry, *Chem. Commun.*, 51 (2015) 7420-7431.
[39] S.A. Wade, S.F. Collins, G.W. Baxter, Fluorescence intensity ratio technique for optical fiber point temperature sensing, *J. Appl. Phys.*, 94 (2003) 4743.
[40] M.D. Shinn, W.A. Sibley, M.G. Drexhage, R.N. Brown, Optical Transitions of Er^{3+} Ions in Fluorozirconate Glass, *Phys. Rev. B*, 27 (1983) 6635-6648.
[41] O.A. Savchuk, J.J. Carvajal, M.C. Pujol, E.W. Barrera, J. Massons, M. Aguilo, F. Diaz, Ho,Yb:KLu$(WO_4)_2$ Nanoparticles: A Versatile Material for Multiple Thermal Sensing Purposes by Luminescent Thermometry, *J. Phys. Chem. C*, 119 (2015) 18546-18558.
[42] S. Zhou, G. Jiang, X. Li, S. Jiang, X. Wei, Y. Chen, M. Yin, C. Duan, Strategy for thermometry via Tm^{3+}doped $NaYF_4$ core-shell nanoparticles, *Opt. Lett.*, 39 (2014) 6687-6690.
[43] H.S. Peng, H.W. Song, B.J. Chen, J.W. Wang, S.Z. Lu, X.G. Kong, J.H. Zhang, Temperature dependence of luminescent spectra and dynamics in nanocrystalline Y_2O_3:Eu^{3+}, *J. Chem. Phys.*, 118 (2003) 3277-3282.
[44] X. Wang, J. Zheng, Y. Xuan, X. Yan, Optical temperature sensing of $NaYbF_4$: Tm^{3+}@SiO_2 core-shell micro-particles induced by infrared excitation, *Opt. Express*, 21 (2013) 21596-21606.
[45] J.R. Lakowicz, 3rd ed., Springer, New York, 2006.
[46] R. Zondervan, F. Kulzer, H. van der Meer, J. Disselhorst, M. Orrit, Laser-driven microsecond temperature cycles analyzed by fluorescence polarization microscopy, *Biophys. J.*, 90 (2006) 2958-2969.

[47] J.S. Donner, S.A. Thompson, M.P. Kreuzer, G. Baffou, R. Quidant, Mapping intracellular temperature using green fluorescent protein, *Nano Lett.*, 12 (2012) 2107-2111.
[48] H.C.Y. Yu, S.G. Leon-Saval, A. Argyros, G.W. Barton, Temperature effects on emission of quantum dots embedded in polymethylmethacrylate, *Appl. Opt.*, 49 (2010) 2749-2752.
[49] L.M. Maestro, C. Jacinto, U.R. Silva, F. Vetrone, J.A. Capobianco, D. Jaque, J.G. Solé, CdTe quantum dots as nanothermometers: towards highly sensitive thermal imaging, *Small*, 7 (2011) 1774-1778.
[50] S. Li, K. Zhang, J.-M. Yang, L. Lin, H. Yang, Single quantum dots as local temperature markers, *Nano Lett.*, 7 (2007) 3102-3105.
[51] J.-M. Yang, H. Yang, L. Lin, Quantum Dot Nano Thermometers Reveal Heterogeneous Local Thermogenesis in Living Cells, *ACS Nano*, 5 (2011) 5067-5071.
[52] B.D.B.a.J.M. Collins, Springer US, 2006.
[53] A.L. Heyes, On the design of phosphors for high-temperature thermometry, *J. Lumin.*, 129 (2009) 2004-2009.
[54] O.A. Savchuk, P. Haro-González, J.J. Carvajal, D. Jaque, J. Massons, M. Aguiló, F. Diaz, Er:Yb:NaY_2F_5O up-converting nanoparticles for sub-tissue fluorescence lifetime thermal sensing, *Nanoscale*, 6 (2014) 9727-9733.
[55] S.F. Collins, G.W. Baxter, S.A. Wade, T. Sun, K.T.V. Grattan, Z.Y. Zhang, A.W. Palmer, Comparison of fluorescence-based temperature sensor schemes: Theoretical analysis and experimental validation, *J. Appl. Phys.*, 84 (1998) 4649-4654.
[56] A.B. Marta Quintanilla, Rafik Naccache and Fiorenzo Vetrone, RSC Nanoscience & Nanotechnology, 2015.
[57] R. Alicki, D.M. Leitner, Size-Dependent Accuracy of Nanoscale Thermometers, *J. Phys. Chem. B*, 119 (2015) 9000-9005.
[58] D. Jaque Garcia, J. Garcia Sole, in: *Thermometry at the Nanoscale: Techniques and Selected Applications*, The Royal Society of Chemistry, 2016, pp. 83-123.
[59] P.F. Gu, Y. Zhang, Y. Feng, T.Q. Zhang, H.R. Chu, T. Cui, Y.D. Wang, J. Zhao, W.W. Yu, Real-time and on-chip surface temperature sensing of GaN LED chips using PbSe quantum dots, *Nanoscale*, 5 (2013) 10481-10486.
[60] B. Han, W.L. Hanson, K. Bensalah, A. Tuncel, J.M. Stern, J.A. Cadeddu, Development of Quantum Dot-Mediated Fluorescence Thermometry for Thermal Therapies, *Ann. Biomed. Eng.*, 37 (2009) 1230-1239.
[61] G.W. Walker, V.C. Sundar, C.M. Rudzinski, A.W. Wun, M.G. Bawendi, D.G. Nocera, Quantum-dot optical temperature probes, *Appl. Phys. Lett.*, 83 (2003) 3555-3557.
[62] L.M. Maestro, E.M. Rodriguez, F.S. Rodriguez, M.C. la Cruz, A. Juarranz, R. Naccache, F. Vetrone, D. Jaque, J.A. Capobianco, J.G. Sole, CdSe quantum dots for two-photon fluorescence thermal imaging, *Nano Lett.*, 10 (2010) 5109-5115.
[63] G. Vancoillie, Q. Zhang, R. Hoogenboom, in: *Thermometry at the Nanoscale: Techniques and Selected Applications*, The Royal Society of Chemistry, 2016, pp. 190-236.
[64] K. Okabe, N. Inada, C. Gota, Y. Harada, T. Funatsu, S. Uchiyama, Intracellular temperature mapping with a fluorescent polymeric thermometer and fluorescence lifetime imaging microscopy, *Nat. Commun.*, 3 (2012) 705.
[65] C. Gota, S. Uchiyama, T. Yoshihara, S. Tobita, T. Ohwada, Temperature-dependent fluorescence lifetime of a fluorescent polymeric thermometer, poly(N-isopropylacrylamide), labeled by polarity and hydrogen bonding sensitive 4-sulfamoyl-7-aminobenzofurazan, *J. Phys. Chem. B*, 112 (2008) 2829-2836.
[66] C. Gota, S. Uchiyama, T. Ohwada, Accurate fluorescent polymeric thermometers containing an ionic component, *Analyst*, 132 (2007) 121-126.
[67] L. Dykman, N. Khlebtsov, Gold nanoparticles in biomedical applications: recent advances and perspectives, *Chem. Soc. Rev.*, 41 (2012) 2256-2282.

[68] P.M. Tiwari, K. Vig, V.A. Dennis, S.R. Singh, Functionalized Gold Nanoparticles and Their Biomedical Applications, *Nanomaterials*, 1 (2011) 31-63.
[69] E. Hutter, J.H. Fendler, Exploitation of Localized Surface Plasmon Resonance, *Adv. Mater.*, 16 (2004) 1685-1706.
[70] L. Shang, F. Stockmar, N. Azadfar, G.U. Nienhaus, Intracellular Thermometry by Using Fluorescent Gold Nanoclusters, *Angew. Chem. Int. Ed.*, 52 (2013) 11154-11157.
[71] X. Chen, J.B. Essner, G.A. Baker, Exploring luminescence-based temperature sensing using protein-passivated gold nanoclusters, *Nanoscale*, 6 (2014) 9594-9598.
[72] M. Bruchhausen, F. Guillard, F. Lemoine, Instantaneous measurement of two-dimensional temperature distributions by means of two-color planar laser induced fluorescence (PLIF), *Exp. Fluids*, 38 (2005) 123-131.
[73] C. Paviolo, A.H. Clayton, S.L. McArthur, P.R. Stoddart, Temperature measurement in the microscopic regime: a comparison between fluorescence lifetime- and intensity-based methods, *Journal of microscopy*, 250 (2013) 179-188.
[74] J. Sakakibara, J.R. Adrian, Whole field measurement of temperature in water using two-color laser induced fluorescence, *Exp. Fluids*, 26 (1999) 7-15.
[75] X.L. Guan, X.Y. Liu, Z.X. Su, Preparation and photophysical behaviors of fluorescent chitosan bearing fluorescein: Potential biomaterial as temperature/pH probes, *J. Appl. Polym. Sci.*, 104 (2007) 3960-3966.
[76] F.H.C. Wong, C. Fradin, Simultaneous pH and Temperature Measurements Using Pyranine as a Molecular Probe, *J. Fluoresc.*, 21 (2011) 299-312.
[77] G. Yang, X. Liu, J. Feng, S. Li, Y. Li, in: *Thermometry at the Nanoscale: Techniques and Selected Applications*, The Royal Society of Chemistry, 2016, pp. 167-189.
[78] R.K.P. Benninger, Y. Koç, O. Hofmann, J. Requejo-Isidro, M.A.A. Neil, P.M.W. French, A.J. deMello, Quantitative 3D Mapping of Fluidic Temperatures within Microchannel Networks Using Fluorescence Lifetime Imaging, *Analytical Chemistry*, 78 (2006) 2272-2278.
[79] S. Bustin, 6th ed., 2015.
[80] P. Sengupta, P. Garrity, Sensing temperature, *Curr. Biol.*, 23 (2013) 304-307.
[81] G.L. Ke, C.M. Wang, Y. Ge, N.F. Zheng, Z. Zhu, C.J. Yang, L-DNA Molecular Beacon: A Safe, Stable, and Accurate Intracellular Nano-thermometer for Temperature Sensing in Living Cells, *J. Am. Chem. Soc.*, 134 (2012) 18908-18911.
[82] J.S. Donner, S.A. Thompson, C. Alonso-Ortega, J. Morales, L.G. Rico, S.I.C.O. Santos, R. Quidant, Imaging of Plasmonic Heating in a Living Organism, *ACS Nano*, 7 (2013) 8666-8672.
[83] E.G. Moore, A.P.S. Samuel, K.N. Raymond, From Antenna to Assay: Lessons Learned in Lanthanide Luminescence, *Accounts of Chemical Research*, 42 (2009) 542-552.
[84] N. Bloembergen, Solid State Infrared Quantum Counters, *Phys. Rev. Lett.*, 2 (1959) 84-85.
[85] F. Auzel, Compteur quantique par transfert d'energie de Yb^{3+} a Tm^{3+} dans un tungstate mixte et dans un verre germanate, *C.R. Acad. Sci. Paris*, 263 (1966) 819–821.
[86] F.P.P. Ovsyankin V. V., Mechanism of Summation of Electronic Excitations in Activated Crystals, *J. Exp. Theor. Phys.*, 3 (1966) 322-323.
[87] C.T. Dominguez, M.S. Vieira, R.M. Oliveira, M. Ueda, C.B. de Araujo, A.S.L. Gomes, Three-photon excitation of an upconversion random laser in ZnO-on-Si nanostructured films, *J. Opt. Soc. Am. B*, 31 (2014) 1975-1980.
[88] J. Wang, R. Deng, M.A. MacDonald, B. Chen, J. Yuan, F. Wang, D. Chi, T.S.A. Hor, P. Zhang, G. Liu, Y. Han, X. Liu, Enhancing multiphoton upconversion through energy clustering at sublattice level, *Nat. Mater.*, 13 (2014) 157-162.
[89] M. Pollnau, D.R. Gamelin, S.R. Luthi, H.U. Gudel, M.P. Hehlen, Power dependence of upconversion luminescence in lanthanide and transition-metal-ion systems, *Phys. Rev. B*, 61 (2000) 3337-3346.

[90] L. Prodi, E. Rampazzo, F. Rastrelli, A. Speghini, N. Zaccheroni, Imaging agents based on lanthanide doped nanoparticles, *Chemical Society Reviews*, 44 (2015) 4922-4952.
[91] M. Haase, H. Schaefer, Upconverting Nanoparticles, *Angew. Chem. Int. Ed.*, 50 (2011) 5808-5829.
[92] A. Nadort, J. Zhao, E.M. Goldys, Lanthanide upconversion luminescence at the nanoscale: fundamentals and optical properties, *Nanoscale*, 8 (2016) 13099-13130.
[93] H. Berthou, C.K. Jörgensen, Optical-fiber temperature sensor based on upconversion-excited fluorescence, *Opt. Lett.*, 15 (1990) 1100-1102.
[94] M.J. Weber, PROBABILITIES FOR RADIATIVE AND NONRADIATIVE DECAY OF ER3+ IN LAF3, *Physical Review*, 157 (1967) 262-&.
[95] F.N. Vetrone, R. de la Fuente, A. J. Sanz-Rodriguez, F. Blazquez-Castro, A. Rodriguez, E. M. Jaque, D. Solé, J. G. Capobianco, J. A., Intracellular imaging of HeLa cells by non-functionalized $NaYF_4$: Er^{3+}, Yb^{3+} upconverting nanoparticles, *Nanoscale*, 2 (2010) 495-498.
[96] S.K. Singh, K. Kumar, S.B. Rai, Er^{3+}/Yb^{3+} codoped Gd_2O_3 nano-phosphor for optical thermometry, *Sens. Actuator A-Phys.*, 149 (2009) 16-20.
[97] X. Zhu, W. Feng, J. Chang, Y.-W. Tan, J. Li, M. Chen, Y. Sun, F. Li, Temperature-feedback upconversion nanocomposite for accurate photothermal therapy at facile temperature, *Nat. Commun.*, 7 (2016).
[98] A. Sedlmeier, D.E. Achatz, L.H. Fischer, H.H. Gorris, O.S. Wolfbeis, Photon upconverting nanoparticles for luminescent sensing of temperature., *Nanoscale*, 4 (2012) 7090-7096.
[99] V. Lojpur, M. Nikolic, L. Mancic, O. Milosevic, M.D. Dramicanin, Y_2O_3:Yb,Tm and Y_2O_3:Yb,Ho powders for low-temperature thermometry based on up-conversion fluorescence, *Ceram. Int.*, 39 (2013) 1129-1134.
[100] N.N. Dong, M. Pedroni, F. Piccinelli, G. Conti, A. Sbarbati, J.E. Ramírez-Hernández, L.M. Maestro, M.C. Iglesias-de la Cruz, F. Sanz-Rodriguez, A. Juarranz, F. Chen, F. Vetrone, J.A. Capobianco, J.G. Solé, M. Bettinelli, D. Jaque, A. Speghini, NIR-to-NIR Two-Photon Excited CaF_2:Tm^{3+},Yb^{3+} Nanoparticles: Multifunctional Nanoprobes for Highly Penetrating Fluorescence Bio-Imaging, *ACS Nano*, 5 (2011) 8665-8671.
[101] S.H. Zheng, W.B. Chen, D.Z. Tan, J.J. Zhou, Q.B. Guo, W. Jiang, C. Xu, X.F. Liu, J.R. Qiu, Lanthanide-doped $NaGdF_4$ core-shell nanoparticles for non-contact self-referencing temperature sensors, *Nanoscale*, 6 (2014) 5675-5679.
[102] M. Xu, D. Chen, P. Huang, Z. Wan, Y. Zhou, Z. Ji, A dual-functional upconversion core@shell nanostructure for white-light-emission and temperature sensing, *J. Mater. Chem. C*, 4 (2016) 6516-6524.
[103] A. Pandey, V.K. Rai, Optical thermometry using FIR of two close lying levels of different ions in Y_2O_3:Ho^{3+}–Tm^{3+}–Yb^{3+} phosphor, *Appl. Phys. B*, 113 (2013) 221-225.
[104] D.L. Dexter, Possibility of Luminescent Quantum Yields Greater than Unity, *Phys. Rev.*, 108 (1957) 630-633.
[105] J.L. Sommerdijk, A. Bril, A.W. de Jager, Two photon luminescence with ultraviolet excitation of trivalent praseodymium, *J. Lumin.*, 8 (1974) 341-343.
[106] W.W. Piper, J.A. DeLuca, F.S. Ham, Cascade fluorescent decay in Pr^{3+}-doped fluorides: Achievement of a quantum yield greater than unity for emission of visible light, *J. Lumin.*, 8 (1974) 344-348.
[107] Z. Liang, F. Qin, Y.D. Zheng, Z.G. Zhang, W.W. Cao, Noncontact thermometry based on downconversion luminescence from Eu^{3+} doped $LiNbO_3$ single crystal, *Sens. Actuator A-Phys.*, 238 (2016) 215-219.
[108] Y.Y. Bu, S.J. Cheng, X.F. Wang, X.H. Yan, Optical thermometry based on luminescence behavior of Dy^{3+}-doped transparent LaF_3 glass ceramics, *Appl. Phys. A Mater. Sci. Process*, 121 (2015) 1171-1178.
[109] Z. Wang, P. Zhang, Q. Yuan, X. Xu, P. Lei, X. Liu, Y. Su, L. Dong, J. Feng, H. Zhang, Nd^{3+}-sensitized $NaLuF_4$ luminescent nanoparticles for multimodal imaging and temperature sensing under 808 nm excitation, *Nanoscale*, 7 (2015) 17861-17870.

[110] N. Ishiwada, S. Fujioka, T. Ueda, T. Yokomori, Co-doped Y_2O_3:Tb^{3+}/Tm^{3+} multicolor emitting phosphors for thermometry, *Opt. Lett.*, 36 (2011) 760-762.
[111] C.D. Brites, P.P. Lima, N.J. Silva, A. Millan, V.S. Amaral, F. Palacio, L.D. Carlos, A luminescent molecular thermometer for long-term absolute temperature measurements at the nanoscale, *Adv. Mater.*, 22 (2010) 4499-4504.
[112] C.D. Brites, P.P. Lima, N.J. Silva, A. Millan, V.S. Amaral, F. Palacio, L.D. Carlos, Ratiometric highly sensitive luminescent nanothermometers working in the room temperature range. Applications to heat propagation in nanofluids, *Nanoscale*, 5 (2013) 7572-7580.
[113] A. Cadiau, C.D.S. Brites, P.M.F.J. Costa, R.A.S. Ferreira, J. Rocha, L.D. Carlos, Ratiometric Nanothermometer Based on an Emissive Ln^{3+}-Organic Framework, *Acs Nano*, 7 (2013) 7213-7218.
[114] Z.P. Wang, D. Ananias, A. Carne-Sanchez, C.D.S. Brites, I. Imaz, D. Maspoch, J. Rocha, L.D. Carlos, Lanthanide-Organic Framework Nanothermometers Prepared by Spray-Drying, *Adv. Funct. Mat.*, 25 (2015) 2824-2830.
[115] L. Marciniak, A. Bednarkiewicz, M. Stefanski, R. Tomala, D. Hreniak, W. Strek, Near infrared absorbing near infrared emitting highly-sensitive luminescent nanothermometer based on Nd^{3+} to Yb^{3+} energy transfer, *PCCP*, 17 (2015) 24315-24321.
[116] R. Weissleder, A clearer vision for in-vivo imaging, *Nat. Biotechnol.*, 19 (2001) 316-317.
[117] A.M. Smith, M.C. Mancini, S. Nie, Second window for in-vivo imaging, *Nat.Nanotechnol.*, 4 (2009) 710-711.
[118] D. Jaque, C. Richard, B. Viana, K. Soga, X. Liu, J. García Solé, Inorganic nanoparticles for optical bioimaging, *Adv. Opt. Photon.*, 8 (2016) 1-103.
[119] B. del Rosal, E. Ximendes, U. Rocha, D. Jaque, *In Vivo* Luminescence Nanothermometry: from Materials to Applications, *Advanced Optical Materials*, 5 (2017).
[120] D. Wawrzynczyk, A. Bednarkiewicz, M. Nyk, W. Strek, M. Samoc, Neodymium(III) doped fluoride nanoparticles as non-contact optical temperature sensors, *Nanoscale*, 4 (2012) 6959-6961.
[121] X. Tian, X. Wei, Y. Chen, C. Duan, M. Yin, Temperature sensor based on ladder-level assisted thermal coupling and thermal-enhanced luminescence in $NaYF_4$:Nd^{3+}, *Opt. Express*, 22 (2014) 30333-30345.
[122] W. Xu, Q. Song, L. Zheng, Z. Zhang, W. Cao, Optical temperature sensing based on the near-infrared emissions from Nd^{3+}/Yb^{3+} codoped $CaWO_4$, *Opt. Lett.*, 39 (2014) 4635-4638.
[123] G.C. Jiang, X.T. Wei, S.S. Zhou, Y.H. Chen, C.K. Duan, M. Yin, Neodymium doped lanthanum oxysulfide as optical temperature sensors, *J. Lumin.*, 152 (2014) 156-159.
[124] E.N. Cerón, D.H. Ortgies, B. Del Rosal, F. Ren, A. Benayas, F. Vetrone, D. Ma, F. Sanz-Rodríguez, J.G. Solé, D. Jaque, E.M. Rodríguez, Hybrid nanostructures for high-sensitivity luminescence nanothermometry in the second biological window, *Adv. Mater.*, 27 (2015) 4781-4787.
[125] E.C. Ximendes, W.Q. Santos, U. Rocha, U.K. Kagola, F. Sanz-Rodriguez, N. Fernandez, A.d.S. Gouveia-Neto, D. Bravo, A.M. Domingo, B. del Rosal, C.D.S. Brites, L.D. Carlos, D. Jaque, C. Jacinto, Unveiling in Vivo Subcutaneous Thermal Dynamics by Infrared Luminescent Nanothermometers, *Nano Lett.*, 16 (2016) 1695-1703.
[126] L. Marciniak, K. Prorok, L. Frances-Soriano, J. Perez-Prieto, A. Bednarkiewicz, A broadening temperature sensitivity range with a core-shell YbEr@ YbNd double ratiometric optical nanothermometer, *Nanoscale*, 8 (2016) 5037-5042.
[127] E.V.G. E. Kolesnikova, M.A. Kurochkin, E. Lähderanta, M.D. Mikhailov, Nd^{3+}-doped YVO_4 nanoparticles for luminescence nanothermometry in the first and second biological windows, *Sens. Actuator B-Chem.*, 235 (2016).
[128] E.C. Ximendes, U. Rocha, K.U. Kumar, C. Jacinto, D. Jaque, LaF_3 core/shell nanoparticles for subcutaneous heating and thermal sensing in the second biological-window, *Appl. Phys. Lett.*, 108 (2016).
[129] W. Xu, H. Qi, L. Zheng, Z. Zhang, W. Cao, Multifunctional nanoparticles based on the Nd^{3+}/Yb^{3+} codoped $NaYF_4$, *Opt. Lett.*, 40 (2015) 5678-5681.

[130] L. Marciniak, K. Prorok, A. Bednarkiewicz, A. Kowalczyk, D. Hreniak, W. Strek, Water dispersible $LiNdP_4O_{12}$ nanocrystals: New multifunctional NIR-NIR luminescent materials for bio-applications, *J. Lumin.*, 176 (2016) 144-148.
[131] L. Marciniak, A. Bednarkiewicz, D. Kowalska, W. Strek, A new generation of highly sensitive luminescent thermometers operating in the optical window of biological tissues, *J. Mater. Chem. C*, 4 (2016) 5559-5563.
[132] L.D.C. Angel Millán, Carlos D. S. Brites, Nuno J. O. Silva, Rafael Piñol and Fernando Palacio in: F.P. Luís Dias Carlos (Ed.) *Thermometry at the Nanoscale : Techniques and Selected Applications*, RSC Nanoscience & Nanotechnology, 2015.
[133] C. Brites, P. Pereira, N. João, A. Millán, V. Amaral, F. Palacio, L.A.D. Carlos, Organic-Inorganic Eu^{3+}/Tb^{3+} codoped hybrid films for temperature mapping in integrated circuits, *Front. Chem.*, 1 (2013).
[134] C.D.S. Brites, P.P. Lima, N.J.O. Silva, A. Millan, V.S. Amaral, F. Palacio, L.D. Carlos, Thermometry at the nanoscale using lanthanide-containing organic-inorganic hybrid materials, *J. Lumin.*, 133 (2013) 230-232.
[135] C.D.S.B. Joao Rocha, and Luis D. Carlos, Lanthanide Organic Framework Luminescent Thermometers, *Chem. Eur. J.*, 2 (2016) 1-15.
[136] H.-C.J. Zhou, S. Kitagawa, Metal-Organic Frameworks (MOFs), *Chem. Soc. Rev.*, 43 (2014) 5415-5418.
[137] X. Rao, T. Song, J. Gao, Y. Cui, Y. Yang, C. Wu, B. Chen, G. Qian, A highly sensitive mixed lanthanide metal-organic framework self-calibrated luminescent thermometer, *J. Am. Chem. Soc.*, 135 (2013) 15559-15564.
[138] Y.J. Cui, Y.F. Yue, G.D. Qian, B.L. Chen, Luminescent Functional Metal-Organic Frameworks, *Chem. Rev.*, 112 (2012) 1126-1162.
[139] M.L. Debasu, D. Ananias, I. Pastoriza-Santos, L.M. Liz-Marzán, J. Rocha, L.D. Carlos, All-in-one optical heater-thermometer nanoplatform operative from 300 to 2000 k based on Er^{3+} emission and blackbody radiation, *Adv. Mater.*, 25 (2013) 4868-4874.
[140] J. Huang, B. He, Z. Cheng, L. Zhou, Upconverting PAAm/PNIPAM/$NaYF_4$:Yb:Er hydrogel with enhanced luminescence temperature sensitivity, *J. Lumin.*, 160 (2015) 254-257.
[141] R. Chen, V.D. Ta, F. Xiao, Q.Y. Zhang, H.D. Sun, Multicolor Hybrid Upconversion Nanoparticles and Their Improved Performance as Luminescence Temperature Sensors Due to Energy Transfer, *Small*, 9 (2013) 1052-1057.
[142] Q.B. Xiao, Y.F. Li, F.J. Li, M.X. Zhang, Z.J. Zhang, H.Z. Lin, Rational design of a thermalresponsive-polymer-switchable FRET system for enhancing the temperature sensitivity of upconversion nanophosphors, *Nanoscale*, 6 (2014) 10179-10186.
[143] J. Liu, L. Huang, X. Tian, X. Chen, Y. Shao, F. Xie, D. Chen, L. Li, Magnetic and fluorescent Gd_2O_3:Yb^{3+}/Ln^{3+} nanoparticles for simultaneous upconversion luminescence/MR dual modal imaging and NIR-induced photodynamic therapy, *Int. J. Nanomedicine*, 12 (2017) 1-14.
[144] Q. Li, J. Lin, J. Wu, Z. Lan, Y. Wang, F. Peng, M. Huang, Improving photovoltaic performance of dye-sensitized solar cell by downshift luminescence and p-doping effect of Gd_2O_3:Sm^{3+}, *J. Lumin.*, 134 (2013) 59-62.
[145] G.-y. Adachi, N. Imanaka, The Binary Rare Earth Oxides, *Chem. Rev.*, 98 (1998) 1479-1514.
[146] M. Zinkevich, Thermodynamics of rare earth sesquioxides, *Prog. Mater Sci.*, 52 (2007) 597-647.
[147] C.R. Stanek, K.J. McClellan, B.P. Uberuaga, K.E. Sickafus, M.R. Levy, R.W. Grimes, Determining the site preference of trivalent dopants in bixbyite sesquioxides by atomic-scale simulations, *Phys. Rev. B*, 75 (2007) 134101.
[148] M.L. Debasu, Lanthanide Oxide and Phosphate Nanoparticles for Thermometry and Bimodal Imaging, in: Departamento de Engenharia de Materiais e Cerâmica, Universidade de Aveiro, 2013, pp. 187.

[149] H. Suo, F. Hu, X. Zhao, Z. Zhang, T. Li, C. Duan, M. Yin, C. Guo, All-in-one thermometer-heater up-converting platform YF_3:Yb^{3+},Tm^{3+} operating in the first biological window, *J. Mater. Chem. C*, 5 (2017) 1501-1507.
[150] Q. Ju, X. Chen, F. Ai, D. Peng, X. Lin, W. Kong, P. Shi, G. Zhu, F. Wang, An upconversion nanoprobe operating in the first biological window, *J. Mater. Chem. B*, 3 (2015) 3548-3555.
[151] U. Rocha, K.U. Kumar, C. Jacinto, J. Ramiro, A.J. Caamano, J.G. Solé, D. Jaque, Nd^{3+} doped LaF_3 nanoparticles as self-monitored photo-thermal agents, *Appl. Phys. Lett.*, 104 (2014) 053703.
[152] M.L. Debasu, D. Ananias, A.G. Macedo, J. Rocha, L.D. Carlos, Emission-decay curves, energy-transfer and effective-refractive Index in Gd_2O_3:Eu^{3+} nanorods, *J. Phys. Chem. C*, 115 (2011) 15297-15303.
[153] G. Jiang, X. Wei, S. Zhou, Y. Chen, C. Duan, M. Yin, Neodymium doped lanthanum oxysulfide as optical temperature sensors, *J. Lumin.*, 152 (2014) 156-159.
[154] M.A.S. de Oliveira, C.B. de Araujo, Y. Messaddeq, Upconversion ultraviolet random lasing in Nd^{3+} doped fluoroindate glass powder, *Opt. Express*, 19 (2011) 5620-5626.
[155] W. Duan, Y. Zhang, Z. Wang, J. Jiang, C. Liang, W. Wei, Synthesis and near-infrared fluorescence of $K_5NdLi_2F_{10}$ nanocrystals and their dispersion with high doping concentration and long Lifetime, *Nanoscale*, 6 (2014) 5634-5638.
[156] J. Planelles-Aragó, E. Cordoncillo, R.A.S. Ferreira, L.D. Carlos, P. Escribano, Synthesis, characterization and optical studies on lanthanide-doped CdS quantum dots: new insights on CdS -> lanthanide energy transfer mechanisms, *J. Mater. Chem.*, 21 (2011) 1162-1170.
[157] A. Miguel, J. Azkargorta, R. Morea, I. Iparraguirre, J. Gonzalo, J. Fernandez, R. Balda, Spectral study of the stimulated emission of Nd^{3+} in fluorotellurite bulk glass, *Opt. Express*, 21 (2013) 9298-9307.
[158] N. Jaba, A. Kanoun, H. Mejri, H. Maaref, A. Brenier, Time-resolved luminescence data on the 1060 nm transition in Nd^{3+}-doped zinc tellurite glasses, *J. Phys.-Condens. Matter.*, 12 (2000) 7303-7309.
[159] A. Benayas, D. Jaque, J. Garcia Solé, N.I. Leonyuk, E. Bovero, E. Cavalli, M. Bettinelli, Effects of neodymium incorporation on the structural and luminescence properties of the $YAl_3(BO_3)_4$-$NdAl(BO_3)_4$ system, *J. Phys.-Condens. Matter.*, 19 (2007) 246204.
[160] L.D. Merkle, M. Dubinskii, K.L. Schepler, S.M. Hegde, Concentration quenching in fine-grained ceramic Nd:YAG, *Opt. Express*, 14 (2006) 3893-3905.
[161] W.T. Carnall, H. Crosswhite, H.M. Crosswhite, Energy level structure and transition probabilities in the spectra of the trivalent lanthanides in LaF_3, in, 1978, pp. Medium: ED; Size: Pages: 185.
[162] J.F. Wyart, A. Meftah, A. Bachelier, J. Sinzelle, W.U.L. Tchang-Brillet, N. Champion, N. Spector, J. Sugar, Energy levels of $4f^3$ in the Nd^{3+} free ion from emission spectra, *J. Phys. B-At. Mol. Opt. Phys*, 39 (2006) L77-L82.
[163] R. Alicki, D.M. Leitner, Size-Dependent Accuracy of Nanoscale Thermometers, *J. Phys. Chem. B*, (2015) DOI: 10.1021/jp508047q.
[164] J.A. Haglund, O. Hunter, Elastic Properties of Polycrystalline Monoclinic Gd_2O_3, *J. Am. Ceram. Soc.*, 56 (1973) 327-330.
[165] A.N. Bashkatov, E.A. Genina, V.I. Kochubey, V.V. Tuchin, Optical properties of human skin, subcutaneous and mucous tissues in the wavelength range from 400 to 2000 nm, *J. Phys. D: Appl. Phys.*, 38 (2005) 2543-2555.
[166] C.-H. Quek, K.W. Leong, Near-infrared fluorescent nanoprobes for in-vivo optical imaging, *Nanomaterials*, 2 (2012) 92-112.
[167] S. Gai, P. Yang, D. Wang, C. Li, N. Niu, F. He, X. Li, Monodisperse Gd_2O_3:Ln (Ln=Eu^{3+}, Tb^{3+}, Dy^{3+}, Sm^{3+}, Yb^{3+}/Er^{3+}, Yb^{3+}/Tm^{3+}, and Yb^{3+}/Ho^{3+}) nanocrystals with tunable size and multicolor luminescent properties, *Crystengcomm*, 13 (2011) 5480-5487.
[168] S. Balabhadra, M.L. Debasu, C.D.S. Brites, L.A.O. Nunes, O.L. Malta, J. Rocha, M. Bettinelli, L.D. Carlos, Boosting the sensitivity of Nd^{3+}-based luminescent nanothermometers, *Nanoscale*, 7 (2015) 17261-17267.

[169] H.P. Christensen, D.R. Gabbe, H.P. Jenssen, Fluoresecnce lifetimes for neodymium-doped Yttrium aluminium garnet and Yttrium-oxide powders, *Phys. Rev. B*, 25 (1982) 1467-1473.
[170] D. Wawrzynczyk, M. Nyk, A. Bednarkiewicz, W. Strek, M. Samoc, Morphology- and size-dependent spectroscopic properties of Eu^{3+}-doped Gd_2O_3 colloidal nanocrystals, *J. Nanopart. Res.*, 16 (2014) 1-13.
[171] G. Blasse, B.C. Grabmaier, Springer-Verlag, Berlin, 1994.
[172] Y. Li, G. Hong, Synthesis and luminescence properties of nanocrystalline Gd_2O_3:Eu^{3+} by combustion process, *J. Lumin.*, 124 (2007) 297-301.
[173] J. She, C. Hou, H. Guol, C. Gao, X. Cui, M. Lu, W. Wei, B. Peng, Effects of the host morphologies on luminescence properties of Nd^{3+}-doped LaF_3 nanoparticles, *J. Nanosci. Nanotech.*, 11 (2011) 8609-8612.
[174] M.M.D. Mann, L. G., Energy levels and spectral broadening of Neodymium ions in laser glass, *J. Appl. Phys.*, 41 (1970) 2951-&.
[175] X. Huang, I.H. El-Sayed, W. Qian, M.A. El-Sayed, Cancer Cell Imaging and Photothermal Therapy in the Near-Infrared Region by Using Gold Nanorods, *J. Am. Chem. Soc.*, 128 (2006) 2115-2120.
[176] Z. Zhang, J. Wang, X. Nie, T. Wen, Y. Ji, X. Wu, Y. Zhao, C. Chen, Near infrared laser-induced targeted cancer therapy using thermoresponsive polymer encapsulated gold nanorods, *J. Am. Chem. Soc.*, 136 (2014) 7317-7326.
[177] M. Virk, K. Xiong, M. Svedendahl, M. Käll, A.B. Dahlin, A Thermal Plasmonic Sensor Platform: Resistive Heating of Nanohole Arrays, *Nano Lett.*, 14 (2014) 3544-3549.
[178] C. Fang, L. Shao, Y. Zhao, J. Wang, H. Wu, A Gold Nanocrystal/Poly(dimethylsiloxane) Composite for Plasmonic Heating on Microfluidic Chips, *Adv. Mater.*, 24 (2012) 94-98.
[179] A.O. Govorov, H.H. Richardson, Generating heat with metal nanoparticles, *Nano Today*, 2 (2007) 30-38.
[180] J. Dong, J.I. Zink, Taking the temperature of the interiors of magnetically heated nanoparticles, *ACS Nano*, 8 (2014) 5199-5207.
[181] R. Piñol, C.D.S. Brites, R. Bustamante, A. Martínez, N.J.O. Silva, J.L. Murillo, R. Cases, J. Carrey, C. Estepa, C. Sosa, F. Palacio, L.D. Carlos, A. Millán, Joining Time-Resolved Thermometry and Magnetic-Induced Heating in a Single Nanoparticle Unveils Intriguing Thermal Properties, *ACS Nano*, 9 (2015) 3134-3142.
[182] M.T. Carlson, A. Khan, H.H. Richardson, Local temperature determination of optically excited nanoparticles and nanodots, *Nano Lett.*, 11 (2011) 1061-1069.
[183] S. Rohani, M. Quintanilla, S. Tuccio, F. De Angelis, E. Cantelar, A.O. Govorov, L. Razzari, F. Vetrone, Enhanced Luminescence, Collective Heating, and Nanothermometry in an Ensemble System Composed of Lanthanide-Doped Upconverting Nanoparticles and Gold Nanorods, *Adv. Opt. Mater.*, (2015) *in press*.
[184] E. Carrasco, B. del Rosal, F. Sanz-Rodríguez, Á.J. de la Fuente, P.H. Gonzalez, U. Rocha, K.U. Kumar, C. Jacinto, J.G. Solé, D. Jaque, Intratumoral Thermal Reading During Photo-Thermal Therapy by Multifunctional Fluorescent Nanoparticles, *Adv. Funct. Mat.*, 25 (2015) 615-626.
[185] L. Shi, C. Dames, J.R. Lukes, P. Reddy, J. Duda, D.G. Cahill, J. Lee, A. Marconnet, K.E. Goodson, J.-H. Bahk, A. Shakouri, R.S. Prasher, J. Felts, W.P. King, B. Han, J.C. Bischof, Evaluating Broader Impacts of Nanoscale Thermal Transport Research, *Nanosc. Microsc. Therm.*, 19 (2015) 127-165.
[186] Z. Qin, J.C. Bischof, Thermophysical and biological responses of gold nanoparticle laser heating, *Chem. Soc. Rev.*, 41 (2012) 1191-1217.
[187] Y. Huang, F. Rosei, F. Vetrone, A single multifunctional nanoplatform based on upconversion luminescence and gold nanorods, *Nanoscale*, 7 (2015) 5178-5185.
[188] Y. Song, G. Liu, X. Dong, J. Wang, W. Yu, J. Li, Au Nanorods@$NaGdF_4$/Yb^{3+},Er^{3+} Multifunctional Hybrid Nanocomposites with Upconversion Luminescence, Magnetism, and Photothermal Property, *J. Phys. Chem. C*, 119 (2015) 18527-18536.

[189] C.-W. Chen, P.-H. Lee, Y.-C. Chan, M. Hsiao, C.-H. Chen, P.C. Wu, P.R. Wu, D.P. Tsai, D. Tu, X. Chen, Plasmon-induced hyperthermia: hybrid upconversion $NaYF_4$:Yb/Er and gold nanomaterials for oral cancer photothermal therapy, *J. Mater. Chem. B*, 3 (2015) 8293-8302.
[190] X. Wang, X.G. Kong, Y. Yu, Y.J. Sun, H. Zhang, Effect of annealing on upconversion luminescence of ZnO:Er^{3+} nanocrystals and high thermal sensitivity, *J. Phys. Chem. C*, 111 (2007) 15119-15124.
[191] L.M. Maestro, P. Haro-González, A. Sánchez-Iglesias, L.M. Liz-Marzán, J. García Solé, D. Jaque, Quantum Dot Thermometry Evaluation of Geometry Dependent Heating Efficiency in Gold Nanoparticles, *Langmuir*, 30 (2014) 1650-1658.
[192] A.L. Feng, M.L. You, L. Tian, S. Singamaneni, M. Liu, Z. Duan, T.J. Lu, F. Xu, M. Lin, Distance-Dependent Plasmon-Enhanced Fluorescence of Upconversion Nanoparticles using Polyelectrolyte Multilayers as Tunable Spacers, *Sci. Rep.*, 5 (2015) 7779.
[193] M. Eichelbaum, K. Rademann, Plasmonic Enhancement or Energy Transfer? On the Luminescence of Gold-, Silver-, and Lanthanide-Doped Silicate Glasses and Its Potential for Light-Emitting Devices, *Adv. Funct. Mat.*, 19 (2009) 2045-2052.
[194] K. Zheng, D. Zhang, D. Zhao, N. Liu, F. Shi, W. Qin, Bright white upconversion emission from Yb^{3+}, Er^{3+}, and Tm^{3+}-codoped Gd_2O_3 nanotubes, *PCCP*, 12 (2010) 7620-7625.
[195] Y. Yang, Q. Shao, R. Deng, C. Wang, X. Teng, K. Cheng, Z. Cheng, L. Huang, Z. Liu, X. Liu, B. Xing, In vitro and in vivo uncaging and bioluminescence imaging by using photocaged upconversion nanoparticles, *Angew. Chem. Int. Ed.*, 51 (2012) 3125-3129.
[196] S.D. Conner, S.L. Schmid, Regulated portals of entry into the cell, *Nature*, 422 (2003) 37-44.
[197] R.J. McNichols, A. Gowda, M. Kangasniemi, J.A. Bankson, R.E. Price, J.D. Hazle, MR thermometry-based feedback control of laser interstitial thermal therapy at 980 nm, *Lasers Surg. Med.*, 34 (2004) 48-55.
[198] B.M. van der Ende, L. Aarts, A. Meijerink, Near-Infrared Quantum Cutting for Photovoltaics, *Adv. Mater.*, 21 (2009) 3073-3077.
[199] R. Shendrik, E.A. Radzhabov, A.I. Nepomnyashchikh, Scintillation properties of pure and Ce^{3+}-doped SrF_2 crystals, *Radiat. Meas.*, 56 (2013) 58-61.
[200] I. Villa, A. Vedda, I.X. Cantarelli, M. Pedroni, F. Piccinelli, M. Bettinelli, A. Speghini, M. Quintanilla, F. Vetrone, U. Rocha, C. Jacinto, E. Carrasco, F.S. Rodríguez, Á. Juarranz, B. del Rosal, D.H. Ortgies, P.H. González, J.G. Solé, D.J. García, 1.3 μm emitting SrF_2:Nd^{3+} nanoparticles for high contrast in vivo imaging in the second biological window, *Nano Research*, 8 (2015) 649-665.
[201] D.V. Pominova, A.V. Ryabova, K.G. Linkov, I.D. Romanishkin, S.V. Kuznetsov, J.A. Rozhnova, V.I. Konov, V.B. Loschenov, Pulsed periodic laser excitation of upconversion luminescence for deep biotissue visualization, *Laser Physics*, 26 (2016) 084001.
[202] P. Rodríguez-Sevilla, H. Rodríguez-Rodríguez, M. Pedroni, A. Speghini, M. Bettinelli, J.G. Solé, D. Jaque, P. Haro-González, Assessing Single Upconverting Nanoparticle Luminescence by Optical Tweezers, *Nano Lett.*, 15 (2015) 5068-5074.
[203] H. Rodríguez-Rodríguez, P.R. Sevilla, E.M. Rodríguez, D.H. Ortgies, M. Pedroni, A. Speghini, M. Bettinelli, D. Jaque, P. Haro-González, Enhancing optical forces on fluorescent up-converting nanoparticles by surface charge tailoring, *Small*, 11 (2015) 1555-1561.
[204] F.P. M. Pedroni, T. Passuello, S. Polizzi, J. Ueda, P. Haro-González, L. Martinez Maestro, D. Jaque, J. García-Solé, M. Bettinelli, and A. Speghini, Water (H_2O and D_2O) Dispersible NIR-to-NIR Upconverting Yb^{3+}/Tm^{3+} Doped MF_2 (M=Ca, Sr) Colloids: Influence of the Host Crystal, *Cryst. Growth Des.*, 13 (2013) 4906-4913.
[205] D. Pugh-Thomas, B.M. Walsh, M.C. Gupta, CdSe(ZnS) nanocomposite luminescent high temperature sensor, *Nanotechnology*, 22 (2011) 185503.
[206] A.M.P. Botas, C.D.S. Brites, J. Wu, U. Kortshagen, R.N. Pereira, L.D. Carlos, R.A.S. Ferreira, A New Generation of Primary Luminescent Thermometers Operating in Different Media Based on Silicon Nanoparticles, *Part. Part. Syst. Charact.*, 33 (2016) 740–748.

[207] A.S. Souza, L.A.O. Nunes, I.G.N. Silva, F.A.M. Oliveira, L.L. da Luz, H.F. Brito, M.C.F.C. Felinto, R.A.S. Ferreira, S.A. Júnior, L.D. Carlos, O.L. Malta, Highly-sensitive Eu^{3+} ratiometric thermometers based on excited state absorption with predictable calibration, *Nanoscale*, 8 (2016) 5327-5333.
[208] F.B. Vetrone, J. C. Capobianco, J. A. Speghini, A. Bettinelli, M., Significance of Yb^{3+} concentration on the upconversion mechanisms in codoped Y_2O_3: Er^{3+}, Yb^{3+} nanocrystals, *J. Appl. Phys.*, 96 (2004) 661-667.
[209] D. Gao, X. Zhang, H. Zheng, W. Gao, E. He, Yb^{3+}/Er^{3+} codoped beta-$NaYF_4$ microrods: Synthesis and tuning of multicolor upconversion, *J. Alloys Compd.*, 554 (2013) 395-399.
[210] J. Sun, J. Xian, H. Du, Facile synthesis of well-dispersed SrF_2:Yb^{3+}/Er^{3+} upconversion nanocrystals in oleate complex systems, *Appl. Surf. Sci.*, 257 (2011) 3592-3595.
[211] J. Sun, J. Xian, X. Zhang, H. Du, Hydrothermal synthesis of SrF_2:Yb^{3+}/Er^{3+} micro-/nanocrystals with multiform morphologies and upconversion properties, *J. Rare Earths*, 29 (2011) 32-38.
[212] Z.H. Cuimiao Zhang, Ruitao Chai, Ziyong Cheng, Zhenhe Xu, Chunxia Li,, a.J.L. Ling Huang, Mesoporous SrF_2 and SrF_2:Ln^{3+} (Ln=Ce, Tb, Yb, Er) Hierarchical Microspheres: Hydrothermal Synthesis, Growing Mechanism, and Luminescent Properties, *J. Phys. Chem. C*, 114 (2010) 6928–6936.
[213] R.D. SHANNON, Revised Effective Ionic Radii and Systematic Studies of Interatomie Distances in Halides and Chaleogenides *Acta Cryst.* , 32A (1976) 751-767.
[214] E. Jansen, W. Schafer, G. Will, R-values in analysis of powder diffraction data using Rietveld refinement *J. Appl. Crystallogr.*, 27 (1994) 492-496.
[215] L.B. McCusker, R.B. Von Dreele, D.E. Cox, D. Louer, P. Scardi, Rietveld refinement guidelines, *J. Appl. Crystallogr.*, 32 (1999) 36-50.
[216] R.A. Young, R.A. Young, Oxford University Press, 1995.
[217] M. Swirkowicz, M. Skorczakowski, J. Jabczynski, A. Bajor, E. Tymicki, B. Kaczmarek, T. Lukasiewicz, Investigation of structural, optical and lasing properties of YAG:Yb single crystals, *Opto-Electron. Rev.*, 13 (2005) 213-220.
[218] Y. Itoh, K. Katoh, K. Hirabayashi, K. Murase, The relation between lattice-parameter and particle-size in ZnS-Cu phosphor *Appl. Phys. A Mater. Sci. Process*, 26 (1981) 227-230.
[219] M.Y.A. Yagoub, H.C. Swart, L.L. Noto, P. Bergman, E. Coetsee, Surface Characterization and Photoluminescence Properties of Ce^{3+}, Eu Co-Doped SrF_2 Nanophosphor, *Materials*, 8 (2015) 2361-2375.
[220] J.C. Boyer, F.C.J.M. van Veggel, Absolute quantum yield measurements of colloidal $NaYF_4$: Er^{3+}, Yb^{3+} upconverting nanoparticles, *Nanoscale*, 2 (2010) 1417-1419.
[221] R.H. Page, K.I. Schaffers, P.A. Waide, J.B. Tassano, S.A. Payne, W.F. Krupke, W.K. Bischel, Upconversion-pumped luminescence efficiency of rare-earth-doped hosts sensitized with trivalent ytterbium, *J. Opt. Soc. Am. B*, 15 (1998) 996-1008.
[222] J.F. Suyver, A. Aebischer, S. García-Revilla, P. Gerner, H.U. Güdel, Anomalous power dependence of sensitized upconversion luminescence, *Phys. Rev. B*, 71 (2005) 125123.
[223] L. Marciniak, K. Waszniewska, A. Bednarkiewicz, D. Hreniak, W. Strek, Sensitivity of a Nanocrystalline Luminescent Thermometer in High and Low Excitation Density Regimes, *J. Phys. Chem. C*, 120 (2016) 8877-8882.
[224] W. Zheng, P. Huang, D.T. Tu, E. Ma, H.M. Zhu, X.Y. Chen, Lanthanide-doped upconversion nano-bioprobes: electronic structures, optical properties, and biodetection, *Chem. Soc. Rev.*, 44 (2015) 1379-1415.
[225] F. Auzel, Upconversion and anti-stokes processes with f and d ions in solids, *Chem. Rev.*, 104 (2004) 139-173.
[226] B. Di Bartolo, X. Chen, I.S.o. Atomic, M. Spectroscopy, World Scientific, 2001.
[227] Y.M. Yang, C. Mi, F.Y. Jiao, X.Y. Su, X.D. Li, L.L. Liu, J. Zhang, F. Yu, Y.Z. Liu, Y.H. Mai, A novel multifunctional upconversion phosphor: Yb^{3+}/Er^{3+} codoped La_2S_3, *J. Am. Ceram. Soc.*, 97 (2014) 1769-1775.

[228] K.W. Kramer, D. Biner, G. Frei, H.U. Gudel, M.P. Hehlen, S.R. Luthi, Hexagonal sodium yttrium fluoride based green and blue emitting upconversion phosphors, *Chem. Mater.*, 16 (2004) 1244-1251.
[229] S. Balabhadra, M.L. Debasu, C.D.S. Brites, R.A.S. Ferreira, L.D. Carlos, A cost-effective quantum yield measurement setup for upconverting nanoparticles, *J. Lumin.*, 189 (2017) 64–70.
[230] Z. Bai, L. Yang, J. Zhang, L. Li, C. Hu, J. Lv, Y. Guo, High-efficiency carbon-supported platinum catalysts stabilized with sodium citrate for methanol oxidation, *J. Power Sources*, 195 (2010) 2653-2658.
[231] J.W. Wang, P.A. Tanner, Upconversion for white light generation by a single compound, *J. Am. Chem. Soc.*, 132 (2010) 947-949.
[232] W. Strek, R. Tomala, M. Lukaszewicz, B. Cichy, Y. Gerasymchuk, P. Gluchowski, L. Marciniak, A. Bednarkiewicz, D. Hreniak, Laser induced white lighting of graphene foam, *Sci. Rep.*, 7 (2017) 41281.
[233] Y.A. Rozhnova, S.V. Kuznetsov, A.A. Luginina, V.V. Voronov, A.V. Ryabova, D.V. Pominova, R.P. Ermakov, V.A. Usachev, N.E. Kononenko, A.E. Baranchikov, V.K. Ivanov, P.P. Fedorov, New $Sr_{1-x-z}Rx(NH_4)_{(z)}F_{2+x-z}$ (R = Yb, Er) solid solution as precursor for high efficiency up-conversion luminophor and optical ceramics on the base of strontium fluoride, *Mater. Chem. Phys.*, 172 (2016) 150-157.
[234] G.M. Hale, M.R. Querry, Optical constants of water in the 200-nm to 200-μm wavelength region, *Appl. Opt.*, 12 (1973) 555-563.
[235] O.A. Savchuk, J.J. Carvajal, J. Massons, M. Aguilo, F. Diaz, Determination of photothermal conversion efficiency of graphene and graphene oxide through an integrating sphere method, *Carbon*, 103 (2016) 134-141.
[236] Y.D. Xing, L.Y. Li, X.C. Ai, L.M. Fu, Polyaniline-coated upconversion nanoparticles with upconverting luminescent and photothermal conversion properties for photothermal cancer therapy, *International Journal of Nanomedicine*, 11 (2016) 4327-4338.
[237] H.C. Jin, G.P. Lin, L.Z. Bai, M. Amjad, E.P. Bandarra, D.S. Wen, Photothermal conversion efficiency of nanofluids: An experimental and numerical study, *Solar Energy*, 139 (2016) 278-289.
[238] H. Zakaria, W.S. Abdelaziz, T. Youssef, Effect of size, concentration, and type of spherical gold nanoparticles on heat evolution following laser irradiation using tissue-simulating phantoms, *Lasers in Medical Science*, 31 (2016) 625-634.
[239] Q.W. Tian, F.R. Jiang, R.J. Zou, Q. Liu, Z.G. Chen, M.F. Zhu, S.P. Yang, J.L. Wang, J.H. Wang, J.Q. Hu, Hydrophilic Cu9S5 Nanocrystals: A Photothermal Agent with a 25.7% Heat Conversion Efficiency for Photothermal Ablation of Cancer Cells in Vivo, *Acs Nano*, 5 (2011) 9761-9771.
[240] B. Liu, C.X. Li, B.G. Xing, P.P. Yang, J. Lin, Multifunctional UCNPs@PDA-ICG nanocomposites for upconversion imaging and combined photothermal/photodynamic therapy with enhanced antitumor efficacy, *Journal of Materials Chemistry B*, 4 (2016) 4884-4894.
[241] G.B. Shan, R. Weissleder, S.A. Hilderbrand, Upconverting Organic Dye Doped Core-Shell Nano-Composites for Dual-Modality NIR Imaging and Photo-Thermal Therapy, *Theranostics*, 3 (2013) 267-274.
[242] N. Rakov, G.S. Maciel, M. Xiao, Upconversion fluorescence and its thermometric sensitivity of Er^{3+}:Yb^{3+} co-doped SrF_2 powders prepared by combustion synthesis, *Electro. Mater. Lett.*, 10 (2014) 985-989.
[243] C.D.S. Brites, A. Millán, L.D. Carlos, in: J.-C.G. Bünzli, V.K. Pecharsky (Eds.) *Handbook on the Physics and Chemistry of Rare Earths*, Elsevier Science, B. V., Amsterdam, 2016, pp. 339-427.
[244] N. Rakov, G.S. Maciel, Near-infrared emission and optical temperature sensing performance of Nd^{3+}: SrF_2 crystal powder prepared by combustion synthesis, *J. Appl. Phys.*, 121 (2017) 113103.
[245] A.L. Patterson, The Scherrer formula for x-ray particle size determination, *Phys. Rev.*, 56 (1939) 978-982.
[246] L. Wei, S. Doughan, Y. Han, M.V. DaCosta, U.J. Krull, D. Ho, The Intersection of CMOS Microsystems and Upconversion Nanoparticles for Luminescence Bioimaging and Bioassays, *Sensors*, 14 (2014) 16829-16855.
[247] S. Shionoya, 1999.